MINES ParisTech | PSL

eman ta zabal zazu

Universidad del País Vasco

Euskal Herriko Unibertsitatea

Cosserat thermo-mechanics under finite deformations: theory and finite element implementation

PhD Thesis

Author:

Raffaele Russo

Supervisors:

Prof. Franck Andrés Girot Mata (UPV/EHU)
Prof. Samuel Forest (MINES ParisTech)

Thesis submitted to the Universtity of the Basque Country and to the MINES ParisTech PSL for the degree of Doctor.

This PhD thesis is part of the Horizon 2020 ITN Marie Curie Skłodowska Action. Project ENABLE, grant agreement n°764979.

(cc) 2022 Raffaele Russo (cc by 4.0)

"Citation."
-Author.

Acknowledgements

I would like to thanks...

Summary - Resumen - Résumé

English

Predicting the performance of manufactured parts is extremely important, especially for industries in which there is almost no room for uncertainties, such as aeronautical or automotive. Good quality manufacturing operation simulations are essential to obtain reliable numerical predictions of the processes. Numerical methods such as Finite Element Methods represent a powerful instrument in achieving high level of reliability of the simulations.

During most metal manufacturing processes, the medium deforms by generating large quantities of plastic strain and relatively high strain rates. Working with metals that are characterized by low thermal conductivity properties inevitably induces heat to be locally retained, thus developing high temperatures where the material deforms the most. Such particular combinations of low thermal-property material and high strain-rates-inducing manufacturing processes might lead to plastic strain localization, also known as *Adiabatic Shear Bands* (ASB). These are unfavorable conditions for the classical mathematical models that are used to predict the behavior of the continuum, because they are not anymore able to deliver predictions that are in good agreement with experimental evidence. Under these circumstances in fact spurious mesh dependency is exhibited.

Since the first evidences of the shortcomings of the classical model were highlighted, many non-classical continuum mechanics theories have been developed to overcome this issue, and most of them introduce dependencies at different levels with the plastic strain gradient. In the first part of the manuscript, some of these theories are presented and their specific regularization properties are addressed. One option which can be used to regularize such a non-physical behavior is to resort to the micromorphic continuum.

The micromorphic theory enhances the continuum description by introducing additional degrees of freedom to the body, such that its position is not the only variable that can uniquely describe the status of the continuum. In the example of the micromorphic theory, the additional degree of freedom might be forced to coincide with the cumulative plastic strain. This manuscript includes the investigations on the extents of the regularization properties of the scalar micromorphic plastic strain gradient theory.

The cumulative plastic strain, however, is not the only field which can be used to regularize the artifacts previously discussed. In fact, we can imagine to enhance the continuum with not only one, but three additional variables, which are meant to represent the parametrized grain rotations. For such specific choice of micromorphic variable, the micromorphic theory takes the name of Cosserat theory, named after the two French Cosserat brothers. In the Cosserat theory the grain rotation is used to define a non-

classical strain measure, in which the difference between material and grain rotation represents an additional deformation measure, thus inducing additional forms of stress.

The Cosserat theory represents the core of the investigation pursued during the PhD that led to the present manuscript. The theory has first been studied in its small deformation framework. The effects of the characteristic lengths on the thickness of the predicted shear bands have been reported, and the simulations of the ASB formation have been carried out using such theory. Subsequently, a large deformation framework of the elasto-visco-plastic Cosserat theory has been proposed. The model has been developed under adiabatic thermomechanically-compatible assumptions, in order to cope with the conditions that are met during machining operations. The model has been implemented in a FE numerical software. Simple and more complex tests have been used to validate the model implementation.

Since deformation localization was the main area of investigation, specific analytical solutions of simplified localization cases have been developed under small deformation framework using the elasto-plastic Cosserat media. The analytical solutions have also been used to verify the correctness of the numerical implementation.

Castellano

La predicción de las prestaciones de una pieza fabricada es extremadamente importante, especialmente para las industrias en las que casi no hay lugar para las incertidumbres, como la aeronáutica o la automoción. Las simulaciones de operaciones de fabricación de buena calidad son esenciales para obtener predicciones numéricas fiables de los procesos. Los métodos numéricos, como los métodos de elementos finitos, representan un poderoso instrumento para lograr un alto nivel de fiabilidad de las simulaciones.

Durante la mayoría de los procesos de fabricación de metales, el medio se deforma generando grandes cantidades de deformación plástica y velocidades de deformación relativamente altas. Trabajar con metales que se caracterizan por sus bajas propiedades de conductividad térmica induce inevitablemente a que el calor se retenga localmente, desarrollando así altas temperaturas donde el material se deforma más. Estas combinaciones particulares de material con bajas propiedades térmicas y procesos de fabricación que inducen altas velocidades de deformación pueden conducir a la localización de la deformación plástica, también conocida como *Adiabatic Shear Bands* (ASB). Estas son condiciones desfavorables para los modelos matemáticos clásicos que se utilizan para predecir el comportamiento del continuo, porque ya no son capaces de ofrecer predicciones que estén en buen acuerdo con la evidencia experimental. En estas circunstancias, de hecho, se exhibe una dependencia espuria de la malla.

Desde que se pusieron de manifiesto las primeras evidencias de las deficiencias del modelo clásico, se han desarrollado muchas teorías de mecánica del continuo no clásicas para superar este problema, y la mayoría de ellas introducen dependencias a diferentes niveles con el gradiente de deformación plástica. En la primera parte del manuscrito, se presentan algunas de estas teorías y se abordan sus propiedades específicas de regularización. Una opción que puede utilizarse para regularizar este comportamiento no físico es recurrir al continuo micromórfico.

La teoría micromórfica mejora la descripción del continuo introduciendo grados de libertad adicionales al cuerpo, de manera que su posición no es la única variable que puede describir de forma única el estado del continuo. En el ejemplo de la teoría micromórfica, el

grado de libertad adicional puede ser forzado a coincidir con el gradiente de la deformación plástica acumulada. Este manuscrito incluye las investigaciones sobre los alcances de las propiedades de regularización de la teoría del gradiente de la deformación plástica micromórfica escalar.

Sin embargo, la deformación plástica acumulativa no es el único campo que puede utilizarse para regularizar los artefactos anteriormente discutidos. De hecho, podemos imaginar mejorar el continuo no sólo con una, sino con tres variables adicionales, que están destinadas a representar las rotaciones de grano parametrizadas. Por esta elección específica de la variable micromórfica, la teoría micromórfica toma el nombre de teoría Cosserat, llamada así por los dos hermanos franceses Cosserat. En la teoría de Cosserat la rotación del grano se utiliza para definir una medida de deformación no clásica, en la que la diferencia entre la rotación del material y del grano representa una medida de deformación adicional, induciendo así formas adicionales de tensión.

La teoría de Cosserat representa el núcleo de la investigación realizada durante el doctorado que dio lugar al presente manuscrito. La teoría se ha estudiado primero en su marco de pequeñas deformaciones. Se ha informado de los efectos de las longitudes características sobre el espesor de las bandas de cizalladura predichas, y se han realizado simulaciones de la formación de ASB utilizando dicha teoría. Posteriormente, se ha propuesto un marco de gran deformación de la teoría elasto-visco-plástica de Cosserat. El modelo se ha desarrollado bajo supuestos adiabáticos compatibles con la termomecánica, con el fin de hacer frente a las condiciones que se dan durante las operaciones de mecanizado. El modelo se ha implementado en un software numérico de elementos finitos. Se han utilizado ensayos simples y más complejos para validar la implementación del modelo.

Dado que la localización de las deformaciones era el área principal de investigación, se han desarrollado soluciones analíticas específicas de casos simplificados de localización en el marco de pequeñas deformaciones utilizando el medio elasto-plástico de Cosserat. Las soluciones analíticas también se han utilizado para verificar la corrección de la implementación numérica.

Français

La prédiction des performances d'une pièce fabriquée est extrêmement importante, en particulier pour les industries dans lesquelles il n'y a pratiquement pas de place pour les incertitudes, comme l'aéronautique ou l'automobile. Des simulations d'opérations de fabrication de bonne qualité sont essentielles pour obtenir des prédictions numériques fiables des processus. Les méthodes numériques telles que la méthode des éléments finis constituent un instrument puissant pour atteindre un haut niveau de fiabilité des simulations.

Pendant la plupart des processus de fabrication des métaux, le milieu se déforme en générant de grandes quantités de déformation plastique et des taux de déformation relativement élevés. Le fait de travailler avec des métaux caractérisés par de faibles propriétés de conductivité thermique induit inévitablement une rétention locale de la chaleur, développant ainsi des températures élevées là où le matériau se déforme le plus. Ces combinaisons particulières de matériaux à faible propriété thermique et de procédés de fabrication induisant des taux de déformation élevés peuvent conduire à une localisation de la déformation plastique, également connue sous le nom de *Bandes de cisaillement adiabatiques* (ASB). Ce sont des conditions défavorables pour les modèles mathématiques

classiques qui sont utilisés pour prédire le comportement du continuum, car ils ne sont plus capables de fournir des prédictions en bon accord avec les résultats expérimentaux. Dans ces circonstances, on observe en fait une dépendance fallacieuse à la taille de maille
.

Depuis les premières preuves de l'insuffisance du modèle classique, de nombreuses théories non classiques de la mécanique des milieux continus ont été développées pour surmonter ce problème, et la plupart d'entre elles introduisent des dépendances à différents niveaux par rapport au gradient de déformation plastique. Dans la première partie du manuscrit, certaines de ces théories sont présentées et leurs propriétés de régularisation spécifiques sont abordées. Une option qui peut être utilisée pour régulariser un tel comportement non-physique est de recourir au milieu micromorphe.

La théorie micromorphe améliore la description du continuum en introduisant des degrés de liberté supplémentaires pour le corps, de sorte que sa position n'est pas la seule variable qui peut décrire de manière unique l'état du continuum. Dans l'exemple de la théorie micromorphe, le degré de liberté supplémentaire peut coïncider avec la déformation plastique cumulée. Ce manuscrit inclut les investigations sur l'étendue des propriétés de régularisation de la théorie scalaire micromorphe du gradient de déformation plastique.

La déformation plastique cumulative, cependant, n'est pas le seul champ qui peut être utilisé pour régulariser les artefacts discutés précédemment. En fait, nous pouvons imaginer d'améliorer le continuum avec non seulement une, mais trois variables supplémentaires, qui sont censées représenter les rotations paramétrées des grains. Pour un tel choix spécifique de variable micromorphique, la théorie micromorphique prend le nom de théorie de Cosserat, du nom des deux frères français Cosserat. Dans la théorie de Cosserat, la rotation du grain est utilisée pour définir une mesure de déformation non classique, dans laquelle la différence entre la rotation du matériau et celle du grain représente une mesure de déformation supplémentaire, induisant ainsi des formes de contrainte supplémentaires.

La théorie de Cosserat représente le cœur de l'investigation poursuivie pendant le doctorat qui a conduit au présent manuscrit. La théorie a d'abord été étudiée dans le cadre des petites déformations. Les effets des longueurs caractéristiques sur l'épaisseur des bandes de cisaillement prédites ont été rapportés, et les simulations de la formation des ASB ont été effectuées en utilisant cette théorie. Par la suite, un cadre de grande déformation de la théorie élasto-visco-plastique de Cosserat a été proposé. Le modèle a été développé sous des hypothèses adiabatiques thermomécaniquement compatibles, afin de faire face aux conditions rencontrées pendant les opérations d'usinage. Le modèle a été implémenté dans un logiciel numérique par éléments finis. Des tests simples et plus complexes ont été utilisés pour valider l'implémentation du modèle.

La localisation de la déformation étant le principal domaine d'investigation, des solutions analytiques spécifiques de localisation simplifiés ont été développées dans un cadre de petites déformations en utilisant le milieu élasto-plastique de Cosserat. Les solutions analytiques ont également été utilisées pour vérifier l'exactitude de l'implémentation numérique.

Contents

1 Introduction **12**

2 Literature review **16**
2.1 Challenges in Manufacturing Processes Simulations 17
2.1.1 Strain localization & Mesh-Size Dependency 19
2.1.2 Material characterization at High Temperatures and High Strain Rates 22
2.1.3 Tool-Workpiece Contact 24
2.2 Historical *Excursus* of GCM in Literature 25
2.2.1 Aifantis' Theory 26
2.2.2 Gradient of the local spin vector - Fleck and Hutchinson 1993 . . 27
2.2.3 Second Gradient of displacement - Fleck and Hutchinson 1997 . . 28
2.2.4 Gradient of the cumulative plastic strain - Fleck and Hutchinson 2001 29
2.2.5 Irrotational plastic flow and Burgers tensor - Gurtin and Anand 2005 30
2.2.6 The common framework - Gudmundson 2004 30
2.2.7 Dislocations-enriched SGT 31
2.2.8 Gradient of micro-structure rotation - Cosserat Media 33
2.2.9 Gradient of micro-structure deformation - Micromorphic Media . . 34
2.3 Reported Applications of GCM in Manufacturing Processes Simulation . . 35
2.3.1 Scalar SGPT applied to flat punch molding 36
2.3.2 SGPT used to model rolling at small scale 37
2.3.3 MSGT applied to orthogonal cutting 38
2.3.4 Micromorphic Media applied to forming 39
2.4 Conclusion 41

3 A micromorphic plasticity explicit scheme for metal manufacturing simulations **43**
3.1 Introduction 44
3.2 Theoretical Formulation and Finite Element Implementation 45
3.2.1 Kinematics and Balance Equations 46
3.2.2 Helmholtz Free Energy Potential 47
3.2.3 Clausius-Duhem Inequality 48
3.2.4 Partial differential equation governing the micromorphic variable and enhanced hardening law 49
3.2.5 Micromorphic-Thermal Analogy 50
3.2.6 Influence on the C_χ parameter 52

3.2.7 Numerical Implementation . . . 52
3.3 Strain Localization in simple shear test . . . 55
3.3.1 Analytical solution . . . 55
3.3.2 FE solution . . . 57
3.4 Numerical examples . . . 59
3.4.1 Shearing Operation . . . 60
3.4.2 Bending . . . 63
3.5 Conclusion . . . 66

4 Application of the infinitesimal Cosserat theory to localization 67
4.1 Generalized Cosserat Media under Small Displacement Assumption . . . 69
4.1.1 Kinematics and Balance Laws . . . 69
4.1.2 Clausius-Duhem inequality . . . 70
4.1.3 General Elastic Material Model . . . 73
4.1.4 General Visco-Plastic Material Model . . . 73
4.1.5 Adiabatic Temperature Evolution . . . 75
4.2 Regularization of the Solution & Choice of the Minimun Mesh Size . . . 78
4.2.1 Minumum Mesh Size Identification . . . 80
4.3 Elastic characteristic length calibration . . . 81
4.4 Plastic characteristic length calibration . . . 83
4.5 Conclusion . . . 86

5 Analytical solutions in Cosserat elasto-plasticity 87
5.1 Reformulation of the equivalent plastic stress in the cosserat media . . . 87
5.2 Set 1 of boundary conditions: free micro-rotations . . . 90
5.2.1 Elastic behavior with free rotations . . . 92
5.2.2 Elasto-plastic behavior with free micro-rotations . . . 94
5.2.3 Softening, H<0: localization of deformation. . . . 97
5.3 Set 2 of boundary conditions: fixed micro-rotations . . . 103
5.3.1 Elastic behavior with fixed micro-rotations . . . 104
5.3.2 Elasto-plastic behavior with fixed micro-rotations . . . 105
5.3.3 Perfect plasticity, H=0 . . . 107
5.3.4 Softening, H<0 . . . 111
5.3.5 Hardening, H>0 . . . 113
5.4 Choice of the mechanical properties. . . . 116
5.5 Summary of the Analytical Solutions . . . 117

6 Large deformation Cosserat thermomechanics 119
6.1 Recalls of algebraic rotations . . . 119
6.2 Cosserat kinematics . . . 121
6.2.1 Choice of the elasto-plastic decomposition . . . 123
6.3 Balance laws . . . 126
6.4 Hyper-elastic material . . . 129
6.5 Rate-dependent elasto-viscoplastic material . . . 131
6.5.1 Rate-dependent elasto-viscoplastic material with no dissipated wryness . . . 134
6.6 Rate-independent elasto-plastic materials . . . 135
6.6.1 Rate-independent elasto-plastic materials with no dissipative wryness 137

6.7 Thermal analysis . . . 138

7 Numerical implementation of the large deformation Cosserat model 140
7.1 Strong form of the equilibrium equation and virtual work principle . . . 141
7.2 Three dimensional model . . . 151
7.2.1 Material tangent matrix . . . 151
7.2.2 Variation of Mandel stress and couple stress tensors . . . 155
7.2.3 Derivatives of R and Gamma . . . 156
7.3 Plane strain model . . . 158
7.3.1 Material tangent matrix in 2D . . . 160
7.3.2 Variation of Mandel stress and couple stress in 2D . . . 164
7.3.3 Derivatives of R and Gamma in 2D . . . 164
7.4 Updating the deformation measures . . . 166

8 Simulations of Cosserat thermo-mechanics at finite deformation 168
8.1 Homogeneous fields: single element tests . . . 169
8.1.1 Hyper-elastic, visco-plastic and elasto-plastic tension test . . . 169
8.1.2 Hyper-elastic, visco-plastic and elasto-plastic glide test . . . 172
8.2 Simple micro-rotation boundary layer . . . 172
8.3 Semi-infinite plane under glide: shear band analysis . . . 175
8.3.1 Shear band broadening for saturating yield stress . . . 177
8.3.2 Viscous and thermal effects on shear band broadening . . . 182
8.4 Hat-shaped specimen . . . 184
8.5 Manufacturing simulations . . . 186

9 Conclusion and future developments 194

Chapter 1

Introduction

Manufacturing processes of metallic materials can be found in almost every engineering field, e.g. aerospace, naval and civil. Performing the numerical simulations of the processes, however, still represents a big challenge in many aspects. The material, in fact, during the process, experiences prohibitive deformation fields, consequently reaching very high temperatures, close to the material melting point. From the physical standpoint, a properly-adapted model is necessary to obtain results from the simulation that would describe the real medium development.

During machining, for example, the metal is shaped into its final form through removal of small quantities of material, which is shredded from the final piece through shear deformation mainly. The material locally experiences high plastic deformation, which induce, if the adiabatic condition is met (the thermal diffusion is characterized by a lower velocity than heat production rate), to locally retain high temperatures, thus leading to material thermal-softening. Upon material softening, a severe mesh dependence is experienced whether these equations were to be solved through *Finite Element Modeling* (FEM) [de Borst and Mühlhaus 1992; Chambon et al. 1998; W. M. Wang et al. 1997]. On top of that, an accurate, thermodynamically-consistent material description must be employed to correctly capture the thermal softening induced by high plastic deformation [Aldakheel et al. 2017; Lele et al. 2009; Cheng et al. 2015; Wcisło and Pamin 2017; Pamin et al. 2017]. Furthermore, the fact that during these processes the deformation is prone to localize in narrow areas makes it necessary to adopt numerical models which are able to predict size-effects [Fleck and Hutchinson 1997; González et al. 2014; Yuan et al. 2001; Joshi et al. 2004; Wu et al. 2010; Marchand et al. 1988; Nguyen et al. 2015; Poole et al. 1996; Stölken et al. 1998].

It is well known that the classical Cauchy continuum description is not sufficient to predict the different responses of the medium when either stresses or strains localize. Although experimental evidence strongly emphasized the existence of size-dependent behaviors, where *smaller is the size, stronger is the response*, the classical continuum mechanics models do not possess a characteristic length scale that allows the prediction of said size-effects. The description of the classical continuum mechanics is, in fact, of a *local nature*, meaning that the configuration of the medium at any location is solely determined by the properties characterizing the continuum at that specific location, and the distribution of the said properties in the neighborhood of this location does not in-

fluence the local properties. Several descriptions of the continuum have been proposed in the literature as alternatives to the classical continuum mechanics, in the attempt of including a gradient-related response of the medium, and these theories are referred to as *non-local* or *higher-order* theories. In general, any continuum mechanics model, different from the classical model, belongs to the family of the *generalized continuum mechanics*. A common feature that is shared by all of them is the appearance of a characteristic length scale in the constitutive framework, which naturally arises when the internal power and the constitutive material model are explicitly defined.This characteristic length scale determines the magnitude with which the model responds to localization of deformation.

Another limitation of the classical theory can be identified when tackling strain localization problems: if a specific form of the constitutive material behavior is chosen, the static boundary value problem loses its ellipticity and assumes a hyperbolic character. This problem characterizes, but is not limited to (same behavior could be found for non-associated plastic flow, e.g., [Sabet et al. 2019; Vardoulakis 1980; Needleman 1979]), the condition in which the material tangent experiences a local negative slope. The change in the form of a boundary value problem causes the solution not to be uniquely determined anymore. The negativeness of the material tangent could be induced by several physical phenomena, and the one which most concerns our research is the thermal softening induced in metallic materials severely deformed. Such behavior can be experienced by the continuum when high temperatures are locally produced by the plastic deformation and subsequently retained due to the the combination between low thermal conductivity of the materials and high strain rates. At relatively high temperatures, the material reduces its yield strength, subsequently experiencing a softening of a thermal nature. From the analytical point of view the boundary value problem is not uniquely defined, and from the numerical point of view (if the problem ought to be discretized through Finite Element Method, for instance), the solution appears to be spuriously mesh-dependent.

As already mentioned, these problems are strongly relevant to manufacturing process simulations because the material is heavily deformed in a short amount of time, thus inducing deformation localization and thermal softening. Moreover, it was already demonstrated that a strong size effect characterizes some manufacturing processes and that the classical continuum mechanics was no longer adequate to predict these behaviors [K. Liu et al. 2007; X. Wang 2007; Pamin et al. 2017; Demiral et al. 2016; Guha et al. 2014].

The research presented in this PhD manuscript is devoted to assess these problems in metal manufacturing simulations. Resorting to a generalized continuum mechanics theory could compensate for the limitations of the classical continuum mechanics both in terms of size-effects and spurious mesh-dependency. At first, a Strain Gredient theory has been used to solve these problems. The implementation of this theory in a FEM software has been done through the micromorphic theory [Eringen 1999a], taking advantage of a specific analogy among the thermal equilibrium equations and the micromorphic balance equations. Therefore, as a first step, this simple approach was adopted, and just with a small effort it was possible to demonstrate that some of the problems characterizing metal manufacturing simulations could be solved by using generalized continuum mechanics.

However, the processes of interest are highly characterized by shear deformation, thus the medium undergoes large material rotations at the locations where the deformation localizes. This line of reasoning, coupled with the fact that the deformations are localized in areas the size of which is comparable with the grain size, led us think that the rotations

experienced by the micro-structure, whose effects are normally neglected during homogeneous deformation, would assume a major role in characterizing the material response during these processes, and a medium description that fits well with this description is the Cosserat theory [Cosserat et al. 1909].

The Cosserat theory finds many applications in geomechanics, because the mechanical behavior of the soil, being a granular material at macroscopic level, is characterized by a size effects already at macroscopic level [Mühlhaus et al. 1987; Tordesillas et al. 2004; Rattez et al. 2018]. However, besides geomechanics, the Cosserat model has also been extensively used both for homogeneous metal materials [Grammenoudis et al. 2001; Bauer, Dettmer, et al. 2012] and polycrystal materials [Forest, Cardona, et al. 2000; Neff 2006; Ask et al. 2019; Jebahi et al. 2020], and many authors focused on different aspects of the Cosserat medium description. Steinmann and Willam investigated on the localization properties of the Cosserat model in elasto-plastic materials under infinitesimal deformations in case the loss of ellipticity was caused by negative material tangent operator [Steinmann and William 1991]. De Borst and Sluys demonstrated that the presence of an internal length in a von Mises plastic model formulated for the Cosserat medium can be used to avoid mesh dependency when localization phenomena were simulated [de Borst 1991a]. Most recently, Sabet and de Borst demonstrated that the Cosserat medium description retains ellipticity also in case the material model is characterized by a non-associated rate-independent plastic flow [Sabet et al. 2019]. Kratochvíl et al. investigated over the characteristic lengths introduced by the Cosserat medium description from a physical point of view, by relating the Cosserat wryness to the Nye's dislocation tensor, thus interpreting the wryness tensor as a measure of geometrically necessary dislocations [Kratochvíl et al. 1999]. Khoei et al. drew a distinction between torsional and bending characteristic lengths, and they investigated the effect of these lengths on the shear bandwidth during different localization processes [Khoei et al. 2010]. Many lines of work can also be found in literature proposing a thermodynamically-consistent model of the Cosserat kinematics [Grammenoudis et al. 2001; Bauer, Dettmer, et al. 2012; Forest and Sievert 2003; Forest and Sievert 2006; Rattez et al. 2018].

This PhD manuscript is structured in different chapters, each one addressing specific topics that have been investigated while attempting at answering the question of solving problems related to manufacturing simulations. In the first chapter a state-of-the-art review on the various technologies used to simulate manufacturing operations will be presented. The second chapter will introduce and explore the topic of strain gradient applied to manufacturing simulations via the thermal-micromorphic analogy; the advantages of adopting such theory will be analyzed by presenting three test cases in which strain localization and size-effect will be tackled. In the fourth chapter the most general thermodynamically-compatible Cosserat theory under a small deformation framework will be described; the advantages of adopting such theory will follow in the same chapter, in which a localization study will serve to demonstrate the full potential of the Cosserat theory. The fifth chapter will address a novel equivalent stress evaluation in the Cosserat media and novel analytical solutions of localization cases again using the Cosserat media. The thermodynamically-compatible finite deformations Cosserat theory will be presented in the sixth chapter, in which the elastic, plastic , viscoplastic and thermal aspects of the formulation will be defined. The seventh chapter includes the discretization and numerical implementation of the Cosserat theory under finite deformations in a FEM software. The eighth chapter presents the tests that have been performed on the implemented theory,

comparison with the developed analytical solutions, and additional simulations of manufacturing operations, such as machining. The ninth chapter will conclude the manuscript with a summary of the developed investigation and the future development.

About the project

The PhD, whose manuscript is here presented, is part of an Innovative Training Networks (**ITN**) **Marie Skłodowska-Curie Action**, and it is included in the Horizon2020 programme. The PhD is part of the **ENABLE** project, acronym for European Network for Alloy Behavior Law Enhancement (http://www.enable-project.com/About). The project, as well as the PhD programme whose manuscript is here presented, have been founded by the European Union under the agreement number 764979.

The investigation proposed in this manuscript has been conducted between Spain and France. This PhD programme is in fact regulated by a cross-border cotutelle agreement signed by the University of the Basque Country in Bilbao (Spain) and MINES ParisTech in Paris (France).

Chapter 2

Literature review

The topic of *Strain Gradient Theories* (SGT) experienced a fervent increase of interest from the scientific community in recent years. Although multiple reasons made the SGT one of the hot topics in the field of *Continuum Mechanics* (CM), the main causes can be identified in the ever-increasing computational power of numerical calculators (thus enabling the implementation of techniques beforehand impossible to use) and in the demand of more sophisticated CM theories which would better predict the medium behavior under specific material deformation conditions. SGTs are specific theories that diverge from the Classical CM, and for this reason they belong to the larger family of *Generalized Continuum Mechanics* (GCM). GCM could be employed whenever the Classical CM framework is not delivering anymore a proper medium behavior description if compared with experimental observations. The features characterizing some models belonging to the GCM can be of crucial importance in several situations, and in this chapter we assess the role that they might play for manufacturing process simulations. However, it must be noted that the adoption of such theories increases the computational cost involved in simulating the observed phenomenon.

The most general feature, shared by many theories of the GCM, is the introduction of one or more scale lengths in the model used to describe the medium behavior. This is done through the definition of additional deformation measures that are meant to capture specific phenomena which cannot be predicted by the classical CM models. In the vast majority of the cases, the magnitude and the influence of these additional deformation measures are negligible if compared with the standard one, i.e. strain. In specific situations, however, the material behavior demonstrates noticeable susceptibility to these supplementary deformation measures, and proper models are required to capture such behaviors through simulations. The gradient of the strain has been widely and unanimously recognized as one of the main feature which needs to be incorporated in the Classical CM theory to predict such behaviors. Among all the SGTs, those that make use of the gradient of the plastic part of the strain are called *Strain Gradient Plasticity Theories* (SGPT).

Experimental observations show that many metal manufacturing processes are affected by these phenomena, demonstrating noticeable sensitivity toward non-conventional deformation measures [Joshi et al. 2004; Royer et al. 2011; Voyiadjis et al. 2009; Wu et al. 2010; J. Huang et al. 2001; Laheurte et al. 2006; Cahuc et al. 2007; K. Liu et al. 2007; X. Wang

2007; Demir 2009; Jing et al. 2013]. The manufacturing techniques in which the strain gradient plays a bigger role result to be those in which the loads are highly localized, e.g. micro-cutting, milling, micro-bending, thin wire drawing, machining, friction stir welding, sheet stamping, inverse drawing, adiabatic cutting. These machining processes favor the development of rather peculiar conditions in the processed material, where a combination of separate factors contribute to produce a relatively complex scenario.

The present research aims at addressing the following research question: *What is the state of the art in using generalized continuum mechanics to simulate manufacturing processes.* This research question can be broken-down in the following sub-questions:

- What is a generalized continuum mechanics model?
- Why such models are required for the simulation of manufacturing operations?
- Which enhanced models of continuum mechanics can be used to simulate manufacturing operations?
- Which contributions can be found in literature that already used enhanced model to simulate manufacturing operations?

In Section 2.1, this multitude of events simultaneously taking place during these processes are singularly assessed, and then the features that represent them are traduced into requirements of a continuum mechanics theory meant to correctly describe them. Section 2.2 presents the milestones in the development of different theories of the GCM and in Section 2.3 the investigations that employed these theories to simulate machining operations will be thoroughly reviewed. Finally, the conclusions of the present review will present advantages and disadvantages of using different theories from GCM to simulate different machining processes.

2.1 Challenges in Manufacturing Processes Simulations

Among the different metal manufacturing techniques, the ones that require a proper theory to be described are those that modify the material through strain localization, or severe plastic strain development or material removal, or a combination of those. During machining, for example, material is removed from the work piece by inducing large amounts of shear in localized areas called *Shear Bands* (SBs) (see Figure 2.1). Due to the high speed of the process (cutting velocities up to 90 m/s)[Ye et al. 2014; Molinari, Musquar, et al. 2002; Dixit et al. 2011; Tang et al. 2018], high strain rates (10^5 s^{-1}) are induced in the SBs [Calamaz et al. 2008; List et al. 2013; Lee et al. 2006]. The high levels of stresses and strains give rise to plastic deformations, therefore inducing softening in the material at this same location. In addition to this, since the SBs usually span an extremely narrow area if compared to the global scale of the work piece, the continuum at this location experiences high stress and high strain gradients as well. To complete the picture, it must be mentioned that plastic deformations usually give rise to heat productions, and considering the case in which the rate of heat production is much larger than the heat flow within the material (especially in metals characterized by low thermal conductivity), high temperature fields are retained, and the SBs are referred to as *Adiabatic Shear Bands* (ASBs). In Figure 2.2 the crystallographic analysis during a

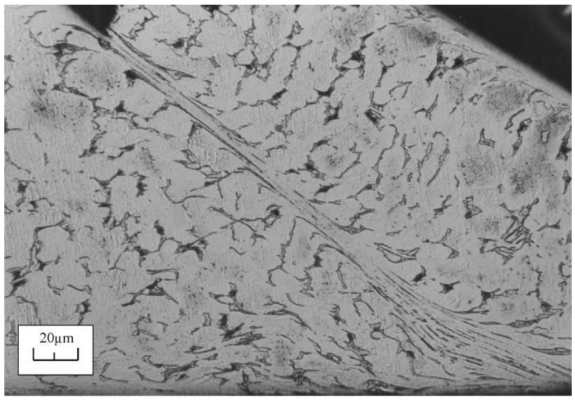

Figure 2.1: Adiabatic Shear Band formation during orthogonal cutting Titanium alloy [Molinari, Musquar, et al. 2002].

Friction Stir Welding process highlights the modification of the grain size and orientation induced during manufacturing. Shear bands have been reported to appear also during a high-temperature compression test on Nickel super-alloy [Tang et al. 2018].

On top of the already complex scenario, at the location where the applied forces are transferred from the tool to the workpiece, the material experiences complex behaviors as well. High stress and shear gradients develop in this zone, leading to the same conditions which are found within the SB. Furthermore, the mechanism with which the loads are transferred from the workpiece to the material must be accurately assessed as well. The extreme conditions in which the contact must be modeled are actually different from the ones for which the classical contact models have been developed

Overall, the problem of simulating machining seems to be composed of several sub-problems, some of them interconnected with each others, and some independent from one another. This complex problem can be more easily assessed if divided into separate and independent blocks. These might be listed as:

- Strain localization in a length scale whose order of magnitude is the same as grain size, therefore violating the limit of validity of material homogeneity;
- Mesh-size hypersensitivity when introducing material softening in the behavior law during the analysis;
- Proper material characterization at high temperatures and high strain rates developing during manufacturing processes;
- The complex material behavior at the tool-workpiece contact location.

These phenomena could take place separately or simultaneously. Several approaches can be found in literature that address these problems individually, but their occurrence, taking place all at once, represents a challenging issue to be addressed. Complex problems, such as the one investigated here, have also addressed through model reduction methods [Chinesta et al. 2011].

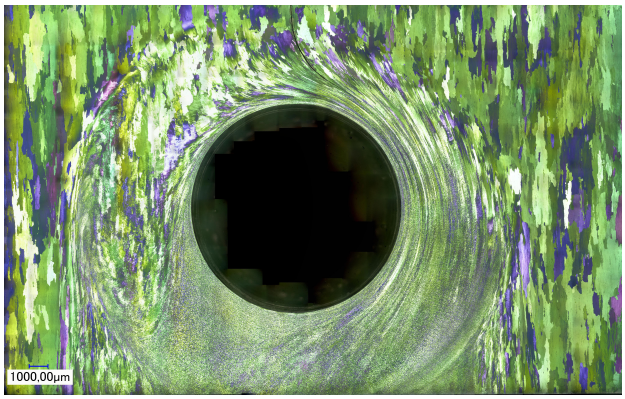

Figure 2.2: Shear bands produced during FSW of AA2050 with an advancing side on the left **(a)**.

2.1.1 Strain localization & Mesh-Size Dependency

Strain localization in a narrow area whose order of magnitude is comparable to the material grain size compels the adoption of a non-classical CM framework that would be able to model the size effect. In literature, several authors highlighted the inadequacy of the classical CM framework whenever it was used to reproduce experimental data in which the size effects were noticeable [Fleck and Hutchinson 1997; Stölken et al. 1998; Begley et al. 1998; Poole et al. 1996; Nix et al. 1998; Ma et al. 1995; González et al. 2014; Stelmashenko et al. 1993; Panteghini and Bardella 2016; Han et al. 2007; Dahlberg and Faleskog 2013; Askes et al. 2011; Gurtin and Anand 2005b; D. Liu and Dunstan 2017; Al-Rub et al. 2005; Duan et al. 2001; E. C. Aifantis 1999]. Overall, the inconsistencies are more pronounced whenever the dimensions of the specimens become comparable to the order of magnitude of the specimen grain size, or, equivalently, when the deformations localize in areas whose size is comparable to the specimen grain size.

Fleck and Hutchinson performed several static torsion and tensile tests on copper wires of different diameters (12-170 μm) [Fleck and Hutchinson 1997]. Their results, reported in Figure 2.3, highlight that smaller diameter wires are characterized by a much stiffer torsional response (scaled with the wire radius), although tensile tests performed on the same specimen demonstrate a very small, thus negligible, size dependency. Similar tests were performed by Liu et al. who reached the same conclusion [D. Liu, Y. He, et al. 2013b; D. Liu, Y. He, et al. 2013a]. Fleck and Hutchinson also reported that the size-effect is present in a Vickers micro-indentation test conducted on single crystal tungsten specimens [Fleck and Hutchinson 1997]. The performed tests demonstrated a strong size-dependency, as the material hardness doubles by using an indent whose diagonal is one order of magnitude smaller. Similar size-effects in a micro-indentation test have also been reported by many other authors [Ma et al. 1995; Poole et al. 1996; González et al. 2014; Nix et al. 1998; Stelmashenko et al. 1993].

The size-effect has also been experimentally investigated by Stölken and Evans [Stölken et al. 1998]. They presented the results of micro-bending tests conducted on 12.5 μm, 25 μm and 50 μm thin Nickel foils (Figure 2.4). The results of their tests highlighted that foils with a smaller thickness were behaving stronger. The applied bending moment

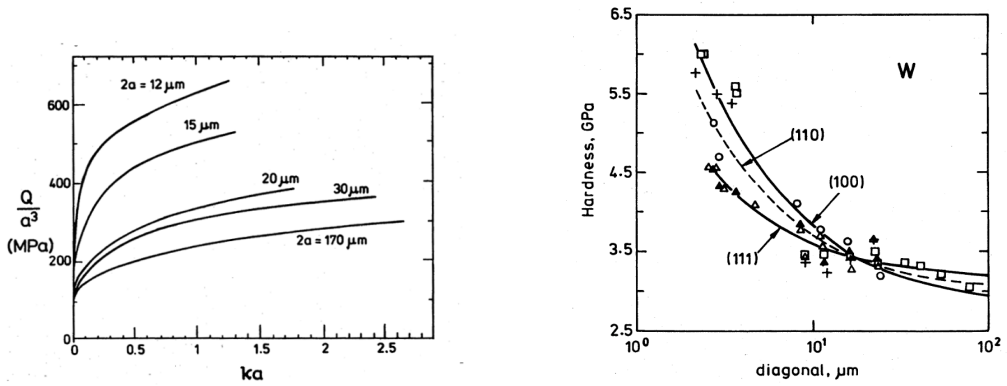

(a) (b)

Figure 2.3: Variation of Torsional stiffness during torsion test on a copper wire **(a)** and variation of Hardness during microindentation test on tungsten single crystal **(b)** [Fleck and Hutchinson 1997].

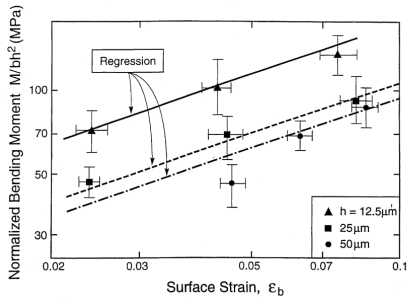

Figure 2.4: Variation of the normalized bending moment on thin Nickle foils during micro-bending test [Stölken et al. 1998].

(normalized with respect to the foil thickness) of the 50 μm thick foil is twice the one recorded with a 12.5 μm thick foil. Similar tests leading to similar conclusions were conducted by Ehrler et al. [Ehrler et al. 2008].

In the same referenced papers, so as in a broad branch of literature [Panteghini and Bardella 2016; Han et al. 2007; Dahlberg and Faleskog 2013; Askes et al. 2011; Gurtin and Anand 2005b; D. Liu and Dunstan 2017; Al-Rub et al. 2005; Duan et al. 2001; E. C. Aifantis 1999], the authors point out that the classical CM is not able to capture these localization phenomena due to the absence of a length scale in the model that would counteract the localization of the fields. Micro-torsion tests also highlighted the shortcoming of the classical CM framework [Dunstan et al. 2009; Fleck, Muller, et al. 1994]. The SGPT, whose mathematical description includes one or more length scales, has been proposed as a valid candidate to capture phenomena of different natures.

The size-effect can be predicted thanks to the definition of an additional deformation measure, i.e. the strain gradient. The dimensional analysis of this quantity reveals that it

is not dimensionless and, unlike strain, it should be adimensionalized by means of a specific length, and the sensitivity of non-classical CM theories to size-effects comes directly from the definition of this non-dimensionless deformation measure. Many researchers investigated over the physical nature of the length scales of the SGPTs. Depending on the degrees of complexity of the observed phenomena, more than one characteristic lengths can be identified. For example, Fleck and Hutchinson identified up to five distinct characteristic lengths, each associated to one of the five invariants of the strain gradient tensor [Fleck and Hutchinson 1997]. These characteristic lengths however can be reduced to three in case of incompressible isotropic medium. In a successive study, Fleck and Hutchinson identified a single characteristic length in an equivalent plastic strain gradient theory [Fleck and Hutchinson 2001]. Liu and Dunstan, based on the SGPT of Fleck and Hutchinson, gave a physical interpretation to the characteristic length by making a connection to physical quantities via critical thickness theory [D. Liu and Dunstan 2017]. Duan et al., based on the same SGPT, associated the additional characteristic length to geometrically necessary dislocations through three different dislocation models [Duan et al. 2001]. Similarly, Dahlberg and Boåsen assumed an equivalence between the microstructural length scale and dislocation density and provided an evolution law of the characteristic length [Dahlberg and Boåsen 2019]. Zhang and Aifantis gave a comprehensive review of the interpretations of the characteristic length associated with SGPTs [X. Zhang et al. 2015].

Several other researchers focused on the calibration procedure and the quantification of this length for metals. Yuan and Chen proposed to identify the characteristic length from micro- and nano- indentation tests [Yuan et al. 2001]. Stölken and Evans developed a micro-bending test to measure the characteristic length [Stölken et al. 1998]. Abu Al-Rub and Voyiadjis also proposed to adopt micro- and nano- indentation tests to calibrate the characteristic length and its evolution law [Al-Rub et al. 2004; Al-Rub et al. 2005].

Thereby, it can be concluded that the problem of properly capturing the size-effect rising during manufacturing simulation due to strain localization can be solved by adopting a medium description that includes the gradient of the strain as a deformation measure. In addition, adding the strain gradient as a deformation measure would solve not only the problem related to size-effect, but also the one related to mesh hypersensitivity.

Mesh hypersensitivity is an issue which has its root in the loss of ellipticity of the partial differential equation governing the medium equilibrium [de Borst and Mühlhaus 1992; Benallal et al. 2010; Wcisło, Pamin, et al. 2018]. In case the non-linear plastic behavior of the material experiences a decreasing flow stress, i.e. softening, the nature of the set of partial differential equations governing the equilibrium changes, and a strong mesh sensitivity is experienced, in particular, the solution does not appear to converge toward an asymptotic value when the mesh size is decreased. The process of recovering the property of mesh independence in literature is referred to as *regularization* procedure.

Jirasek and Rolshoven provided an extensive comparison of the regularization properties of many SGPT by analyzing the response of a mono-dimensional bar under tension, whose plastic behavior is characterized purely by softening [Jirásek et al. 2009]. They explored the regularization mechanics of the Toupin-Mindlin elastic SGT [Toupin 1962; Mindlin 1963], the plastic version of Toupin-Mindlin SGT developed by Chambon et al. [Chambon et al. 1998], the Fleck and Hutchinson plastic SGT [Fleck and Hutchinson 1997] and the Mechanism-based SGT [Qiu et al. 2003]. Nguyen et al. coupled a non-local plasticity model with damage to successfully capture the softening behavior experienced

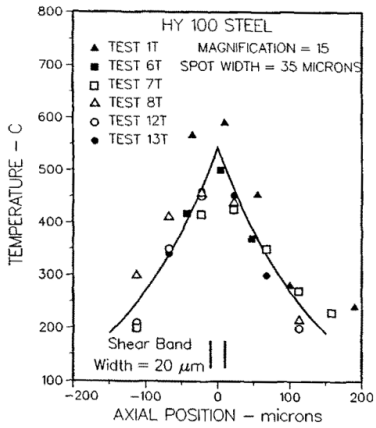

Figure 2.5: Measured Temperature field in a torsional Kolsky test at a strain rate of 1600 s^{-1} [Marchand et al. 1988]

by the material during ductile failure in the post-peak regime [Nguyen et al. 2015]. Lele and Anand demonstrated that SGPTs are able to provide mesh independent results in case of viscoplastic material as well [Lele et al. 2009].

Several other researchers overcame the mesh hypersensitivity issue through other solutions besides the SGT. Mediavilla et al. used a damage-enriched material model, in which the gradient of the damage field would enter in the material model, thereby achieving the same regularization effect produced by the SGTs [Mediavilla et al. 2006]. Many other researchers included the gradient of the damage variable in the model to regularize the solution [Brepols et al. 2017; Saanouni and Hamed 2013; Peerlings et al. 1996; Nguyen et al. 2015]. Higher Order continuum descriptions (see Section 2.2) are also well known equivalent solution to avoid the pathological mesh dependence [Sabet et al. 2019; Mazière et al. 2013; Ling et al. 2018; Forest 2009].

Therefore, the issues of mesh hypersensitivity due to localization during machining simulations can be simultaneously addressed through the adoption of non-local theories, to which the SGPT belong.

2.1.2 Material characterization at High Temperatures and High Strain Rates

The high strain rate fields produced during machining are inevitably intertwined with thermal-related consequences. Materials experiencing high strain rate are likely to plasticize and subsequently to generate heat. If the rate of heat production is higher than the rate of heat conduction, high temperatures will be retained in the plasticized zone. The consequences of high temperatures on material behavior can be easily modeled and they might be independently analyzed and simply assessed by performing material tests at high temperatures; on the contrary, the reliability of the model relating high strain rates with mechanical behavior, due to unavoidable raises in temperature, is dependent on the fidelity of the research done on the thermal behaviors.

In general, it must be recognized that reproducing the same level of shear deformation

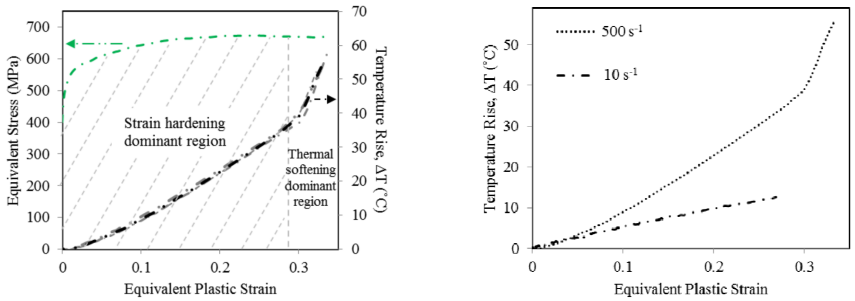

Figure 2.6: **(a)** Correlation between the measured temperature field and the stress-strain curve in a shear test performed at a strain rate of 500 s^{-1}. **(b)** Difference between the temperature fields measured during two shear tests at different strain rates [Rahmaan et al. 2018].

($\approx$ 2.0) and strain rate ($\approx 10^5 s^{-1}$) that takes place during manufacturing processing under controlled lab conditions is not an easy task. The thermal aspect involved in the development of high strain rates was reported by Marchand and Duffy, who collected experimental data of both temperatures and shear strain fields during a dynamic torsion test [Marchand et al. 1988]. They tested a thin hollow tube of HY-100 steel in a torsional Kolsky (split-Hopkinson) bar properly modified to provide torsional loading at high strain rate (1600 s^{-1}). The specimen was 0.38 mm thick and 2.5 mm long, with an inner diameter of 9.5 mm. The authors adopted such high strain rates so as to induce the formation of adiabatic shear bands and then measure the temperatures that developed in the ASB. This condition is equivalent to the one that can occur during machining processes. From the collected data, reported in Figure 2.5, it can be inferred that the thermal contribution to the energy balance cannot be neglected when SBs develop during machining.

The influence of the thermal field and strain rates on the mechanical behavior was also recently investigated by Rahmaan et al. [Rahmaan et al. 2018] (Figure 2.6). They performed dynamic shear tests on 2 mm thick AA7075-T6 sheets at different strain rates (from 0.01 to 10^3 s−1) inducing increments in temperatures of up to 60 º C in the specimen due to plasticity. The authors distinguished between a strain hardening dominant region and thermal softening dominant region. From their results, it is evident that plastic strain at high strain rates (500 s^{-1}) induce a temperature raise causing material softening. Additionally, the temperatures profiles obtained using different strain rates were directly compared, and the analysis showed that the influence of the strain rate on the developed temperature is considerably lower when the strain rates are reduced.

The researches reported in this section proves the fact that in the sought of a complete theory to model machining, the thermal and dynamic contributions cannot absolutely be neglected. Therefore, besides the usual governing equations relative to force equilibrium, a thermodynamical approach must be adopted so that energetic equilibrium equations would be included in the CM model. Therefore, the simulations of manufacturing processes involving very high deformation rates require an approach that would encompass thermodynamical considerations. This can be achieved by properly characterizing the media behavior from a deeper thermodynamical standpoint (from which the material

constitutive behavior naturally derives), while solving the energy equation (heat equation) in addition to the standard set of equations governing the force equilibrium. This approach requires the temperature to be included as an additional degree of freedom of the continuum whose field is the solution of the energy equation. However, if the heat dissipation rate is very small compared to the heat production rate, the boundary value problem can be considered as adiabatic, thus demoting the temperature from a degree of freedom of the system to a state variable [X. Wang 2007; G. Chen et al. 2011; Ye et al. 2014; Calamaz et al. 2008].

Another crucial consideration is that thermal-induced effects could be isolated and separately analyzed, but the opposite cannot be done with high strain rates, which are unavoidably related with heat productions. High temperatures soften the material, whereas higher strain rate have an opposite hardening effect. However, if high levels of strains are rapidly obtained, the material plasticize and temperature developments are expected to occur, thus interconnecting the strain rate effect with the thermal effect. So the ideal approach would be to separate these two aspects: first developing a model of the mechanical behavior that delivers the correct effect of thermal variation on the medium response, and then to successively incorporate the effect of the strain rate on mechanical behavior in terms of hardening.

2.1.3 Tool-Workpiece Contact

During machining processes, the contacts conditions between the tool and the workpiece lie beyond the assumptions made for the contact models usually used in mechanics. Especially the high temperatures and the high pressures, in fact, induce the material to behave more liquid-like than solid-like (see Figure 2.7). The simple Coulomb law is not a good model anymore [Astakov 2006].

Zorev's model is a well-known refined friction model that is widely used for machining simulation. It recognizes two different zones at the tool-workpiece contact zone, each characterized by two different frictional behavior [Zorev 1963]. He individuates a sliding zone, where the material response is purely elastic, and a sticking zone, that is instead characterized by plastic flow.

This special condition does not only require a modification of the classical CM governing equations, but it also impels the adoption of a proper numerical contact model able to cope with a change in the friction conditions from a sliding form to a sticking form (transversely promoted by high temperatures and stresses also). Based on this model, further modifications have been reported in literature attempting at delivering a precise model characterizing the metal behavior in the sliding and sticking regime [Shirakashi et al. 1973; Childs 2006; Bahi et al. 2012; Bahi et al. 2011; Ackroyd et al. 2003].

A throughout review of experimental data on the topic of tool-workpiece interaction was collected by Astakov [Astakov 2006]. In this book chapter he reported many experiments which attempt to extrapolate many features of the phenomena from a tribological point of view such as the friction coefficient (assuming Coulomb law), contact stress distribution, thermal distribution and more.

Towards the development of a more appropriate contact model, the *Friction Stir Welding* (FSW) benchmark, as suggested by Cahuc et al. [Cahuc et al. 2007], might result in a useful mean which could be used to test the validity of the model itself. However, being FSW characterized by some on the main above-cited typical problems

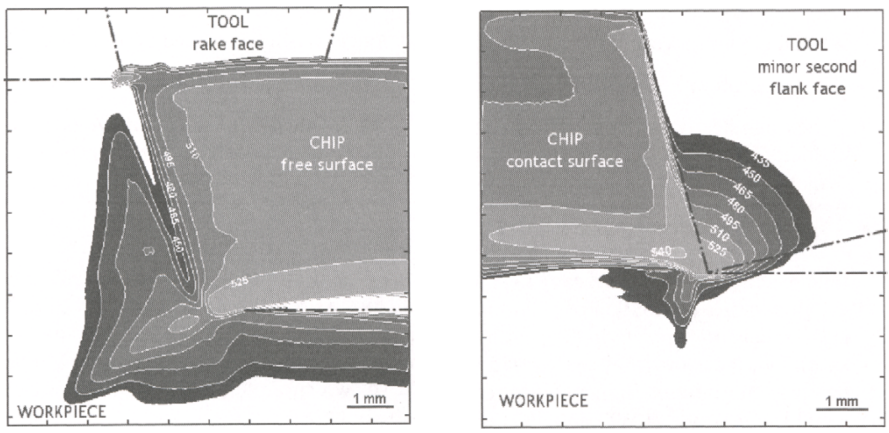

(a) (b)

Figure 2.7: Temperature distribution in the chip during orthogonal cutting on AISI 1045 steel obtained with a camera in circumferential **(a)** and axial **(b)** directions [Astakov 2006].

affecting machining, other independent features must be assesses before being able to test a more complex model.

The enhancement of the governing equations of the continuum mechanics from a classical to a generalized framework will likely bring the introduction of more complex variables associated with status of the continuum, such as strain gradients. Therefore, further considerations must be made on how these additional unknowns will fit into the proposed contact model, or even more important, how the contact conditions affect material deformations in enhanced continua.

2.2 Historical *Excursus* of GCM in Literature

The GCM belongs to a branch of mechanics that aims to describe the continuum behavior through a set of equations which differ from the one belonging to the Classical CM [Eringen 1962; Gurtin 1982]. This definition is attributed to a quite large group of theories, and, they can be further grouped into other two categories: *Higher Order Theories* and *Higher Grade Theories* [Forest and Sievert 2006; Forest 2009]. The former group aims to enhance the continuum with additional degrees of freedom, and the latter adopts the same quantities characterizing the classical CM framework, in addition to their higher spacial gradients. Although the distinction here is quite net, some proposed theories present features that are common to both classes. Most of the GCM belongs to the Higher Order Theories, because they include partial or full contributions of the second gradient of the displacements.

Another major distinction that can be drawn among the GCM theories consists in using the additional deformation measure as internal variable or as additional degree of freedom of the media, and this choice has significant repercussions also at the level of numerical implementation. In the first case, the only degrees of freedom of the continuum

are the displacements, and the additional deformation measure is evaluated purely from them. In the second case, the additional deformation measure is used as a degree of freedom (or it derives from the additional degrees of freedom) and its distribution resolves as the solution of the set of partial differential equation, so as the displacement field. The theories here reported are explored in their small deformation framework.

Notation

Einstein's convention is employed in the whole chapter. Tensors are indicated through compact notation or index notation, regardless of capital or not-capital letters:

$$\begin{aligned}
\underline{\boldsymbol{a}} &\implies a_i; \\
\underset{\sim}{\boldsymbol{a}} &\implies a_{ij}; \\
\underset{\approx}{\boldsymbol{a}} &\implies a_{ijk}; \\
\underset{\approx}{\boldsymbol{a}} &\implies a_{ijkl};
\end{aligned}$$

The outer product is indicated with $\otimes$ and it operates in the following manner:

$$\underset{\sim}{\mathbf{A}} \otimes \underset{\sim}{\mathbf{B}} = \underset{\approx}{\mathbf{C}} \implies A_{ij}B_{kl} = C_{ijkl};$$

Single and double contraction operators are respectively indicated as follows:

$$\begin{aligned}
\underset{\approx}{\mathbf{A}} \cdot \underset{\approx}{\mathbf{B}} = \underset{\approx}{\mathbf{C}} &\implies A_{ijk}B_{klm} = C_{ijlm}; \\
\underset{\approx}{\mathbf{A}} : \underset{\approx}{\mathbf{B}} = \underset{\sim}{\mathbf{C}} &\implies A_{ijk}B_{jkl} = C_{il};
\end{aligned}$$

Divergence and gradient operators are represented as:

$$\begin{aligned}
\underset{\sim}{\mathbf{A}} \otimes \underline{\boldsymbol{\nabla}} = \underset{\approx}{\mathbf{B}} &\implies \frac{\partial A_{ij}}{\partial x_k} = B_{ijk}; \\
\underset{\sim}{\mathbf{A}} \cdot \underline{\boldsymbol{\nabla}} = \underline{\mathbf{B}} &\implies \frac{\partial A_{ij}}{\partial x_j} = B_i;
\end{aligned}$$

where x_i is the *i-th* Cartesian coordinate of an Eulerian space. When handling with skew-symmetric second order tensors, it might be easier to define the first order tensor associated to it as:

$$\underline{\mathbf{A}} = -\frac{1}{2}\underset{\approx}{\boldsymbol{\epsilon}} : \underset{\sim}{\mathbf{B}}; \tag{2.1}$$

where $\underset{\approx}{\boldsymbol{\epsilon}}$ is the Levi-Civita permutation symbol.

2.2.1 Aifantis' Theory

The pioneering work of Aifantis belongs to a class of SGTs known as *Mechanics-Based Strain Gradient* (MSGT). The original idea of Aifantis was to enhance the classical Equation for the flow stress with a term related to the spacial gradient of the plastic strain in order to represent the effect of dislocation-state evolution on a macroscopic scale [E. C. Aifantis 1984; E. C. Aifantis 1987]. The yield stress as defined by Aifantis reads [E. C. Aifantis 1999]:

$$\sigma^Y = \sigma_0 + k\varepsilon^p_{eq} - c_1|\nabla\varepsilon^p_{eq}| - c_2\nabla^2\varepsilon^p_{eq}; \tag{2.2}$$

where σ^Y is the flow stress, σ_0 is the initial flow stress, k, c_1 and c_2 are parameters, ε^p_{eq} is the von Mises cumulative plastic strain and ∇ is the nabla operator, returning the gradient/Laplacian of the field. By using this flow stress evolution law, the strain field in the medium has to be found through solution of partial differential equation. The two characteristic lengths are embedded in the definition of the constants c_1 and c_2. The work of Aifantis was one of the first researches linking micro-defects, such as dislocations, to macro-deformation measures , such as strain. However, the definition of the internal power of the theory was not explicitly stated, and it was not declared whether the inelastic deformations were dissipative or not (the thermodynamic of the model was not originally defined). Successively, Gudmundson [Gudmundson 2004] incorporated the Aifantis model into the broader framework that he proposed, identifying the internal power density definition as:

$$p^{(i)} = \underset{\sim}{\boldsymbol{\sigma}} : \underset{\sim}{\dot{\boldsymbol{\varepsilon}}}^e + q\,\dot{\varepsilon}^p_{eq} + \underline{\mathbf{m}} \cdot \left(\underline{\boldsymbol{\nabla}}\varepsilon^p_{eq}\right); \tag{2.3}$$

where the stress has been partitioned into the contribution conjugate to the elastic deformation ($\underset{\sim}{\boldsymbol{\varepsilon}}$), $\underset{\sim}{\boldsymbol{\sigma}}$, and the part conjugate to the equivalent inelastic strain (ε^p_{eq}), that is a scalar q, and, in addition, the gradient of the equivalent plastic strain is introduced into the internal power definition, where its power conjugate, the moment stress $\underline{\mathbf{m}}$, naturally arises. Gudmundson interpreted this stress as derived from a free energy potential in a quadratic form, as originally suggested by Steinmann [Steinmann 1996]:

$$\psi = L^2\, E\, \underline{\boldsymbol{\nabla}}\varepsilon^p_{eq} \cdot \underline{\boldsymbol{\nabla}}\varepsilon^p_{eq}/2; \tag{2.4}$$

from which, the constitutive model for the moment stress derives as:

$$\underline{\mathbf{m}} = L^2\, E\, \underline{\boldsymbol{\nabla}}\varepsilon^p_{eq}; \tag{2.5}$$

Later on, the thermodynamical considerations related to the Aifantis model have been investigated by Gurtin and Anand [Gurtin and Anand 2009], and they outlined that the Aifantis model cannot be thermodynamically compatible in absence of a defect energy.

2.2.2 Gradient of the local spin vector - Fleck and Hutchinson 1993

Fleck and Hutchinson developed a phenomenological SGT based on the couple-stress theory [Toupin 1964; Toupin 1962; Mindlin 1963], with the idea of relating the strain gradient to the dislocations developed at microstructural level [Fleck and Hutchinson 1993]. Besides the standard definition of strain, they considered also the effects of the skew-symmetric part of the displacement gradient, i.e. the local spin tensor $\underset{\sim}{\boldsymbol{\theta}}$, defined as:

$$\underset{\sim}{\boldsymbol{\theta}} = \text{skew}\left(\underline{\mathbf{u}} \otimes \underline{\boldsymbol{\nabla}}\right); \tag{2.6}$$

being this a skew-symmetric tensor, it can rewritten in a pseudo-vectorial form as:

$$\overset{\times}{\underline{\boldsymbol{\theta}}} = -\frac{1}{2}\underset{\approx}{\boldsymbol{\epsilon}} : \underset{\sim}{\boldsymbol{\theta}}; \tag{2.7}$$

where $\underset{\approx}{\boldsymbol{\epsilon}}$ is the Levi-Civita permutation tensor. The gradient of the local spin vector, which could be though as a material curvature gradient, is:

$$\underset{\sim}{\boldsymbol{\chi}} = \overset{\times}{\underline{\boldsymbol{\theta}}} \otimes \underline{\boldsymbol{\nabla}}; \tag{2.8}$$

and an additional decomposition in plastic and elastic part of curvature is proposed:

$$\underset{\sim}{\boldsymbol{\chi}} = \underset{\sim}{\boldsymbol{\chi}}^{e} + \underset{\sim}{\boldsymbol{\chi}}^{p}; \tag{2.9}$$

Based on the definition of the given deformation measures, the internal power would assume the following shape:

$$p^{(i)} = \underset{\sim}{\boldsymbol{\sigma}} : \dot{\underset{\sim}{\boldsymbol{\varepsilon}}} + \underset{\sim}{\mathbf{m}} : \dot{\underset{\sim}{\boldsymbol{\chi}}}; \tag{2.10}$$

where $\underset{\sim}{\boldsymbol{\sigma}}$ is the Cauchy stress, energetically conjugate to the strain, thereby symmetric tensor, and $\underset{\sim}{\mathbf{m}}$ is the not-symmetric couple stress tensor as also introduced by Toupin and Mindlin [Toupin 1964; Toupin 1962; Mindlin 1963].The definition of the strain energy density function for an isotropic material was given in a quadratic form as:

$$u^{(i)} = \frac{\lambda}{2}\varepsilon^{e}_{ii}\varepsilon^{e}_{jj} + \mu\,\varepsilon^{e}_{ij}\varepsilon^{e}_{ij} + \mu\,l_{el}\chi^{e}_{ij}\chi^{e}_{ij}; \tag{2.11}$$

where λ and μ are the Lamé parameters and l_{el} is an elastic characteristic length used to a-dimensionalize the curvature tensor. The plastic behavior is governed by an equivalent plastic deformation measure that was defined as:

$$\Xi^{p^2} = \varepsilon^{p^2}_{eq} + l^2_{pl}\chi^{p^2}_{eq}; \tag{2.12}$$

where ε^{p}_{eq} is the von Mises strain invariant $\sqrt{2/3\varepsilon^{p}_{ij}\varepsilon^{p}_{ij}}$ and similar definition corresponds to χ^{p}_{eq}. The length l_{pl} is used to a-dimensionalize the plastic contribution of the material curvature tensor (defined as gradient of the plastic part of the local spin tensor), and it was though as the free-slip distance between statistically stored dislocations on an average sense. If the condition $l_{el} \ll l_{pl}$ is applied, then the material curvature is assumed to be mostly plastic, therefore providing a sensitive contribution in characterizing plastic phenomena, while being negligible in elastic regimes.

2.2.3 Second Gradient of displacement - Fleck and Hutchinson 1997

In 1997 Fleck and Hutchinson enriched the Mindlin-Toupin theory [Toupin 1964; Toupin 1962; Mindlin 1963] with a J2 plasticity contribution [Fleck and Hutchinson 1997]. Instead of considering only the gradient of the material spin tensor as done in [Fleck and Hutchinson 1993], they used the full second gradient of the displacement vector $\underset{\approx}{\boldsymbol{\eta}} = \underline{\mathbf{u}} \otimes \underline{\boldsymbol{\nabla}} \otimes \underline{\boldsymbol{\nabla}}$:

$$p^{(i)} = \underset{\sim}{\boldsymbol{\sigma}} : \dot{\underset{\sim}{\boldsymbol{\varepsilon}}} + \underset{\approx}{\boldsymbol{\tau}} \vdots \dot{\underset{\approx}{\boldsymbol{\eta}}}; \tag{2.13}$$

where $\underset{\sim}{\boldsymbol{\sigma}}$ is the Cauchy stress, $\underset{\sim}{\boldsymbol{\varepsilon}}$ is the strain, $\underset{\approx}{\boldsymbol{\tau}}$ is commonly referred to as higher order stress and $\vdots$ is the triple contraction. By assuming an additive decomposition of the second gradient of displacement:

$$\underset{\approx}{\boldsymbol{\eta}} = \underset{\approx}{\boldsymbol{\eta}}^{e} + \underset{\approx}{\boldsymbol{\eta}}^{p} \tag{2.14}$$

the definition of the strain energy density function is given once again in a quadratic form:

$$u^{(i)} = \frac{\lambda}{2}\varepsilon^{e}_{ii}\varepsilon^{e}_{jj} + \mu\,\varepsilon^{e}_{ij}\varepsilon^{e}_{ij} + a_1\,\eta^{e}_{ijj}\eta^{e}_{ikk} + a_2\,\eta^{e}_{iik}\eta^{e}_{kjj} + a_3\,\eta^{e}_{iik}\eta^{e}_{jjk} + a_4\,\eta^{e}_{ijk}\eta^{e}_{ijk} + a_5\,\eta^{e}_{ijk}\eta^{e}_{kji}; \tag{2.15}$$

where a_i are material parameters to be calibrated and they include characteristic lengths. For incompressible medium, some of the terms in the internal energy definition would drop, and the internal energy would be function of the terms associated to μ, a_3, a_4 and a_5 only [Smyshlyaev et al. 1996]. An equivalent deformation measure is then defined as function of the remaining terms, and it will characterize the standard plastic behavior of the medium:

$$\Xi^{p^2} = \varepsilon_{eq}^{p^2} + \sum_{i=1}^{3} l_{pl_i}^2 \chi_{eq_i}^{p^2}; \tag{2.16}$$

where l_{pl_i} are three additional plastic characteristic lengths in the model, which will govern the three different deformation modes each of one embodied by the three remaining contributions of the second displacement gradient in the equivalent deformation measure definition, that are, $\chi_{eq_i}^{p^2}$.

2.2.4 Gradient of the cumulative plastic strain - Fleck and Hutchinson 2001

Successively, in 2001, Fleck and Hutchinson proposed even another version of the theory, in which the additional variable was not the whole second gradient of displacement (that also includes the gradient of the local rotation), but they focused on the gradient of the plastic strain only [Fleck and Hutchinson 2001]:

$$\underset{\sim}{\boldsymbol{\varepsilon}}^p \otimes \underline{\boldsymbol{\nabla}}; \tag{2.17}$$

A direct comparison can be made between the SGPTs of Fleck1997 and Fleck2001 if we compare the definition of the additional deformation measures they enriched their theory with:

$$[\mathrm{sym}\,(\underline{\mathbf{u}} \otimes \underline{\boldsymbol{\nabla}})]^p \otimes \underline{\boldsymbol{\nabla}} \quad \neq \quad (\underline{\mathbf{u}} \otimes \underline{\boldsymbol{\nabla}} \otimes \underline{\boldsymbol{\nabla}})^p\,; \tag{2.18}$$

This comparison highlights that the gradient of the plastic strain does not necessarily coincides with the plastic part of the second gradient of displacement. In this case, the strain energy potential would not depend on the gradient of the plastic strain, effectively achieving the same description as in Fleck1993 if the characteristic length was set to be much smaller than the plastic one:

$$u^{(i)} = \frac{\lambda}{2} \varepsilon_{ii}^e \varepsilon_{jj}^e + \mu\, \varepsilon_{ij}^e \varepsilon_{ij}^e; \tag{2.19}$$

while the total power would still feels the contribution of the gradient:

$$p^{(i)} = \underset{\sim}{\boldsymbol{\sigma}} : \underset{\sim}{\dot{\boldsymbol{\varepsilon}}} + \underline{\underline{\boldsymbol{\psi}}} \vdots \left(\underset{\sim}{\dot{\boldsymbol{\varepsilon}}}^p \otimes \underline{\boldsymbol{\nabla}} \right); \tag{2.20}$$

where $\underline{\underline{\boldsymbol{\psi}}}$ is an higher order stress that activates only in case gradients of plastic deformation are presents. The equivalent plastic strain in the present theory measures:

$$\Xi^{p^2} = \varepsilon_{eq}^{p^2} + l_{pl}^2 |\underline{\boldsymbol{\nabla}} \varepsilon_{eq}^p|^2; \tag{2.21}$$

However, two subsequent contributions from Gurtin and Anand [Gurtin and Anand 2009] and Gudmundson [Gudmundson 2004], when analyzing the thermodynamical compatibility of this model, found out that it violates the requirement on the positiveness of

the dissipation. Following these considerations, Fleck and Willis first [Fleck and Willis 2009a], and Hutchinson later [Hutchinson 2012], provided a reformulation of the theory with the constitutive model of incremental nature, so that it fits in a thermodynamically-compatible framework.

2.2.5 Irrotational plastic flow and Burgers tensor - Gurtin and Anand 2005

In 2005 Gurtin and Anand proposed a SGPT characterized by an irrotational plastic flow and by Burgers tensor as an energetically deformation measure [Gurtin and Anand 2005b; Gurtin and Anand 2005a]. Being the plastic strain irrotational, it means that, contrary to Fleck1993, the condition $\underset{\sim}{\boldsymbol{\theta}}^p = 0$ is valid, therefore this term has no energetic contribution:

$$p^{(i)} = \underset{\sim}{\boldsymbol{\sigma}} : \dot{\underset{\sim}{\boldsymbol{\varepsilon}}}^e + \underset{\sim}{\boldsymbol{\tau}} : \dot{\underset{\sim}{\boldsymbol{\theta}}}^e + \underset{\sim}{\boldsymbol{\sigma}}^p : \dot{\underset{\sim}{\boldsymbol{\varepsilon}}}^p + \underset{\sim}{\underline{\boldsymbol{\psi}}} \vdots \left(\dot{\underset{\sim}{\boldsymbol{\varepsilon}}}^p \otimes \underline{\boldsymbol{\nabla}} \right); \tag{2.22}$$

The definition of the density of free energy of the medium was explicitly made dependent on elastic strain, $\underset{\sim}{\boldsymbol{\varepsilon}}^e$, and Burgers tensor, $\underset{\sim}{\mathbf{G}}$, that reads:

$$\underset{\sim}{\mathbf{G}} = \mathrm{curl} \underset{\sim}{\boldsymbol{\varepsilon}}^p; \tag{2.23}$$

therefore, this means that the part of $\underset{\approx}{\boldsymbol{\tau}}$ associated with $\underset{\sim}{\mathbf{G}}$ is recoverable, and it plays the role of a back-stress. They identify a dissipative characteristic length, l_{pl}, that comes into plays when an equivalent plastic deformation is defined as:

$$\Xi^{p^2} = |\underset{\sim}{\boldsymbol{\varepsilon}}^p|^2 + l_{pl}^2 | \left(\underset{\sim}{\boldsymbol{\varepsilon}}^p \otimes \underline{\boldsymbol{\nabla}} \right) |^2; \tag{2.24}$$

together with an energetic characteristic length, l_{el}, that associates the deformation measures in the definition of the internal recoverable energy in a quadratic form:

$$u^{(i)} = \frac{\lambda}{2} \varepsilon^e_{ii} \varepsilon^e_{jj} + \mu \, \varepsilon^e_{ij} \varepsilon^e_{ij} + \frac{1}{2} \mu l_{el}^2 G_{ij} G_{ij}; \tag{2.25}$$

2.2.6 The common framework - Gudmundson 2004

Gudmundson provided a general framework with the potential to incorporate many SG-PTs[Gudmundson 2004]. The internal power definition is his model depends of the elastic strain, full plastic strain tensor and the gradient of the full plastic strain:

$$p^{(i)} = \underset{\sim}{\boldsymbol{\sigma}} : \dot{\underset{\sim}{\boldsymbol{\varepsilon}}} + \left(\underset{\sim}{\mathbf{q}} - \underset{\sim}{\boldsymbol{\sigma}}' \right) : \dot{\underset{\sim}{\boldsymbol{\varepsilon}}}^p + \underset{\sim}{\underline{\boldsymbol{\psi}}} \vdots \left(\dot{\underset{\sim}{\boldsymbol{\varepsilon}}}^p \otimes \underline{\boldsymbol{\nabla}} \right); \tag{2.26}$$

where $\underset{\sim}{\mathbf{q}}$ is a deviatoric microstress, power conjugate to the plastic strain, $\underset{\sim}{\boldsymbol{\sigma}}'$ is the deviatoric part of the Cauchy stress and $\underset{\sim}{\underline{\boldsymbol{\psi}}}$ is an higher order stress, power conjugate to the gradient of the plastic strain. From the application of the divergence theorem, it is possible to write the equilibrium governing equations of the medium:

$$\underset{\sim}{\boldsymbol{\sigma}} \cdot \underline{\boldsymbol{\nabla}} = \underline{0}; \tag{2.27}$$

$$\underset{\sim}{\underline{\boldsymbol{\psi}}} \cdot \underline{\boldsymbol{\nabla}} + \underset{\sim}{\boldsymbol{\sigma}}' - \underset{\sim}{\mathbf{q}} = \underset{\sim}{0}; \tag{2.28}$$

Additionally, Gudmundson defined the constitutive equations through thermodynamical considerations, by explicitly evaluating the medium dissipation and by applying the Clausius-Duhem inequality. The innovation of the theory lies in the identification of a stress conjugate to the plastic strain and plastic strain gradient from the thermodynamical point of view, such that the dissipation can be easily defined as:

$$\left(\underset{\sim}{\boldsymbol{\sigma}} - \frac{\partial \phi}{\partial \underset{\sim}{\boldsymbol{\varepsilon}^e}}\right) : \dot{\underset{\sim}{\boldsymbol{\varepsilon}}}^e + \left(\underset{\sim}{\mathbf{q}} - \frac{\partial \phi}{\partial \underset{\sim}{\boldsymbol{\varepsilon}^p}}\right) : \dot{\underset{\sim}{\boldsymbol{\varepsilon}}}^p + \left[\underline{\underline{\boldsymbol{\psi}}} - \frac{\partial \phi}{\partial \left(\underset{\sim}{\boldsymbol{\varepsilon}^p} \otimes \bar{\boldsymbol{\nabla}}\right)}\right] : \left(\dot{\underset{\sim}{\boldsymbol{\varepsilon}}}^p \otimes \underline{\boldsymbol{\nabla}}\right); \tag{2.29}$$

where ϕ is the Helmholtz free energy potential. By imposing the second thermodynamic principle (positive dissipation), Equation (2.29) defines the constitutive model of the medium (elastic part) and the dissipation:

$$\underset{\sim}{\boldsymbol{\sigma}} = \frac{\partial \phi}{\partial \underset{\sim}{\boldsymbol{\varepsilon}^e}}; \tag{2.30}$$

$$\pi = \left(\underset{\sim}{\mathbf{q}} - \frac{\partial \phi}{\partial \underset{\sim}{\boldsymbol{\varepsilon}^p}}\right) : \dot{\underset{\sim}{\boldsymbol{\varepsilon}}}^p + \left[\underline{\underline{\boldsymbol{\psi}}} - \frac{\partial \phi}{\partial \left(\underset{\sim}{\boldsymbol{\varepsilon}^p} \otimes \bar{\boldsymbol{\nabla}}\right)}\right] : \left(\dot{\underset{\sim}{\boldsymbol{\varepsilon}}}^p \otimes \underline{\boldsymbol{\nabla}}\right); \tag{2.31}$$

where π is the medium density dissipation. He showed that, with this mathematical description, it is possible to retrieve the Aifantis1987 SGPT, the Fleck1997 SGPT and Fleck2001 SGPT.

2.2.7 Dislocations-enriched SGT

Gao and coworkers proposed in 1999 a *Mechanism-Based Strain Gradient Theory* (MSGT) [Gao, Y. Huang, et al. 1999; Y. Huang et al. 2000]. This SGT aims at correlating the strain gradient with *Statistically Stored Dislocations* (SSD) and *Geometrically Necessary Dislocations* (GND), and it is built upon the dislocations-based Taylor's flow stress [Taylor 1938], whose shear stress law description reads:

$$\sigma = \alpha \mu b \sqrt{\rho_{SSD} + \rho_{GND}}; \tag{2.32}$$

where σ is the flow stress, α is a constant usually assumed to be 0.5 [Nix et al. 1998], μ is the shear modulus and b is the magnitude of the Burgers vector. In a single crystal, the GNDs are directly related with the plastic strain gradient [Nye 1953; Ashby 1970; Stölken et al. 1998]:

$$\rho_{GND} = \frac{\bar{r}\eta_{eq}}{b}; \tag{2.33}$$

where $\bar{r}$ is the Nye factor and η_{eq} is an equivalent measure of the strain gradient, that they evaluated as:

$$\eta_{eq} = \sqrt{\frac{1}{4}\underline{\underline{\boldsymbol{\eta}}} : \underline{\underline{\boldsymbol{\eta}}}}; \tag{2.34}$$

The flow stress, assuming von Mises plasticity, can be written as [Nix et al. 1998]:

$$\sigma = \sigma_Y \sqrt{f^2(\varepsilon) + l\, \eta_{eq}^p}; \tag{2.35}$$

where σ_Y is the yield stress measured without strain gradient effect ($\rho_{GND} = 0$), $f^2(\varepsilon)$ is a function of the strain, and l is a characteristic length that reads:

$$l = 3\,\alpha^2 \left(\frac{\mu}{\sigma_Y}\right)^2 b; \tag{2.36}$$

The introduction of the strain gradient in the MSGT, entails the introduction of an additional term in the internal power density definition:

$$p^{(i)} = \underset{\sim}{\boldsymbol{\sigma}} : \dot{\underset{\sim}{\boldsymbol{\varepsilon}}} + \underset{\approx}{\boldsymbol{\psi}} \vdots \dot{\underset{\approx}{\boldsymbol{\eta}}}; \tag{2.37}$$

where $\underset{\sim}{\boldsymbol{\sigma}}$ and $\underset{\sim}{\boldsymbol{\varepsilon}}$ are the usual Cauchy stress and usual strain, and $\underset{\approx}{\boldsymbol{\psi}}$ and $\underset{\approx}{\boldsymbol{\eta}}$ are higher order stress tensor and strain gradient tensor. One of the conclusions outlined by Gao et al. was that due to the fact that:

$$\frac{\partial \sigma_{ij}}{\partial \eta_{klm}} \neq \frac{\partial \psi_{klm}}{\partial \varepsilon_{ij}} \tag{2.38}$$

a potential for the strain energy density cannot exist. In the MSGT, the size effect is induced by including the influence of the strain gradient in the flow stress model.

In 2004 Huang proposed a simplified model, based on the MSGT, called the Conventional Mechanism-Based Strain Gradient Theory (CMSGT). This theory is called a low-order theory, whereas the MSGT is a high order theory, and the difference lies in the fact that the CMSGT makes use of the plastic strain gradient only at the constitutive level, leaving the contribution of the higher order stress out of the theory. This notably simplifies the implementation of the theory, although the well-posedness of the associated boundary value problem is not ensured [Niordson et al. 2003].

Another major contribution in the development of dislocations-based strain gradient theories can be identified in the work of Menzel and Steinmann [Menzel et al. 2000]. They proposed a phenomenological description of the hardening process through introduction of second and fourth order gradient of the plastic deformation for single crystals and polycrystals materials respectively. They exploited the second thermodynamic principle (Clausius-Duhem inequality), in which the definition of the dissipation was given in an additive decomposition. One of the terms composing the dissipation was dependent upon the dislocation density, which was measured as incompatibility of the plastic part of the gradient of the displacement field:

$$\underset{\sim}{\boldsymbol{\alpha}}^p = \operatorname{curl}\left(\underline{\mathbf{u}} \otimes \underline{\boldsymbol{\nabla}}\right)^p; \tag{2.39}$$

As an example, they proposed, for single crystals, a quadratic Helmholtz potential function of $\underset{\sim}{\boldsymbol{\alpha}}^p$, in which a characteristic length appears to adimentionalize the curvature. By defining the free energy as such, the yield condition, which depends on the stress conjugate to the dislocation measure, depends on the curvature, therefore, the yield conditions become a partial differential equation in which there exists a dependency on the second gradient of the displacement field.

Regarding polycrystals, they adopted another measure to quantify the incompatibility of the plastic field:

$$\underset{\approx}{\boldsymbol{\eta}}^p = \operatorname{curl}\left(\operatorname{curl}\underset{\sim}{\boldsymbol{\varepsilon}}^p\right); \tag{2.40}$$

where $\underset{\sim}{\varepsilon}$ is the usual strain. Once again, the Clausius-Duhem inequality is explicitly given as summation of terms, and one of them depends on this incompatibility measure. By identifying the stress conjugate to this measure, and by giving the yield condition as function of this stress, it is possible to verify that the yield condition contains fourth order gradient of the displacement field.

Among the SGTs incorporating dislocation measures, the research line initiated by Wulfinghoff et al. also deserves to be mentioned. This viscoplastic theory was originally developed in [Wulfinghoff and Böhlke 2012], and then successively modified to incorporate the effect of grain boundary resistance on the plastic flow [Wulfinghoff, Bayerschen, et al. 2013]. They adopted the combination of a micromorphic-like approach (see Section 2.2.9) with a penalty term in the free energy to incorporate the effect of the plastic strain and its gradient on the yield limit development.

2.2.8 Gradient of micro-structure rotation - Cosserat Media

The Cosserat model derives from the work of the Cosserat brother at the beginning of the 20th century [Cosserat et al. 1909]. This continuum mechanics theory enhances the kinematics of the continuum with additional degrees of freedom, that are meant to represent the microstructural rotation. In the three-dimensional space, the Cosserat theory possesses three additional degrees of freedom: the three components of the pseudo-vector $\underline{\boldsymbol{\omega}}$ that represents the local rotation of the microstructure. This vectorial field is defined, as the displacement field, over the entire domain under consideration. Another additional feature of the Cosserat kinematics is the definition of the gradient of the vector of microrotation, $\underline{\boldsymbol{\omega}} \otimes \underline{\boldsymbol{\nabla}}$, which is sometimes referred to as wryness, and it incorporates both the curvature and the torsion of the microstructure. Based on the defined kinematic measures, the internal power reads:

$$p^{(i)} = \underset{\sim}{\boldsymbol{\sigma}} : \dot{\underset{\sim}{\mathbf{e}}} + \underset{\sim}{\boldsymbol{\xi}} : \dot{\underset{\sim}{\boldsymbol{\Gamma}}}; \tag{2.41}$$

where $\underset{\sim}{\mathbf{e}}$ and $\underset{\sim}{\boldsymbol{\Gamma}}$ are the Cosserat strain and wryness, defined as:

$$\underset{\sim}{\mathbf{e}} = \underline{\mathbf{u}} \otimes \underline{\boldsymbol{\nabla}} + \underset{\sim}{\boldsymbol{\Omega}}; \tag{2.42}$$

$$\underset{\sim}{\boldsymbol{\Gamma}} = \underline{\boldsymbol{\omega}} \otimes \underline{\boldsymbol{\nabla}}; \tag{2.43}$$

where $\underset{\sim}{\boldsymbol{\xi}}$ is the couple stress conjugate of the wryness, and the tensor $\underset{\sim}{\boldsymbol{\Omega}}$ is obtained from the micro-rotation vector $\underline{\boldsymbol{\omega}}$ through the Levi-Civita permutation operator:

$$\underset{\sim}{\boldsymbol{\Omega}} = -\frac{1}{2}\underset{\simeq}{\boldsymbol{\epsilon}} \cdot \underline{\boldsymbol{\omega}}; \tag{2.44}$$

which returns a second order tensor. To be noted that if material and microstructure rotations are equivalent, the Cosserat strain coincides with the classical strain, the wryness becomes equal to the curvature in the Fleck1997 SGPT, and the Cosserat theory becomes a constrained Cosserat theory [Koiter 1964]. The Cosserat theory therefore employs the gradient of the rotation vector to regularize the boundary value problem. Assuming an elastic isotropic behavior, the constitutive model of the Cosserat media can be written as:

$$\underset{\sim}{\boldsymbol{\sigma}} = \lambda \operatorname{tr}\left(\underset{\sim}{\mathbf{e}}^e\right) \underset{\sim}{\mathbf{I}} + 2\,\mu \operatorname{sym}\left(\underset{\sim}{\mathbf{e}}^e\right) + 2\,\mu_c \operatorname{skw}\left(\underset{\sim}{\mathbf{e}}^e\right); \tag{2.45}$$

$$\underset{\sim}{\boldsymbol{\mu}} = \alpha \operatorname{tr}\left(\underset{\sim}{\boldsymbol{\Gamma}}^e\right) \underset{\sim}{\mathbf{I}} + 2\,\beta \operatorname{sym}\left(\underset{\sim}{\boldsymbol{\Gamma}}^e\right) + 2\,\gamma \operatorname{skw}\left(\underset{\sim}{\boldsymbol{\Gamma}}^e\right); \tag{2.46}$$

from which, two (more can be identified [Forest 2009]) elastic characteristic lengths can be identified as [Khoei et al. 2010]:

$$l_{el}^{b} = \sqrt{\frac{\gamma}{\mu}}; \tag{2.47}$$

$$l_{el}^{t} = \sqrt{\frac{\alpha+\beta+\gamma}{2\mu}}; \tag{2.48}$$

where the superscripts t and b indicate whether the characteristic length governs the torsional or bending response of the material respectively. The constrained Cosserat theory can also be obtained by enforcing the skew symmetric part of the Cosserat strain to be negligible through the employment of high enough values of the coefficient relating this term to the stress (μ_c) in Equation (2.45). The plastic framework of the Cosserat media can be taken from the one developed by de Borst [de Borst 1991a], in which the J2 von Mises plasticity is extended to the Cosserat framework, and the equivalent stress measure reads:

$$\sigma_{\text{eq}} = \sqrt{\frac{3}{2}\left(\mathrm{a}\underset{\sim}{\boldsymbol{\sigma}}' : \underset{\sim}{\boldsymbol{\sigma}}' + \mathrm{a}\underset{\sim}{\boldsymbol{\sigma}}' : \underset{\sim}{\boldsymbol{\sigma}}'^{\mathrm{T}} + \mathrm{b}\underset{\sim}{\boldsymbol{\mu}} : \underset{\sim}{\boldsymbol{\mu}} + \mathrm{b}\underset{\sim}{\boldsymbol{\mu}} : \underset{\sim}{\boldsymbol{\mu}}^{\mathrm{T}}\right)}; \tag{2.49}$$

from which the plastic characteristic length of the Cosserat Media can be obtained as:

$$l_p = \sqrt{\frac{\mathrm{a}}{\mathrm{b}}}; \tag{2.50}$$

2.2.9 Gradient of micro-structure deformation - Micromorphic Media

The Cosserat medium allows the continuum to have an independent rotation from the material one. Similarly, the micro-strain framework allows the continuum to have an additional, independently defined strain (six additional degrees of freedom) that differs from the classical strain definition [Forest and Sievert 2006]. In reality, these two models are nothing but a constrained micromorphic model in which the micro-strain is constrained (Cosserat or *Micropolar*) or the micro-rotation is constrained (micro-strain). This theory, independently developed by Mindlin [Mindlin 1963] and Eringen and Suhubi [Eringen and Suhubi 1964], adopts the gradient of the additional independent microdeformation field to describe the complete status of the domain, thus adding nine more independent variables to describe the media [Eringen 1999a]. The internal power in the micromorphic media reads:

$$p^{(i)} = \underset{\sim}{\boldsymbol{\sigma}} : (\underline{\mathbf{u}} \otimes \underline{\boldsymbol{\nabla}}) + \underset{\sim}{\boldsymbol{a}} : \underset{\sim}{\boldsymbol{\phi}} + \underset{\approx}{\mathbf{b}} \vdots \left(\underset{\sim}{\boldsymbol{\phi}} \otimes \underline{\boldsymbol{\nabla}}\right); \tag{2.51}$$

where $\underset{\sim}{\boldsymbol{\phi}}$ is the second order micromorphic deformation tensor containing the additional nine degrees of freedom, $\underset{\sim}{\boldsymbol{a}}$ and $\underset{\approx}{\mathbf{b}}$ are power conjugates to the micromorphic deformation and to its gradient. In this framework, following Eringen [Eringen 1999a], a single characteristic length arises naturally from the angular moment balance equation:

$$\underset{\sim}{\boldsymbol{\phi}} - l^2\nabla^2\underset{\sim}{\boldsymbol{\phi}} = \underline{\mathbf{u}} \otimes \underline{\boldsymbol{\nabla}}; \tag{2.52}$$

that links the displacements with the Micromorphic degrees of freedom [Dillard et al. 2006].

The full micromorphic theory enhances the continuum with 9 additional degrees of freedom, but it is still possible to take advantage of the versatility and the easiness of the numerical implementation of this theory by adopting a scalar modification of the micromorphic theory. Such solution was exploited by Anand et al., who used a single additional degree of freedom provided by the simplified micromorphic theory to model an equivalent measure of the cumulative equivalent plastic strain [Anand et al. 2012]. In this case, the micromorphic theory assumes a form similar to the previously discussed SGT, but it distinguishes itself from the others in the solid thermodynamic foundations on which it relies.

The micromorphic approach has also been used by Poh et al. as an implicit formulation that accommodates the gradient of the plastic strain [Poh et al. 2011]. The internal power that they defined has the following form:

$$p^{(i)} = \underset{\sim}{\boldsymbol{\sigma}} : \dot{\underset{\sim}{\boldsymbol{\varepsilon}}} + \underset{\sim}{\mathbf{Q}} : \dot{\tilde{\underset{\sim}{\boldsymbol{\varepsilon}}}}^{p} + \underset{\approx}{\boldsymbol{\tau}} \vdots \left(\dot{\tilde{\underset{\sim}{\boldsymbol{\varepsilon}}}}^{p} \otimes \underline{\boldsymbol{\nabla}} \right); \tag{2.53}$$

where $\underset{\sim}{\boldsymbol{\sigma}}$ and $\underset{\sim}{\boldsymbol{\varepsilon}}$ are the usual Cauchy stress and strain, $\tilde{\underset{\sim}{\boldsymbol{\varepsilon}}}^{p}$ is the microscopic plastic strain, $\underset{\sim}{\mathbf{Q}}$ and $\underset{\approx}{\boldsymbol{\tau}}$ are the work conjugate to the microscopic plastic strain and its gradient. The microscopic plastic is a non-local measure of plastic deformation of the continuum and it is different form the the plastic strain. The governing equation of the microscopic plastic strain is obtained by developing the local equilibrium condition of the angular moment, that transforms into a governing equation of the higher degree of freedom, that is, the microscopic plastic strain, and it reads:

$$\tilde{\underset{\sim}{\boldsymbol{\varepsilon}}}^{p} = \underset{\sim}{\boldsymbol{\varepsilon}}^{p} + l_p^2 \underline{\boldsymbol{\nabla}}^2 \tilde{\underset{\sim}{\boldsymbol{\varepsilon}}}^{p}; \tag{2.54}$$

where l_p is a plastic characteristic length tuning the magnitude of the non-locality of the formulation. If $l_p = 0$, the classical theory is retrieved. Equation (2.54) is a Helmholtz-type differential equation. The scalar version of this theory was previously developed by Peerlings [Peerlings 2007], and it can be easily retrieved by adopting a scalar plastic microstrain instead of a tensorial one. In the scalar version, the definition of the free energy was given in a quadratic form as:

$$u^{(i)} = \frac{1}{2} \underset{\sim}{\boldsymbol{\varepsilon}}^{e} : \underset{\approx}{\mathbf{C}} : \underset{\sim}{\boldsymbol{\varepsilon}}^{e} + \frac{h}{n+1} p^{n+1} + \frac{1}{2} \left(\frac{3}{2} \tilde{h} \right) (\tilde{p} - p)^2 + \frac{1}{2} \left(\frac{3}{2} \tilde{h} \right) l_p^2 \left(\nabla \tilde{p} \right)^2; \tag{2.55}$$

where $\underset{\approx}{\mathbf{C}}$ is the elastic fourth-order tensor, h and $\tilde{h}$ are hardening moduli, incorporated in the is free energy to model hardening, p and $\tilde{p}$ are equivalent plastic strain and equivalent plastic microstrain, n a material parameter.

2.3 Reported Applications of GCM in Manufacturing Processes Simulation

The implementation of GCM in a FEM solver is not an easy task, and the more complex the model, the more difficult is the implementation. Furthermore, if the theory has to be used for machining simulation, this represents an additional element of difficulty due

to the additional features that must be taken care of, such as friction, temperature and strain rate influence, large deformation framework and so on.

From the point of view of FE implementation, in GCM two different groups can be delineated: one that only requires to access and enhance the material behavior of the Finite Elements, and another one that requires a deeper level of accessibility. For the latter, a total new Element formulation must be provided. The key feature to differentiate between the two groups is the necessity of defining new degrees of freedom for the element. Whether it is demanded to add another degree of freedom or not, it depends on the nature of the continuum description that must be used: if the strain gradient needs to be evaluated through solution of PDEs, then the variable carrying the strain gradient measure requires to be treated as an additional degree of freedom, otherwise, the strain gradient will be treated as a solution-dependent variable. In the latter case, the strain gradient depends on the displacement field on a similar way the classical strain measure does, and the classical structure of the continuum description is unaltered.

Among the theories previously presented, the CMSGT is the only one that does not require modifications of the element formulation. This traduces in a easier implementation of the theory, and this represent an advantage that should not be superficially neglected, especially if combined with the already mentioned difficulties characterizing machining simulations. Nonetheless, on a similar low-order theory developed by Acharya and Bassani [Acharya et al. 1996] and Bassani [Bassani 2001], doubts have been raised on the physicality of the obtained response and on the well-posedness of the boundary value problem.

In the present section, several applications of SGPTs to machining operations will be presented. Although it is possible to find plenty of researches in literature focusing on the implementation and verification of SGPTs, here the objective is to gather the main contributions toward the application of SGPTs for manufacturing processes. Important advancements were done in the theoretical understanding of the phenomenon occurring during machining operations[J. Huang et al. 2001; Laheurte et al. 2006], but unfortunately not many contributions on the implementation of these SGPT for machining were found.

2.3.1 Scalar SGPT applied to flat punch molding

The first example of applications of SGPT in manufacturing operations is the one provided by Guha et al. [Guha et al. 2014]. They implemented the Fleck1997 SGPT as revisited by Fleck and Hutching in 2001 (ref. Section 2.2.4) in a viscoplastic isothermal large deformation framework to simulate flat punch molding. This manufacturing process is similar to the indentation test in case the size of the surface of the punch is comparable to the material grain size, thus achieving similar deformation fields to the ones developed during an indentation test. This test is of particular interest for manufacturing processes acting at macroscale ($\approx \mu m$).

The main disadvantage of this SGPT is that the equivalent plastic strain is treated as an independent variable of the continuum, therefore it requires to be embedded as an additional degree of freedom in a Finite Element Procedure. Consequently, the independent field of the equivalent plastic strain must be solved through PDEs, and since the plastic deformation is not intrinsically defined over the domain (but rather it derives from the current deformation state of the media) the domain of definition of the equivalent plastic strain field requires to be updated at every iteration. The procedure of finding

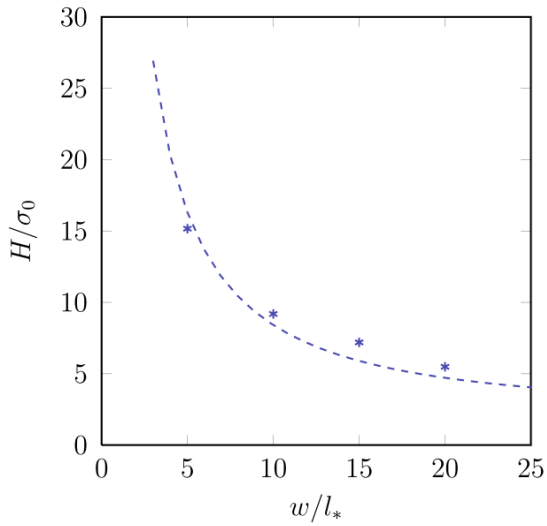

Figure 2.8: Predicted characteristic hardness against the characteristic length using the viscoplastic model of Fleck2001 SGT [Guha et al. 2014]. w is half the punch width, H is the hardness, σ_0 is the initial material yield stress and l_* is the characteristic length as in Equation (2.21).

the boundaries of the definition domain of the equivalent plastic strain is facilitated if a Corotational approach or an Updated approach are used.

They performed simulations of a flat punch molding using different values of characteristic length. A strong dependency of the characteristic hardness on the characteristic length (or on the punch width) is predicted, as reported in Figure 2.8. As expected, this trend is very similar to the one characterizing the indentation tests [Nix et al. 1998; Shu et al. 1998; Poole et al. 1996]. Their research further emphasize the necessity of adopting a SGPT to simulate manufacturing operations acting on the micro scale.

2.3.2 SGPT used to model rolling at small scale

The employment of the full gradient of plastic strain for manufacturing operations is reported in a recent contribution by Nielsen et al. [Nielsen et al. 2016]. They used the SGPT described by Gudmunson [Gudmundson 2004] first, and Fleck and Willis [Fleck and Willis 2009b] later, to simulate rolling processes of metal sheets of up to 5 μm of thickness in 2D. Simulations were performed under steady-state condition, integrations were done with forward Euler scheme, and the continuum was enhanced with 9 additional degrees of freedom, being the components of the plastic strain tensor. Gaussian integration schemes were used for integration over the element. The contact between the plate and the roll was modeled through a sticking-sliding model. The material hardening was set to be dependent on the strain gradient.

Rolling simulations were carried out using different ratios of the characteristic length over the sheet thickness, and the results replicated the experimental values accurately.

The simulated rolling force demonstrated sensitivity over the size-effect, similarly to what was experienced experimentally. The authors outlined that large size-effects were measured when the characteristic length over thickness ratio was 0.25.

2.3.3 MSGT applied to orthogonal cutting

The first line of research here reported is the one originated from Liu et al. [K. Liu et al. 2007; Kai Liu 2005; K. Liu et al. 2006]. They implemented the Mix-Gao MSGT, thereby adopting a non-local Taylor-derived material hardening description as in Equation (2.35), where the equivalent measure of the strain gradient was evaluated as in Equation (2.34), and they used a non-local volume integral to evaluate the strain gradient at every integration point as proposed by Gao and Huang [Gao and Y. Huang 2001]:

$$\eta_{ijk} = \int_V \left[\varepsilon_{ik}\xi_j + \varepsilon_{jk}\xi_i - \varepsilon_{ij}\xi_k - \frac{1}{4}\left(\delta_{ik}\xi_j + \delta_{jk}\xi_i\right)\varepsilon_{pp} \right] dV \left(\int_V \xi_m \xi_k dV \right)^{-1}; \quad (2.56)$$

where ξ_i is the i-th local coordinate over which integration is performed. In this framework, the classical continuum mechanics description stays the same, and the strain gradient effects only the plastic flow, acting as an additional source of hardening (this is after all the reasoning behind the MSTG). The flow stress they used is the one in Equation (2.35), and they used the Johnson-Cook evolution of the flow stress to replace f [Johnson et al. 1985]. The characteristic length was identified with:

$$l = 18\,\alpha^2 \left(\frac{\mu}{\sigma_Y} \right)^2 b; \quad (2.57)$$

They implemented this model in a Finite Element Procedure, using ABAQUS® Implicit through a UMAT FORTRAN subroutine, and they used this model to study the effect of the radius of the cutting tool during orthogonal micro-cutting [K. Liu et al. 2007], and to verify the increments in material hardening and cutting energy by using the SGPT [K. Liu et al. 2006]. In Figure 2.9a a comparison is reported from the work of Liu et al. in terms of Specific Cutting energy while using different tool radii. In Figure 2.9b instead, the effect of using the SGPT is reported again in terms of Specific Cutting Energy. They used a sticking-sliding friction model as the one developed by Zorev [Zorev 1963]. The thermal fields during simulations have been solved through the classical heat equation. Heat was assumed to generate at the tool-workpiece contact location due to friction and at the plastic zones due to plastic work; the Taylor-Quinney constant was set to 0.9 (90% of the plastic work would transform into heat) [Taylor and Quinney 1934]. An adaptive remeshing algorithm was used to obtain chip separation. The minimum mesh size they used measured 0.06 μm in the cutting zone, with a chip thickness of 0.5 μm.

The work of Liu et al. represents a big contribution toward the application of SGPTs for machining simulation, both in terms of progress toward the objective and in terms of proof of the fact that SGPT are necessary to achieve it. However, the disadvantages of using a MSGT are that the system of PDE describing the continuum behavior have not been rigorously derived and thermodynamical consistency of the model has not been proved, therefore, for future development, a more complete and rigorous SGPT would be ideally used, or a thermodynamically-consistent MSGT would have be provided.

Another contribution in simulating machining with SGPTs is the one provided by Asad, Mabrouki et al. [Asad et al. 2010; Asad 2010; Mabrouki et al. 2016]. They

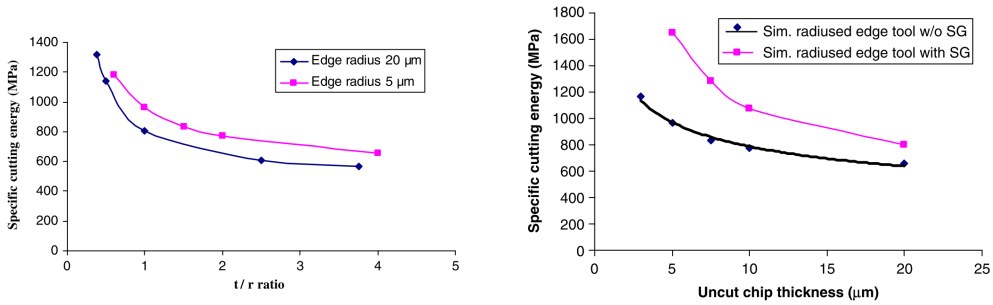

(a) (b)

Figure 2.9: Predicted effect of the tool radius on the Specific Cutting Energy Variation during orthogonal cutting test (a), and effect of the adoption of a SGT on the predicted Specific Cutting Energy (b) [K. Liu et al. 2007].

also used the MSGT as the one used by Liu et al., but they estimated the equivalent strain gradient measure based on geometrical consideration of the workpiece and the tool used for machining operation [Asad 2010]. This has large implications on the limited applicability of this theory for a generic simulation. They also quantified the characteristic length as in Equation (2.57). Besides the evaluation of the strain gradient, they used the same flow stress description as the one used by Liu et al., but the chip formation was induced through a damage-enriched Johnson-Cook behavior law, where damage initiation and propagation were defined based on ductile Johnson-Cook fracture behavior [Asad et al. 2010]. They also used an ABAQUS® Explicit VUMAT subroutine to implement the model. In Figure 2.10 the difference between using this variety of MSGT and the classical continuum mechanics description is reported for different cutting speeds.

2.3.4 Micromorphic Media applied to forming

The discussed Micromorphic theory is enhancing the medium by 9 additional degrees of freedom, this being an equivalent deformation tensor of the microstructure defined at each point of the continuum. It has also been said that the Micropolar and the Microstrain theories are nothing but a constrained version of the Micromorphic theory. Due to the physics that Eringen described with the Micromorphic theory, this terminology associates to the introduction of additional degrees of freedom in the system that are connected with the microstructure. Through the years, many theories that enhance the continuum with additional degrees of freedom have been semantically linked with the Micromorphic theory, although the physics they described was not related to microstructure. However, in the literature, this became an established nomenclature for continuum mechanics theories enhancing the media with additional degrees of freedom.

The additional degree of freedom can be used for different purposes, it can be used for carrying an equivalent measure of the cumulative plastic strain [Peerlings 2007; Poh et al. 2011; Mazière et al. 2013; Anand et al. 2012] or for an equivalent damage variable [Saanouni and Hamed 2013; Forest 2009]. In any case, the equation governing the angular momentum (that for classical continuum mechanics ensures the symmetry of the Cauchy stress tensor) transforms into a balance equation for the additional degrees of freedom

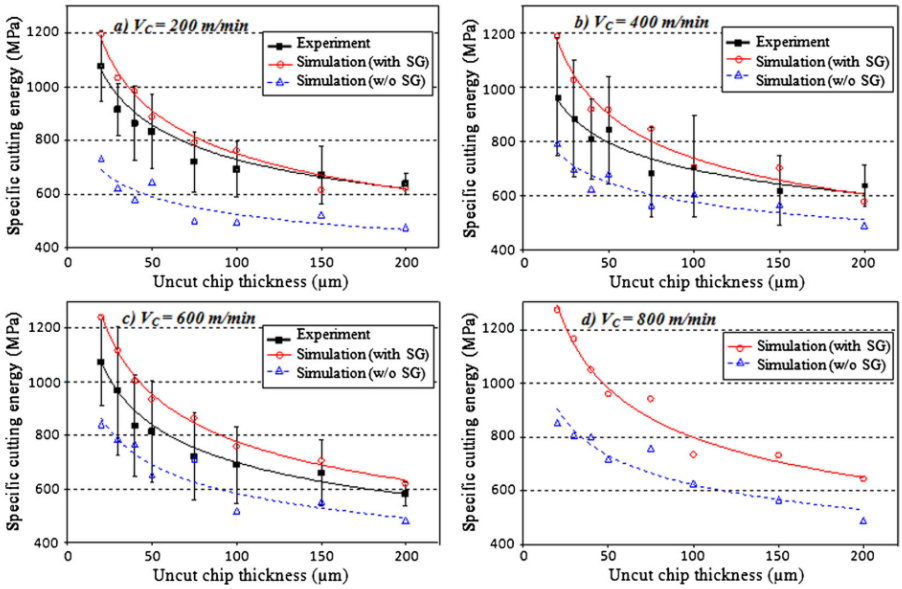

Figure 2.10: Predicted Specific Cutting Energy Variation during orthogonal cutting test for different cutting speed with and without SGT [Mabrouki et al. 2016].

and it is referred to as generalized balance equation. In case these additional variables are meant to replace already existing variables, the generalized balance equation transforms into a coupling equation between additional and already existing variables.

In 2017, Diamantopoulou et al. used the Micromorphic theory to enhance the continuum with one scalar additional degree of freedom (meant to represent the damage variable of the medium) and they simulated some metal forming processes with this theory [Diamantopoulou et al. 2017]. The enhanced internal power of the continuum reads:

$$p^{(i)} = \underset{\sim}{\boldsymbol{\sigma}} : \left(\underset{\sim}{\dot{\mathbf{u}}} \otimes \underset{}{\boldsymbol{\nabla}} \right) + Y\, \dot{d} + \underline{\mathbf{Z}} \cdot \underline{\boldsymbol{\nabla}} \dot{d}; \tag{2.58}$$

where $\underset{\sim}{\boldsymbol{\sigma}}$ is the Cauchy stress tensor, d is the additional Micromorphic damage variable, Y and $\underline{\mathbf{Z}}$ are higher order stresses associated to the damage variable and its gradient respectively. The description of the theory continues with the considerations related to the thermodynamical admissibility of the theory: the definition of the Helmholtz free energy, the definition of the dissipation potential and the subsequent derivation of the material constitutive behavior and the elastoplastic flow rules from the previously defined potentials. In this medium description, the characteristic length appears in the generalized balance equation coupled with the gradient of the Micromorphic damage variable.

The theory was implemented in ABAQUS® Explicit, through a VUEL subroutine. The introduction of an additional degree of freedom implies a modification of the system of PDEs to be solved, thereby compelling the modification of the Finite Element description rather than an higher-level modification of the material module.

The authors verified the developed formulation through tensile test and bending both performed using the material parameters of the DP1000 steel. The results of their analysis

demonstrated an embedded mesh regularization property of the model, that was proven by varying the mesh size, whereas the global force-displacement graphs remained unchanged.

2.4 Conclusion

By distinguishing between higher order and higher grade formulations, the choice of implementing a continuum mechanics theory belonging to one group or the other depends on the specifications of the process that must be simulated. In general, higher grade theories are more complex to be implemented from a FEM point-of-view, whereas higher order theories are, in most cases, an extension of the classical FEM implementation to an higher number of degrees of freedom, thereby they result more straightforwardly implementable. In Table 2.1 the main characteristics of the presented theories of GCM are reported.

Name	d.o.f.	Additional feature	Higher Order/Grade
Aifantis (Sec. 2.2.1)	3	$\sigma^Y \propto \nabla^2 \varepsilon^p_{eq}$	Higher Grade
Fleck1993 (Sec. 2.2.2)	3	$p^{(i)} \propto \text{skew}\,(\dot{\underline{\mathbf{u}}} \otimes \underline{\boldsymbol{\nabla}})$	Higher Grade
Fleck1997 (Sec. 2.2.3)	3	$p^{(i)} \propto \underline{\mathbf{u}} \otimes \underline{\boldsymbol{\nabla}} \otimes \underline{\boldsymbol{\nabla}}$	Higher Grade
Fleck2001 (Sec. 2.2.4)	3	$p^{(i)} \propto \underset{\sim}{\boldsymbol{\varepsilon}}^p \otimes \underline{\boldsymbol{\nabla}}$	Higher Grade
Gurtin (Sec. 2.2.5)	3	$p^{(i)} \propto (\underset{\sim}{\boldsymbol{\varepsilon}}^p \otimes \underline{\boldsymbol{\nabla}}, \underset{\sim}{\boldsymbol{\theta}})$	Higher Grade
Gudmundson (Sec. 2.2.6)	3	$p^{(i)} \propto \underset{\sim}{\boldsymbol{\varepsilon}}^p \otimes \underline{\boldsymbol{\nabla}}$	Higher Grade
Gao (Sec. 2.2.7)	3	$\sigma^Y \propto \underline{\mathbf{u}} \otimes \underline{\boldsymbol{\nabla}} \otimes \underline{\boldsymbol{\nabla}}$	Higher Grade
Cosserat (Sec. 2.2.8)	6	$p^{(i)} \propto (\underset{\sim}{\boldsymbol{\theta}}, \underset{\sim}{\boldsymbol{\Gamma}})$	Higher Order
Micromorphic (Sec. 2.2.9)	12	$p^{(i)} \propto (\underset{\sim}{\boldsymbol{\phi}}, \underset{\sim}{\boldsymbol{\phi}} \otimes \underline{\nabla})$	Higher Order

Table 2.1: Summary of the presented theories belonging to GCM.

For the simulation of machining operations that involve the development of high temperatures, regardless of the choice between higher order or higher degree, it is require the adoption of a theory incorporating a thermodynamical description that would ensures a proper thermodynamically-consistent description. The suggested approach would be to define the dissipation potential and the Helmholtz free energy from which the constitutive behavior of the medium would directly follow. If higher temperatures are foreseen, the dissipation potential assumes a fundamental role in determining the material response, thereby a proper calibration of the potential at operational conditions is required. If extremely high temperature develops, e.g. through the friction stir welding technique, melting temperature is likely to occur, and the solid description of the medium is not adequate anymore, since the continuum behaves as liquid rather than solid, therefore a mixed *Lagrangian-Eulerian* formulation is required to performed the simulation. However, the effect of the strain gradient during friction stir welding is not the main character of the whole process, therefore this manufacturing technique is left out of this manuscript.

One of the main drawback of the majority of the higher order theories is that, since the plastic strain is an additional variable of the system, the boundary conditions in terms of plastic strain must be applied at the moving elasto-plastic boundary, so another additional step is required to identify this boundary inside the original domain. Furthermore, if the simulated manufacturing technique involves the development of plastic strain at the domain boundaries, e.g. orthogonal cutting, then the choice related to the type of boundary conditions (in terms of plastic strain) that must be applied at this boundary is very important. If, however, the process that must be simulated does not involve the production of plastic strain at the boundary, then this question does not need to be posed, and the choice of using this type of continuum theory is not unfavorable. Two simulations of orthogonal cutting using SGPTs were reported, and both of them are using MSGT. In light of the previous discussion, the choice of the MSGT is a smart solution, since it has already been mentioned that this type of SGPT does not require the plastic strain field to be solved through PDEs, therefore it is not characterized by this type of problem.

To conclude, the choice of the SGPT to be adopted for simulations of manufacturing operations must be taken while looking at several characteristic of the observed phenomena occurring during the process:

- The forces/moments used to shear/shape the continuum localize in areas that are comparable to the grain size of the metal; in this case a further hardening due to the dislocations movement must be properly captured by adopting a SGPT;
- The velocity with which the continuum is deformed might induce material to behave viscously, and this must be covered by a proper design of the material behavior;
- The temperature developed during the process might be relatively high, and this imposes to considerate the thermal behavior (often adiabatic) that are taken into account by the definition of a thermodynamically-consistent description of the continuum;
- Implementation-wise if the plastic deformation is expected to occur at the boundaries, a higher degree theory is favorable.

Chapter 3

A micromorphic plasticity explicit scheme for metal manufacturing simulations

Good quality manufacturing operation simulations are essential to obtain reliable numerical predictions of the processes. In many cases, it is possible to observe that the deformation localizes in narrow areas, and since the primary deformation mode is under shear, these areas are called *shear bands*. In classical continuum mechanics models, the deformation localization may lead to spurious mesh dependency if the material locally experiences thermal or plastic strain softening. One option to regularize such a non-physical behavior is to resort to non-local continuum mechanics theories. The research presented in this chapter adopts a scalar micromorphic approach, which includes a characteristic length scale in the constitutive framework to enforce the plastic strain gradient theory to regularize the solution. Since many manufacturing process simulations are often assessed through finite element methods with an explicit solver to facilitate convergence, we present an original model formulation and procedure for the implementation of the micromorphic continuum in an explicit finite element code. The approach is illustrated in the case of the VPS explicit solver from ESI GROUP. According to the original formulation, an easy way to implement a scalar micromorphic approach is proposed by taking advantage of an analogy with the thermal balance equation. The numerical implementation is verified against the analytical solution of a semi-infinite glide problem. Finally, the correctness of the method is addressed by successfully predicting size effects both in a cutting and a bending tests.

The layout of the chapter is as follows. The formulation of the micromorphic analytical model is provided in Section 3.2 in which both the kinematics and the energetic aspects of the theory are presented, alongside its thermodynamic description, so that the recoverable and dissipative contributions are explicitly stated as such. The section concludes with the pivotal analogy between the thermal and the micromorphic balance equations, which further simplifies any possible implementation of the theory in a Finite Element software. In Section 3.2.7 the discretization of the equations and the implementation of the method in the explicit finite element software VPS/Pam-Crash ® from ESI [ESI Group 2000] will

be described. Section 3.3 will be used to present a simple analytical solution that will be useful to verify the implementation of the model in a finite element framework. Finally, in Section 3.4 the numerical method will be used to simulate two manufacturing operations in which significant strain gradient effects are expected to take place, namely the shear/trimming operation and the bending test. The mesh-dependency will be analyzed, along with the size-effect in terms of cumulative plastic strain distribution. Conclusions follow in section 3.5.

3.1 Introduction

In recent years, different generalized continuum mechanics theories have been used to simulate manufacturing operations. A flat punch molding process was simulated by Guha and co-workers using the plastic strain gradient theory [Guha et al. 2014]. A similar theoretical framework was used to simulate steady-state rolling processes in [Nielsen et al. 2016]. Other relevant contributions in the application of non-local theories for manufacturing operation simulations can be found in the investigations of Liu et al. [K. Liu et al. 2007; Kai Liu 2005; K. Liu et al. 2006] and Asad et al. [Asad et al. 2010], who both reproduced orthogonal cutting simulations using strain gradient effects. More recently, Diamantopoulou and co-workers [Diamantopoulou et al. 2017] used a non-local continuum mechanics theory enhanced with the gradient of a scalar damage variable to simulate metal forming.

Besides the strain gradient theories, other generalized continuum mechanics theory could solve the aforementioned problems. The micromorphic approaches, for instance, involve the gradient of a tensor of any rank, supposed to perform the targeted strain gradient operation [Forest 2009], and they can also be used to overcome the limitations of the classical continuum mechanics. The micromorphic approach introduces additional degrees of freedom in the problem, and, depending on the type of theory that is required, the computational cost might dramatically increase. For instance, a full-order micro-curl model, as the one proposed by Cordero et al. [Cordero et al. 2010], requires at least 5 additional degrees of freedom in two-dimensional settings. In contrast, the micromorphic approach involving a scalar micromorphic variable, so-called reduced-order micromorphic model, includes only one additional degree of freedom.

In this context, our contribution aims at investigating the size-effect predictions and regularization properties of a time-dependent strain gradient theory that is implemented through a scalar micromorphic framework using an explicit formulation, in which a viscoplastic micromorphic-related variable is included, but no micromorphic inertia is present. The main novelty of the proposed method lies in the easiness of the implementation of the theory in an already-well-structured finite element solver. It represents an alternative to existing implementations of such micromorphic models like the one proposed by Saanouni and Hamed [Saanouni and Hamed 2013]. The framework that we will present can, in fact, simply be solved through a common thermal-field solver, and such crucial aspect will be properly addressed in the present chapter.

Notations

In this work, the following notations are used. The first, second and fourth-order tensors will be indicated by a bar, tilde or double tilde, respectively, underneath the tensor: $\underline{\boldsymbol{a}}, \underset{\sim}{\boldsymbol{a}}$

and $\underset{\approx}{\ddot{\boldsymbol{a}}}$. The single or double dot above of a degree of freedom indicates the first or second time derivative respectively. Single and double contractions are indicated by single dot or double dots between the tensors and they operate on the inner indices of the tensors:

$$\underset{\sim}{\boldsymbol{a}} \cdot \underset{\sim}{\mathbf{b}} = \underset{\sim}{\mathbf{c}}; \quad \Longleftrightarrow \quad \mathrm{a}_{ij}\mathrm{b}_{jk} = c_{ik}, \tag{3.1}$$

$$\underset{\sim}{\boldsymbol{a}} : \underset{\sim}{\mathbf{b}} = \mathrm{c}; \quad \Longleftrightarrow \quad \mathrm{a}_{ij}\mathrm{b}_{ij} = \mathrm{c}, \tag{3.2}$$

where Einstein index summation convention applies. The single and double tensor products operate as:

$$\underline{\boldsymbol{a}} \otimes \underline{\mathbf{b}} = \underset{\sim}{\mathbf{c}}; \quad \Longleftrightarrow \quad \mathrm{a}_i\mathrm{b}_j = \mathrm{c}_{ij}, \tag{3.3}$$

$$\underset{\sim}{\boldsymbol{a}} \otimes \underset{\sim}{\mathbf{b}} = \underset{\approx}{\mathbf{c}}, \quad \Longleftrightarrow \quad \mathrm{a}_{ij}\mathrm{b}_{kl} = \mathrm{c}_{ijkl}, \tag{3.4}$$

3.2 Theoretical Formulation and Finite Element Implementation

The micromorphic scheme has been proven to be a straightforward and relatively simple procedure to introduce additional degrees of freedom to the continuum in order to achieve non-local regularization effects [Forest 2009; Forest 2016], and it has been used already in several other contributions [Poh et al. 2011; Anand et al. 2012; Mazière et al. 2015; Saanouni and Hamed 2013; Saanouni 2013; Diamantopoulou et al. 2017; Davaze et al. 2021]. Among the cited works, the only ones to adapt and implement the micromorphic approach for an explicit time-dependent problems can be found in [Saanouni and Hamed 2013; Saanouni 2013; Diamantopoulou et al. 2017; Davaze et al. 2021]. The aforementioned authors presented a time-dependent framework, in which the governing equations for the micromorphic variables include a second-order time derivative of the micromorphic variables. Additional coefficients associated with this term were included to characterize the inertia of the micromorphic variables, a role that is usually assigned to the density for the governing equations of displacement fields. Furthermore, Davaze and co-workers [Davaze et al. 2021] included some dissipation terms associated with the first-order time derivative of the micromorphic variable in governing equation so as to avoid any oscillation of the solution caused by the form of the partial differential equation (specifically induced by the presence of a second-order time derivative term). However, the authors of this research used the theory to achieve mesh-regularization for fracture growth simulations in metals. Exploring the extent of such an approach for manufacturing operation simulations was not their target.

In the present work, we make use of a scalar micromorphic approach to govern the strain gradient effect and to restore mesh independence. The classical continuum mechanics model is enhanced with one additional degree of freedom. The governing equations for such an additional variable will be directly derived from the definition of the internal power. The micromorphic approach will be used to control the distribution of the cumulative plastic strain. Therefore, the additional degree of freedom will be enforced to follow this quantity through a penalty term.

In this section, the kinematics of the theory will first be provided, from which the balance equations can be derived, the definition of the Helmholtz free energy and of the

Clausius Duhem inequality will follow. Finally, the section will conclude with the analogy between the micromorphic-balance equation and the thermal field equation.

3.2.1 Kinematics and Balance Equations

The kinematics of the model follows the one commonly used in the classical continuum mechanics. The second-order strain tensor is defined as:

$$\underset{\sim}{\boldsymbol{\varepsilon}} = \operatorname{sym}\left[\underline{\mathbf{u}} \otimes \underline{\boldsymbol{\nabla}}\right], \tag{3.5}$$

with $\underline{\mathbf{u}}$ being the displacement vector and $\underline{\boldsymbol{\nabla}}$ denotes the gradient of a vector. Furthermore, the total strain tensor is additively decomposed into an elastic part $\underset{\sim}{\boldsymbol{\varepsilon}}_e$ and a plastic part $\underset{\sim}{\boldsymbol{\varepsilon}}_p$ as follows:

$$\underset{\sim}{\boldsymbol{\varepsilon}} = \underset{\sim}{\boldsymbol{\varepsilon}}_e + \underset{\sim}{\boldsymbol{\varepsilon}}_p, \tag{3.6}$$

By indicating the velocity $\underline{\mathbf{v}}$ as $\dot{\underline{\mathbf{u}}}$, we can define the strain rate as:

$$\dot{\underset{\sim}{\boldsymbol{\varepsilon}}} = \operatorname{sym}\left[\underline{\mathbf{v}} \otimes \underline{\boldsymbol{\nabla}}\right]. \tag{3.7}$$

The variables which are supposed to carry the targeted strain gradient effects are selected among the available state variables which can be tensors of any rank. Here, we consider a scalar variable. Two types of degrees of freedom (DOFs) are applied to the material point: the classical displacement vector $\underline{\mathbf{u}}$ and the additional scalar micromorphic variable p_χ associated with the cumulative plastic strain p through the penalty term H_χ to be defined later. Therefore, every node is endowed with 3 displacement and 1 micromorphic variable:

$$\text{DOF} = \{\underline{\mathbf{u}}, p_\chi\}. \tag{3.8}$$

Based on the definition of the strain and of the micromorphic variable, we are allowed to write the internal and kinetic power densities of the body as dependent on the strain, the micromorphic variable and its gradient[1]:

$$p^{(i)} = \underset{\sim}{\boldsymbol{\sigma}} : \dot{\underset{\sim}{\boldsymbol{\varepsilon}}} + a\,\dot{p}_\chi + \underline{\mathbf{b}} \cdot \underline{\boldsymbol{\nabla}}\,\dot{p}_\chi, \tag{3.9}$$

$$p^{(k)} = \rho\ddot{\underline{\mathbf{u}}} \cdot \dot{\underline{\mathbf{u}}}, \tag{3.10}$$

where ρ is the mass density and $\ddot{\underline{\mathbf{u}}}$ is the acceleration vector. Here, a and $\underline{\mathbf{b}}$ are generalized stresses associated with the micromorphic variable and its gradient, respectively. In this formulation, the densities of power generated by external forces and contact forces can be written as:

$$p^{(e)} = \underline{\mathbf{f}}^e \cdot \dot{\underline{\mathbf{u}}} + a^e\,\dot{p}_\chi + \underline{\mathbf{b}}^e \cdot \underline{\boldsymbol{\nabla}}\dot{p}_\chi, \tag{3.11}$$

$$p^{(c)} = \underline{\mathbf{f}}^c \cdot \dot{\underline{\mathbf{u}}} + a^c\,\dot{p}_\chi, \tag{3.12}$$

with $\underline{\mathbf{f}}^e$ being the density of body force, a^e and $\underline{\mathbf{b}}^e$ are the generalized body stresses associated to p_χ and its gradient. $\underline{\mathbf{f}}^c$ and a^c are the classical traction and the micromorphic

[1] There is a possibility here to explicitly define the kinetic and damping energy of the continuum as function of the micromorphic variable as well. Such type of descriptions have already been proposed by other researchers[Nedjar 2001; Saanouni and Hamed 2013; Davaze et al. 2021]. In the present work, however, we will include instead a viscous contribution of the micromorphic variable in the constitutive model of the continuum.

traction. The contact power density defined in Eq. (3.12) clearly states that the gradient of the micromorphic variable is not linked to any boundary effect. The global power balance law can be written as:

$$\int_{\Omega} \left(p^{(i)} + p^{(k)} \right) d\Omega = \int_{\partial\Omega} p^{(c)} d\mathrm{S} + \int_{\Omega} p^{(e)} d\Omega, \tag{3.13}$$

which, through Eq.s (3.9), (3.10), (3.11) and (3.12), transforms into:

$$\begin{aligned} \int_{\Omega} \underline{\dot{\mathbf{u}}} \cdot \left[-\underset{\sim}{\boldsymbol{\sigma}} \cdot \underline{\boldsymbol{\nabla}} - \underline{\mathbf{f}}^{e} + \rho \underline{\ddot{\mathbf{u}}} \right] \mathrm{d}\Omega + \int_{\Omega} \dot{p}_{\chi} \left[(\underline{\mathbf{b}}^{e} - \underline{\mathbf{b}}) \cdot \underline{\boldsymbol{\nabla}} + a - a^{e} \right] \mathrm{d}\Omega \\ + \int_{\partial\Omega} \underline{\dot{\mathbf{u}}} \cdot \left[-\underline{\mathbf{f}}^{c} + \underset{\sim}{\boldsymbol{\sigma}} \cdot \underline{\mathbf{n}} \right] \mathrm{dS} + \int_{\partial\Omega} \dot{p}_{\chi} \left[-a^{c} + (\underline{\mathbf{b}}^{e} - \underline{\mathbf{b}}) \cdot \underline{\mathbf{n}} \right] \mathrm{dS} = 0, \end{aligned} \tag{3.14}$$

Based on the principle of virtual power, the equilibrium equations are obtained as:

$$\begin{cases} \rho \underline{\ddot{\mathbf{u}}} = \underset{\sim}{\boldsymbol{\sigma}} \cdot \underline{\boldsymbol{\nabla}} + \underline{\mathbf{f}}^{e}, & (3.15) \\ (\underline{\mathbf{b}} - \underline{\mathbf{b}}^{e}) \cdot \underline{\boldsymbol{\nabla}} = a - a^{e}, & (3.16) \end{cases}$$

which are bounded by the following Neumann boundary conditions:

$$\begin{cases} \underset{\sim}{\boldsymbol{\sigma}} \cdot \underline{\mathbf{n}} = \underline{\mathbf{f}}^{c}, & (3.17) \\ (\underline{\mathbf{b}} - \underline{\mathbf{b}}^{e}) \cdot \underline{\mathbf{n}} = a^{c}, & (3.18) \end{cases}$$

where $\underline{\mathbf{n}}$ is the outer normal to the surface closing the domain Ω.

3.2.2 Helmholtz Free Energy Potential

The constitutive model of the medium characterizing the shape of both the classical and the generalized stresses is provided via the definition of their associated potential. The free energy density function is assumed to depend on the following state variables:

$$\{ \underset{\sim}{\boldsymbol{\varepsilon}}^{e},\, p,\, p_{\chi},\, \underline{\boldsymbol{\nabla}} p_{\chi} \} \tag{3.19}$$

namely, the elastic strain, the cumulative plastic strain, the micromorphic variable, and its gradient. The chosen potential has the form:

$$\psi(\underset{\sim}{\boldsymbol{\varepsilon}}^{e}, p, p_{\chi}, \nabla p_{\chi}) = \frac{1}{2} \underset{\sim}{\boldsymbol{\varepsilon}}^{e} : \underset{\approx}{\mathbf{C}} : \underset{\sim}{\boldsymbol{\varepsilon}}^{e} + \psi_{p}(p) + \psi_{\chi}(p, p_{\chi}, \nabla p_{\chi}), \tag{3.20}$$

where $\underset{\approx}{\mathbf{C}}$ is the elastic fourth-order stiffness tensor, ψ_p is the plastic contribution to the Helmholtz free energy (in case of hardening/softening it accounts for the expansion/shrinking of the yield surface in the stress space), and ψ_χ is the additional micromorphic contribution. A simple quadratic potential is adopted for the latter:

$$\psi_{\chi}(p, p_{\chi}, \nabla p_{\chi}) = \frac{1}{2} H_{\chi} (p - p_{\chi})^{2} + \frac{1}{2} \underline{\nabla} p_{\chi} \cdot \underset{\sim}{\mathbf{A}} \cdot \underline{\nabla} p_{\chi}, \tag{3.21}$$

where $\underset{\sim}{\underset{\sim}{\mathbf{A}}}$ is the higher-order modulus. For an isotropic material, the elastic stiffness tensor $\underset{\approx}{\mathbf{C}}$ and the tensor of higher-order moduli reduce to the following forms:

$$\underset{\approx}{\mathbf{C}} = \lambda \operatorname{trace}\left(\underset{\sim}{\boldsymbol{\varepsilon}}\right) \underset{\sim}{\mathbf{I}} \otimes \underset{\sim}{\mathbf{I}} + 2\,\mu \underset{\approx}{\mathbf{I}}, \tag{3.22}$$

$$\underset{\sim}{\underset{\sim}{\mathbf{A}}} = A\,\underset{\sim}{\mathbf{I}}, \tag{3.23}$$

with λ and μ as the classical Lamé parameters and A the new higher order modulus. The following linear isotropic plastic behavior is assigned to the material:

$$\psi_p(p) = \frac{1}{2} H_p\, p^2; \tag{3.24}$$

where H_p is the hardening modulus. Nonlinear hardening laws are possible but not considered here for simplicity.

3.2.3 Clausius-Duhem Inequality

The Clausius-Duhem inequality will be used to ensure the thermodynamic consistency of the model and to define the recoverable and dissipative parts of the mechanical contributions. The local form of the second law of thermodynamic for an iso-thermal transformation can be expressed for a continuum body as:

$$p^{(i)} - \dot{\psi} \geq 0. \tag{3.25}$$

Expanding the time derivative of Helmholtz free potential with respect to the variables on which it depends, and by retrieving the additive elasto-plastic decomposition of the strain rates, the Clausius-Duhem inequality reads:

$$\left(\underset{\sim}{\boldsymbol{\sigma}} - \frac{\partial \psi}{\partial \underset{\sim}{\boldsymbol{\varepsilon}}^e}\right) : \dot{\underset{\sim}{\boldsymbol{\varepsilon}}}^e + \underset{\sim}{\boldsymbol{\sigma}} : \dot{\underset{\sim}{\boldsymbol{\varepsilon}}}^p - \frac{\partial \psi}{\partial p}\dot{p} + \left(a - \frac{\partial \psi}{\partial p_\chi}\right)\dot{p}_\chi + \left(\underline{\mathbf{b}} - \frac{\partial \psi}{\partial \underline{\boldsymbol{\nabla}} p_\chi}\right) \cdot \underline{\boldsymbol{\nabla}} \dot{p}_\chi \geq 0. \tag{3.26}$$

At this stage, the choice on the elastic part of the strain to be energetically recoverable can be made. It implies that the terms multiplying $\dot{\underset{\sim}{\boldsymbol{\varepsilon}}}^e$ must vanish so as to ensure that the elastic strain does not contribute in entropy production, leading to:

$$\underset{\sim}{\boldsymbol{\sigma}} = \frac{\partial \psi}{\partial \underset{\sim}{\boldsymbol{\varepsilon}}^e} = \underset{\approx}{\mathbf{C}} : \underset{\sim}{\boldsymbol{\varepsilon}}^e, \tag{3.27}$$

The distinction between recoverable and dissipative parts of the generalized stress terms must also be drawn. For the gradient of the micromorphic variable, we assume that it is fully recoverable, therefore:

$$\underline{\mathbf{b}} = \frac{\partial \psi}{\partial \underline{\boldsymbol{\nabla}} p_\chi}, \tag{3.28}$$

This means that the gradient of plastic strain solely contributes to the free energy potential. In the case of metals, this can be justified by the fact that the plastic strain gradient contains contributions of the dislocation density tensor which is known to be associated with energy storage [Forest, Sievert, and E. Aifantis 2002; Gurtin 2002]. Regarding now the dissipation produced by the variation of the micromorphic variable, its positiveness

can be ensured, as originally suggested by Gurtin [Gurtin 1996; Forest 2009], by imposing that the generalized stress a possesses a recoverable part and a dissipative part that depends on $\dot{p}_\chi$ itself:

$$a = \frac{\partial \psi}{\partial p_\chi} + C_\chi \, \dot{p}_\chi, \tag{3.29}$$

where C_χ is a parameter related to viscous micromorphic effects. Lastly, for the plastic part of the Helmholtz free energy:

$$\frac{\partial \psi}{\partial p} = R, \tag{3.30}$$

where R is a thermodynamic force associated to variation of the cumulative plastic strain. The residual dissipation rate can now be written as:

$$\underset{\sim}{\boldsymbol{\sigma}} : \underset{\sim}{\dot{\boldsymbol{\varepsilon}}}^p - R \, \dot{p} + C_\chi \dot{p}_\chi^2 \geq 0. \tag{3.31}$$

The positiveness of the new parameters A and C_χ then ensures the positive definiteness of the micromorphic contributions in the free energy density and in the dissipation rate.

3.2.4 Partial differential equation governing the micromorphic variable and enhanced hardening law

By considering the explicit definition of the Helmholtz free energy potential given in Eq. (3.21), the generalized stresses read:

$$a = -H_\chi \, (p - p_\chi) + C_\chi \, \dot{p}_\chi, \tag{3.32}$$

$$\underline{\mathbf{b}} = A \, \underline{\boldsymbol{\nabla}} p_\chi. \tag{3.33}$$

The previous equation ((3.32)) indicates that the micromorphic variable p_χ and cumulative plastic strain p are related to each other through the penalty term H_χ. In order for the micromorphic variable to closely match the value of the cumulative plastic strain, it is necessary to ensure that the value of H_χ is relatively large. At this stage, it is possible to re-write the additional partial differential equation governing the micromorphic distribution by plugging the selected constitutive behavior into it. In absence of higher-order body forces (a^e and $\underline{\mathbf{b}}^e$), Eq. (3.16) can be written as:

$$C_\chi \dot{p}_\chi = A \, \nabla^2 p_\chi + H_\chi \, (p - p_\chi) \tag{3.34}$$

where ∇^2 indicates the Laplacian differential operator. The previous equation represents the only additional equation that must be solved combined with the ones governing the displacement fields.

Previous researchers already explored the potential of the micromorphic theory in rate-dependent analysis under explicit integration schemes using a modified version of Eq. (3.34). For instance, Saanouni and Hamed proposed a theory in which the second-order time derivative (acceleration) of p_χ takes the place of the first-order time derivative in Eq. (3.34) [Saanouni and Hamed 2013; Diamantopoulou et al. 2017]. Therefore, in analogy with the PDE governing the displacement fields, a form of inertia was associated to the micromorphic variable, whereas, in case of the present investigation, a viscous

term associated to the micromorphic variable is considered. The PDE governing the micromorphic field can be rewritten as:

$$\tau_{ch}\dot{p}_\chi = l_{ch}^2\nabla^2 p_\chi + (p - p_\chi) \quad \text{with} \quad l_{ch} = \sqrt{\frac{A}{H_\chi}} \quad \text{and} \quad \tau_{ch} = \frac{C_\chi}{H_\chi}, \tag{3.35}$$

where l_{ch} is the characteristic length scale endowing the theory with the spatial regularization property, and τ_{ch} is a characteristic time. To fully solve Eq. (3.35), it must be coupled with a constitutive model for the plastic behavior of the medium. Starting from the yield function:

$$f(\underset{\sim}{\boldsymbol{\sigma}}, R) = \boldsymbol{\sigma}_{eq} - \boldsymbol{\sigma}_0 - R \tag{3.36}$$

where $\boldsymbol{\sigma}_{eq}$ is the von Mises equivalent stress measure and $\boldsymbol{\sigma}_0$ is the initial yield stress. Assuming associated plasticity and the normality rule to hold, the rate of the plastic strain can be written as:

$$\underset{\sim}{\dot{\boldsymbol{\varepsilon}}}^p = \dot{p}\,\frac{\partial f}{\partial \underset{\sim}{\boldsymbol{\sigma}}} = \dot{p}\,\underset{\sim}{\mathbf{n}}, \tag{3.37}$$

and the dissipation in Eq. (3.31) takes the form:

$$(\underset{\sim}{\boldsymbol{\sigma}} : \underset{\sim}{\mathbf{n}} - R)\,\dot{p} + C_\chi \dot{p}_\chi^2 \geq 0; \tag{3.38}$$

and in case of plastic loading:

$$(\sigma_{eq} - R)\,\dot{p} + C_\chi \dot{p}_\chi^2 = \sigma_0\,\dot{p} + C_\chi \dot{p}_\chi^2 \geq 0; \tag{3.39}$$

From the specific form of the plastic part of the Helmholtz free energy and from Eq. (3.30), one can infer the stress that is thermodynamically associated with the cumulative plastic strain:

$$R = H_p\,p + H_\chi(p - p_\chi) \tag{3.40}$$

This represents the hardening law enhanced by a new micromorphic contribution. This shows the coupling arising in the theory between plasticity and the micromorphic variable. After substituting the equation (3.35), the following alternative expression of the enhanced hardening law is obtained:

$$R = H_p\,p - A\,\nabla^2 p_\chi + C_\chi \dot{p}_\chi \tag{3.41}$$

The linear hardening/softening contribution (depending on the sign of H_p) to the yield stress is enhanced by the Laplacian of the micromorphic variable, a usual term in regularization methods, but also by an additional viscous term whose magnitude is controlled by the value of parameter C_χ.

3.2.5 Micromorphic-Thermal Analogy

The comparison between the scalar micromorphic model described in the previous section and the classical thermo-mechanical theory is here outlined. The development of the latter theory will not be fully reported, but we will make use of the main governing equations of the thermal field to draw the comparison with the micromorphic theory previously developed. On the one hand, the additional variable in the present theory, p_χ, ought to

Table 3.1: Analogy between micromorphic gradient plasticity and thermal analysis.

	Micromorphic	Heat
DOF	p_χ	T
Constitutive law	$\underline{\mathbf{b}} = A\nabla p_\chi$	$\underline{\mathbf{q}} = -k\nabla T$
Balance law	$C_\chi \dot{p}_\chi = A\,\nabla^2 p_\chi + H_\chi\,(p - p_\chi)$	$\rho C\dot{T} = k\,\nabla^2 T + r$
Source term	$H_\chi\,(p - p_\chi)$	r

be solved through the PDE (3.34), whereas, on the other hand, the additional degree of freedom of the classical thermo-mechanical theory, that is temperature T, must be solved through a different PDE, and here the two equations are reported (where the Fourier conduction law is assumed to be valid for the heat flux)

$$C_\chi \dot{p}_\chi = A\,\nabla^2 p_\chi + H_\chi\,(p - p_\chi)\,, \tag{3.42}$$

$$\rho C\dot{T} = k\,\nabla^2 T + r, \tag{3.43}$$

where C is the specific heat capacity of the material, r is a source term and k is the thermal conductivity of the material, that we assumed to be independent from temperature. Although the two equations are used to govern completely different physical fields, a straightforward parallelism among them can be identified. In Table 3.1, a comparison between different aspects of the two theories is reported. The analogy between these two theories inspired the idea of adapting an already implemented numerical resolution scheme (meant to be used for the thermal field) for the micromorphic variable. The main objective of the present investigation is, in fact, the analysis of the feasibility of such idea. The main advantage of the proposed method is that the micromorphic theory can be easily implemented in an explicit resolution scheme, while requiring very limited access and marginal effort in modifying the original code. This aspect obviously makes the implementation of this theory more attractive than other methodologies which would require high level of accessibility to the main solver, since both new element and material definitions would need to be developed. Such an analogy has been used in the past for coupling chemical diffusion and mechanics in the implicit version of the numerical solver ABAQUS [Diaz et al. 2016]. The analogy has also been recognized and used to implement gradient plasticity and gradient damage models, again, in the implicit version of ABAQUS [A. et al. 2018]. Note that in these implementations, the viscous term, i.e. the transient term proposed in the present work, is absent.

The two PDEs are in fact so similar that in order to solve for the micromorphic variable, instead of the temperature, only two minor modifications need to be done. Given the comparison between the two PDEs (Eq. (3.42) and Eq. (3.43)), and given the form of the yield function in Eq. (3.36), the elements that require non-trivial modifications are the source term r and the yield radius: the former has to coincide with the difference between the cumulative plastic strain and the micromorphic variable (amplified by the H_χ parameter), and the latter has to take into account the extra hardening due to the

micromorphic variable:

$$r = H_\chi(p - p_\chi); \tag{3.44}$$

$$f = \sigma_{eq} - \sigma_0 - H_p\, p - H_\chi(p - p_\chi); \tag{3.45}$$

whereas the coefficients present in the thermal balance equation can be easily substituted with the parameters characterizing the micromorphic PDE. Implementing the conditions (3.44) and (3.45) represents the only real, yet minor, effort that is required to make use of the present theory, assuming the existence of a thermal solver and the possibility of applying small modifications.

3.2.6 Influence on the C_χ parameter

The additional parameter C_χ naturally arises from the development of the chosen constitutive material model for the generalized stress a. In order to obtain the final form of the governing Eq. (3.34), so that the thermal-micromorphic analogy is valid, the presence of the C_χ parameter is required, and it should not vanish in the case of the implementation of the transient problem. However, from the analysis of Eq. (3.32), it is clear that the parameter C_χ regulates the development of the viscous part of the micromorphic variable, and therefore that a viscous part of the micromorphic variable exists. Being this an additional material parameter, the question on the calibration of such value must be addressed.

The purpose of using the micromorphic analysis, in the present investigation, is to gain indirect control on the distribution of the cumulative plastic strain and its gradient, thus the constraint on the micromorphic variable to closely follow the value of the cumulative plastic strain through the penalty parameter. The present theory also accounts for the development of viscous stresses generated by not-negligible strain rates, and the micromorphic variable follows the value of the cumulative plastic strain, regardless of whether the plastic strain increment is caused by quasi-static or viscous stresses. The adoption of large values of the C_χ parameters (compared to H_χ) would allow the viscous part of the micromorphic variable to produce additional meaningful generalized stress (see Eq. (3.32)), therefore altering the value that it should have, based only on the difference between micromorphic variable and cumulative plastic strain (effectively producing the same stress as if this difference was larger). Therefore, too large values of C_χ would somehow corrupt and interfere with the equivalence between cumulative plastic strain and micromorphic variable. On the contrary, by neglecting any meaningful contribution of the viscous micromorphic term to exist, we lose the analogy with transient thermal analysis proposed here for the implementation.

Therefore, for the present investigation, the C_χ parameter must exist, so that the thermal-micromorphic analogy holds, but its value should not be too large. The allowed magnitude for this parameter will be tested by checking an analytical solution in the static case, considered in Section 3.3.1.

3.2.7 Numerical Implementation

The micromorphic plasticity model has been implemented in VPS Explicit [ESI Group 2000], a finite element software developed by ESI Group solving both dynamics and heat problems. In order to account for the large deformation expected during manufacturing

operations, the theory has been developed according to the VPS standard method, that is, using rate-type constitutive equations. This does not alter the theory so far presented, since the micromorphic part remains unchanged. For the same reason, the space gradients that are encountered in this chapter are meant to be evaluated with respect to the current configuration of the medium, as in an Updated-Lagrangian approach. The additive decomposition is applied to the strain rate tensor, which can be split into elastic and plastic contributions:

$$\underset{\sim}{\mathbf{D}} = \underset{\sim}{\mathbf{D}}^e + \underset{\sim}{\mathbf{D}}^p, \tag{3.46}$$

where $\underset{\sim}{\mathbf{D}}$ is the strain rate, and the elastic constitutive model is rewritten by means of a hypoelasticity relation:

$$\overset{\circ}{\underset{\sim}{\boldsymbol{\sigma}}} = \underset{\approx}{\mathbf{C}} : \underset{\sim}{\mathbf{D}}^e, \tag{3.47}$$

where $\overset{\circ}{\underset{\sim}{\boldsymbol{\sigma}}}$ is the Jaumann stress rate, and it can be re-written as:

$$\overset{\circ}{\underset{\sim}{\boldsymbol{\sigma}}} = \dot{\underset{\sim}{\boldsymbol{\sigma}}} - \underset{\sim}{\boldsymbol{W}} \cdot \underset{\sim}{\boldsymbol{\sigma}} + \underset{\sim}{\boldsymbol{\sigma}} \cdot \underset{\sim}{\boldsymbol{W}}, \tag{3.48}$$

where $\underset{\sim}{\boldsymbol{W}}$ is the spin tensor. The finite element solution is obtained by establishing the weak form of Eqs. (3.15) and (3.16) using the Galerkin method. The dynamic balance Equation (3.15) is weighted with the test velocities $\underline{\dot{\mathbf{u}}}$ whereas the micromorphic balance Equation (3.16) is weighted with the test micromorphic variable rates $\dot{p}_\chi$. Integration over the domain is achieved by the use of the divergence theorem to lower the order of the derivatives. The natural boundary conditions are incorporated as forcing terms, leading to the equations to be discretized by finite-element interpolations. The discretization of the displacement and micromorphic fields over the domain is achieved by using proper-order interpolation functions. The following algebraic equations are derived:

$$\underset{\sim}{\mathbf{M}} \cdot \underline{\ddot{\mathbf{U}}} = \underline{\mathbf{F}}_{ext} - \underline{\mathbf{F}}_{int}; \tag{3.49}$$

$$\underset{\sim}{\mathbf{C}}_\chi \cdot \underline{\dot{\mathbf{p}}}_\chi = \underline{\boldsymbol{a}}_r - \underline{\boldsymbol{a}}_{int}; \tag{3.50}$$

where $\underset{\sim}{\mathbf{M}}$ is the mass matrix, $\underline{\mathbf{F}}_{ext}$ is the vector of external nodal forces, $\underline{\mathbf{F}}_{int}$ is the vector of internal nodal forces, $\underset{\sim}{\mathbf{C}}_\chi$ is the viscosity parameter matrix, $\underline{\boldsymbol{a}}_r$ is the vector containing the nodal generalized forces generated by the source terms and $\underline{\boldsymbol{a}}_{int}$ is the vector of nodal generalized forces induced by Laplacian of the micromorphic variable. In Eq. (3.50) the similarity with the discretized algebraic equation to solve the heat equation in thermal analysis can be appreciated once again. In fact, VPS Explicit uses the same form of equation to solve the heat equation:

$$\underset{\sim}{\mathbf{C}} \cdot \underline{\dot{\mathbf{T}}} = \underline{\mathbf{Q}}_{\partial\Omega} + \underline{\mathbf{Q}}_{\Omega} - \underline{\mathbf{Q}}_{K}; \tag{3.51}$$

where $\underline{\mathbf{T}}$ is the nodal temperature vector, $\underset{\sim}{\mathbf{C}}$ is the heat capacity matrix, $\underline{\mathbf{Q}}_{\partial\Omega}$ is the nodal heat flow depending on the heat flux on the outer surface $\partial\Omega$, $\underline{\mathbf{Q}}_{\Omega}$ is the nodal heat flow depending on the internal heat source and $\underline{\mathbf{Q}}_{K}$ is the internal nodal heat flow depending on the heat flux inside the domain Ω.

A central difference explicit scheme associated to the lumped mass matrix is used to solve Eq. (3.49). Assuming that the problem is initially found at time t_0 and that the objective is to evaluate its status at time $t_1 = t_0 + \Delta t$, the following standard steps are

taken:

$$\underline{\ddot{\mathbf{U}}}_{t_0} = \underset{\sim}{\mathbf{M}}_{t_0}^{-1} \cdot \left[\underline{\mathbf{F}}_{ext_{t_0}} - \underline{\mathbf{F}}_{int_{t_0}} \right]; \tag{3.52}$$

$$\underline{\dot{\mathbf{U}}}_{t_0+\frac{\Delta t}{2}} = \underline{\dot{\mathbf{U}}}_{t_0-\frac{\Delta t}{2}} + \Delta t\, \underline{\ddot{\mathbf{U}}}_{t_0}; \tag{3.53}$$

$$\underline{\mathbf{U}}_{t_1} = \underline{\mathbf{U}}_{t_0} + \Delta t\, \underline{\dot{\mathbf{U}}}_{t_0+\frac{\Delta t}{2}}; \tag{3.54}$$

A forward Euler scheme associated with the viscosity lumped matrix is implemented to solve Eq. (3.50):

$$\dot{p}_{\chi_{t_0}} = \underset{\sim}{\mathbf{C}}_{\chi_{t_0}} \cdot \left[\underline{\boldsymbol{a}}_{r_{t_0}} - \underline{\boldsymbol{a}}_{int_{t_0}} \right]; \tag{3.55}$$

$$p_{\chi_{t_1}} = p_{\chi_{t_0}} + \Delta t\, \dot{p}_{\chi_{t_0}}; \tag{3.56}$$

A weak micromorphic-mechanical coupling is implemented in VPS Explicit, that is, the two equations are solved separately so that displacements are considered constants while solving for p_χ and vice-versa. The micromorphic field influences the plastic behavior of the continuum (through condition (3.44)), and, in return, the cumulative plastic strain (the difference between the cumulative plastic strain and the micromorphic variable) acts as a source term in the micromorphic balance equation (in condition (3.45)).

Regarding the mechanical behavior, a user material routine implements the mechanical model as previously defined. The values of the micromorphic variables at the Gauss quadrature points are interpolated by mean of the interpolation functions from the nodal values. So the user material routine not only integrates the mechanical behavior but also computes the source term $H_\chi(p - p_\chi)$ at the Gauss points. Regarding the micromorphic treatment, a specific function is developed inside the thermal solver in order to recover the source term from the material computations previously evaluated. The main algorithmic steps of the explicit resolution over the time increment Δt may be summarized by the following scheme:

Algorithm 1: Algorithmic steps of the explicit resolution scheme implemented in VPS Explicit.

1. **Micromorphic:** at time t_n, compute $\underset{\sim}{\mathbf{C}}_\chi$, $\underline{\boldsymbol{a}}_r$ and $\underline{\boldsymbol{a}}_{int}$;
2. **Stability condition:** compute the time step Δt;
3. **Micromorphic:** explicit time integration, compute $p_{\chi_{t_1}}$;
4. **Mechanics:** explicit time integration, compute $\underline{\mathbf{u}}_{n+1}$;
5. **Next Step:** compute $t_{n+1} = t_n + \Delta t$.

The critical time step for the time integration of the equations is taken as the minimum between the critical time step for the mechanical and the micromorphic integration. The critical time step for the mechanical integration follows the standard definition, whereas the critical time step for the integration of the micromorphic variable is the the same used for the thermal variable (following the micromorphic-thermal analogy exploited in Section 3.2.5).

3.3 Strain Localization in simple shear test

3.3.1 Analytical solution

The analytical solution is developed for the rate-independent static case as a reference for validation of the FE scheme at the static limit. It is inspired from similar solution proposed by [Mazière et al. 2015; Scherer, Besson, et al. 2019; Scherer, Phalke, et al. 2020a]. Consider a periodic strip made of a thick rectangular plate of the width W along X_1 direction, the length L along X_2 direction, and the thickness T along X_3 direction (Fig. 3.1) undergoing simple shear. A macroscopic deformation $\bar{\varepsilon}$ is applied such that

$$\underline{\mathbf{u}} = \underset{\sim}{\bar{\boldsymbol{\varepsilon}}} \cdot \underline{\mathbf{X}} + \underline{\boldsymbol{\nu}}(\underline{\mathbf{X}}), \quad \text{with} \quad \underset{\sim}{\bar{\boldsymbol{\varepsilon}}} = \bar{\varepsilon}_{12}(\underline{\mathbf{e}}_1 \otimes \underline{\mathbf{e}}_2 + \underline{\mathbf{e}}_2 \otimes \underline{\mathbf{e}}_1), \tag{3.57}$$

where $\underline{\boldsymbol{\nu}}$ is the periodic displacement fluctuation. Due to equilibrium conditions, the shear stress component is homogeneous so that the equivalent stress σ_{eq} is invariant along $\underline{\mathbf{X}}_1$, $\underline{\mathbf{X}}_2$ and $\underline{\mathbf{X}}_3$, hence

$$\sigma_{eq}(\underline{\mathbf{X}}_1, \underline{\mathbf{X}}_2, \underline{\mathbf{X}}_3) = \sigma_{eq}. \tag{3.58}$$

The yield condition including the linear softening term and the micromorphic contribution (with $C_\chi = 0$ here) can be written as

$$f = \sigma_{eq} - (\sigma_0 + H_p p + H_\chi(p - p_\chi)) = 0 \quad \text{with} \quad H_p < 0. \tag{3.59}$$

The PDE governing the micromorphic variable is given by

$$A\frac{\partial^2 p_\chi}{\partial X_2^2} = H_\chi(p_\chi - p). \tag{3.60}$$

Elimination of the variable p in the previous equation by means of the yield condition (3.59) leads to the following form of the PDE to be solved for p_χ:

$$A\frac{\partial^2 p_\chi}{\partial X_2^2} - \frac{H_p H_\chi}{H_p + H_\chi} p_\chi + \frac{H_\chi}{H_p + H_\chi}(\sigma_{eq} - \sigma_0) = 0. \tag{3.61}$$

In case of linear softening (3.61) takes the form

$$\frac{\partial^2 p_\chi}{\partial X_2^2} - \left(\frac{2\pi}{\lambda}\right)^2 p_\chi = -\left(\frac{2\pi}{\lambda}\right)^2 \kappa, \tag{3.62}$$

where λ is the characteristic width of the deformation zone. The expressions for constants λ and κ are:

$$\lambda = 2\pi\sqrt{\frac{A(H_p + H_\chi)}{|H_p| H_\chi}}; \tag{3.63}$$

$$\kappa = \left(\frac{\lambda}{2\pi}\right)^2 \frac{H_\chi}{A(H_p + H_\chi)}(\sigma_{eq} - \sigma_0), \tag{3.64}$$

where width of the deformation zone λ is a characteristic length scale. Note that for large value of H_χ ($H_\chi \gg H_p$), the characteristic length scale λ takes the form:

$$\lambda \simeq 2\pi\sqrt{\frac{A}{H_p}}. \tag{3.65}$$

The gradient parameter A controls the width of the shear band. With increasing A value, width of the shear band increases. The PDE (3.62) governing p_χ is only valid in the region $X_2 \in [\frac{-\lambda}{2}, \frac{\lambda}{2}]$ and the solution is of the form

$$p_\chi(X_2) = \alpha_1 \cos\left(2\pi\frac{X_2}{\lambda}\right) + \alpha_2 \sin\left(2\pi\frac{X_2}{\lambda}\right) - \kappa. \tag{3.66}$$

For symmetry reasons, $p_\chi(X_2) = p_\chi(-X_2)$ leads to $\alpha_2 = 0$. At the elastic/plastic interfaces, i.e at $X_2 = \pm\frac{\lambda}{2}$, continuity of micromorphic variable p_χ and of the generalized stress normal to the interface $\underline{\mathbf{M}} \cdot \underline{\mathbf{X}}_2$ must hold, hence

$$p_\chi\left(\pm\frac{\lambda}{2}\right) \simeq p\left(\pm\frac{\lambda}{2}\right) = 0, \tag{3.67}$$

$$\underline{\mathbf{M}}\left(\pm\frac{\lambda}{2}\right) \cdot \underline{\mathbf{X}}_2 = A\frac{dp_\chi}{dX_2}\bigg|_{X_2=\pm\frac{\lambda}{2}} = 0. \tag{3.68}$$

where we make the approximation that p_χ is sufficiently close to p, i.e. that the penalty coefficient is large enough. Combining (3.67) and (3.68) with (3.66) leads to

$$\alpha_1 = \frac{(\sigma_{eq} - \sigma_0)}{H_p}. \tag{3.69}$$

Moreover, the equivalent stress is expressed as

$$\sigma_{eq} = \frac{\mu}{L}\int_{\frac{-L}{2}}^{\frac{L}{2}} \left(\frac{\varepsilon_{12} - p}{2}\right) dX_2, \tag{3.70}$$

where μ is the elastic shear modulus. From the yield condition:

$$p = \frac{\sigma_{eq} - \sigma_0 + H_\chi p_\chi}{H_p + H_\chi} \tag{3.71}$$

which can be substituted in Eq. (3.70) and integration gives an expression for σ_{eq} as a function of applied macroscopic shear $\bar{\varepsilon}_{12}$ and then the uniform shear stress writes

$$\sigma_{eq} = \frac{\bar{\varepsilon}_{12} + \frac{\sigma_0}{Z_e}}{\frac{1}{\mu} + \frac{1}{Z_e}}, \quad \text{with} \quad \frac{1}{Z_e} = \frac{\lambda}{H_p L}. \tag{3.72}$$

where μ is the shear modulus of the material.

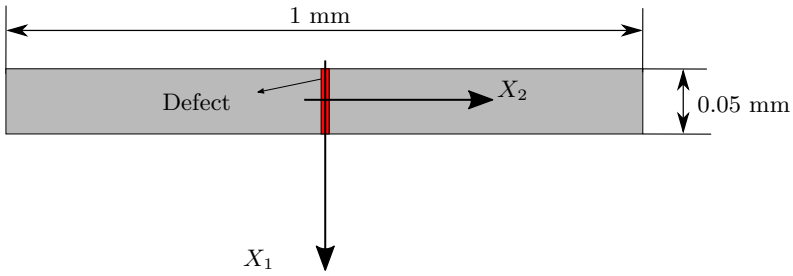

Figure 3.1: Geometry of the shear localization strip problem.

Table 3.2: Numerical values of material parameters used for the simulation of a periodic strip undergoing simple shear.

E	ν	ρ	σ_0	H_p	H_χ	A	C_χ
75 GPa	0.3	2.8×10^3 Kg/m^3	100 MPa	-500 MPa	10^6 MPa	0.08 N	90 MPa.s

3.3.2 FE solution

The FE simulations are performed with a periodic strip. The associated 2D coordinate system and geometry are shown in Fig. 3.1. The strip has been meshed with 3D 8-nodes elements onto which plane strain conditions were applied by imposing zero out-of-plane displacement to all the nodes. The nodes at the bottom of the strip ($X_2 = -L/2$) were clamped along X_1 and X_2. The nodes on the top surface ($X_2 = L/2$) were clamped along X_2 and a Dirichlet type of boundary condition was applied along X_1 whereas the displacements along X_2 were fixed. Linear shape functions have been used to interpolate the nodal fields, and full integration schemes have been used for the material behavior. Numerically, in order to trigger the strain localization in a periodic strip, a small defect is introduced at the centre (Fig. 3.1). The defect is one element having an initial yield stress 3% less than the matrix. Isotropic elasticity is considered. The material parameters used for the analytical solution and FE simulations are presented in Table 3.2.

Fig. 3.2a and 3.2b show the cumulative plastic strain fields with the classical and the micromorphic models using two different mesh discretizations, one *coarse* and one *fine* mesh (using 0.010 mm and 0.003 mm thick elements respectively). Given the fact that in this example the shear band is already known to have a thickness of ≈ 0.08 mm, the chosen mesh size lies well within a safe regime for the gradient effects to be properly captured. The classical plasticity model exhibits pathological mesh dependency and width of the shear band always collapse to one element irrespective of the mesh size. In contrast, the width of the formed shear band with the micromorphic model is finite and independent of the mesh size. This indicates the capabilities of the implemented micromorphic theory in an explicit scheme to solve the shear strain localization problem.

Furthermore, the cumulative plastic strain variation along X_2 obtained from the FE solution is validated against the analytical solution developed for the rate-independent case (cf. Eq. (3.66)), see Fig. 3.3. The FE simulation is validated for $\bar{\varepsilon}_{12} = 0.01$. Moreover, simulations are performed by changing the simulation time while keeping the same applied

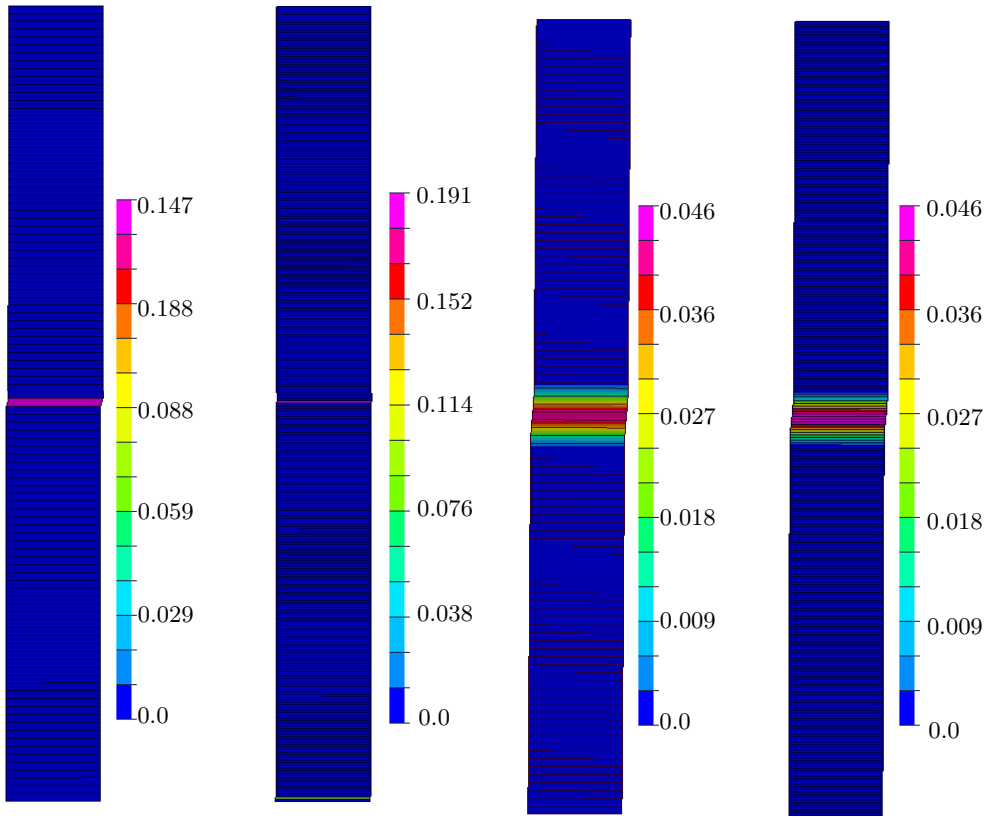

(a) Classical Plasticity. (b) Micromorphic Continuum.

Figure 3.2: Localization of plastic strain in a periodic strip undergoing simple shear for two different mesh sizes.

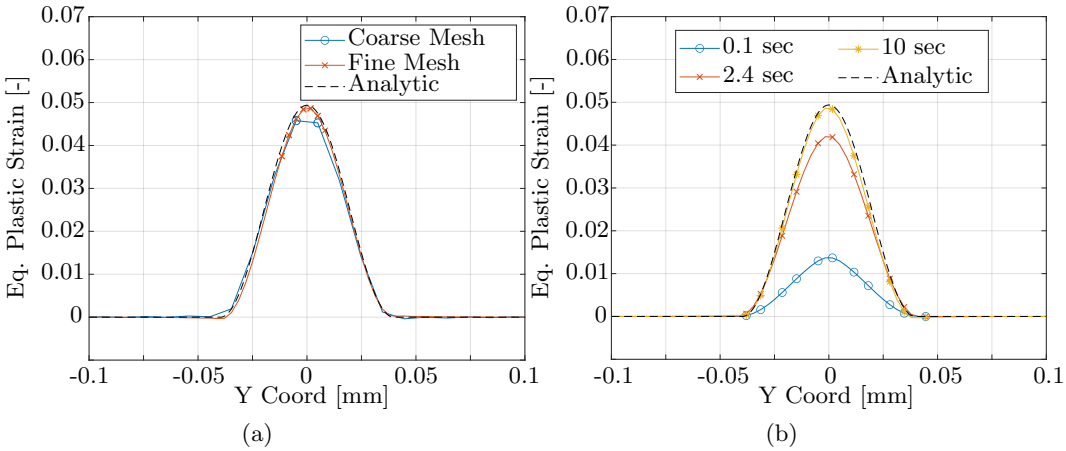

Figure 3.3: Validation of FE solution against the analytical solution. (a) Equivalent plastic strain distribution obtained for a simulation of 10 seconds for two different mesh discretizations (101 vs. 303 elements); (b) equivalent plastic strain distribution obtained with a fine mesh for different total time.

total shear strains. Fig. 3.3b shows that the perfect agreement with an analytical solution is obtained for $t = 10$ sec. which corresponds to low enough strain rate to make the viscous contribution in Eq. (3.41) negligible. Larger strain rates are observed to limit the localization since the maximum strain in the band decreases for increasing strain rates. Since the total strain is imposed, this means that a higher elastic strain compensates the lower plastic strain which means that stress values are higher.

In order to retrieve the quasi-static solution, also the viscous parameter C_χ had to be chosen small enough. The reason is to minimize as much as possible any viscous-like component of the generalized stress a in Eq. (3.32) to retrieve the rate–independent solution.

Metals at high temperatures are known to be strain rate sensitive. This effect is generally taken into account by means of an appropriate viscoplastic flow rule, for instance based on a Norton power law. In the present work, rate-independent plasticity only has been considered but the generalization to viscoplasticity is straightforward in the proposed framework. Note that the proposed model presents an additional strain rate sensitivity, via the viscosity parameter C_χ. This will require appropriate calibration for instance using strain field measurements during localization.

3.4 Numerical examples

In this section, the applicability of the implemented scalar micromorphic strain gradient theory is tested for two additional cases: a shearing operation process and a bending test. The aim of this section is to exploit the analogy explained in section 3.2.5, whose numerical implementation has been previously presented, to prove that simulations of manufacturing operations using the micromorphic continuum under an explicit integration scheme can be successfully performed.

Industry best practice discourages the employment of complex numerical methods to produce simulations, mainly to guarantee a high degree of reliability of the results and computational efficiency in terms of CPU time. Regarding this reasonable concerns, the results that will be presented here are to be considered as proof of the simplicity of the method, which requires only one additional parameter to be calibrated, that is A (see the discussion on the C_χ parameter in Section 3.2.6).

As previously explained in the introduction, the relevance of the application of regularization procedures in manufacturing operations is vital, especially in cases in which the thermal power has a major presence. Thermal softening can take place when high rates of plastic strain are produced, and similar softening can be reproduced by assigning a negative slope to the hardening function in Eq. (3.40). The regularization potential of the proposed method is investigated in the shearing operation section. Moreover, one of the missing features of the classical continuum mechanics is the capability of predicting any size effect. This becomes of major relevance whenever the deformation localizes is small regions or in the case of forming of micro-components [Zhu et al. 2020; L. Li et al. 2009]. The ability of the proposed method to capture the size effect is proven in the bending section.

3.4.1 Shearing Operation

The shear band formation is a commonly observed phenomenon in manufacturing operations in case of heavy deformation, for instance, high-speed shaping, forging, machining, and several other processes [Molinari, Musquar, et al. 2002; Burns et al. 2002]. Numerically, the shear band simulation shows spurious mesh dependency when we consider a classical plasticity approach with strain softening. Dynamics combined with viscosity or/and heat conduction are known to provide regularization but the involved length scales are often too small for efficient FE modeling so that strain gradient or micromorphic plasticity is still useful to introduce physically more realistic length scales [Stathas et al. 2022; Wcisło and Pamin 2017].

Shearing operation is most commonly used in the metal forming industries for sheet metal cutting. In this section, the implemented micromorphic approach is used for the regularization of shear band formation in shearing operation.

The shearing operation is performed on a sheet of 5 mm thickness under plane strain conditions with one element across the width. The geometry is shown in Fig. 3.4. The sheet has been meshed with 3D 8-nodes elements with linear shape functions and full integration schemes. The lower tool is fixed, while velocity is applied to the upper tool in the downward direction. At the initial deformation stage, a linearly increasing velocity up to 4 mm/sec. is applied. Once the velocity of 4 mm/sec. is achieved, it is kept constant in the later stage of the deformation. The contact between the deformable sheet and tools is taken into account using a constant coefficient of friction 0.3. The tools are considered as rigid bodies, while the sheet is assigned with an elastoplastic material behavior using linear strain softening. Isotropic elasticity is considered. The used material parameters in the numerical simulations are presented in Table 3.3.

At first, simulations are performed with classical plasticity using three different mesh discretizations. The elements size of the different meshes in the region of interest span from 0.2 to 0.04 mm respectively, and, as it will be possible to appreciate in Figure 3.6, this element size is extremely small if compared with the shear band thickness, thus

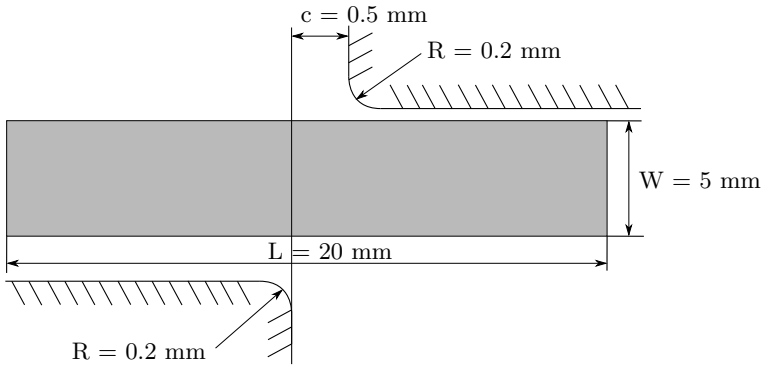

Figure 3.4: Geometry used for the shear operation simulation.

Table 3.3: Numerical values of material parameters used for the simulation of the shearing operation.

E	ν	ρ	σ_0	H_p	H_χ	A	C_χ
75 GPa	0.3	2.8×10^3 kg/m^3	100 MPa	-500 MPa	10^6MPa	128-800 N	90 MPa.s

ensuring that the gradient effect are correctly captured. The limitation of the classical plasticity model, known as pathological mesh dependency in the strain localization problem can be observed from Fig. 3.5a and 3.5e by the contours of the cumulative plastic strain. The magnitude of the cumulative plastic strain is different for two different mesh discretizations, and it increases with finer mesh. Furthermore, the observed width of the shear band is different for two different mesh discretizations and it always collapses to one element size irrespective of the mesh size. In contrast, the formed width of the shear band using the micromorphic approach is finite and does not depend on the mesh density as seen from Fig. 3.5b and 3.5f. In addition, the magnitude of the cumulative plastic strain reaches asymptotic values while reducing the mesh size.

Furthermore, the effect of the diffusivity coefficient A on the shear band widths is investigated. Fig. 3.6 shows the variation of cumulative plastic strain for three different values of the gradient parameters A, 128 N, 320 N, and 800 N. As the value of A increases the intensity of plastic strain gradient within the shear region reduces. As expected from the analytical expression for the length scale in Eq. (3.63), the width of the shear band increases with an increase in the A value. For the three different values of the A parameter, 128 N, 320 N and 800 N, the observed widths of the shear bands are 2.4 mm, 2.8 mm, and 3.5 mm, respectively. If the characteristic length was evaluated through Equation (3.63), the values of 3 mm, 5 mm and 8 mm would be the results. The divergence of these values is due to the fact that the boundary conditions are not the same, thus the deformation state is not pure shear.

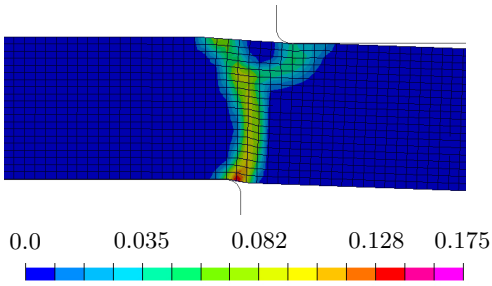

(a) Classical plasticity model. Coarse Mesh.

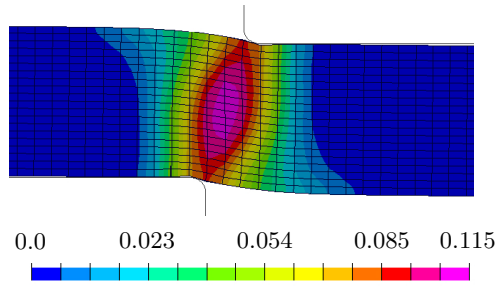

(b) Micromorphic model. Coarse Mesh.

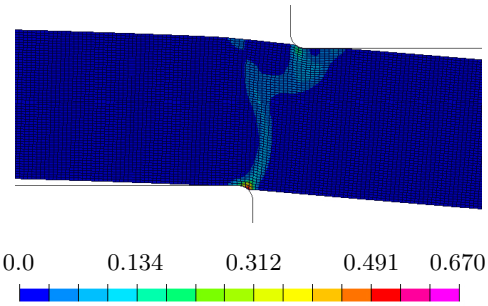

(c) Classical plasticity model. Intermediate Mesh.

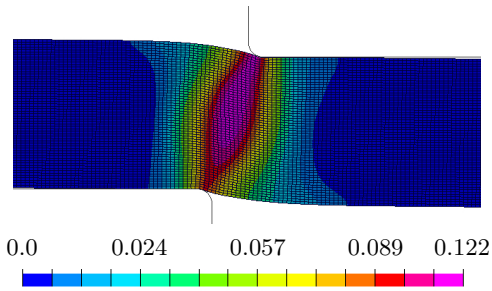

(d) Micromorphic model. Intermediate Mesh.

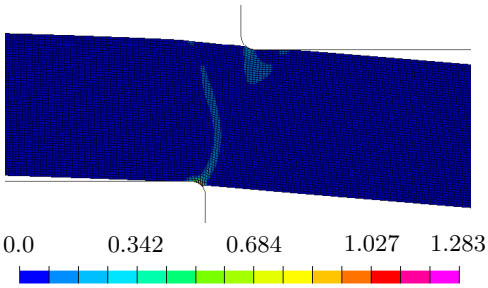

(e) Classical plasticity model. Fine Mesh.

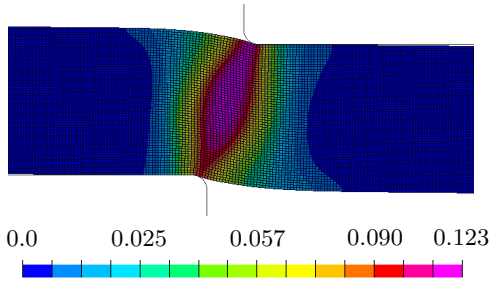

(f) Micromorphic model. Fine Mesh.

Figure 3.5: Mesh size effect on the plastic strain localization during shearing simulation. On the left the results were predicted by the classical plasticity model, on the right by the micromorphic. From the top to the bottom, increasing mesh size.

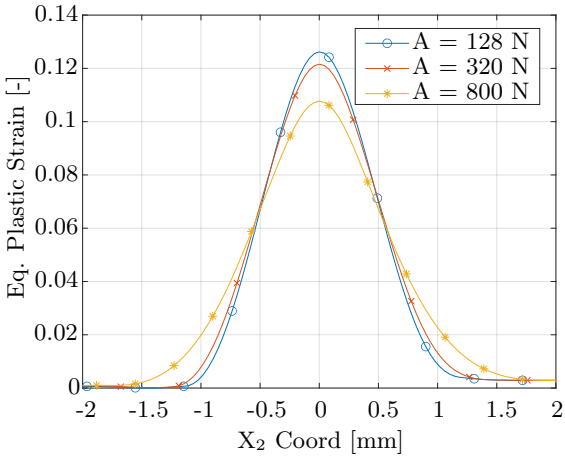

Figure 3.6: Effect of the variation of the characteristic length scale on the plastic strain distribution during shearing simulation.

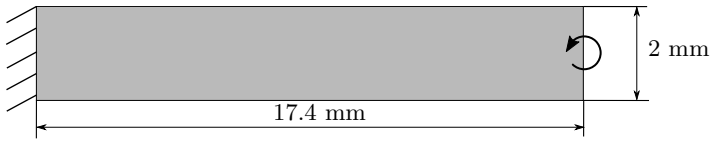

Figure 3.7: Geometry and the applied boundary conditions on the beam used for the bending simulations.

3.4.2 Bending

The bending test is used to verify that the implemented micromorphic model is able to capture the size effect for hardening plasticity. It is possible to find in literature many studies that experimentally highlighted the presence of extra hardening in the bending moment, whenever the specimen geometry was reaching sub-millimeters dimension, approaching grain size. In 1994 Fleck and co-workers [Fleck, Muller, et al. 1994] reported hardening behavior in a copper wire under torsion for wire diameters in the order of $10 - 100$ micro-meters, whereas tensile tests performed on the same wires found no evidence of size effect. Stölken and Evans [Stölken et al. 1998] designed a micro-bend test to measure the plastic characteristic length scale associated with the strain gradient, subsequently reporting the results pertaining to thin ($12.5\mu m \mapsto 50\mu m$) Nickel foils.

In Fig. 3.7, the geometry and the boundary conditions of the specimen are reported. The specimen has been discretized using 3D type of elements under plane strain conditions. Linear shape functions are used to interpolate nodal values, and full integration scheme is used for the elements. One element spans the 1 mm width and 10 elements span half the thickness of the beam (mesh size of 0.1 mm) so that there should be enough elements to capture the size effect. The left face of the beam is clamped, whereas a material rotation is enforced on the nodes of the right face through a coupling involving the nodes of the right face and an auxiliary node. The resultant bending moment is probed at the auxiliary node. A total rotation of 45°is applied.

Table 3.4: Numerical values of material parameters used for the simulation of the bending test

E	ν	ρ	σ_0	H_p	H_χ	A	C_χ
75 GPa	0.3	$2.8\,10^3$ kg/m^3	100 MPa	200 MPa	10^6MPa	128-800 N	90 MPa.s

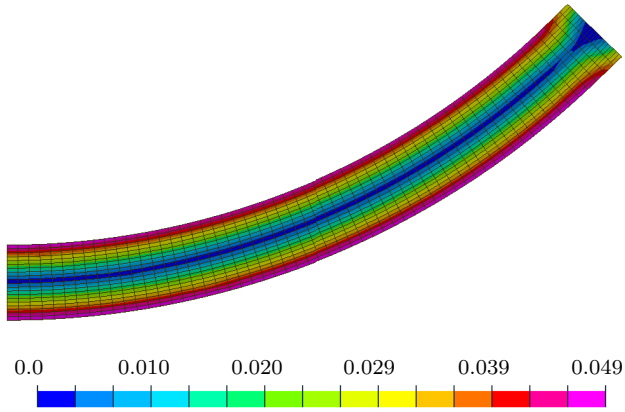

Figure 3.8: Cumulative plastic strain field during bending process using micromorphic medium.

The size effect can be experimentally encountered whenever the geometry of the specimen reduces down to approximately the grain size of the metal. Virtually, the same phenomenon could be achieved by keeping constant the geometry of the specimen and simultaneously increasing the characteristic length scale. The effectiveness of the formulation in predicting the size effect through the bending test has been verified by employing the latter method. The numerical framework previously presented does not explicitly make use of the grain size, but a characteristic length scale in Eq. (3.35) was identified, and this will serve the same purpose. The use of larger or smaller characteristic lengths will respectively induce a stiffer or softer global response of the specimen. Three different values of gradient parameter A have been used. The other material parameters used in the simulation of the bending tests are reported in Table 3.4. In the attempt of replicating a quasi-static bending test, the chosen value of the C_χ parameters is relatively small, so that any viscous contribution of the micromorphic variable would be negligible.

In Fig. 3.8 the distribution of the cumulative plastic strain for the bending test using the micromorphic model is reported. Besides the edge effect induced by the boundary condition at the right surface, the solution appears to be invariant along the longitudinal direction of the strip.

The classical and micromorphic solutions in terms of normalized bending moment vs. applied rotation are shown in Fig. 3.9. The probed bending moment has been normalized with respect to the first moment of area of the beam cross-section, that is $b\,h^2$, where b is the width of the rectangular cross-section, and h is the height of the rectangular cross-section. From Figure 3.9, it can be appreciated that the classical solution is retrieved

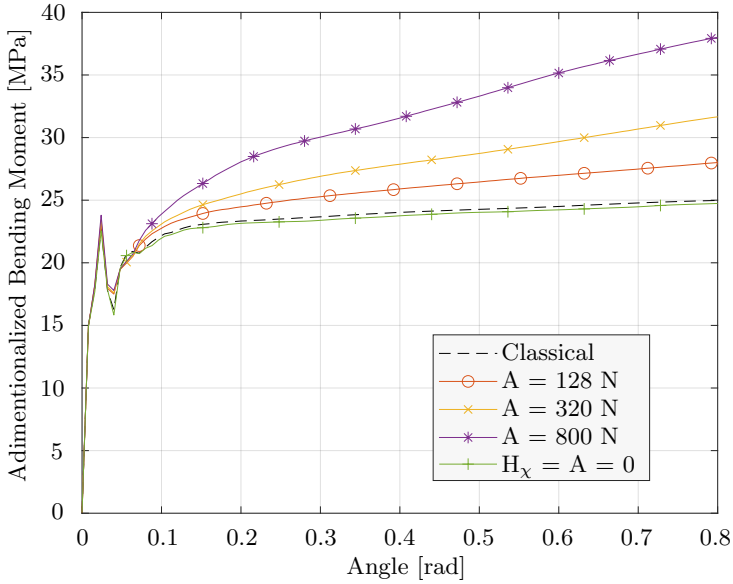

Figure 3.9: Normalized bending moment vs rotation angle for different high order moduli.

by using the micromorphic approach with a null penalty term H_χ and null higher-order modulus (A). Three values of the higher-order modulus (respectively three different characteristic lengths scales) are used for the test: 128 N, 320 N, and 800 N. The curves belonging to the micromorphic theory clearly demonstrate the ability of the method to capture the size effect. The extra hardening reported in Fig. 3.9 follows the same trend as the one relative to the experimental tests reported by Stölken and Evans [Stölken et al. 1998].

In the case of bending, the micromorphic medium does not need to regularize any localization phenomenon; rather, it has to predict an additional hardening, as presented in this section. The characteristic length scale can be identified in this case by:

$$l_{ch} = \sqrt{\frac{A(H_p + H_\chi)}{|H_p|H_\chi}}; \tag{3.73}$$

The obtained characteristic length scales using $A = 128$ N, 320 N, and 800 N are 0.8 mm, 1.26 mm, and 2.0 mm, respectively. These characteristic length scales can be normalized by the thickness h of the beam. The obtained l_{ch}/h ratios for $A = 128$ N, 320 N and 800 N are 0.40 mm, 0.63 mm and 1.0 mm, respectively. Fig. 3.9 shows that for high l_{ch}/h ratio, i.e. high A value, stronger response can be predicted.

The plasticity material model used for the bending test is characterized by a linear hardening behavior (Tab. 3.4). From the analysis of the curves, it can be inferred that the regularization, and subsequently the size effect, is affecting the solution only in the plastic regime, whereas the initial elastic stiffness of the curves is the same regardless of the characteristic length scale used in the model. This is the expected behavior, given the fact that the present micromorphic theory regulates the localization of the plastic field. Thus there should be no difference between the curves in the elastic regime. In hardening

plasticity, the plastic strain gradient contribution leads to an increased apparent hardening of the beam in the plastic regime. The peak in terms of adimentionalized bending moment in Figure 3.9 is to be attributed to the dynamic nature of the test, and it affects all the curves regardless of the classical or micromorphic nature of the theory used.

3.5 Conclusion

In this chapter, a micromorphic strain gradient plasticity model has been formulated and implemented in a commercial explicit finite element code in order to perform simulations of manufacturing operations in time-dependent environments. The reasons to account for the strain gradient while simulating manufacturing operations deal with regularization of strain localization phenomena in softening plasticity, on the one hand, and prediction of size effects in hardening plasticity. The originality of the approach lies in the use of the micromorphic model instead of strict strain gradient plasticity and in the introduction of a viscosity contribution to the micromorphic plastic evolution. The advantage of these two ingredients is that they ease the numerical implementation in a commercial finite element code by mimicking the transient heat equations. Earlier formulations are based on strict strain gradient plasticity without transient term, on the one hand, or on the introduction of micromorphic inertia instead of the proposed viscous term.

The main outcome of the research presented in this chapter lies in the proof that it is possible to implement an explicit micromorphic model in a relatively easy and straightforward manner. This was achieved by slightly modifying the pre-existing routines of material integration and thermal field resolution in the VPC/PAMCRASH software developed by ESI. This proof of concept is meant to demonstrate that limited effort is required to implement the micromorphic theory in any other software that allows for minor modification in their procedures.

The implemented theory has been demonstrated to recover the analytical solution for a semi-infinite glide layer under quasi-static loading conditions. The supplementary shearing tests highlighted the need to use of the strain gradient theory in case deformation localizes, and the typical extra hardening in bending has also been modeled.

Most importantly, it has been proven that the size effect can be predicted with this method and that manufacturing operations can be simulated with such theory with a limited increase in computational cost and only one additional material parameter (the characteristic length). The same model can therefore be used to address regularization issues in softening plasticity and "smaller is harder" size effects in microforming. Further work should be dedicated to develop case studies involving real material data and more complex 3D specimen geometries. In particular the consideration of adiabatic shear banding can be included in the approach in a way similar to the work done in [Russo, Forest, et al. 2020] whereas full coupling with heat conduction phenomenon would require more intrusive programming in the considered commercial code.

Chapter 4

Application of the infinitesimal Cosserat theory to localization

During most metal manufacturing processes, the medium deforms by generating large quantities of plastic strain at relatively high strain rates, inevitably inducing rises in temperature. Metals characterized by low thermal conductivity properties might locally retain high temperatures, consequently undergoing thermal softening. The classical balance laws governing the continuum equilibrium show severe mesh sensitivity if they were numerically discretized through Finite Element Methods. Furthermore, the plastic deformation tends to localize in narrow areas whose characteristic length is comparable to grain size, thereby requiring the adoption of theories able to predict size-effects. In this chapter we demonstrate that the Cosserat medium, even under a small displacement assuption, is able to overcome these issues related to manufacturing processes simulation. We first provide a thermodynamically-consistent description of the Cosserat medium, and then we propose a method to calibrate the two additional characteristic lengths introduced by the Cosserat medium description by enriching the model with the TANH stress flow rule under adiabatic conditions.

The problems related with metal manufacturing simulations are already well known issues, and previous researches adopted a strain gradient theory approach to overcome them [X. Wang 2007; J. Huang et al. 2001; Joshi et al. 2004; Royer et al. 2011], however, to the best of of the author's knowledge, no research has been conducted so far on the application of the Cosserat medium for metal manufacturing simulations. Therefore, in this chapter, the authors aim to cover this gap by providing a thermodynamically-consistent Cosserat medium description, which would be able to predict size effects even for relatively high temperatures, while retaining a compatible physical description and without loss of ellipticity. Furthermore, via the provided framework, it would be possible to unambiguously and uniquely correlate plastic deformations with temperature variations, allowing the calibration procedure to be performed through comparison of thermal fields.

In order to reproduce the same phenomena occurring in manufacturing processes, the Hat-Shaped Specimen [Peirs, Verleysen, Degrieck, and Coghe 2010] was chosen as benchmark test. The combination of specific load case and specimen geometry drives the shear deformation to localize in a narrow band that takes the name of *Adiabatic*

Shear Band (ASB). The same ASB develops during machining operations [Ye et al. 2014; Calamaz et al. 2008; List et al. 2013; Molinari, Soldani, et al. 2013; X. Wang 2007]. Regarding the material model to be plugged in the Cosserat framework, the Johnson-Cook (JC) model is widely used in machining simulations [Peirs, Verleysen, Degrieck, and Coghe 2010; J. C. Li et al. 2010; G. Chen et al. 2011; Cahuc et al. 2007; Guo et al. 2006], however, it underestimates the softening effect on the flow stress [Guo et al. 2006]. Many models have been derived from the JC to overcome this issue, and we decided to use the TANH model among the others [Calamaz et al. 2008].

The chapter follows the structure here reported: Section 4.1 provides the description of the most general Cosserat model under a small deformation assumption, included the kinematics, energetic (Helmholtz free energy potential) and thermodynamic (Claudidu-Duhem inequality) aspects of the Cosserat model; the problem of spurious mesh dependency is presented in Section 4.2, and the Cosserat media is presented as a solution of the problem, highlighting the regulartization properties of the Cosserat media; Sections 4.3 and 4.4 present the methodology used to calibrate the additional characteristic lengths introduced by the Cosserat medium, and finally the conlusions terminate this chapter in Section 4.5.

Notation and Recalls of Tensorial Algebra

Einstein's convention is employed in the whole chapter. Tensors are indicated through compact notation or index notation, regardless of capital or not-capital letters:

$$\begin{aligned}
\underline{\boldsymbol{a}} &\implies a_i;\\
\underset{\sim}{\boldsymbol{a}} &\implies a_{ij};\\
\underline{\underline{\boldsymbol{a}}} &\implies a_{ijk};\\
\underset{\approx}{\boldsymbol{a}} &\implies a_{ijkl};
\end{aligned}$$

The outer product is indicated with $\otimes$ and it operates in the following manner:

$$\underset{\sim}{\mathbf{A}} \otimes \underset{\sim}{\mathbf{B}} = \underset{\approx}{\mathbf{C}} \implies A_{ij}B_{kl} = C_{ijkl};$$

Single and double contraction operators are respectively indicated as follows:

$$\begin{aligned}
\underline{\underline{\mathbf{A}}} \cdot \underline{\underline{\mathbf{B}}} = \underline{\underline{\mathbf{C}}} &\implies A_{ijk}B_{klm} = C_{ijlm};\\
\underline{\underline{\mathbf{A}}} : \underline{\underline{\mathbf{B}}} = \underset{\sim}{\mathbf{C}} &\implies A_{ijk}B_{jkl} = C_{il};
\end{aligned}$$

Divergence and gradient operators are represented as:

$$\begin{aligned}
\underset{\sim}{\mathbf{A}} \otimes \underline{\boldsymbol{\nabla}} = \underline{\underline{\mathbf{B}}} &\implies \frac{\partial A_{ij}}{\partial x_k} = B_{ijk};\\
\underset{\sim}{\mathbf{A}} \cdot \underline{\boldsymbol{\nabla}} = \underline{\mathbf{B}} &\implies \frac{\partial A_{ij}}{\partial x_j} = B_i;
\end{aligned}$$

where x_i is the *i-th* Cartesian coordinate of an Eulerian space. When handling with skew-symmetric second order tensors, it might be easier to define the first order tensor associated to it as:

$$\underline{\mathbf{A}} = -\frac{1}{2}\underline{\underline{\boldsymbol{\epsilon}}} : \underset{\sim}{\mathbf{B}}; \tag{4.1}$$

where $\underline{\underline{\boldsymbol{\epsilon}}}$ is the Levi-Civita permutation symbol.

4.1 Generalized Cosserat Media under Small Displacement Assumption

4.1.1 Kinematics and Balance Laws

The Cosserat model [Cosserat et al. 1909] enhances the Classical Continuum Mechanics (CM) model by introducing three additional degrees of freedom, being the microstucture infinitesimal rotation around the three axis. The degrees of freedom of the continuum can then be written as:

$$\{u_i,\, \theta_i\}, \quad i = 1, 2, 3 \tag{4.2}$$

where u_i is the spacial displacement along the i-th direction, and θ_i is the micro-structural rotation around the i-th axis. The superscript $\times$ indicates the fact that the quantity is a pseudo-vector. As function of these degrees of freedom, the deformation measures in the Cosserat medium are defined as:

$$\underset{\sim}{\mathbf{e}} = \underline{\mathbf{u}} \otimes \underline{\boldsymbol{\nabla}} - \underset{\sim}{\boldsymbol{\Theta}}; \tag{4.3}$$

$$\underset{\sim}{\mathbf{k}} = \underline{\boldsymbol{\theta}} \otimes \underline{\boldsymbol{\nabla}}; \tag{4.4}$$

where the nabla operator $\underline{\boldsymbol{\nabla}}$ is referring to the initial frame of reference and $\underset{\sim}{\boldsymbol{\Theta}}$ is the skew-symmetric second order tensor associated with the pseudo-vector $\underline{\boldsymbol{\theta}}$:

$$\underset{\sim}{\boldsymbol{\Theta}} = -\underline{\underline{\boldsymbol{\epsilon}}} \cdot \underline{\boldsymbol{\theta}}; \tag{4.5}$$

The first deformation measure, $\underset{\sim}{\mathbf{e}}$, is commonly referred to as Cosserat deformation, while the second, $\underset{\sim}{\mathbf{k}}$, is addressed as Cosserat wryness. It must be noted here that the former incorporates the difference between material infinitesimal rotation and micro-structure rotation in addition to the strain measure usually used in linearized (small deformation) CM as can be seen in the following:

$$\underset{\sim}{\mathbf{e}} = \mathrm{sym}\left(\underline{\mathbf{u}} \otimes \underline{\boldsymbol{\nabla}}\right) + \mathrm{skew}\left(\underline{\mathbf{u}} \otimes \underline{\boldsymbol{\nabla}}\right) - \underset{\sim}{\boldsymbol{\Theta}}; \tag{4.6}$$

where sym and skew indicate the symmetric and the skew-symmetric parts of a tensor respectively. The balance laws governing the Cosserat medium equilibrium can be derived by explicitly expressing the internal and external power related to the deformation measures defined in Eq. (4.3) and (4.4):

$$P^{(i)} = \int_{\Omega} \left(\underset{\sim}{\boldsymbol{\sigma}} : \dot{\underset{\sim}{\mathbf{e}}} + \underset{\sim}{\boldsymbol{\mu}} : \dot{\underset{\sim}{\mathbf{k}}} \right) \mathrm{d}\Omega; \tag{4.7}$$

where $\underset{\sim}{\boldsymbol{\sigma}}$ is the power conjugate to the Cosserat strain rate and $\underset{\sim}{\boldsymbol{\mu}}$ is the power conjugate to the Cosserat wryness rate; in literature they are commonly referred to as stress and couple stress tensors. It is important to highlight here that due to the not-symmetric nature of the Cosserat strain and Cosserat wryness, both the stress and couple stress tensors are not symmetric as well. Equivalently, the external power can be defined as:

$$P^{(e)} = \int_{\Omega} \left(\underline{\mathbf{f}} \cdot \dot{\underline{\mathbf{u}}} + \underline{\mathbf{c}} \cdot \dot{\underline{\boldsymbol{\theta}}} \right) \mathrm{d}\Omega + \int_{\partial\Omega} \left(\underline{\mathbf{t}} \cdot \dot{\underline{\mathbf{u}}} + \underline{\mathbf{m}} \cdot \dot{\underline{\boldsymbol{\theta}}} \right) \mathrm{dS}; \tag{4.8}$$

where $\underline{\mathbf{f}}$ is the body force per unit volume conjugate with displacement, $\underline{\mathbf{c}}$ is the body couple per unit volume conjugate with micro-structure rotation, $\underline{\mathbf{t}}$ is the surface traction conjugate with displacement, and finally $\underline{\mathbf{m}}$ is the surface couple per unit surface conjugate with micro-structure rotation. The internal power can be equivalently written as:

$$\int_{\Omega} \left(\underset{\sim}{\boldsymbol{\sigma}} : \underset{\sim}{\dot{\mathbf{e}}} + \underset{\sim}{\boldsymbol{\mu}} : \underset{\sim}{\dot{\mathbf{k}}} \right) \mathrm{d}\Omega = \int_{\Omega} \left[2\underline{\boldsymbol{\sigma}} \cdot \dot{\underline{\boldsymbol{\theta}}} - \dot{\underline{\mathbf{u}}} \cdot \left(\underset{\sim}{\boldsymbol{\sigma}} \cdot \underline{\boldsymbol{\nabla}} \right) - \dot{\underline{\boldsymbol{\theta}}} \cdot \left(\underset{\sim}{\boldsymbol{\mu}} \cdot \underline{\boldsymbol{\nabla}} \right) \right] \mathrm{d}\Omega + \int_{\partial\Omega} \left[\dot{\underline{\mathbf{u}}} \cdot \underset{\sim}{\boldsymbol{\sigma}} \cdot \underline{\mathbf{n}} + \dot{\underline{\boldsymbol{\theta}}} \cdot \underset{\sim}{\boldsymbol{\mu}} \cdot \underline{\mathbf{n}} \right] \mathrm{dS}; \tag{4.9}$$

where the vector $\underline{\boldsymbol{\sigma}}$ is the axial vector associated with the skew-symmetric part of the stress tensor $\underset{\sim}{\boldsymbol{\sigma}}$ as in Eq. 4.1, and $\underline{\mathbf{n}}$ is the unit vector normal to the outer surface of the domain Ω. The equality between internal and external power can be expressed in its weak form as:

$$\int_{\Omega} \dot{\underline{\mathbf{u}}} \cdot \left[\left(\underset{\sim}{\boldsymbol{\sigma}} \cdot \underline{\boldsymbol{\nabla}} \right) + \underline{\mathbf{f}} \right] \mathrm{d}\Omega + \int_{\Omega} \dot{\underline{\boldsymbol{\theta}}} \cdot \left[2\underline{\boldsymbol{\sigma}} + \underline{\mathbf{c}} + \left(\underset{\sim}{\boldsymbol{\mu}} \cdot \underline{\boldsymbol{\nabla}} \right) \right] \mathrm{d}\Omega + + \int_{\partial\Omega} \dot{\underline{\mathbf{u}}} \cdot \left[\underline{\mathbf{t}} - \underset{\sim}{\boldsymbol{\sigma}} \cdot \underline{\mathbf{n}} \right] \mathrm{dS} + \int_{\partial\Omega} \dot{\underline{\boldsymbol{\theta}}} \cdot \left[\underline{\mathbf{m}} - \underset{\sim}{\boldsymbol{\mu}} \cdot \underline{\mathbf{n}} \right] \mathrm{dS} = 0; \tag{4.10}$$

from which, given the arbitrariness of $\dot{\underline{\mathbf{u}}}$ and $\dot{\underline{\boldsymbol{\theta}}}$, the strong forms of the linear and angular momentum balances can be derived as:

$$\underset{\sim}{\boldsymbol{\sigma}} \cdot \underline{\boldsymbol{\nabla}} + \underline{\mathbf{f}} = \underline{\mathbf{0}}; \tag{4.11}$$

$$\underset{\sim}{\boldsymbol{\mu}} \cdot \underline{\boldsymbol{\nabla}} + 2\underline{\boldsymbol{\sigma}} + \underline{\mathbf{c}} = \underline{\mathbf{0}}; \tag{4.12}$$

which are vectorial partial differential equations in the variables $\underline{\mathbf{u}}$ and $\underline{\boldsymbol{\theta}}$, bounded by:

$$\underset{\sim}{\boldsymbol{\sigma}} \cdot \underline{\mathbf{n}} = \underline{\mathbf{t}}; \tag{4.13}$$

$$\underset{\sim}{\boldsymbol{\mu}} \cdot \underline{\mathbf{n}} = \underline{\mathbf{m}}; \tag{4.14}$$

4.1.2 Clausius-Duhem inequality

The material behavior can be explicitly stated in terms of stress-strain relationship or by expressing the Helmholtz free energy and resorting to the Clausius-Duhem inequality. Given that our objective is to characterize the energetic behavior of the Cosserat medium, in this work we employ the second method. The following decompositions of strain and wryness are adopted:

$$\underset{\sim}{\mathbf{e}} = \underset{\sim}{\mathbf{e}}^e + \underset{\sim}{\mathbf{e}}^p + \underset{\sim}{\mathbf{e}}^{th}; \tag{4.15}$$

$$\underset{\sim}{\mathbf{k}} = \underset{\sim}{\mathbf{k}}^e + \underset{\sim}{\mathbf{k}}^p + \underset{\sim}{\mathbf{k}}^{th}; \tag{4.16}$$

in which the relation between elastic, plastic and thermal deformation has an additive character, due to the linearization performed under small displacements and small rotations assumptions. It is then necessary to define the state variables of the medium, and in this work they are the following:

$$\{\underset{\sim}{\mathbf{e}}^e, \underset{\sim}{\mathbf{k}}^e, T, \alpha\}; \tag{4.17}$$

namely, elastic strain, elastic wryness, temperature and a hardening variable, which can be a tensor of any rank. Based on the choice of the state variables, the Helmholtz free energy density per unit volume can be written as:

$$\psi = \psi\left(\underset{\sim}{\mathbf{e}}^e, \underset{\sim}{\mathbf{k}}^e, T, \alpha\right); \tag{4.18}$$

Here a more explicit definition of the Helmholtz free energy, linearized with respect to the initial conditions $\{\underset{\sim}{\mathbf{e}}^e_0 = 0, \underset{\sim}{\mathbf{k}}^e_0 = 0, T_0, \alpha_0 = 0\}$, is provided in a still quite generic form. It assumes quadratic potentials for the elastic deformation measures, typical energy definition related to thermal deformations, standard energy definition related to heat exchange and an additional term concerning the stored energy relative to plastic deformations:

$$\begin{aligned}\psi\left(\underset{\sim}{\mathbf{e}}^e, \underset{\sim}{\mathbf{k}}^e, T, \alpha\right) = \frac{1}{2}\underset{\sim}{\mathbf{e}}^e : \underset{\approx}{\mathbf{\Lambda}} : \underset{\sim}{\mathbf{e}}^e + \frac{1}{2}\underset{\sim}{\mathbf{k}}^e : \underset{\approx}{\mathbf{C}} : \underset{\sim}{\mathbf{k}}^e - (T - T_0)\,\underset{\sim}{\mathbf{P}} : \underset{\sim}{\mathbf{e}}^e \\ - (T - T_0)\,\underset{\sim}{\mathbf{P}}_k : \underset{\sim}{\mathbf{k}}^e - \frac{1}{2}\rho\frac{C_\varepsilon}{T_0}(T - T_0)^2 + \psi_\alpha;\end{aligned} \tag{4.19}$$

where $\underset{\approx}{\mathbf{\Lambda}}$ and $\underset{\approx}{\mathbf{C}}$ are the fourth-order elastic stiffness tensors, relating stress-strain and couple stress-wryness respectively, $\underset{\sim}{\mathbf{P}}$ and $\underset{\sim}{\mathbf{P}}_k$ are second order tensors relating thermal variations with elastic expansions or wrynesses respectively, C_ε is the specific heat capacity, ρ is the density and ψ_α is the part of the Helmholtz free energy that accounts for variation in the recoverable energy of the continuum due to variation in the material yield limit, e.g. hardening or softening. Subsequently, we employ the first and second thermodynamic principles to write the Clausius-Duhem inequality and to explicitly express the dissipation of the continuum. From the first thermodynamic principle:

$$\dot{u} = \underset{\sim}{\boldsymbol{\sigma}} : \dot{\underset{\sim}{\mathbf{e}}} + \underset{\sim}{\boldsymbol{\mu}} : \dot{\underset{\sim}{\mathbf{k}}} - \underline{\mathbf{q}} \cdot \underline{\boldsymbol{\nabla}} + r; \tag{4.20}$$

where $\dot{u}$ is the internal energy rate density per unit volume, not to be mistaken with the displacement rate, $\underline{\mathbf{q}}$ is the heat flux and r is the heat production. The second thermodynamic principle reads:

$$\dot{\eta} - \frac{r}{T} + \left(\frac{\underline{\mathbf{q}}}{T}\right) \cdot \underline{\boldsymbol{\nabla}} \geq 0; \tag{4.21}$$

where $\dot{\eta}$ is the entropy rate density per unit volume. Considering that the Helmholtz free energy is defined as:

$$\psi\left(\underset{\sim}{\mathbf{e}}^e, \underset{\sim}{\mathbf{k}}^e, T, \alpha\right) \;=\; u - T\eta; \tag{4.22}$$

and by expressing its differential as:

$$\dot{\psi} = \left[\frac{\partial \psi}{\partial \underset{\sim}{\mathbf{e}}^e} \underset{\sim}{\dot{\mathbf{e}}}^e + \frac{\partial \psi}{\partial \underset{\sim}{\mathbf{k}}^e} \underset{\sim}{\dot{\mathbf{k}}}^e + \frac{\partial \psi}{\partial T} \dot{T} + \frac{\partial \psi}{\partial \alpha} \dot{\alpha} \right] = \dot{u} - T\dot{\eta} - \dot{T}\eta; \tag{4.23}$$

the second thermodynamic principle assumes the following form:

$$\begin{aligned} &\left(\underset{\sim}{\boldsymbol{\sigma}} - \frac{\partial \psi}{\partial \underset{\sim}{\mathbf{e}}^e} \right) : \underset{\sim}{\dot{\mathbf{e}}}^e + \left(\underset{\sim}{\boldsymbol{\mu}} - \frac{\partial \psi}{\partial \underset{\sim}{\mathbf{k}}^e} \right) : \underset{\sim}{\dot{\mathbf{k}}}^e + \underset{\sim}{\boldsymbol{\sigma}} : \underset{\sim}{\dot{\mathbf{e}}}^p + \underset{\sim}{\boldsymbol{\mu}} : \underset{\sim}{\dot{\mathbf{k}}}^p \\ &\quad - \left(\frac{\partial \psi}{\partial T} + \eta + \underset{\sim}{\boldsymbol{\sigma}} : \frac{\partial \underset{\sim}{\mathbf{e}}^{th}}{\partial T} + \underset{\sim}{\boldsymbol{\mu}} : \frac{\partial \underset{\sim}{\mathbf{k}}^{th}}{\partial T} \right) \dot{T} - \frac{\partial \psi}{\partial \alpha} \dot{\alpha} - \frac{\underline{q} \cdot (\boldsymbol{\nabla} T)}{T} \geq 0; \end{aligned} \tag{4.24}$$

from which, assuming that the elastic strain, elastic wryness and thermal variation are fully recoverable, the followings can be derived:

$$\underset{\sim}{\boldsymbol{\sigma}} = \frac{\partial \psi}{\partial \underset{\sim}{\mathbf{e}}^e}; \tag{4.25}$$

$$\underset{\sim}{\boldsymbol{\mu}} = \frac{\partial \psi}{\partial \underset{\sim}{\mathbf{k}}^e}; \tag{4.26}$$

$$\eta = -\frac{\partial \psi}{\partial T} + \underset{\sim}{\boldsymbol{\sigma}} : \frac{\partial \underset{\sim}{\mathbf{e}}^{th}}{\partial T} + \underset{\sim}{\boldsymbol{\mu}} : \frac{\partial \underset{\sim}{\mathbf{k}}^{th}}{\partial T}; \tag{4.27}$$

and, by expanding Eq. (4.25) and (4.26), the following relation between thermal deformations, elastic deformations and stress/couple stress can be found:

$$\underset{\sim}{\boldsymbol{\sigma}} = \frac{\partial \psi}{\partial \underset{\sim}{\mathbf{e}}^e} = \underset{\approx}{\boldsymbol{\Lambda}} : \underset{\sim}{\mathbf{e}}^e - \underset{\sim}{\mathbf{P}} (T - T_0) = \underset{\approx}{\boldsymbol{\Lambda}} : \left[\underset{\sim}{\mathbf{e}}^e - \underset{\approx}{\boldsymbol{\Lambda}}^{-1} : \underset{\sim}{\mathbf{P}} (T - T_0) \right] = \underset{\approx}{\boldsymbol{\Lambda}} : \left[\underset{\sim}{\mathbf{e}}^e - \underset{\sim}{\mathbf{e}}^{th} \right]; \tag{4.28}$$

$$\underset{\sim}{\boldsymbol{\mu}} = \frac{\partial \psi}{\partial \underset{\sim}{\mathbf{k}}^e} = \underset{\approx}{\mathbf{C}} : \underset{\sim}{\mathbf{k}}^e - \underset{\sim}{\mathbf{P}}_k (T - T_0) = \underset{\approx}{\mathbf{C}} : \left[\underset{\sim}{\mathbf{k}}^e - \underset{\approx}{\mathbf{C}}^{-1} : \underset{\sim}{\mathbf{P}}_k (T - T_0) \right] = \underset{\approx}{\mathbf{C}} : \left[\underset{\sim}{\mathbf{k}}^e - \underset{\sim}{\mathbf{k}}^{th} \right]; \tag{4.29}$$

where:

$$\underset{\sim}{\mathbf{e}}^{th} = \underset{\approx}{\boldsymbol{\Lambda}}^{-1} : \underset{\sim}{\mathbf{P}} (T - T_0) = \underset{\sim}{\boldsymbol{\Gamma}} (T - T_0); \tag{4.30}$$

$$\underset{\sim}{\mathbf{k}}^{th} = \underset{\approx}{\mathbf{C}}^{-1} : \underset{\sim}{\mathbf{P}}_k (T - T_0) = \underset{\sim}{\boldsymbol{\Gamma}}_k (T - T_0); \tag{4.31}$$

and the tensors $\underset{\sim}{\boldsymbol{\Gamma}}$ and $\underset{\sim}{\boldsymbol{\Gamma}}_k$ are operators used to compute the thermal expansion/wryness. The remaining terms in Eq. (4.24) define the medium dissipation, here referred to as $\boldsymbol{\Pi}$:

$$\boldsymbol{\Pi} = \underset{\sim}{\boldsymbol{\sigma}} : \underset{\sim}{\dot{\mathbf{e}}}^p + \underset{\sim}{\boldsymbol{\mu}} : \underset{\sim}{\dot{\mathbf{k}}}^p - \frac{\partial \psi}{\partial \alpha} \dot{\alpha} - \frac{\underline{q} \cdot (\boldsymbol{\nabla} T)}{T} \geq 0; \tag{4.32}$$

Furthermore, we can write the heat equation from Eq. (4.20) and (4.23) as:

$$\underset{\sim}{\boldsymbol{\sigma}} : \underset{\sim}{\dot{\mathbf{e}}}^p + \underset{\sim}{\boldsymbol{\mu}} : \underset{\sim}{\dot{\mathbf{k}}}^p - \underline{\mathbf{q}} \cdot \boldsymbol{\nabla} + r = \frac{\partial \psi}{\partial \alpha} \dot{\alpha} + T\dot{\eta}; \tag{4.33}$$

4.1.3 General Elastic Material Model

From Eq. (4.25) and (4.26) it can be observed that the form of the constitutive equations of stress and couple-stress directly derives from the chosen form of the Helmholtz free energy, it is then essential to give a proper shape to this potential. The Helmholtz free energy form adopted in Eq. (4.19) is still quite general, and many mechanical behaviors can be modeled using this form. The most simple model used for isotropic materials can be expressed as [de Borst and Sluys 1991]:

$$\underset{\sim}{\boldsymbol{\sigma}} = \lambda \operatorname{tr}\left(\underset{\sim}{\mathbf{e}}^{e}\right) \underset{\sim}{\mathbf{I}} + 2\,\mathrm{G}\operatorname{sym}\left(\underset{\sim}{\mathbf{e}}^{e}\right) + 2\,\mathrm{G}_{c}\operatorname{skw}\left(\underset{\sim}{\mathbf{e}}^{e}\right); \tag{4.34}$$

$$\underset{\sim}{\boldsymbol{\mu}} = \xi \operatorname{tr}\left(\underset{\sim}{\mathbf{k}}^{e}\right) \underset{\sim}{\mathbf{I}} + 2\,\beta\operatorname{sym}\left(\underset{\sim}{\mathbf{k}}^{e}\right) + 2\,\gamma\operatorname{skw}\left(\underset{\sim}{\mathbf{k}}^{e}\right); \tag{4.35}$$

where $\underset{\sim}{\mathbf{I}}$ is the Identity second-order tensor, and the following conditions on the material parameters must be valid:

$$\begin{cases} 3\lambda + 2\mathrm{G} \geq 0 \\ \mathrm{G} \geq 0 \\ \mathrm{G}_{c} \geq 0 \end{cases} \quad \& \quad \begin{cases} 3\xi + 2\beta \geq 0 \\ \beta \geq 0 \\ \gamma \geq 0 \end{cases} \tag{4.36}$$

In this constitutive model, λ and G are the usual Lamé parameters and G_c, ξ, β and γ are additional material coefficients. In the 2D case, it is customary to assume $\beta = \gamma$ for simplicity [de Borst 1991a]. For our computations, we are prone to use relatively high values of G_c when compared to G, such that the mismatch would be characterized by a stiffer response, and the value of $\operatorname{skw}\{\underline{\mathbf{u}} \otimes \underline{\boldsymbol{\nabla}}\}$ would be negligible if compared to $\operatorname{sym}\{\underline{\mathbf{u}} \otimes \underline{\boldsymbol{\nabla}}\}$. In this case, the Cosserat theory would recover the characteristics of a couple-stress theory, also known as constrained Cosserat theory [Koiter 1964]. There is, however, a conceptual difference between the hydrostatic term of the wryness and its deviatoric counterpart: while, in fact, the former is related to variation of the micro-structure rotation along the axis in which it is defined (torsion), the latter expresses the variation of the micro-structure rotation along the other two directions (bending), and in general these two deformations might be characterized by different responses. After a simple dimensional analysis, the following elastic characteristic length of the Cosserat medium can be defined:

$$l_{el} = \sqrt{\frac{\beta}{G}} \tag{4.37}$$

To be noted that in case no simplifications were done on the constitutive behavior of the Cosserat model, other characteristic lengths were identifiable, as done in other researches [Khoei et al. 2010].

4.1.4 General Visco-Plastic Material Model

In the same way we defined the material response by defining the Helmholtz free energy instead of the stress-strain relation, it is possible to explicitly state the shape of the viscoplastic potential associated to the plastic deformation. A general shape of the multi-criterion Cosserat viscoplastic potential is retrieved [Forest and Sievert 2003] where two

potentials are defined, one related to $\underset{\sim}{\mathbf{e}}^p$ and one related to $\underset{\sim}{\mathbf{k}}^p$. They can be modeled using the general viscoplastic potential form as the one proposed by Chaboche in case of standard continuum mechanics [J. Chaboche 1989] :

$$\Omega = \frac{D}{k+1}\left(\frac{\langle f\left(\underset{\sim}{\boldsymbol{\sigma}}, p, T\right)\rangle}{D}\right)^{k+1} + \frac{L}{\xi+1}\left(\frac{\langle g\left(\underset{\sim}{\boldsymbol{\mu}}, p_k, T\right)\rangle}{L}\right)^{\xi+1}; \tag{4.38}$$

where Ω is the viscoplastic potential, D and L are the drag stress and couple stress, k and ξ are parameters to be calibrated and $\langle f\rangle$ and $\langle g\rangle$ are over-stress and over-couple-stress between the Macaulay brackets. If we assume associated plasticity and explicitly give the form of Ω, the plastic behavior would be completely defined. This is because the plastic strain rate and plastic wryness rate can be written as:

$$\dot{\underset{\sim}{\mathbf{e}}}^p = \frac{\partial\Omega}{\partial f}\frac{\partial f}{\partial\underset{\sim}{\boldsymbol{\sigma}}}, \quad \dot{\underset{\sim}{\mathbf{k}}}^p = \frac{\partial\Omega}{\partial g}\frac{\partial g}{\partial\underset{\sim}{\boldsymbol{\mu}}}; \tag{4.39}$$

from which, the first ratios are equal to the rates of the viscoplastic multipliers:

$$\dot{p} = \frac{\partial\Omega}{\partial f}, \quad \dot{p}_k = \frac{\partial\Omega}{\partial g} \tag{4.40}$$

and the second ones define the direction of the plastic flows, being equal to the one of the associated stress/couple stress:

$$\frac{\partial f}{\partial\underset{\sim}{\boldsymbol{\sigma}}} = \underset{\sim}{\mathbf{n}}_\sigma, \quad \frac{\partial g}{\partial\underset{\sim}{\boldsymbol{\mu}}} = \underset{\sim}{\mathbf{n}}_\mu; \tag{4.41}$$

The choice of expressing the viscoplastic potential as in Eq. (4.38) would impose the calibration of additional parameters related with both the contributions coming from plastic deformation and plastic wryness. However, the expression of the viscoplastic potential usually used with the Cosserat medium is simplified by assuming a single criterion, thus a single viscoplastic multiplier, which is common to both plastic deformation and plastic wryness:

$$\Omega = \frac{D}{k+1}\left(\frac{\langle f\left(\underset{\sim}{\boldsymbol{\sigma}}, \underset{\sim}{\boldsymbol{\mu}}, p, T\right)\rangle}{D}\right)^{k+1}; \tag{4.42}$$

and:

$$\dot{p} = \frac{\partial\Omega}{\partial f}, \quad \dot{\underset{\sim}{\mathbf{e}}}^p = \dot{p}\frac{\partial f}{\partial\underset{\sim}{\boldsymbol{\sigma}}}, \quad \dot{\underset{\sim}{\mathbf{k}}}^p = \dot{p}\frac{\partial f}{\partial\underset{\sim}{\boldsymbol{\mu}}}; \tag{4.43}$$

with f depending both on stresses and couple stresses:

$$f = f(\underset{\sim}{\boldsymbol{\sigma}}, \underset{\sim}{\boldsymbol{\mu}}, p, T) = \sigma_{eq}(\underset{\sim}{\boldsymbol{\sigma}}, \underset{\sim}{\boldsymbol{\mu}}) - R(p, T); \tag{4.44}$$

where R represents the radius of the yield surface above which plasticity is activated. In the Cosserat framework, several equivalent stress measures can be adopted :

$$\sigma_{\text{eq}} = \sqrt{\frac{3}{2}\left(\mathrm{a}_1 \underset{\sim}{\boldsymbol{\sigma}}' : \underset{\sim}{\boldsymbol{\sigma}}' + \mathrm{a}_2 \underset{\sim}{\boldsymbol{\sigma}}' : \underset{\sim}{\boldsymbol{\sigma}}'^{\mathrm{T}} + \mathrm{b} \underset{\sim}{\boldsymbol{\mu}} : \underset{\sim}{\boldsymbol{\mu}}\right)}; \tag{4.45}$$

$$\sigma_{\text{eq}} = \sqrt{\frac{3}{2}\left(\mathrm{a}_1 \underset{\sim}{\boldsymbol{\sigma}}' : \underset{\sim}{\boldsymbol{\sigma}}' + \mathrm{a}_2 \underset{\sim}{\boldsymbol{\sigma}}' : \underset{\sim}{\boldsymbol{\sigma}}'^{\mathrm{T}} + \mathrm{b}_1 \underset{\sim}{\boldsymbol{\mu}} : \underset{\sim}{\boldsymbol{\mu}} + \mathrm{b}_2 \underset{\sim}{\boldsymbol{\mu}} : \underset{\sim}{\boldsymbol{\mu}}^{\mathrm{T}}\right)}; \tag{4.46}$$

$$\sigma_{\text{eq}} = \sqrt{\frac{3}{2}\left[\mathrm{a}_3 \left(\underset{\sim}{\boldsymbol{\sigma}}'_{\text{sym}} : \underset{\sim}{\boldsymbol{\sigma}}'_{\text{sym}}\right) + \mathrm{a}_4 \left(\underset{\sim}{\boldsymbol{\sigma}}'_{\text{skw}} : \underset{\sim}{\boldsymbol{\sigma}}'^{\mathrm{T}}_{\text{skw}}\right) + \mathrm{b}_3 \left(\underset{\sim}{\boldsymbol{\mu}}_{\text{sym}} : \underset{\sim}{\boldsymbol{\mu}}_{\text{sym}}\right) + \mathrm{b}_4 \left(\underset{\sim}{\boldsymbol{\mu}}_{\text{skw}} : \underset{\sim}{\boldsymbol{\mu}}^{\mathrm{T}}_{\text{skw}}\right)\right]}; \tag{4.47}$$

where the first one was proposed by de Borst [de Borst 1991a; de Borst 1993], the second one by Forest [Forest and Sievert 2003], and the third one is based on the invariant decomposition of a second order tensor [Zheng 1994]. The operator $\underset{\sim}{\boldsymbol{\sigma}}'$ returns the deviatoric part of the tensor $\underset{\sim}{\boldsymbol{\sigma}}$. Based on the dimensional analysis of the coefficients appearing in the Equations above, and assuming that the terms a_i are equal to each other, as well as the b_i terms, the plastic characteristic length arises from the model as:

$$l_p = \sqrt{\frac{\mathrm{a}}{\mathrm{b}}}; \tag{4.48}$$

The last remark regarding the completeness of the plastic model concerns the definition of the plastic part of the Helmholtz free energy, that is, ψ_α in Eq. (4.19). This is, in general, equal to [Śloderbach et al. 2018]:

$$\psi_\alpha = \int_0^\alpha \pi(\xi) d\xi; \tag{4.49}$$

where π is a general stress thermodynamically associated to the internal variable α. In most plastic evolution laws the equivalent cumulative plastic strain is used as hardening parameters, such that $\dot{p} = \dot{\alpha}$, and π is essentially the stress thermodynamically conjugated to the equivalent cumulative plastic strain. Given the integral formulation of this term, its closed form does not necessarily exist, and it could be eventually found once the plastic flow rules are defined.

4.1.5 Adiabatic Temperature Evolution

The derivation of the temperature rate can be derived starting from the definition of the entropy from Eq. (4.27) and assuming the Helmholtz free energy function as in Eq. (4.21):

$$\begin{aligned}
\eta \;=\; & -\frac{1}{2}\underset{\sim}{\mathbf{e}}^e : \frac{\partial \underset{\approx}{\boldsymbol{\Lambda}}}{\partial T} : \underset{\sim}{\mathbf{e}}^e - \frac{1}{2}\underset{\sim}{\mathbf{k}}^e : \frac{\partial \underset{\approx}{\mathbf{C}}}{\partial T} : \underset{\sim}{\mathbf{k}}^e + (T - T_0)\frac{\partial \underset{\sim}{\mathbf{P}}}{\partial T} : \underset{\sim}{\mathbf{e}}^e \\
& + \underset{\sim}{\mathbf{P}} : \underset{\sim}{\mathbf{e}}^e + (T - T_0)\frac{\partial \underset{\sim}{\mathbf{P}}_k}{\partial T} : \underset{\sim}{\mathbf{k}}^e + \underset{\sim}{\mathbf{P}}_k : \underset{\sim}{\mathbf{k}}^e \\
& + \frac{C_\varepsilon}{T_0}(T - T_0) - \frac{\partial \psi_\alpha}{\partial T} + \underset{\sim}{\boldsymbol{\sigma}} : \frac{\partial \underset{\sim}{\mathbf{e}}^{th}}{\partial T} + \underset{\sim}{\boldsymbol{\mu}} : \frac{\partial \underset{\sim}{\mathbf{k}}^{th}}{\partial T};
\end{aligned} \tag{4.50}$$

then, by then taking the time variation of the entropy:

$$\dot{\eta} = \frac{\partial \eta}{\partial \underset{\sim}{\mathbf{e}}^e} : \dot{\underset{\sim}{\mathbf{e}}}^e + \frac{\partial \eta}{\partial \underset{\sim}{\mathbf{k}}^e} : \dot{\underset{\sim}{\mathbf{k}}}^e + \frac{\partial \eta}{\partial T}\dot{T} + \frac{\partial \eta}{\partial \alpha}\dot{\alpha}; \tag{4.51}$$

where:

$$\frac{\partial \eta}{\partial \underset{\sim}{\mathbf{e}}^e} = -\underset{\sim}{\mathbf{e}}^e : \frac{\partial \underset{\approx}{\mathbf{\Lambda}}}{\partial T} + \underset{\sim}{\mathbf{P}} + (T - T_0)\frac{\partial \underset{\sim}{\mathbf{P}}}{\partial T} + \frac{\partial \underset{\sim}{\mathbf{e}}^{th}}{\partial T} : \underset{\approx}{\mathbf{\Lambda}}; \tag{4.52}$$

$$\frac{\partial \eta}{\partial \underset{\sim}{\mathbf{k}}^e} = -\underset{\sim}{\mathbf{k}}^e : \frac{\partial \underset{\approx}{\mathbf{C}}}{\partial T} + \underset{\sim}{\mathbf{P}}_k + (T - T_0)\frac{\partial \underset{\sim}{\mathbf{P}}_k}{\partial T} + \frac{\partial \underset{\sim}{\mathbf{k}}^{th}}{\partial T} : \underset{\approx}{\mathbf{C}}; \tag{4.53}$$

$$\frac{\partial \eta}{\partial \alpha} = -\frac{\partial^2 \psi_\alpha}{\partial T \, \partial \alpha}; \tag{4.54}$$

and:

$$\begin{aligned}\frac{\partial \eta}{\partial T} = \rho\frac{C_\epsilon}{T_0} + \rho\frac{\partial C_\epsilon}{\partial T}\frac{(T - T_0)}{T_0} + \frac{\partial \underset{\sim}{\mathbf{P}}}{\partial T} : \underset{\sim}{\mathbf{e}}^e + \frac{\partial \underset{\sim}{\mathbf{P}}_k}{\partial T} : \underset{\sim}{\mathbf{k}}^e - \frac{1}{2}\underset{\sim}{\mathbf{e}}^e : \frac{\partial^2 \underset{\approx}{\mathbf{\Lambda}}}{\partial T^2} : \underset{\sim}{\mathbf{e}}^e - \frac{1}{2}\underset{\sim}{\mathbf{k}}^e : \frac{\partial^2 \underset{\approx}{\mathbf{C}}}{\partial T^2} : \underset{\sim}{\mathbf{k}}^e \\ + \frac{\partial \underset{\sim}{\mathbf{e}}^{th}}{\partial T} : \left[\frac{\partial \underset{\approx}{\mathbf{\Lambda}}}{\partial T} : \left(\underset{\sim}{\mathbf{e}}^e - \underset{\sim}{\mathbf{e}}^{th}\right) - \underset{\approx}{\mathbf{\Lambda}} : \frac{\partial \underset{\sim}{\mathbf{e}}^{th}}{\partial T}\right] + \frac{\partial \underset{\sim}{\mathbf{k}}^{th}}{\partial T} : \left[\frac{\partial \underset{\approx}{\mathbf{C}}}{\partial T} : \left(\underset{\sim}{\mathbf{k}}^e - \underset{\sim}{\mathbf{k}}^{th}\right) - \underset{\approx}{\mathbf{C}} : \frac{\partial \underset{\sim}{\mathbf{k}}^{th}}{\partial T}\right] \\ + \frac{\underset{\sim}{\mathbf{P}}}{\partial T} : \underset{\sim}{\mathbf{e}}^e + \frac{\underset{\sim}{\mathbf{P}}_k}{\partial T} : \underset{\sim}{\mathbf{k}}^e + (T - T_0)\left(\frac{\partial^2 \underset{\sim}{\mathbf{P}}}{\partial T^2} : \underset{\sim}{\mathbf{e}}^e + \frac{\partial^2 \underset{\sim}{\mathbf{P}}_k}{\partial T^2} : \underset{\sim}{\mathbf{k}}^e\right) - \frac{\partial^2 \psi_\alpha}{\partial T^2};\end{aligned} \tag{4.55}$$

and by plugging them it into the heat Equation Eq. (4.33), we obtain:

$$\underset{\sim}{\boldsymbol{\sigma}} : \dot{\underset{\sim}{\boldsymbol{\varepsilon}}}^p + \underset{\sim}{\boldsymbol{\mu}} : \dot{\underset{\sim}{\mathbf{k}}}^p - \underline{\mathbf{q}} \cdot \underline{\boldsymbol{\nabla}} + r = \frac{\partial \psi_\alpha}{\partial \alpha} + T\left(\frac{\partial \eta}{\partial \underset{\sim}{\mathbf{e}}^e} : \dot{\underset{\sim}{\mathbf{e}}}^e + \frac{\partial \eta}{\partial \underset{\sim}{\mathbf{k}}^e} : \dot{\underset{\sim}{\mathbf{k}}}^e + \frac{\partial \eta}{\partial T}\dot{T} + \frac{\partial \eta}{\partial \alpha}\dot{\alpha}\right); \tag{4.56}$$

from which the temperature rate can be evaluated as:

$$\dot{T} = \frac{\underset{\sim}{\boldsymbol{\sigma}} : \dot{\underset{\sim}{\boldsymbol{\varepsilon}}}^p + \underset{\sim}{\boldsymbol{\mu}} : \dot{\underset{\sim}{\mathbf{k}}}^p - \underline{\mathbf{q}} \cdot \underline{\boldsymbol{\nabla}} + r - \frac{\partial \psi_\alpha}{\partial \alpha} - T\left(\frac{\partial \eta}{\partial \underset{\sim}{\mathbf{e}}^e} : \dot{\underset{\sim}{\mathbf{e}}}^e + \frac{\partial \eta}{\partial \underset{\sim}{\mathbf{k}}^e} : \dot{\underset{\sim}{\mathbf{k}}}^e + \frac{\partial \eta}{\partial \alpha}\dot{\alpha}\right)}{T\frac{\partial \eta}{\partial T}}; \tag{4.57}$$

The one reported in Eq. (4.57) is an expression of the temperature rate which contains many terms whose magnitude is well below the magnitude of the larger terms as $\underset{\sim}{\boldsymbol{\sigma}} : \underset{\sim}{\mathbf{e}}^p$ for example, therefore assumptions were made on some of the quantities populating Eq. (4.57) in order to make it usable, and here follows the list of hypotheses:

- $\underline{\mathbf{q}} = \mathrm{r} = 0$;
- $\dfrac{\partial C_\varepsilon}{\partial T} = 0$;
- $\dfrac{\partial \underset{\approx}{\mathbf{\Lambda}}}{\partial T} = \dfrac{\partial \underset{\approx}{\mathbf{C}}}{\partial T} = 0$;

Parameter	Order of Magnitude	Parameters	Order of Magnitude
$\underset{\sim}{\boldsymbol{\sigma}} : \underset{\sim}{\dot{\mathbf{e}}}^p$	10^{11} [J / m^3·s]	$\underset{\sim}{\mathbf{P}} : \underset{\sim}{\dot{\mathbf{e}}}^e$	10^{6} [J / m^3·s·K]
$\underset{\sim}{\boldsymbol{\mu}} : \underset{\sim}{\dot{\mathbf{k}}}^p$	10^{10} [J / m^3·s]	$\underset{\sim}{\boldsymbol{\sigma}} : \underset{\sim}{\boldsymbol{\Gamma}}$	10^{6} [J / m^3·K]
ρC_ε	10^{10} [J / m^3·K]	$\dfrac{\partial^2 \psi_\alpha}{\partial T^2}$	10^{-1} [J / m^3·K^2]
$\dfrac{\partial \psi_\alpha}{\partial \alpha}$	10^{10} [J / m^3]	$\dfrac{\partial^2 \psi_\alpha}{\partial T \partial p}$	10^{-1} [J / m^3·K]

Table 4.1: Order of magnitudes of the terms in Eq. (4.57).

- $\psi_\alpha = \psi_\alpha(\alpha, T) \implies \dfrac{\psi_\alpha}{\underset{\sim}{\mathbf{e}}^e} = \dfrac{\psi_\alpha}{\underset{\sim}{\mathbf{k}}^e} = 0$;
- T = 500K;
- $\underset{\sim}{\boldsymbol{\Gamma}} = \Gamma \underset{\sim}{\mathbf{I}} = 10^{-5}\mathrm{K}^{-1}$;
- $\underset{\sim}{\boldsymbol{\Gamma}}_k = \underset{\sim}{0}\,\mathrm{K}^{-1}\mathrm{m}^{-1}$;
- $\dfrac{\partial \boldsymbol{\Gamma}}{\partial T} = \dfrac{\partial \boldsymbol{\Gamma}_k}{\partial T} = 0$;
- $|\underset{\sim}{\mathbf{e}}^e| = 10^{-3}$;
- $|\underset{\sim}{\dot{\mathbf{e}}}^e| = 10^{-1}\mathrm{s}^{-1}$;
- $|\underset{\sim}{\dot{\mathbf{e}}}^p| = 10^{3}\mathrm{s}^{-1}$;
- $|\underset{\sim}{\mathbf{k}}^e| = 10^{-2}\,\mathrm{m}^{-1}$;
- $|\underset{\sim}{\dot{\mathbf{k}}}^e| = 10^{-4}\,\mathrm{m}^{-1}\mathrm{s}^{-1}$;
- $|\underset{\sim}{\dot{\mathbf{k}}}^p| = 10^{2}\,\mathrm{m}^{-1}\mathrm{s}^{-1}$;
- $|\underset{\sim}{\boldsymbol{\sigma}}| = 10^{8}\mathrm{Pa}$;
- $|\underset{\sim}{\boldsymbol{\mu}}| = 10^{8}$ Pa m;

Furthermore, by assuming the material elastic and plastic models to be the ones described in Tables 4.2 and 4.3, the terms in Eq. (4.57) have the orders of magnitudes listed in Table 4.1. From the comparison of the order of magnitudes of the terms in Eq. (4.57) that are presented in Table 4.1, the temperature flow rule can assume the following form:

$$\dot{T} = \frac{\underset{\sim}{\boldsymbol{\sigma}} : \underset{\sim}{\dot{\mathbf{e}}}^p + \underset{\sim}{\boldsymbol{\mu}} : \underset{\sim}{\dot{\mathbf{k}}}^p - \dfrac{\partial \psi_\alpha}{\partial \alpha}\dot{\alpha} + T\dfrac{\partial^2 \psi_\alpha}{\partial T \partial \alpha}\dot{\alpha}}{\rho T\left[\dfrac{C_\varepsilon}{T_0} + \dfrac{\partial C_\varepsilon}{\partial T}\dfrac{(T - T_0)}{T_0}\right] - \dfrac{\partial^2 \psi_\alpha}{\partial T^2}T}; \tag{4.58}$$

which in case of further simplification becomes:

$$\dot{T} = \frac{\underset{\sim}{\boldsymbol{\sigma}} : \underset{\sim}{\dot{\mathbf{e}}}^p + \underset{\sim}{\boldsymbol{\mu}} : \underset{\sim}{\dot{\mathbf{k}}}^p - \dfrac{\partial \psi_\alpha}{\partial p}\dot{p}}{\rho T \dfrac{C_\varepsilon}{T_0}}; \tag{4.59}$$

Note that it is possible, with this formulation, to evaluate the part of plastic work converted into adiabatic temperature increment without any additional calibration to be

performed. Many researches can be found in literature where the effects of hardening/softening on the temperature increment is incorporated in a unique parameter, namely the Taylor-Quinney coefficient Ξ [Taylor and Quinney 1934], that requires calibration in different condition:

$$\dot{T} = \frac{\Xi}{\rho C_\varepsilon} \left(\underset{\sim}{\boldsymbol{\sigma}} : \dot{\underset{\sim}{\mathbf{e}}}^p + \underset{\sim}{\boldsymbol{\mu}} : \dot{\underset{\sim}{\mathbf{k}}}^p \right); \tag{4.60}$$

By using this temperature evolution law and the evolution of the plastic deformations defined in Eq. (4.43), the elastic predictor can then be written as:

$$\dot{\underset{\sim}{\mathbf{e}}}^e = \dot{\underset{\sim}{\mathbf{e}}} - \dot{\underset{\sim}{\mathbf{e}}}^{th} - \dot{\underset{\sim}{\mathbf{e}}}^p = \dot{\underset{\sim}{\mathbf{e}}} - \dot{T}\,\underset{\sim}{\boldsymbol{\Gamma}} - \dot{p}\frac{\partial f}{\partial \underset{\sim}{\boldsymbol{\sigma}}}; \tag{4.61}$$

$$\dot{\underset{\sim}{\mathbf{k}}}^e = \dot{\underset{\sim}{\mathbf{k}}} - \dot{\underset{\sim}{\mathbf{k}}}^{th} - \dot{\underset{\sim}{\mathbf{k}}}^p = \dot{\underset{\sim}{\mathbf{k}}} - \dot{T}\,\underset{\sim}{\boldsymbol{\Gamma}}_k - \dot{p}\frac{\partial f}{\partial \underset{\sim}{\boldsymbol{\mu}}}; \tag{4.62}$$

4.2 Regularization of the Solution & Choice of the Minimun Mesh Size

The model described in the previous section is here proposed to be a suitable solution for manufacturing processes simulations. The main reason is the embodied property of the model to enlarge the domain of the vectorial solution space $\{\underline{\mathbf{u}}\}$ for which the ellipticity of the PDEs is retained. In most of the plastic models employed to simulate manufacturing processes, the strain hardening effect overcompensates the thermal softening, thus the PDEs rarely experience a loss of ellipticity. However, when high temperatures are expected to develop, material softening could most likely exceed the strain hardening, but not many material models are able to properly predict the flow stress at high temperatures ($\approx 0.8\, T_m$–melting temperature), therefore thermal softening might not be correctly captured. The Johnson-Cook model, widely used in manufacturing processes, is known to underestimate the softening effect [Guo et al. 2006], and its implementation in a strain-gradient theory was already documented [X. Wang 2007]. Due to the limitation of the JC model in capturing material softening, many modified versions model can be found in literature. Among the others, we decided to use the TANH model [Calamaz et al. 2008]. Both the Classical CM model and the Cosserat model have been fetched with this material description. Therefore, acknowledging the lacking of a proper material plastic model able to predict flow stress models at high operational temperature, in this section we limit ourself to demonstrate the procedure by which the two additional Cosserat characteristic lengths might be calibrated. Given our final object of employing the Cosserat medium to simulate manufacturing processes, the calibration procedure will be performed by modeling a Hat-Shaped Specimen under compression [Peirs, Verleysen, Degrieck, and Coghe 2010]. The Hat-Shaped test is characterized by the development of an ASB inside the specimen, followed by an increase in temperature due to the high levels of localized plastic strain. Since most of the manufacturing processes that export material from the final piece are designed to do so through the development of ASBs and subsequent material removal, this example could represent a simplified condition of the one occurring during manufacturing. In fact, the calibration procedure has been performed precisely while looking at the fields developed at the ASB location. The geometry of the specimen was taken from the work of Peirs et al. [Peirs, Verleysen, Degrieck, and Coghe 2010].

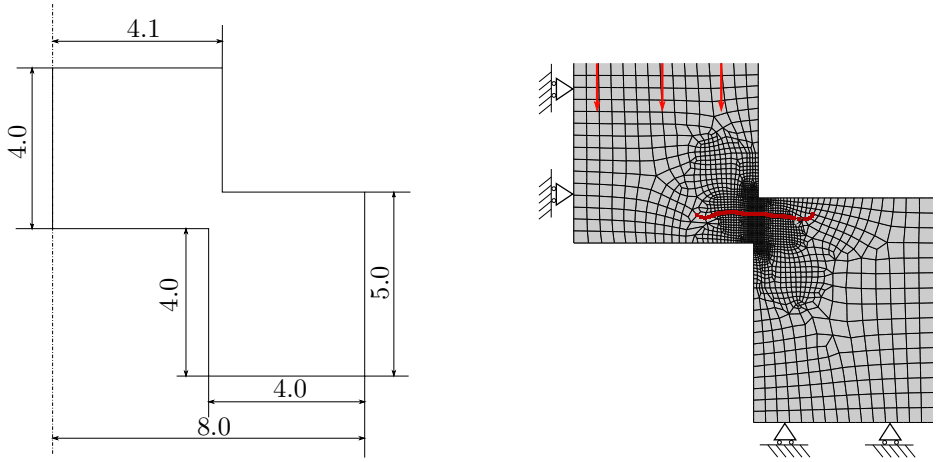

Figure 4.1: Hat-Shaped Specimen [Peirs, Verleysen, Degrieck, and Coghe 2010], geometry (a) and mesh with boundary conditions (b). Units in millimeters. In (b) the cross section along the shear band is indicated with red nodes.

Although the same geometry and material properties were used, the plastic behavior chosen for this test is different than the one adopted by Peirs et al. The specification of the plastic model and the material properties will be assessed in Section 4.4, and aim to reproduce the behavior of the Titanium alloy Ti6Al4V. Given the axial-symmetry of the specimen, only half of the cross section has been modeled in 2D under axial-symmetric conditions. In Figure 4.1 the geometry and the boundary conditions of the benchmark tests are reported. A vertical downward velocity of 5.5 m/s was imposed at the top surface of the specimen, and the simulations lasted until a vertical negative displacement of -0.275 mm was reached. The simulations have been produced using the FEM solver Z-set [Z-set 2013], in which the Cosserat element description and material behavior are implemented. Quadratic interpolation has been used to discretize displacement and rotation fields between nodal values, thereby quadratic elements have been used. One of the reasons for us to employ a Cosserat medium description is to avoid the mesh dependency developed when the material softens at high temperatures. Therefore, a preliminary verification was performed in order to be sure that the Cosserat medium description would be able to produce mesh-insensitive results. Simulations of the Hat-Shaped specimen under compression were carried out using the Classical CM and the Cosserat descriptions both fetched with a plastic behavior that reproduces pure softening. For these simulations, the mechanical and thermal properties reported in Table 4.2 were used. In addition to the ones indicated in the table, the couple stress moduli β and γ were both equal to 0.114 MPa·mm^2. Although this model might not be descriptive of the behavior of any material, this numerical exercise allow us to verify the mesh independence in the most sever condition of pure softening. The flow stress adopted for this exercise reads:

$$R(p) = R_0 + H\,p; \tag{4.63}$$

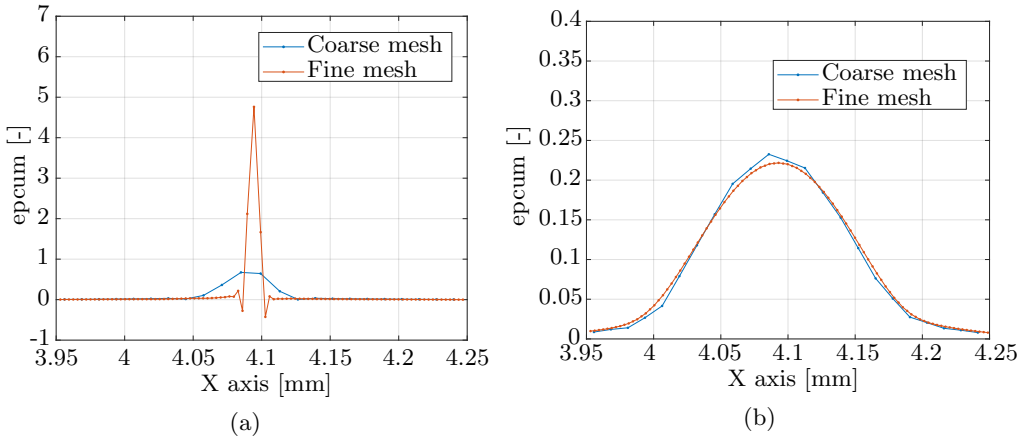

Figure 4.2: Cumulative plastic distribution for different mesh sizes using Classical CM (a) and Cosserat medium (b).

where H is the softening modulus, which was set equal to - 30 MPa. As it can be seen from Eq. (4.63), the equivalent cumulated plastic strain in this case is causing the same effect that is usually induced by the temperature on the flow stress. According to Eq. (4.63), the material softening is induced whenever plastic strain cumulates, while normally the softening is a thermally-activated phenomena. The same simulation was performed for two different mesh size, a finer mesh of 20 μm x 15 μm and a coarser mesh of double the size for both the Classical CM and the Cosserat medium, and the plastic distributions across the ASB were compared. In Figure 4.2 the comparison is appreciable. The equivalent plastic strain distribution has been plotted across the ASB. While the Classical CM description exhibits a strong mesh-dependency, the Cosserat medium does not show such dependency. More discussion related to the differences in cumulative plastic distribution between Classical CM and Cosserat medium will be provided in the Section 4.3, but this results clearly shows that the Cosserat medium can retain mesh independence results under conditions for which the Classical CM cannot.

4.2.1 Minumum Mesh Size Identification

In order to ensure the mesh size to be smaller than the elastic characteristic length of the model, a preliminary investigation was made to find the characteristic length for which the simulations would converge. In this analysis, the assumptions that both a_i and b_i are equal to 0 in Eq. (4.46) were made. Consequently, both the deformation and the wryness are fully elastic. Under this assumptions, the Hat-Specimen under compression was simulated using an initial mesh size of 20 μm x 15 μm, and using the material properties as Table 4.2. The results in terms of load-displacement of the Hat-Shaped Specimen are reported in Figure 4.3. The values of the elastic characteristic length range from 10^1 mm to 10^{-4} mm. The curves achieve convergence already for values of the elastic characteristic length of 10^{-2} mm, therefore suggesting the adoption of a mesh size, along the direction orthogonal to the ASB, smaller than 100 μm. Subsequently, using a mesh size of 40 μm x 30 μm can be considered a safe choice. Furthermore, for all the

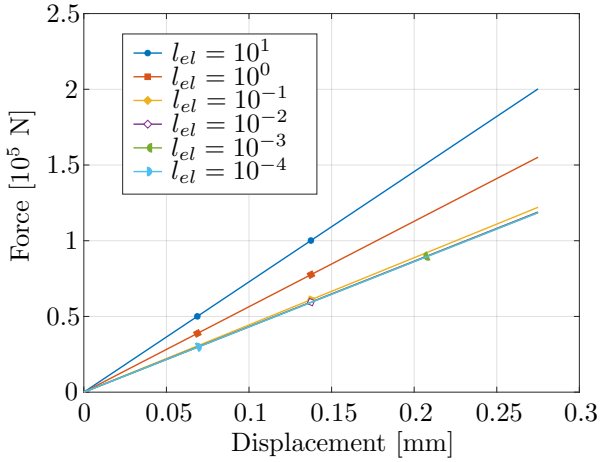

Figure 4.3: Convergence analysis of the elastic characteristic length performed on the load-displacement graph of the Hat-Shaped Specimen using $b_i = a_i = 0$ as assumption in Eq. (4.46). Values of the characteristic lengths are given in millimeters.

simulations, quadratic elements are used, so that the distance between the nodes spanning the element edges is ulteriorly halved.

4.3 Elastic characteristic length calibration

In our case, since we are modeling in 2D, there is no torsional component in the wryness ($\mathrm{k}^e_{ii} = 0$, $ii = 1, 2, 3$), therefore the parameter α does not have any influence and it must not be calibrated. Throughout the calibration process the value of G_c was set constant and imposed to be higher than the second Lame parameter (shear modulus), such that the Cosserat model would assume similar nature of a strain gradient theory. The value of G_c was set to be equal to 114000.0 MPa. The calibration of the elastic characteristic length can be performed by simply varying the coefficient β in Eq. (4.37). The Classical CM framework can be retrieved by imposing the elastic characteristic length to vanish, and in this case the deformation localizes as if it was unaffected by the "diffusing" effect induced by not-vanishing $\widetilde{\mathbf{k}}$. The calibration procedure shall start from large values of β and then its values should progressively reduce. Differently from the analysis done in the previous section, for the current calibration procedure only the condition $b_1 = b_2 = 0$ was used in Eq. (4.46), that is, the plastic characteristic length was set equal to infinity. Consequently, the developed curvature is fully elastic, but the strain is also plastic, and $\dot{p}$ depends on the stress only in Eq. (4.46).

The calibration procedure could be performed by comparing data of different nature between experiments and simulations. Following the complete thermodynamic description outlined in Section 4.1 we could compare the temperature distribution in the ASB, especially because this can be easily measured through thermal camera or, in case the plastic deformation localizes inside the specimen, by positioning thermocouples at the location where the ASB is expected to develop. Since the magnitude of the characteristic length influences the area over which the developed deformation spreads (thickness of

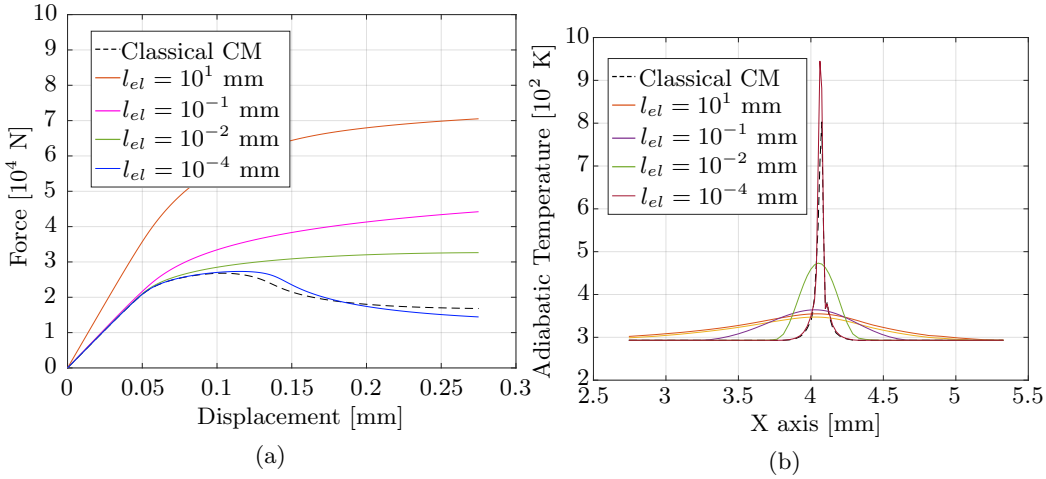

Figure 4.4: Effects of the characteristic elastic length on the load-displ graph (a) and on the temperature distribution (b). Values of the characteristic lengths are given in millimeters.

ASB), many thermocouples might be necessary to capture both the thermal distribution and its peak value. To be noted here that in adiabatic conditions the thermal variation is only driven by local development of plastic deformation, since there is no time for the temperature to diffuse, thus the measured temperature is a direct indication of the developed plastic deformation. Six values of the elastic characteristic length were used, from 10^1 mm to 10^{-4} mm. The effects of the elastic characteristic length have been investigated by looking both at the load-displacement curve and at the temperature distribution at the ASB.

As already observed in case of a hyper-elastic material model, the adoption of an elastic characteristic length, whose order of magnitude is comparable with the geometry size, extends the stiffening effect to a macroscopic level, inducing the whole system to behave stiffer. In case a plastic component is introduced in the Cosserat strain, the same behavior is observed, as inferred by Figure 4.4a. It can be observed from this Figure that the over-prediction of the initial elastic stiffness is negligible for values of the characteristic length smaller or equal than $\approx 10^{-1}$ mm. Furthermore, it can be appreciated from the same Figure the trend of the load-displ curve of converging toward the results produced for a Classical CM simulation for values of the characteristic length that approach zero. The curve, however, should not overlap with the one obtained from the adoption of the TANH model in a Classical CM framework because, although the curvature is providing a null energetic contribution, the part of the Cosserat strain accounting for the mismatch between macro and micro rotation is still playing a role.

In Figure 4.5 the thermal fields across the ASB are reported. From the Figure, it is possible to identify the effect of the characteristic length on the thermal distribution. The elastic characteristic lengths indicate the range over which the thermal field, in this case, is spreading: smaller elastic characteristic length will induce the fields to spread over smaller domains. It can be noted that the temperatures reached in the Classical CM case are lower than the ones in the Cosserat model with a characteristic length of 10^{-4} mm,

E [MPa]	ν	G_c [MPa]	ρ [kg/m^3]	C_ε [J/kg·K]	T_m [K]	Γ [1/K]	Γ_k [1/K·mm]
114000.0	0.3	114000.0	4428.0	580.0	1926.0	8.5e-6	0.0

Table 4.2: Elastic and thermal material properties corresponding to the Titanium alloy Ti6Al4V [Peirs, Verleysen, Degrieck, and Coghe 2010].

however, it should be reminded that the results of this simulation strongly depend on the mesh size.

4.4 Plastic characteristic length calibration

Although the model previously described defines the plastic behavior of the medium by providing the explicit function of the plastic potential Ω, most of the models used in literature are simply provided through their flow stress definition. The flow stress used here derives from the one developed by Calamaz et al. [Calamaz et al. 2008], but the dependence of the flow stress on the rate of the equivalent plastic strain has been omitted in order to simplify the model and focus only on strain hardening and thermal softening behaviors. This flow stress model has been used several times in literature [Hor et al. 2013; L. He et al. 2018], but it has never been coupled with the Cosserat medium description. The radius of the yield surface is defined as:

$$R = \left[A + \frac{Bp^n}{\exp\left(p^a\right)}\right]\left[1 - \left(\frac{T - T_0}{T_m - T_0}\right)^m\right]\left[D + (1 - D)\tanh\left(\frac{1}{(p + S)^c}\right)\right]; \tag{4.64}$$

where:

$$D = 1 - \left(\frac{T}{T_m}\right)^d; \tag{4.65}$$

$$S = \left(\frac{T}{T_m}\right)^b; \tag{4.66}$$

and the flow rule of the viscoplastic multiplier p follows:

$$\dot{p} = \exp\left(\frac{\langle f \rangle}{RC}\right) - 1 = \exp\left[\frac{1}{C}\left(\frac{\sigma_{eq}}{R} - 1\right)\right] - 1; \tag{4.67}$$

It must be remembered that since we are using a single viscoplastic multiplier, $\dot{p}$ depends on both plastic strain and wryness contributions. The material properties are listed in Table 4.2, and they belong to the Titanium alloy Ti6Al4V, and the TANH flow stress model parameters have been summarized in Table 4.3. The calibration of the plastic characteristic length has been done under the hypothesis that $a_1 = a_2$ and $b_1 = b_2$ in Eq. (4.46). The characteristic plastic length was chosen in the range between 10^0 mm and 10^{-4} mm. From the previous calibration procedure it was evident that the elastic characteristic length for this problem had to be smaller or equal than 10^{-2} mm for the deformation to localize. However, excessively low values of β induce the development of a relatively low values of couple stress if compared to the stress, therefore obliging

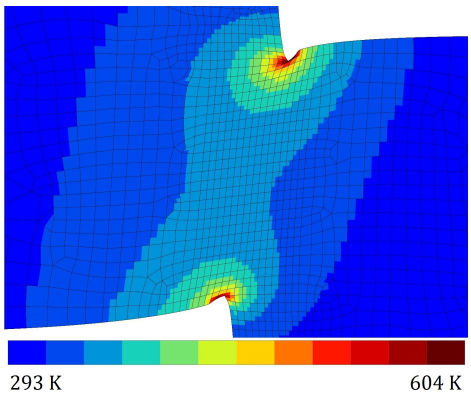

(a) $l_{el} = 10^{0}$ mm

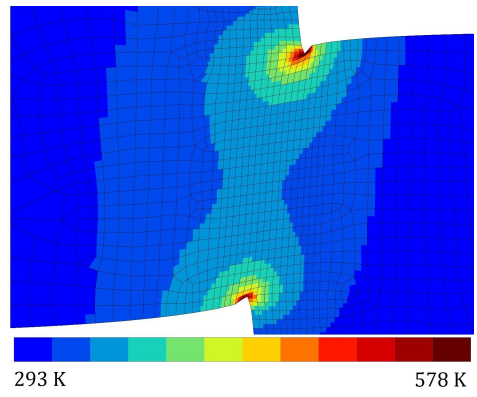

(b) $l_{el} = 10^{-1}$ mm

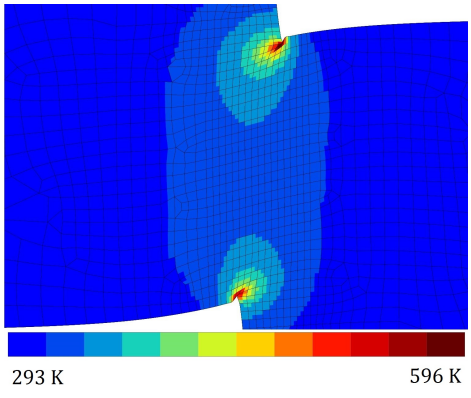

(c) $l_{el} = 10^{-2}$ mm

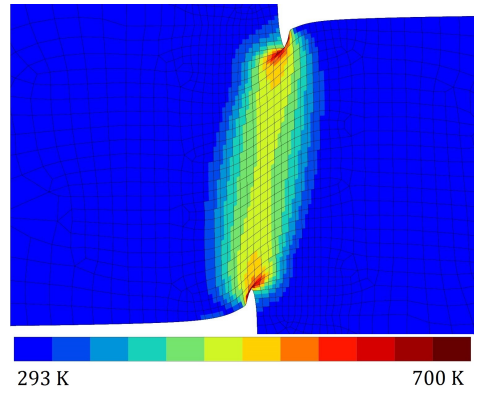

(d) $l_{el} = 10^{-3}$ mm

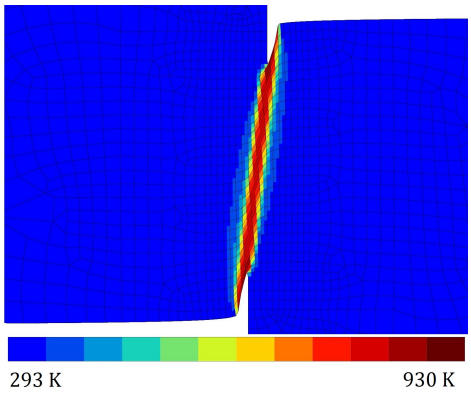

(e) $l_{el} = 10^{-4}$ mm

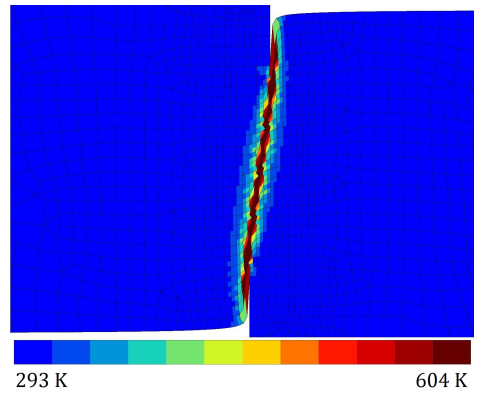

(f) Classical CM

Figure 4.5: Temperature distribution in a Hat-Shaped specimen using the Cosserat framework with different values of β compared to the Classical CM result.

A [MPa]	B [MPa]	C	m	n	a	b	c	d
1120.0	667.0	0.0270	1.33	0.47	1.	1.	1.	1.

Table 4.3: Visco-plastic coefficients used in the TANH model [Peirs, Verleysen, Degrieck, and Coghe 2010].

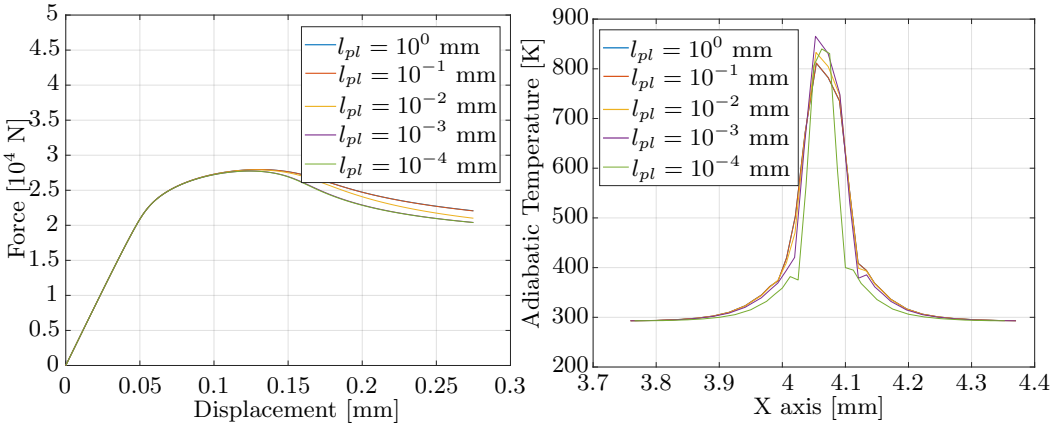

(a) (b)

Figure 4.6: Effects of the characteristic plastic length on the load-displ graph (a) and on the temperature distribution (b). Values of the characteristic lengths are given in millimeters.

the adoption of high values of the coefficient b in Eq. (4.46) if we wanted the couple stresses to have an effect on σ_{eq}. Thus for the plastic characteristic length calibration, an elastic characteristic length of 10^{-2} mm has been chosen. Once again, we look at the effects on the global load-displacement graph and to the temperature distribution inside the ASB, which are reported in Figures 4.6a and 4.6b respectively. In Figure 4.6a it can be observed that the load-displacement curves are bounded between the curves obtained for $l_{pl} = 10^0$ mm and $l_{pl} = 10^{-4}$ mm, which represent the asymptotic results for larger or smaller characteristic plastic lengths respectively. This behavior suggests that the plastic development is simultaneously driven by both strain and wryness in case the characteristic plastic length belongs to the range $\approx [10^{-1}$ mm$\div 10^{-3}$ mm], and that it is purely dominated by strain or wryness only in case the characteristic plastic length falls respectively before or after this domain. If we look at the temperature distribution across the ASB in Figure 4.6b, it shows an increasing peak of predicted temperature at the center of the shear band, and a narrower localization of the thermal field with a decreasing plastic characteristic length. The maximum difference between the peaks of the temperatures belonging to the different plastic characteristic lengths measures 65 K. This difference lies well beyond the resolution of instruments, like thermocouples or thermal camera, thus the effect of different plastic characteristic lengths could be probed. Nonetheless, 65 K of difference is still a relative low value if compared with the total produced temperature, that is around 500 K. This indicates a relative weaker influence of the characteristic plastic length on the developed thermal field if compared with the

effects produced by different values of elastic characteristic lengths on the thermal fields.

4.5 Conclusion

Simulations of manufacturing processes can provide valuable information that help optimizing machined materials and machining benches. Furthermore, the knowledge related to the deformation history of the material is a key factor in addressing the post-processed status of the medium, for example in terms of residual stresses. In order to achieve more reliable simulations of these processes, we proposed the adoption of the Cosserat model as description of the medium behavior. A thermodynamically-consistent geometrically linearized formulation of the Cosserat theory was proposed in Section 4.1, where a thermo-elasto-visco-plastic framework was provided for the material characterization through the definition of visco-plastic potential, Helmholtz free energy and dissipation potential.

Using a purely-softening plastic behavior, the Cosserat medium was first proven to provide mesh-independent results, then the TANH flow-stress model was implemented, and it was used to describe an example of the calibration procedure of the elastic and plastic characteristic lengths using a hat-shaped specimen. The calibration of the elastic characteristic length was done by comparing the global load-displacement graph, and, for the specific plastic model used here, its values was found to be in the range of microns, that is comparable to grain size of the Titanium alloy used for the simulation [Dong et al. 2018]. By fixing the value of the elastic characteristic length to be equal to 10^{-2} mm, the calibration of the plastic characteristic length was performed once again by comparing the load-displacement graphs. The analysis suggested the existence of a range for the plastic characteristic length in which the contribution of plastic strain and plastic wryness were playing a comparable role. Outside these limits the plastic developments were fully dominated by the plastic components of one of the two deformation measures. However, finally the elastic characteristic length was found to have greater effects than the plastic ones.

Nonetheless, since the effects of the plastic characteristic length are highlighted at large plastic deformation, it is advisable to use a large deformation theory for the Cosserat medium. This remains the topic for the future research. For future research it is also foreseen the adoption of a physically-based material plastic law, ideally dislocation-based, and the validation of the Cosserat model for more complex manufacturing operations, such as machining or orthogonal cutting.

Chapter 5

Analytical solutions in Cosserat elasto-plasticity

In this chapter, are derived the analytical solutions of the glide problem for the elasto-plastic Cosserat media under small deformation. For the plastic part of the solutions, a relatively-new formulation of the equivalent stress measure is here proposed. This specific choice of properly picked invariants of the second order stress tensor allowed the analytical solution of this particular problem to be found straightforwardly.

Two sets of boundary conditions will be considered: the first set leaves the micro-rotations free at the boundaries of the specimen, whereas the second set contains an additional constraint on the micro-rotations. Different mechanical properties will be used for each set of boundary conditions. Both cases are analyzed in elasticity and elasto-plasticity.

The first set of boundary conditions (free micro-rotation) is of specific interest for this research, since it recreates the conditions for localization of deformation and subsequent formation of a shear band. Analyzing this case is of pivotal importance to improve the understanding of the shear band formation during metal manufacturing. The exact width of the shear band predicted using the Cosserat medium will be analytically derived.

This chapter is structured in three sections: in the first one, the relatively-new formulation of the equivalent stress will first be presented, then the second and third section will focus on the analytical solutions of the free-rotations and the fixed-rotations sets of boundary conditions, both in elasticity and elasto-plasticity.

5.1 Reformulation of the equivalent plastic stress in the cosserat media

The formulation of the equivalent stress that has been previously used derives from the research of de Borst [de Borst 1991b], and it reads:

$$\sigma_{eq}^{\text{de Borst}} = \sqrt{\frac{3}{2}}\sqrt{a_1(\underset{\sim}{\boldsymbol{\sigma}}_d : \underset{\sim}{\boldsymbol{\sigma}}_d) + a_2(\underset{\sim}{\boldsymbol{\sigma}}_d : \underset{\sim}{\boldsymbol{\sigma}}_d^T) + b_1(\underset{\sim}{\mathbf{m}} : \underset{\sim}{\mathbf{m}}) + b_2(\underset{\sim}{\mathbf{m}} : \underset{\sim}{\mathbf{m}}^T)}; \tag{5.1}$$

where the subscript d indicates the deviatoric part of the tensor. Several features of this specific formulation can be pointed out:

- In case of a plane 2D analysis only the entries m_{31} and m_{32} are not zero, and using a coefficient b2≠0 can induce the formation of some not-physical plastic wryness k^p_{13} and k^p_{23} if the normality rule is applied;
- In the specific case analyzed in the next Section 5.3, if a_1 and a_2 are chosen to be 0 and 1 respectively, then the J_2 is imaginary (in the example of the next section, this happens in a region close to the edges);
- For general values of a_1 and a_2, there exist no clear distinction between the action belonging to the additional part of the deformation (skew($\underset{\sim}{\mathbf{e}}$)) and to the classical-Cauchy part of the deformation (sym($\underset{\sim}{\mathbf{e}}$)). Ideally, we want to split these two contributions and treat them separately.

In literature, other forms of equivalent stress for the Cosserat media can be found, namely the one proposed by Lippmann, Mühlhaus and Vardoulakis, Steinmann[Lippmann 1969; Mühlhaus et al. 1987; Steinmann 1994], in which the symmetric and skew-symmetric parts of the stress tensor are multiplied with two different parameters. In a large deformation framework of the Cosserat media, the Cauchy stress, Kirchhoff stress and the Mandel stress have been used for the definition of the equivalent stresses, by Bauer et al. [Bauer, Dettmer, et al. 2012], Steinmann [Steinmann 1994] and by Grammenoudis and Tsakmakis [Grammenoudis et al. 2001; Grammenoudis et al. 2005] respectively.

In the attempt of proposing a different formulation for the equivalent stress, one possible solution would be to look at the invariants of the tensors that should contribute to the equivalent stress measure. From the work of Zheng, [Zheng 1994], the invariants of a generic tensor $\underset{\sim}{\mathbf{C}}$ are a combination of the invariants of its symmetric and skew symmetric parts, referred to as $\underset{\sim}{\mathbf{A}}$ and $\underset{\sim}{\boldsymbol{W}}$ respectively. The invariants of $\underset{\sim}{\mathbf{A}}$ are:

- $\text{trace}\left(\underset{\sim}{\mathbf{A}}\right)$,
- $\text{trace}\left(\underset{\sim}{\mathbf{A}}^2\right)$,
- $\text{trace}\left(\underset{\sim}{\mathbf{A}}^3\right)$,

the invariant of $\underset{\sim}{\boldsymbol{W}}$ is:

- $\text{trace}\left(\underset{\sim}{\boldsymbol{W}}^2\right)$,

and the mixed invariants are:

- $\text{trace}\left(\underset{\sim}{\mathbf{A}}\underset{\sim}{\boldsymbol{W}}^2\right)$,
- $\text{trace}\left(\underset{\sim}{\mathbf{A}}^2\underset{\sim}{\boldsymbol{W}}^2\right)$,
- $\text{trace}\left(\underset{\sim}{\mathbf{A}}^2\underset{\sim}{\boldsymbol{W}}^2\underset{\sim}{\mathbf{A}}\underset{\sim}{\boldsymbol{W}}\right)$.

Based on the invariants of its second order tensor, the following formulation of the equivalent stress is proposed:

$$\sigma_{eq} = \sqrt{\frac{3}{2}}\sqrt{a_3(\underset{\sim}{\boldsymbol{\sigma}}^s_d : \underset{\sim}{\boldsymbol{\sigma}}^s_d) + a_4(\underset{\sim}{\boldsymbol{\sigma}}^k_d : \underset{\sim}{\boldsymbol{\sigma}}^k_d) + b_3\,[\text{trace}(\underset{\sim}{\mathbf{m}})]^2 + b_4(\underset{\sim}{\mathbf{m}}^s_d : \underset{\sim}{\mathbf{m}}^s_d) + b_5(\underset{\sim}{\mathbf{m}}^k_d : \underset{\sim}{\mathbf{m}}^k_d)}; \tag{5.2}$$

Here it is important to mention that same analysis on the equivalent stress measure in the Cosserat media has been done simultaneously and independently by Pantegini and et. [Panteghini and Lagioia 2021]. If this formulation is compared with the one of de

Borst (Eq. (5.1)), we can see that in the previous formulation the symmetric and skew-symmetric parts of the stress are not treated separately, and we can appreciate this difference by explicitly expressing the stresses in Equation (5.1) with their symmetric and skew-symmetric parts $\underset{\sim}{\boldsymbol{\sigma}} = \underset{\sim}{\boldsymbol{\sigma}}^s + \underset{\sim}{\boldsymbol{\sigma}}^k$ (subscript $_d$ removed for clarity):

$$\begin{aligned} a_1 \left(\underset{\sim}{\boldsymbol{\sigma}} : \underset{\sim}{\boldsymbol{\sigma}} \right) + a_2 \left(\underset{\sim}{\boldsymbol{\sigma}} : \underset{\sim}{\boldsymbol{\sigma}}^T \right) &= a_1 \left(\underset{\sim}{\boldsymbol{\sigma}}^s : \underset{\sim}{\boldsymbol{\sigma}}^s + \underset{\sim}{\boldsymbol{\sigma}}^s : \underset{\sim}{\boldsymbol{\sigma}}^k + \underset{\sim}{\boldsymbol{\sigma}}^k : \underset{\sim}{\boldsymbol{\sigma}}^s + \underset{\sim}{\boldsymbol{\sigma}}^k : \underset{\sim}{\boldsymbol{\sigma}}^k \right) + \\ &+ a_2 \left(\underset{\sim}{\boldsymbol{\sigma}}^s : \underset{\sim}{\boldsymbol{\sigma}}^{s^T} + \underset{\sim}{\boldsymbol{\sigma}}^s : \underset{\sim}{\boldsymbol{\sigma}}^{k^T} + \underset{\sim}{\boldsymbol{\sigma}}^k : \underset{\sim}{\boldsymbol{\sigma}}^{s^T} + \underset{\sim}{\boldsymbol{\sigma}}^k : \underset{\sim}{\boldsymbol{\sigma}}^{k^T} \right) = \\ &a_1 \left(\underset{\sim}{\boldsymbol{\sigma}}^s : \underset{\sim}{\boldsymbol{\sigma}}^s + \underset{\sim}{\boldsymbol{\sigma}}^k : \underset{\sim}{\boldsymbol{\sigma}}^k \right) + a_2 \left(\underset{\sim}{\boldsymbol{\sigma}}^s : \underset{\sim}{\boldsymbol{\sigma}}^s + \underset{\sim}{\boldsymbol{\sigma}}^k : \underset{\sim}{\boldsymbol{\sigma}}^{k^T} \right); \end{aligned} \tag{5.3}$$

By remembering that, for a generic tensor $\underset{\sim}{\mathbf{A}}$, both $\underset{\sim}{\mathbf{A}}^s : \underset{\sim}{\mathbf{A}}^s$ and $\underset{\sim}{\mathbf{A}}^k : \underset{\sim}{\mathbf{A}}^k$ are two of its invariants [Zheng 1994], the question arises on why these invariants are combined as such in the formulation of the equivalent stress in Equation (5.1). By using such combination of invariants, if the coefficients a_1 and a_2 are equal, the contribution to the equivalent stress of the skew-symmetric part of the stress disappears ($\underset{\sim}{\boldsymbol{\sigma}}^k : \underset{\sim}{\boldsymbol{\sigma}}^{k^T} = -\underset{\sim}{\boldsymbol{\sigma}}^k : \underset{\sim}{\boldsymbol{\sigma}}^k$), effectively recovering the formulation of the equivalent stress for the Cauchy continuum. On the other hand, if the objective was to emphasize the effect of the skew-symmetric part of the stress on the equivalent stress, then the difference between the two a coefficient should be increased. On the contrary, an important advantage of the newly proposed decomposition is that we can clearly identify and explicitly quantify the classical contributions of the Cauchy stress and the additional part coming from the Cosserat theory, therefore, the coefficients a_3 and a_4 act as a direct amplifier of the symmetric and skew-symmetric parts of the equivalent stress measure.

If all the terms related to the couple stress were assumed to be null, the old formulation can be retrieved by the new formulation through the following conditions:

$$\begin{cases} a_3 = a_1 + a_2, & (5.4) \\ a_4 = a_1 - a_2, & (5.5) \end{cases}$$

In a simplified 2D condition, the trace of the couple stress tensor in null, therefore the assumption on the b_i terms can be removed, and, in general, the following conditions must applied to retrive the old formulation:

$$\begin{cases} a_3 = a_1 + a_2, & (5.6) \\ a_4 = a_1 - a_2, & (5.7) \\ b_3 = 0, & (5.8) \\ b_4 = b_1 + b_2, & (5.9) \\ b_5 = b_1 - b_2. & (5.10) \end{cases}$$

Table 5.1: Elasto-plastic material properties used for the free rotations problem.

E	ν	β	σ_0	H
200000 MPa	0.3	77 MPa mm^2	250 MPa	0 MPa / $\pm$1000 MPa

5.2 Set 1 of boundary conditions: free micro-rotations

For the semi-infinite glide planar Cosserat problem under plain strain condition, the following degrees of freedom are considered:

$$\underline{\mathbf{u}} = \begin{bmatrix} u(y) \\ 0 \\ 0 \end{bmatrix} \quad \text{and} \quad \underline{\boldsymbol{\theta}} = \begin{bmatrix} 0 \\ 0 \\ \theta(y) \end{bmatrix} \tag{5.11}$$

thus there exist only two degrees of freedom: displacement u and micro-rotation θ. Since a semi-infinite layer of material is considered, the problem effectively becomes a one-dimension problem (both the variables are function of y only). The Cosserat strain and wryness are defined as:

$$\underset{\sim}{\mathbf{e}} = \underline{\mathbf{u}} \otimes \underline{\boldsymbol{\nabla}} + \underset{\sim}{\boldsymbol{\epsilon}} \cdot \boldsymbol{\theta} = \begin{bmatrix} 0 & u_{,2} + \theta & 0 \\ -\theta & 0 & 0 \\ 0 & 0 & 0 \end{bmatrix}; \tag{5.12}$$

$$\underset{\sim}{\mathbf{k}} = \underline{\boldsymbol{\theta}} \otimes \underline{\boldsymbol{\nabla}} = \begin{bmatrix} 0 & 0 & 0 \\ 0 & 0 & 0 \\ 0 & \theta_{,2} & 0 \end{bmatrix}; \tag{5.13}$$

where the subscript $_{,2}$ indicates the first derivative of the function with respect to the y coordinate. The balance Equations for the Cosserat media have been previously derived, and they are the following:

$$\underset{\sim}{\boldsymbol{\sigma}} \cdot \underline{\boldsymbol{\nabla}} + \underline{\mathbf{f}} = \underline{\mathbf{0}}; \tag{5.14}$$

$$\underset{\sim}{\mathbf{m}} \cdot \underline{\boldsymbol{\nabla}} + \mathrm{axl}(\underset{\sim}{\boldsymbol{\sigma}}) + \underline{\mathbf{c}} = \underline{\mathbf{0}}; \tag{5.15}$$

which, in absence of body and contact forces, can be particularized for the current problem as:

$$\sigma_{12,2} = 0; \tag{5.16}$$

$$m_{32,2} = \sigma_{12} - \sigma_{21}; \tag{5.17}$$

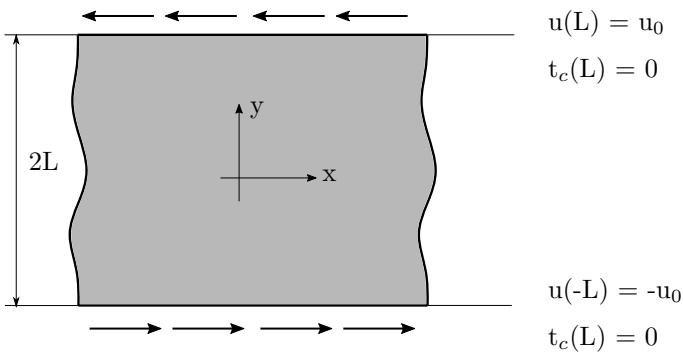

Figure 5.1: First set of boundary conditions used for the glide test using the Cosserat continuum.

The definition of the normals at the boundaries of the domain are:

$$\underline{\mathbf{n}}^{-} = \underline{\mathbf{n}}\,(y = -L) = \begin{bmatrix} 0 \\ -1 \\ 0 \end{bmatrix}; \tag{5.18}$$

$$\underline{\mathbf{n}}^{+} = \underline{\mathbf{n}}\,(y = L) = \begin{bmatrix} 0 \\ 1 \\ 0 \end{bmatrix}; \tag{5.19}$$

The tractions and couple tractions can then be defined, for example at the top most boundary of the domain ($y = L$, $\underline{\mathbf{n}} = \underline{\mathbf{n}}^{+}$), as:

$$\underline{\boldsymbol{t}} = \underset{\sim}{\boldsymbol{\sigma}} \cdot \underline{\mathbf{n}}^{+}, \tag{5.20}$$

$$\underline{\boldsymbol{t}}_c = \underset{\sim}{\mathbf{m}} \cdot \underline{\mathbf{n}}^{+} \tag{5.21}$$

Dirichlet boundary conditions were applied to the displacement fields at the top and bottom of the strip, opposite in magnitude:

$$u\,(y = L) = u_0; \tag{5.22}$$

$$u\,(y = -L) = -u_0; \tag{5.23}$$

and Neumann boundary conditions were applied on the micro-rotational fields, in terms of couple traction, at the top and bottom of the strip, and they were set to be null:

$$t_{c_3}\,(y = L) = 0; \tag{5.24}$$

$$t_{c_3}\,(y = -L) = 0; \tag{5.25}$$

and this means that the rotations fields should have a null derivative at the top and bottom of the strip. The geometry and the boundary conditions are reported in Figure 5.1. Using this set of boundary condition in classical continuum mechanics would lead to a simple homogeneous solution in which the shear is equal to the applied displacement divided by the length of the specimen. In terms of material properties, in Table 5.1 the mechanical properties used for the free-rotations boundary value problem have been reported.

5.2.1 Elastic behavior with free rotations

The standard Cosserat isotropic constitutive behavior is considered for stress and couple stress:

$$\underset{\sim}{\boldsymbol{\sigma}} = \lambda\,\mathrm{trace}(\underset{\sim}{\mathbf{e}}^e)\underset{\sim}{\mathbf{I}} + 2\,\mu\,\mathrm{sym}(\underset{\sim}{\mathbf{e}}^e) + 2\,\mu_c\,\mathrm{skew}(\underset{\sim}{\mathbf{e}}^e); \tag{5.26}$$

$$\underset{\sim\sim}{\mathbf{m}} = \alpha\,\mathrm{trace}(\underset{\sim}{\mathbf{k}}^e)\underset{\sim}{\mathbf{I}} + 2\,\beta\,\mathrm{sym}(\underset{\sim}{\mathbf{k}}^e) + 2\,\gamma\,\mathrm{skew}(\underset{\sim}{\mathbf{k}}^e); \tag{5.27}$$

where the superscript ^{e} indicates the elastic part of the deformation, and since we are only considering fully elastic solutions in this sub-section, it would correspond to the total deformation. In this case, the stress and couple stress are:

$$\underset{\sim}{\boldsymbol{\sigma}} = \begin{bmatrix} 0 & u_{,2}(\mu+\mu_c)+2\mu_c\,\theta & 0 \\ u_{,2}(\mu-\mu_c)-2\mu_c\,\theta & 0 & 0 \\ 0 & 0 & 0 \end{bmatrix}, \tag{5.28}$$

$$\underset{\sim\sim}{\mathbf{m}} = \begin{bmatrix} 0 & 0 & 0 \\ 0 & 0 & 0 \\ 0 & 2\beta\,\theta_{,2} & 0 \end{bmatrix}, \tag{5.29}$$

and the tractions and couple tractions would be:

$$\underline{\boldsymbol{t}} = \begin{bmatrix} u_{,2}\,(\mu+\mu_c)+2\mu_c\theta \\ 0 \\ 0 \end{bmatrix}, \tag{5.30}$$

$$\underline{\boldsymbol{t}}_c = \begin{bmatrix} 0 \\ 0 \\ 2\beta\theta_{,2} \end{bmatrix}, \tag{5.31}$$

and, by substituting the stresses and couple stresses in the balance equation (5.16) and (5.17), they become:

$$u_{,22} = -\frac{2\mu_c}{\mu_c+\mu}\theta_{,2}, \tag{5.32}$$

$$\beta\,\theta_{,22} = \mu_c u_{,2} + 2\,\mu_c\,\theta. \tag{5.33}$$

The general solution to the boundary value problem can be found by differentiating Eq. (5.33) and substituting the function $u_{,22}$ in Eq. (5.32):

$$\beta\,\theta_{,222} = \mu_c u_{,22} + 2\,\mu_c\,\theta_{,2} \quad \Longrightarrow \quad \theta_{,222} = \omega_e^2\,\theta_{,2}, \tag{5.34}$$

where we defined the inverse of the intrinsic elastic length as:

$$\omega_e = \sqrt{\frac{2\,\mu\mu_c}{\beta(\mu+\mu_c)}}, \tag{5.35}$$

and the general solutions of the differential equation have the following forms:

$$\theta(y) = A\,\cosh(\omega_e\,y) + B\,\sinh(\omega_e\,y) + C, \tag{5.36}$$

$$u(y) = -\frac{2\,\mu_c}{(\mu+\mu_c)\,\omega_e}\,[A\,\sinh(\omega_e\,y) + B\,\cosh(\omega_e\,y)] + D\,y + E. \tag{5.37}$$

However, we have to consider also the not-derived form of Equation (5.33) as additional differential equation, and this extra equation establishes the value of the constant C:

$$A\,\cosh(\omega_e y)\left[\beta\omega_e^2 + 2\frac{\mu_c^2}{\mu+\mu_c} - 2\mu_c\right] + B\,\sinh(\omega_e y)\left[\beta\omega_e^2 + 2\frac{\mu_c^2}{\mu+\mu_c} - 2\mu_c\right] = 2\mu_c(D+2\,C), \tag{5.38}$$

where the terms in parenthesis can be elided and be found to be zero, therefore leading to:

$$C = -\frac{D}{2}, \tag{5.39}$$

and the general solutions of the micro-rotation and the displacements are:

$$\theta(y) = A\,\cosh(\omega_e\,y) + B\,\sinh(\omega_e\,y) + C, \tag{5.40}$$

$$u(y) = -\frac{2\,\mu_c}{(\mu+\mu_c)\,\omega_e}\,[A\,\sinh(\omega_e\,y) + B\,\cosh(\omega_e\,y)] - 2\,C\,y + E. \tag{5.41}$$

The specific solution can be found by imposing the set of boundary conditions. By substituting the general solutions in the displacement boundary conditions Equations (5.22) and (5.23), they transform into:

$$A\,\sinh(-\omega_e\,L) + B\,\cosh(-\omega_e\,L) = (2\,C\,L + E + u_0)\,\omega_e\frac{\mu+\mu_c}{2\,\mu_c}, \tag{5.42}$$

$$A\,\sinh(\omega_e\,L) + B\,\cosh(\omega_e\,L) = (-2\,C\,L + E - u_0)\,\omega_e\frac{\mu+\mu_c}{2\,\mu_c}, \tag{5.43}$$

whereas the boundary conditions on the tractions in Equations (5.24) and (5.25) can be rewritten as:

$$2\,\beta\,\omega_e\,[A\,\sinh(\omega\,L) + B\,\cosh(\omega_e\,L)] = 0, \tag{5.44}$$

$$2\,\beta\,\omega_e\,[A\,\sinh(-\omega_e\,L) + B\,\cosh(-\omega_e\,L)] = 0, \tag{5.45}$$

From the Newman boundary conditions (Equations (5.44) and (5.45)):

$$\begin{cases} A = 0 \\ B = 0 \end{cases} \tag{5.46}$$

So, the Dirichlet boundary conditions (Equations (5.42) and (5.43)) can be written as:

$$\begin{cases} -2\,C\,L = E + u_0, \\ -2\,C\,L = -E + u_0, \end{cases} \quad \Longrightarrow \quad \begin{cases} C = \dfrac{-u_0}{2\,L}, \\ E = 0. \end{cases} \tag{5.47}$$

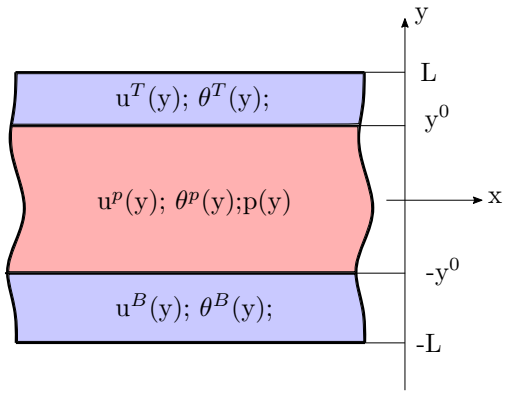

Figure 5.2: Identification of the elastic and plastic zones expected for the strip test.

At the end, the particular solutions for the given boundary conditions are:

$$u(y) = \frac{u_0}{L}\, y, \tag{5.48}$$

$$\theta(y) = -\frac{u_0}{2\,L}, \tag{5.49}$$

where it can be appreciated that the solution from the classical Cauchy continuum is retrieved. In this case the Cosserat rotation follows the material rotation, since no restriction has been posed on it.

5.2.2 Elasto-plastic behavior with free micro-rotations

Given the fact that the fields are homogeneous, in the present case of boundary conditions, the stress will also be homogeneous, therefore the equivalent stress has the same value throughout the specimen, and if this value goes beyond the yield, the whole specimen turns plastic. In case of a softening plastic behavior, the material experiences a point of un-stable equilibrium, and it requires some triggering in order to exploit the instability. In order to numerically induce instability at a specific location, often the material in this region is characterized with a slightly smaller yield stress, such as to trigger plastic deformation to initially nucleate here. We suppose that the nucleation occurs in the middle of the specimen, therefore leading to a symmetric solution with respect to the x axis, and the elastic and plastic domains will develop as depicted in Figure 5.2.

The aim now is to find the general and specific solutions to the boundary value problem for the plastic domain. Differently from the elastic problem, we introduce another unknown field, which plays as an additional variable for the problem, that is the cumulative equivalent plastic strain. The governing differential equations which have been previously presented are still valid for the plastic zone, here they are reported:

$$\sigma_{12,2} = 0, \tag{5.50}$$

$$m_{32,2} = \sigma_{12} - \sigma_{21}, \tag{5.51}$$

in addition to these, we must also include the yield condition (that must hold in the plastic zone) and the assumption on the load that should be monotonically increasing. In

order to do so, the following linear plastic behavior is considered here:

$$R(p) = R_0 + H\,p, \tag{5.52}$$

where R_0 is the initial yield value, H is the slope of the curve and p is the plastic multiplier. Assuming an equivalent stress measure as presented in Equation (5.2), and by considering that $b_i = 0$, $a_4 = 0$, the wryness is fully elastic (Equation (5.29) is still valid), the yield condition assumes the following form:

$$f = \sigma_{eq}(y) - R_0 - H\,p = 0; \quad \Longrightarrow \quad \sigma_{eq}(y) = R_0 + H\,p, \tag{5.53}$$

which can be written as:

$$|\sigma_{12} + \sigma_{21}| = \left[\frac{2}{\sqrt{3\,a_3}}\,(R_0 + H\,p)\right]. \tag{5.54}$$

Furthermore, the constitutive model for the stress within the elasto-plastic domain reads:

$$\underset{\sim}{\boldsymbol{\sigma}} = \lambda\,\mathrm{trace}(\underset{\sim}{\mathbf{e}}^e)\underset{\sim}{\mathbf{I}} + 2\,\mu\,\mathrm{sym}(\underset{\sim}{\mathbf{e}}^e) + 2\,\mu_c\,\mathrm{skew}(\underset{\sim}{\mathbf{e}}^e), \tag{5.55}$$

assuming an additive elasto-plastic decomposition:

$$\underset{\sim}{\boldsymbol{\sigma}} = \lambda\mathrm{trace}(\underset{\sim}{\mathbf{e}} - \underset{\sim}{\mathbf{e}}^p)\underset{\sim}{\mathbf{I}} + 2\,\mu\,\mathrm{sym}(\underset{\sim}{\mathbf{e}} - \underset{\sim}{\mathbf{e}}^p) + 2\,\mu_c\mathrm{skew}(\underset{\sim}{\mathbf{e}} - \underset{\sim}{\mathbf{e}}^p), \tag{5.56}$$

and, by assuming the normality rule to hold (and monotonic proportional loading), the following relation can be considered:

$$\underset{\sim}{\mathbf{e}}^p = p\,\underset{\sim}{\mathbf{n}} = p\,\frac{\partial \sigma_{eq}}{\partial \underset{\sim}{\boldsymbol{\sigma}}} = p\,\frac{\sqrt{3\,a_3}}{2}\,\frac{(\sigma_{12} + \sigma_{21})}{|\sigma_{12} + \sigma_{21}|}\begin{bmatrix} 0 & 1 & 0 \\ 1 & 0 & 0 \\ 0 & 0 & 0 \end{bmatrix}, \tag{5.57}$$

then, by considering the following:

$$\underset{\sim}{\mathbf{e}} = \underline{\mathbf{u}} \otimes \underline{\boldsymbol{\nabla}} + \underset{\approx}{\boldsymbol{\epsilon}} \cdot \underline{\boldsymbol{\theta}} = \begin{bmatrix} 0 & u_{,2} + \theta & 0 \\ -\theta & 0 & 0 \\ 0 & 0 & 0 \end{bmatrix} = \begin{bmatrix} 0 & u_{,2}/2 & 0 \\ u_{,2}/2 & 0 & 0 \\ 0 & 0 & 0 \end{bmatrix} + \begin{bmatrix} 0 & \theta + u_{,2}/2 & 0 \\ -\theta - u_{,2}/2 & 0 & 0 \\ 0 & 0 & 0 \end{bmatrix}, \tag{5.58}$$

the stress reads:

$$\underset{\sim}{\boldsymbol{\sigma}} = \begin{bmatrix} 0 & u_{,2}[\mu + \mu_c] + 2\,\mu_c\theta + \mu p\sqrt{3\,a_3} & 0 \\ u_{,2}[\mu - \mu_c] - 2\,\mu_c\theta + \mu p\sqrt{3\,a_3} & 0 & 0 \\ 0 & 0 & 0 \end{bmatrix}, \tag{5.59}$$

from which, the traction and couple traction would be:

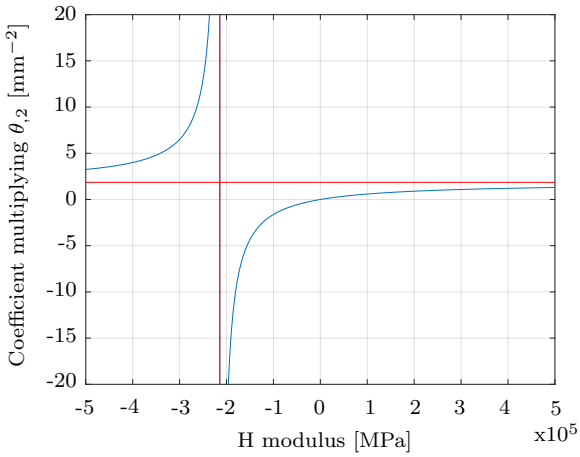

Figure 5.3: Value of the coefficient multiplying $\theta_{,2}$ in Equation (5.65) computed by using the mechanical properties reported in Table 5.1.

$$\underline{\boldsymbol{t}} = \begin{bmatrix} u_{,2}\,(\mu + \mu_c) + 2\mu_c\theta + \mu\, p\,\sqrt{3\,a_3} \\ 0 \\ 0 \end{bmatrix}, \tag{5.60}$$

$$\underline{\boldsymbol{t}}_c = \begin{bmatrix} 0 \\ 0 \\ 2\beta\theta_{,2} \end{bmatrix}, \tag{5.61}$$

Finally, by substituting the formulation of the stress in the yield condition (5.54), this can be explicitly written, and the full set of governing equations in the plastic domain will look like:

$$\begin{cases} u_{,22}[\mu + \mu_c] + 2\,\mu_c\theta_{,2} = -\mu p_{,2}\sqrt{3\,a_3} \\ 2\,\mu_c u_{,2} + 4\,\mu_c\theta = 2\,\beta\theta_{,22} \\ 2\,\mu u_{,2} + 2\,\mu\, p\sqrt{3\,a_3} = -\left[\dfrac{2}{\sqrt{3\,a_3}}\,(R_0 + H\,p)\right] \end{cases} \tag{5.62}$$

The general solution to the problem can be found by deriving the second equation with respect to y:

$$u_{,22} = -2\,\theta_{,2} + \frac{\beta}{\mu_c}\theta_{,222}; \tag{5.63}$$

same can be done to the last equation:

$$p_{,2} = -\mu\, u_{,22} \left[\frac{\sqrt{3\, a_3}}{\mu\, 3\, a_3 + H} \right], \tag{5.64}$$

and by plugging both of them in the first equation, the following condition on θ can be found:

$$\theta_{,222} = \left\{ \frac{2\,\mu\,\mu_c\,H}{\beta\,[(\mu+\mu_c)H + \mu\mu_c\,3\,a_3]} \right\} \theta_{,2}. \tag{5.65}$$

Depending on the sign of the coefficient multiplying $\theta_{,2}$, the solution has different forms. In Figure 5.3 this coefficient is depicted as function of the hardening/softening modulus (using the mechanical material properties reported in Table 5.1). If the snapback region is excluded ($H < -\dfrac{3\,\mu\mu_c\,a_3}{\mu+\mu_c} \approx -2.3 \cdot 10^5$), the coefficient assumes the same sign as the plastic hardening modulus, therefore we can identify different families of solutions based on the values of H. The most interesting condition for our investigation, however, is the one in which the material experiences a softening behavior, which is introduced in order to simulate thermal softening occurring in the material during manufacturing operations. It is already well known that the classical plasticity theory, combined with softening plastic behavior, is characterized by a spurious mesh dependency, whereas the strain gradient theory, or the Cosserat theory in this case, regularizes the localization. In Figure 5.4 the difference in terms of cumulative plastic strain can be appreciated from the numerical simulation. For this reason, in this section (first set of boundary condition) we will focus on the softening behavior, and we will investigate over the analytical solution of the fields in this specific case.

5.2.3 Softening, H<0: localization of deformation.

In case a softening behavior is assigned to the material, the coefficient multiplying $\theta_{,2}$ in Eq. (5.65) is negative, and the Equation can be re-written as:

$$\theta_{,222} = \left\{ \frac{2\,\mu\,\mu_c\,H}{\beta\,[(\mu+\mu_c)H + \mu\mu_c\,3\,a_3]} \right\} \theta_{,2} = -\left\{ -\frac{2\,\mu\,\mu_c\,H}{\beta\,[(\mu+\mu_c)H + \mu\mu_c\,3\,a_3]} \right\} \theta_{,2} = -\omega_p^2\,\theta_{,2}, \tag{5.66}$$

where ω_p is the inverse of the plastic length associated with the plastic zone. Given the negativity of the coefficient multiplying $\theta_{,2}$, the solutions of the differential equations in the plastic domain are based on sine/cosine functions:

$$\begin{cases} \theta_P(y) = F\,\cos(\omega_p\,y) + G\,\sin(\omega_p\,y) + I \\ u_P(y) = -\left[\dfrac{2\,\mu_c + \beta\,\omega_p^2}{\omega_p\,\mu_c} \right] [F\,\sin(\omega_p\,y) - G\,\cos(\omega_p\,y)] - 2\,I\,y + M \\ p(y) = \left[\dfrac{\mu\sqrt{3\,a_3}}{\mu 3\,a_3 + H} \right] \left[\dfrac{2\,\mu_c + \beta\,\omega_p^2}{\mu_c} \right] [F\,\cos(\omega_p\,y) + G\,\sin(\omega_p\,y)] \\ \qquad\qquad + \dfrac{2\,\mu\sqrt{3\,a_3}}{\mu 3\,a_3 + H} I - \dfrac{R_0}{3\,\mu\,a_3 + H} \end{cases} \tag{5.67}$$

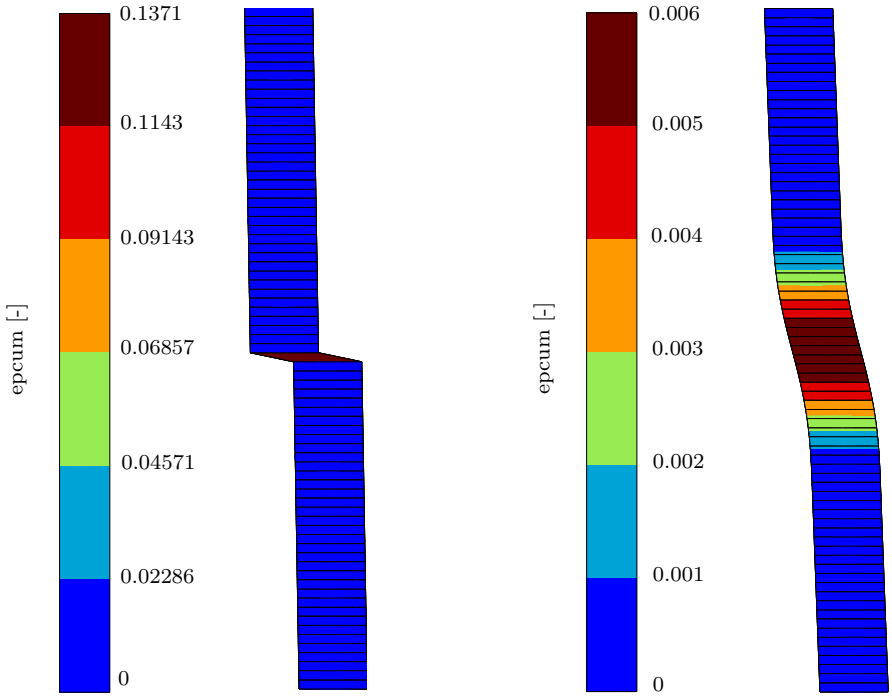

(a) Classical. (b) Cosserat.

Figure 5.4: Numerical solutions of the plastic field distribution for the classical and the Cosserat model using the softening plastic behavior.

In which case, the total system of differential equations to be solved is (once again we divide the problem into three domains as in Figure 5.2):

$$\text{Top Elastic} \begin{cases} \theta_T(y) = A\,\cosh(\omega_e\,y) + B\,\sinh(\omega_e\,y) + C \\ u_T(y) = -\dfrac{2\,\mu_c}{(\mu+\mu_c)\,\omega_e}\,[A\,\sinh(\omega_e\,y) + B\,\cosh(\omega_e\,y)] - 2\,C\,y + E \end{cases} \tag{5.68}$$

$$\text{Center Plastic} \begin{cases} \theta_P(y) = F\,\cos\left(\omega_p\,y\right) + G\,\sin\left(\omega_p\,y\right) + I \\ u_P(y) = -\left[\dfrac{2\,\mu_c + \beta\,\omega_p^2}{\omega_p\,\mu_c}\right][F\,\sin\left(\omega_p\,y\right) - G\,\cos\left(\omega_p\,y\right)] - 2\,I\,y + M \\ p(y) = \left[\dfrac{\mu\sqrt{3\,a_3}}{\mu 3\,a_3 + H}\right]\left[\dfrac{2\,\mu_c + \beta\,\omega_p^2}{\mu_c}\right][F\,\cos\left(\omega_p\,y\right) + G\,\sin\left(\omega_p\,y\right)] \\ \qquad\qquad + \dfrac{2\,\mu\sqrt{3\,a_3}}{\mu 3\,a_3 + H}\,I - \dfrac{R_0}{3\,\mu\,a_3 + H} \end{cases} \tag{5.69}$$

$$\text{Bottom Elastic} \begin{cases} \theta_B(y) = Q\,\cosh(\omega_e\,y) + R\,\sinh(\omega_e\,y) + S \\ u_B(y) = -\dfrac{2\,\mu_c}{(\mu+\mu_c)\,\omega_e}\,[Q\,\sinh(\omega_e\,y) + R\,\cosh(\omega_e\,y)] - 2\,S\,y + U \end{cases} \tag{5.70}$$

which must be coupled to the symmetric boundary conditions:

$$\begin{cases} u_T(L) = u_0 \\ t_{c_T}(L) = 0 \\ u_B(-L) = -u_0 \\ t_{c_B}(-L) = 0 \end{cases} \tag{5.71}$$

Given the symmetry of the boundary conditions, we can assume that the solutions are even/odd functions. Therefore, the following conditions can be imposed:

$$\begin{cases} \theta_T(y) = \theta_B(-y) \quad \Longrightarrow \quad [A-Q]\cosh(\omega_e\, y) + [B+R]\sinh(\omega_e\, y) + [C-S] = 0 \\ \theta_T(y) = \theta_T(-y) \quad \Longrightarrow \quad [A-A]\cosh(\omega_e\, y) + [B+B]\sinh(\omega_e\, y) + [C-C] = 0 \\ u_T(y) = -u_B(-y) \quad \Longrightarrow \quad 2\,[C-S]\; y + [E+U] = 0 \\ \theta_P(y) = \theta_P(-y) \quad \Longrightarrow \quad [F-F]\cos(\omega_p\, y) + [G+G]\sin(\omega_p\, y) = 0 \\ u_P(y) = -u_P(-y) \quad \Longrightarrow \quad [M+M] = 0 \\ y_T^p = -y_B^p; \end{cases} \tag{5.72}$$

leading to the following conditions on the coefficients:

- $A = Q$
- $B = R = 0$
- $C = S$
- $E = -U$
- $G = 0$
- $M = 0$
- $y_T^p = -y_B^p = y^0$

and by using such conditions, the number of coefficients reduces, and the system of equations as well:

$$\text{Top Elastic} \begin{cases} \theta_T(y) = A\,\cosh(\omega_e\, y) + C \\ u_T(y) = -\dfrac{2\,\mu_c}{(\mu+\mu_c)\,\omega_e}\,[A\,\sinh(\omega_e\, y)] - 2\,C\,y + E \end{cases} \tag{5.73}$$

$$\text{Center Plastic} \begin{cases} \theta_P(y) = F\,\cos(\omega_p\, y) + I \\ u_P(y) = -\left[\dfrac{2\,\mu_c + \beta\,\omega_p^2}{\omega_p\,\mu_c}\right][F\,\sin(\omega_p\, y)] - 2\,I\,y \\ p(y) = \left[\dfrac{\mu\sqrt{3\,a_3}}{\mu 3\,a_3 + H}\right]\left[\dfrac{2\,\mu_c + \beta\,\omega_p^2}{\mu_c}\right][F\,\cos(\omega_p\, y)] \\ \qquad\qquad + \dfrac{2\,\mu\sqrt{3\,a_3}}{\mu 3\,a_3 + H} I - \dfrac{R_0}{3\,\mu\,a_3 + H} \end{cases} \tag{5.74}$$

$$\text{Bottom Elastic} \begin{cases} \theta_B(y) = A\,\cosh(\omega_e\, y) + C \\ u_B(y) = -\dfrac{2\,\mu_c}{(\mu+\mu_c)\,\omega_e}\,[A\,\sinh(\omega_e\, y)] - 2\,C\,y - E \end{cases} \tag{5.75}$$

Through Equations (5.60) and (5.61), the tractions can be written as:

$$t_T(y) = -2\,C\mu, \tag{5.76}$$

$$t_{c_T}(y) = 2\,\beta\,\omega_e\,[A\,\sinh\,(\omega_e\,y)]\,, \tag{5.77}$$

$$t_P(y) = -2\,I\left[\frac{\mu\,H}{H + 3\,a_3\,\mu}\right] - \frac{\sqrt{3\,a_3}\mu\,R_0}{3\,a_3\mu + H}, \tag{5.78}$$

$$t_{c_P}(y) = -2\,\beta\,\omega_p\,[F\,\sin\,(\omega_p\,y)]\,. \tag{5.79}$$

At this point, the boundary conditions and the continuity of tractions and couple tractions can be applied. The Dirichlet boundary condition is:

$$u_T(L) = u_0, \tag{5.80}$$

the Neumann condition is:

$$t_{c_T}(L) = 0, \tag{5.81}$$

the boundary condition on the equivalent plastic strain is:

$$p(y^0) = 0, \tag{5.82}$$

and the continuity of the fields must be superimposed at the coordinate y^0:

$$u_T(y^0) = u_P(y^0), \tag{5.83}$$

$$\theta_T(y^0) = \theta_P(y^0), \tag{5.84}$$

$$t_T(y^0) = t_P(y^0), \tag{5.85}$$

$$t_{c_T}(y^0) = t_{c_P}(y^0). \tag{5.86}$$

By combing all the conditions, the following system of Equations can be written:

$$\begin{cases} u_T(L) = u_0, & (5.87)\\ t_{c_T}(L) = 0, & (5.88)\\ u_T(y^0) = u_P(y^0), & (5.89)\\ \theta_T(y^0) = \theta_P(y^0), & (5.90)\\ t_T(y^0) = t_P(y^0), & (5.91)\\ t_{c_T}(y^0) = t_{c_P}(y^0), & (5.92)\\ p(y^0) = 0, & (5.93) \end{cases}$$

which is a system of 7 Equations linearly dependent (6 linearly independent), with 6 unknowns (which are the coefficients in the general solutions of the fields in Equations (5.73), (5.74) and (5.75)), and it can be solved numerically in general. The comparison between

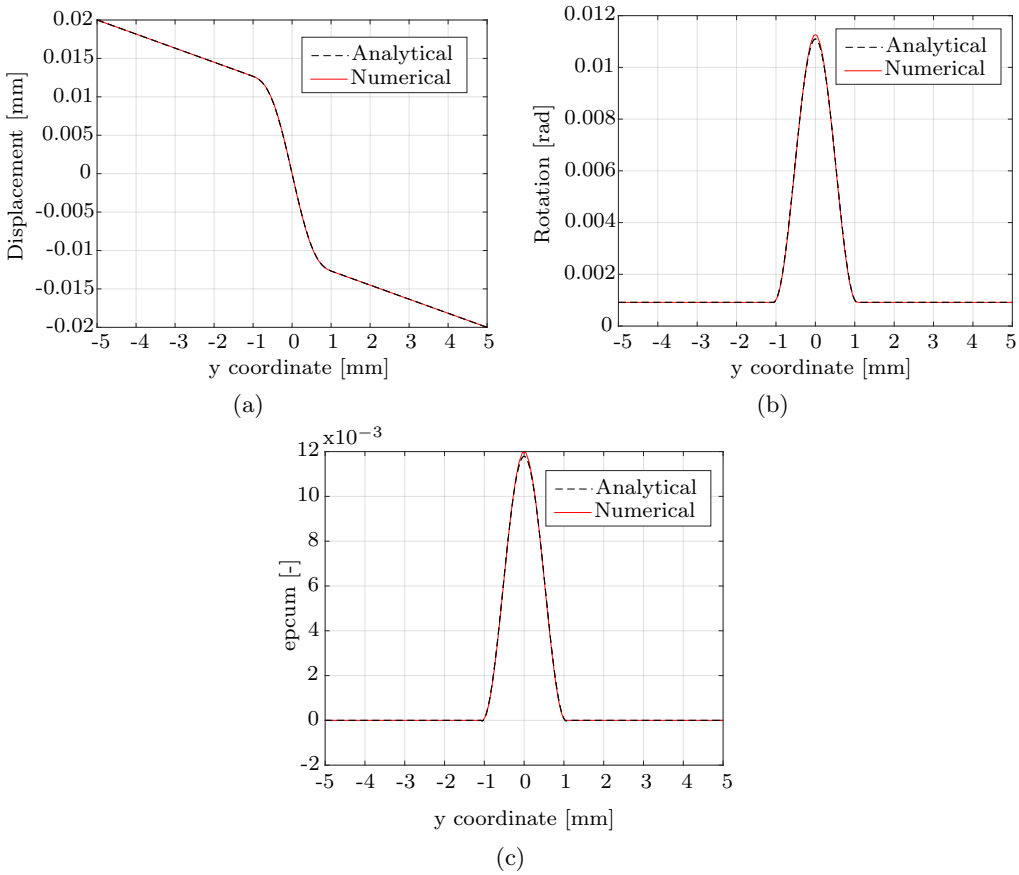

Figure 5.5: Stripe under glide with free rotational boundary conditions. Softening plastic behavior. Material parameters in Table 5.1.

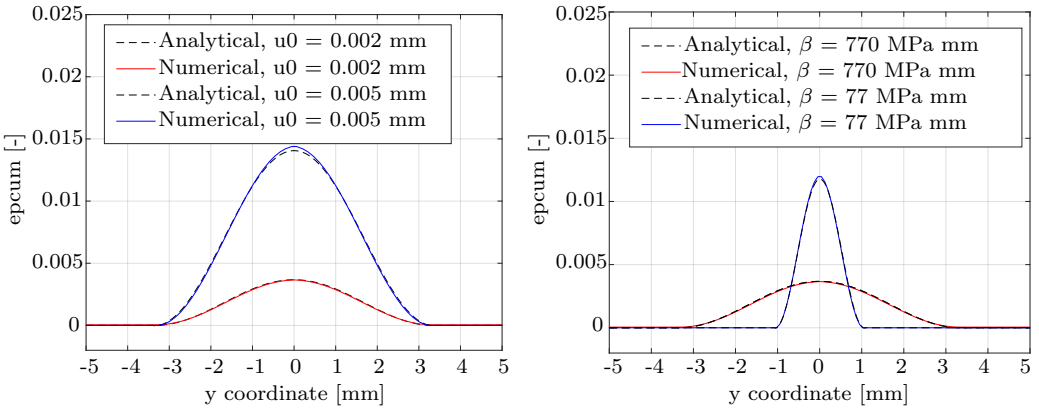

Figure 5.6: Comparison in terms of cumulative plastic strain for the localization case using different applied displacements (a) and different values of β (b). Material parameters in Table 5.1.

analytical and numerical solutions can be found in Figure 5.5, and it can be observed that they match closely. The thickness of the shear band is expected to be invariant with respect to the applied displacement, and in order to verify that this is behavior is correctly captured, two different values of the external applied displacements have been used and the results are reported in Figure 5.6a. As expected, the localization zone does not get broader with an increasing applied displacement. From the analytical solution, the thickness of the shear band for the present analysis can then be evaluated as:

$$l_{ch}^{p} = \frac{2\,\pi}{\omega_p^2} = -\frac{\pi\beta\,[(\mu+\mu_c)H + \mu\mu_c\,3\,a_3]}{\mu\,\mu_c\,H}, \tag{5.94}$$

and it can be observed that the only parameters affecting the size of the localization zone are the ones that can be found in Equation (5.94). The thickness of the shear band is linearly dependent on the couple stress modulus β, therefore, the same localization problem has been studied with different values of β, and the the results can be found in Figure 5.6b. This small demonstration has been done to prove that the thickness of the simulated shear band using the Cosserat media in case of softening material is directly dominated by this additional material parameter, thus it can be straightforwardly calibrated based on the measured shear band during experimental analysis.

5.3 Set 2 of boundary conditions: fixed micro-rotations

This set of boundary conditions can be considered as a modification of the previous one, where an extra constraint is enforced on the Cosserat rotation. It is known from the previous solution that the Cosserat rotation tends to follow the material rotation, but in this section we investigate the solution in case the Cosserat rotation is enforced to be null at the boundaries. Dirichlet boundary conditions were applied to the displacement fields

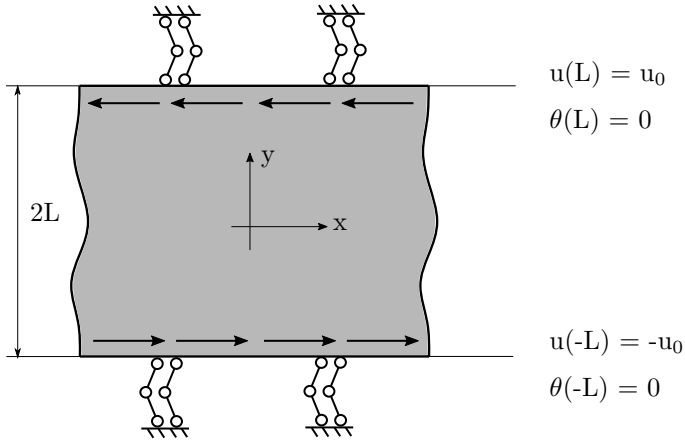

Figure 5.7: Second set of boundary conditions used for the glide test using the Cosserat continuum.

at the top and bottom of the strip, opposite in magnitude:

$$u\,(y = L) = u_0; \tag{5.95}$$
$$u\,(y = -L) = -u_0; \tag{5.96}$$

and Dirichlet boundary conditions were also applied on the micro-rotational fields, and they were set to be null:

$$\theta\,(y = L) = 0; \tag{5.97}$$
$$\theta\,(y = -L) = 0; \tag{5.98}$$

The geometry and the boundary conditions are reported in Figure 5.7.

5.3.1 Elastic behavior with fixed micro-rotations

The general solutions previously found for the first set of boundary conditions holds in this case as well, however, in this case we can particularize the general solutions by applying different sets of boundary conditions. The general solutions in Equations (5.40) and (5.41)are reported here:

$$\theta(y) = A\,\cosh(\omega_e\,y) + B\,\sinh(\omega_e\,y) + C, \tag{5.99}$$
$$u(y) = -\frac{2\,\mu_c}{(\mu + \mu_c)\,\omega_e}\,[A\,\sinh(\omega_e\,y) + B\,\cosh(\omega_e\,y)] - 2\,C\,y + E. \tag{5.100}$$

The particular solution can be found by substituting the general solution into the boundary conditions. By coupling the Dirichlet boundary conditions on θ (Equations (5.97) and (5.98)):

$$B = 0, \tag{5.101}$$
$$A = -\frac{C}{\cosh(\omega_e\,L)}, \tag{5.102}$$

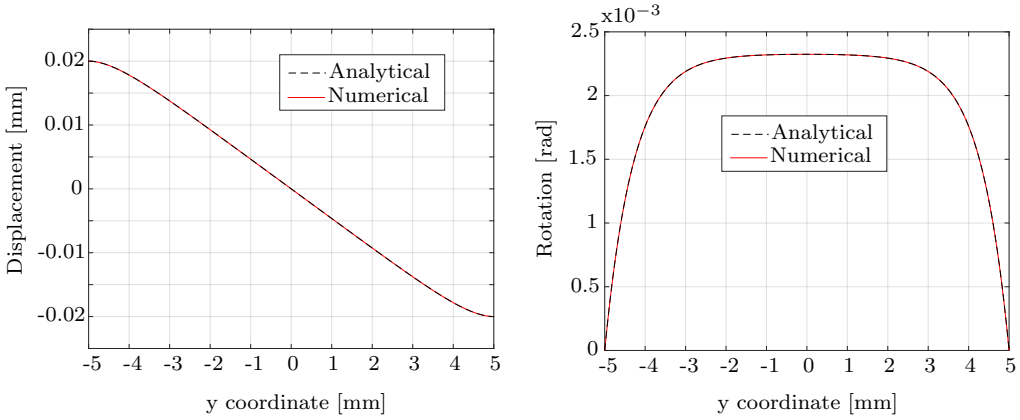

Figure 5.8: Solutions of the field distribution using the fixed-rotation set of boundary conditions and elastic behavior. Comparison with the FEM solution is reported. Mechanical properties in Table 5.2.

then, from the conditions on the displacement fields (Equations (5.95) and (5.96)):

$$E = 0, \tag{5.103}$$

$$C = -\frac{u_0(\mu+\mu_c)\omega_e}{2\left[L\,\omega_e(\mu+\mu_c) - \mu_c\,\tanh(\omega_e L)\right]}. \tag{5.104}$$

Finally, the specific solutions for the imposed set of boundary conditions look like:

$$\theta(y) = -\frac{u_0(\mu+\mu_c)\omega_e}{2\,\left[L\,\omega_e(\mu+\mu_c) - \mu_c\,\tanh(\omega_e L)\right]}\left(1 - \frac{\cosh(\omega_e y)}{\cosh(\omega_e L)}\right), \tag{5.105}$$

$$u(y) = \left\{-\frac{u_0(\mu+\mu_c)\omega_e}{2\,\left[L\omega_e(\mu+\mu_c) - \mu_c\tanh(\omega_e L)\right]}\right\}\left[\frac{2\,\mu_c\sinh(\omega_e y)}{\omega_e(\mu+\mu_c)\cosh\left(\omega_e\,L\right)} - 2\,y\right], \tag{5.106}$$

which are reported in Figure 5.8, alongside the comparison with the FEM solutions. The mechanical properties used for this tests are reported in Table 5.2.

5.3.2 Elasto-plastic behavior with fixed micro-rotations

In the previously investigated case (localization) the first plastic zone could be found at the center of the specimen because it was imposed by us by triggering localization at the center of the specimen. Positioning the shear band somewhere else (as long as it was far from the boundaries) would have not altered anything about the solution inside the plastic domain. In the present case, however, we must first investigate over the location at which the first plastic section would appear. In order to do so, we could increase the loading factor (u_0) until the stress reaches the initial yield value. The maximum value of the Equivalent stress and its position in the domain $y \in [-L; L]$ can be easily found. The first objective would be to find the location in the specimen where the yield condition

Table 5.2: Elasto-plastic material properties used for fixed rotations problem.

E	ν	β	σ_0	H
200000 MPa	0.3	77000 MPa mm^2	250 MPa	0 MPa / $\pm$1000 MPa

will be initially met. This can be achieved by expressing the equivalent stress measure (Equation (5.1)) for the present case, in which $a_4 = b_i = 0$:

$$\sigma_{eq}(y) = \sqrt{\frac{3}{2}}\sqrt{a_3\, 2\left(\frac{\sigma_{12}+\sigma_{21}}{2}\right)^2} = \frac{\sqrt{3\,a_3}}{2}\left|\sigma_{12}+\sigma_{21}\right|. \tag{5.107}$$

The stress tensor is here reported as:

$$\underset{\sim}{\boldsymbol{\sigma}} = \begin{bmatrix} 0 & u_{,2}(\mu+\mu_c)+2\mu_c\,\theta & 0 \\ u_{,2}(\mu-\mu_c)-2\mu_c\,\theta & 0 & 0 \\ 0 & 0 & 0 \end{bmatrix}, \tag{5.108}$$

from which, the equivalent stress measure can be written as:

$$\sigma_{eq}(y) = \pm\sqrt{3\,a_3}\;|u_{,2}|\;\mu, \tag{5.109}$$

and, given the distribution of $u(y)$ depicted in Figure 5.8a, we expect the maximum equivalent stress to be located away from the boundaries (where $u_{,2}$ is null), that is, in the middle of the specimen. Given the hyperbolic cosine distribution of the equivalent stress, and given the fact that the function is concave, we know that the maximum will occur at the location $y = 0$, thus we can analyze the equivalent stress measure as function of the loading factor u_0 to identify the exact load for which the plastic condition is met for the first time. Given the following yield criterion:

$$f(\sigma_{eq}, R) = \sigma_{eq} - R = 0, \tag{5.110}$$

where R is the radius of the yield surface, we can superimpose that this criterion is met, while solving for the loading factor, that is, u_0:

$$\sigma_{eq}(y=0) = \sqrt{3\,a_3}\mu\left|u_0\left[-\frac{\omega_e}{2\,\cosh(\omega_e L)\,(L\omega_e - \tanh(\omega_e L))} + \frac{1}{2L}\left(1+\frac{\tanh(\omega_e L)}{\omega_e L + \tanh(\omega_e L)}\right)\right]\right| = R, \tag{5.111}$$

and, considering that the yield stress is the initial one, the first plastic development should take place for the following loading value:

$$u_0 = \pm\frac{R_0}{\mu\,\sqrt{3\,a_3}\left[-\frac{\omega_e}{2\,\cosh(\omega_e L)\,(L\omega_e - \tanh(\omega_e L))} + \frac{1}{2L}\left(1+\frac{\tanh(\omega_e L)}{\omega_e L + \tanh(\omega_e L)}\right)\right]}, \tag{5.112}$$

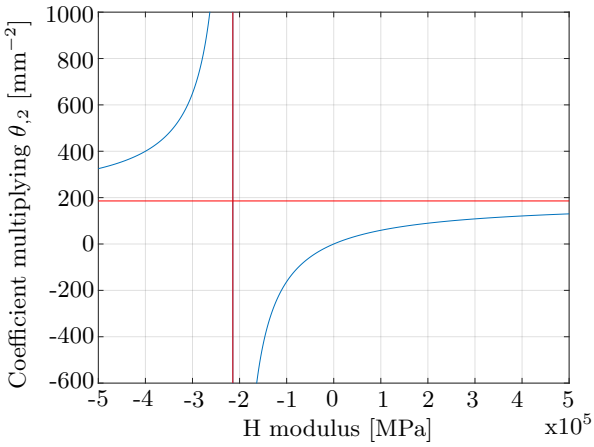

Figure 5.9: Value of the Coefficient multiplying $\theta_{,2}$ in Equation (5.65) computed by using the mechanical properties resumed in Table 5.2.

Therefore, as in the previous case, it is expected that the domain is divided into top-bottom elastic parts and central plastic zone, as in Figure 5.2. The analytical solutions in the plastic domain still obey the differential equation (5.65), which is here reported:

$$\theta_{,222} = \left\{ \frac{2\,\mu\,\mu_c\,H}{\beta\,[(\mu+\mu_c)H + \mu\mu_c\,3\,a_3]} \right\} \theta_{,2}; \tag{5.113}$$

and, once again, the type of solution depends on the sign of this coefficient. In Figure 5.9 the coefficient has been pictured as function of the H value by using the mechanical properties listed in Table 5.2. Depending on the choice of the hardening modulus H, different families of solutions can be found.

5.3.3 Perfect plasticity, H=0

In case of perfectly plastic behavior, the balance equations, together with the yield condition, can be written as:

$$\begin{cases} u_{,22}[\mu+\mu_c] + 2\,\mu_c\theta_{,2} = -\mu p_{,2}\sqrt{3\,a_3}; \\ 2\,\mu_c u_{,2} + 4\,\mu_c\theta = 2\,\beta\theta_{,22}; \\ 2\,\mu u_{,2} + 2\,\mu\,p\sqrt{3\,a_3} = -\dfrac{2\,R_0}{\sqrt{3\,a_3}}; \end{cases} \tag{5.114}$$

these equations can be solved by deriving the second one and the third one with respect to y, then, by plugging them into the first one, the result is:

$$\theta_{,222} = 0; \tag{5.115}$$

which means that the we can simply derive the general solution of the rotational field. Together with the other differential equations, we are able to write the general solution for $u(y), \theta(y)$ and $p(y)$ in the plastic zone as:

$$\text{Perfect Plasticity} \quad \begin{cases} \theta_P(y) = F\,y^2 + G\,y + I; \\ u_P(y) = -\dfrac{2\,F}{3}\,y^3 - G\,y^2 + y\left[\dfrac{2\,\beta\,F}{\mu_c} - 2\,I\right] + M; \\ p(y) = \dfrac{2}{\sqrt{3\,a_3}}\left[F\,y^2 + G\,y - \dfrac{\beta\,F}{\mu_c} + I\right] - \dfrac{R_0}{3\,\mu\,a_3}; \end{cases} \tag{5.116}$$

The governing equations for the plastic domain must be coupled with the one that are valid in the elastic domain (see Figure 5.2). The system of differential equations in the end will look like:

$$\text{Top Elastic} \begin{cases} \theta_T(y) = A\,\cosh(\omega_e\,y) + B\,\sinh(\omega_e\,y) + C; \\ u_T(y) = -\dfrac{2\,\mu_c}{(\mu+\mu_c)\,\omega_e}\left[A\,\sinh(\omega_e\,y) + B\,\cosh(\omega_e\,y)\right] - 2\,C\,y + E; \end{cases} \tag{5.117}$$

$$\text{Center Plastic} \begin{cases} \theta_P(y) = F\,y^2 + G\,y + I; \\ u_P(y) = -\dfrac{2\,F}{3}\,y^3 - G\,y^2 + y\left[\dfrac{2\,\beta\,F}{\mu_c} - 2\,I\right] + M; \\ p(y) = \dfrac{2}{\sqrt{3\,a_3}}\left[F\,y^2 + G\,y - \dfrac{\beta\,F}{\mu_c} + I\right] - \dfrac{R_0}{3\,\mu\,a_3}; \end{cases} \tag{5.118}$$

$$\text{Bottom Elastic} \begin{cases} \theta_B(y) = N\,\cosh(\omega_e\,y) + Q\,\sinh(\omega_e\,y) + R; \\ u_B(y) = -\dfrac{2\,\mu_c}{(\mu+\mu_c)\,\omega_e}\left[N\,\sinh(\omega_e\,y) + Q\,\cosh(\omega_e\,y)\right] - 2\,R\,y + T; \end{cases} \tag{5.119}$$

which must be coupled with the following symmetric boundary conditions:

$$\begin{cases} u_T(L) = u_0; \\ \theta_T(L) = 0; \\ u_B(-L) = -u_0; \\ \theta_B(-L) = 0; \end{cases} \tag{5.120}$$

which will allow us to assume that the solutions are even/odd functions:

$$\begin{cases} \theta_T(y) = \theta_B(-y) \quad \Longrightarrow \quad [A - N]\cosh(\omega_e\, y) + [B + Q]\sinh(\omega_e\, y) + [C - R] = 0; \\ \theta_T(y) = \theta_T(-y) \quad \Longrightarrow \quad [A - A]\cosh(\omega_e\, y) + [B + B]\sinh(\omega_e\, y) + [C - C] = 0; \\ u_T(y) = -u_B(-y) \quad \Longrightarrow \quad -2\,[C - C]\; y + [E + T] = 0; \\ \theta_P(y) = \theta_P(-y) \quad \Longrightarrow \quad [F - F]\; y^2 + [G + G]\; y + [I - I] = 0; \\ u_P(y) = -u_P(-y) \quad \Longrightarrow \quad \dfrac{2}{3} y^3\,[F - F] - y^2\,[G + G] + [M + M] \\ \qquad\qquad\qquad\qquad + 2\,y\left[\dfrac{\beta\, F}{\mu_c} - I - \dfrac{\beta\, F}{\mu_c} + I\right] = 0; \\ y_T^p = -y_B^p = y^0; \end{cases} \tag{5.121}$$

thus producing the following constraints:

- $A = N$
- $B = Q = 0$
- $C = R$
- $E = -T$
- $G = 0$
- $M = 0$
- $y_T^p = -y_B^p = y^0$

that simplifies the system of equations in the following:

$$\text{Top Elastic} \begin{cases} \theta_T(y) = A\,\cosh(\omega_e\, y) + C; \\ u_T(y) = -\dfrac{2\,\mu_c}{(\mu + \mu_c)\,\omega_e}\,[A\,\sinh(\omega_e\, y)] - 2\,C\,y + E; \end{cases} \tag{5.122}$$

$$\text{Center Plastic} \begin{cases} \theta_P(y) = F\, y^2 + I; \\ u_P(y) = -\dfrac{2\,F}{3}\, y^3 + y\left[\dfrac{2\,\beta\, F}{\mu_c} - 2\,I\right]; \\ p(y) = \dfrac{2}{\sqrt{3\,a_3}}\left[F\, y^2 - \dfrac{\beta\, F}{\mu_c} + I\right] - \dfrac{R_0}{3\,\mu\, a_3}; \end{cases} \tag{5.123}$$

$$\text{Bottom Elastic} \begin{cases} \theta_B(y) = A\,\cosh(\omega_e\, y) + C; \\ u_B(y) = -\dfrac{2\,\mu_c}{(\mu + \mu_c)\,\omega_e}\,[A\,\sinh(\omega_e\, y)] - 2\,C\,y - E; \end{cases} \tag{5.124}$$

which contains 6 unknowns to be found. The tractions in the elastic and plastic zones

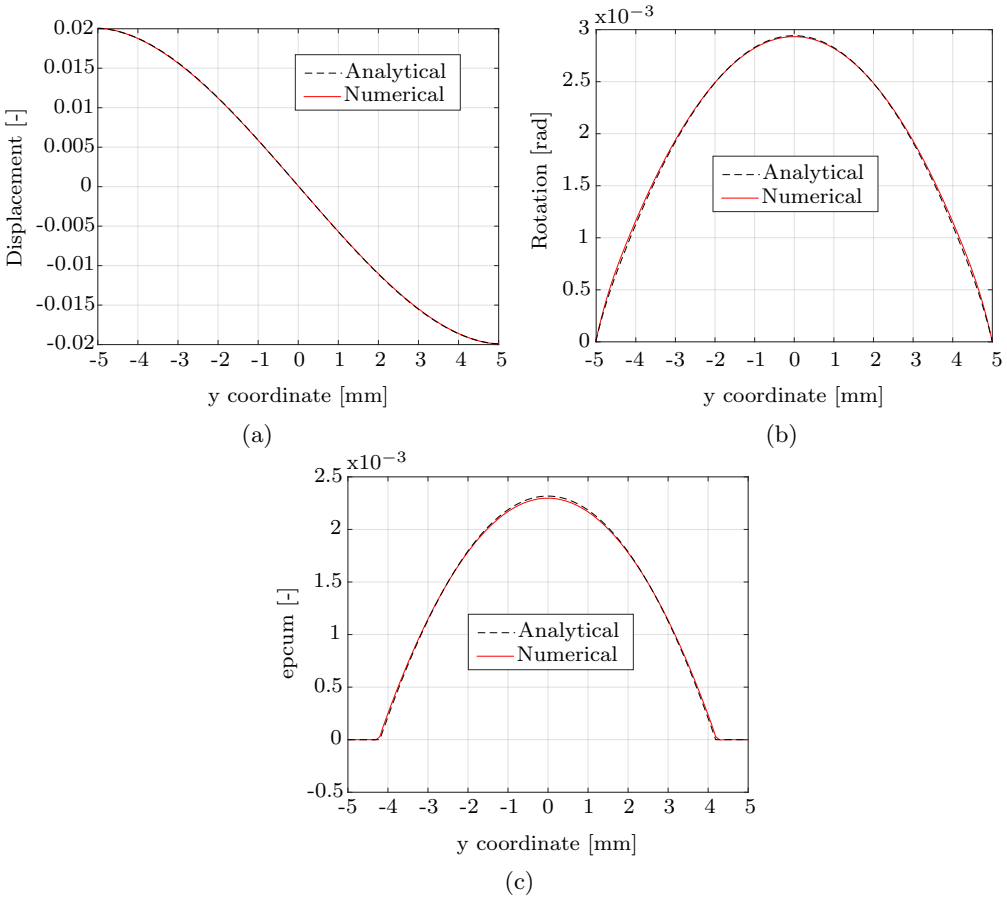

Figure 5.10: Stripe under glide with fixed rotational boundary conditions. Perfectly plastic behavior. Mechanical properties resumed in Table 5.2

are:

$$t_T(y) = -2\,\mu\,C; \tag{5.125}$$

$$t_{c_T}(y) = 2\,\beta\,\omega_e\,[A\,\sinh\,(\omega_e\,y)]\,; \tag{5.126}$$

$$t_P(y) = -\frac{R_0}{\sqrt{3}\,a_3}; \tag{5.127}$$

$$t_{c_P}(y) = 4\,\beta\,F\,y; \tag{5.128}$$

The system can be solved by imposing the Dirichlet boundary conditions (Equations (8.19d) and (8.19d)) coupled with the continuity condition of the displacements,micro-rotations, tractions and couple tractions at the elasto-plastic interface, that is y^0. The system can be solved numerically, leading to the semi-analytical solution that can be appreciated in

Figure 5.10.

5.3.4 Softening, H<0

The general solutions for the governing equations in case of softening have already been derived (Equations (5.73), (5.74) and (5.75)), and after the application of the symmetry condition of the solution, the fields for the top, center and bottom domains are:

$$\text{Top Elastic} \begin{cases} \theta_T(y) = A\,\cosh(\omega_e\,y) + C \\ u_T(y) = -\dfrac{2\,\mu_c}{(\mu+\mu_c)\,\omega_e}\,[A\,\sinh(\omega_e\,y)] - 2\,C\,y + E \end{cases} \tag{5.129}$$

$$\text{Center Plastic} \begin{cases} \theta_P(y) = F\,\cos\left(\omega_p\,y\right) + I \\ u_P(y) = -\left[\dfrac{2\,\mu_c + \beta\,\omega_p^2}{\omega_p\,\mu_c}\right]\,[F\,\sin\left(\omega_p\,y\right)] - 2\,I\,y \\ p(y) = \left[\dfrac{\mu\sqrt{3\,a_3}}{\mu 3\,a_3 + H}\right]\left[\dfrac{2\,\mu_c + \beta\,\omega_p^2}{\mu_c}\right]\,[F\,\cos\left(\omega_p\,y\right)] \\ \qquad\qquad + \dfrac{2\,\mu\sqrt{3\,a_3}}{\mu 3\,a_3 + H} I - \dfrac{R_0}{3\,\mu\,a_3 + H} \end{cases} \tag{5.130}$$

$$\text{Bottom Elastic} \begin{cases} \theta_B(y) = A\,\cosh(\omega_e\,y) + C \\ u_B(y) = -\dfrac{2\,\mu_c}{(\mu+\mu_c)\,\omega_e}\,[A\,\sinh(\omega_e\,y)] - 2\,C\,y - E \end{cases} \tag{5.131}$$

Through Equations (5.30) and (5.31), the tractions can be written as:

$$t_T(y) = -2\,C\mu, \tag{5.132}$$

$$t_{c_T}(y) = 2\,\beta\,\omega_e\,[A\,\sinh\left(\omega_e\,y\right)], \tag{5.133}$$

$$t_P(y) = -2\,I\left[\frac{\mu\,H}{H + 3\,a_3\,\mu}\right] - \frac{\sqrt{3\,a_3}\mu\,R_0}{3\,a_3\mu + H}, \tag{5.134}$$

$$t_{c_P}(y) = -2\,\beta\,\omega_p\,[F\,\sin\left(\omega_p\,y\right)]. \tag{5.135}$$

The application of the boundary conditions and the continuity conditions will be used to find the 6 unknown coefficients. The system has been solved numerically. The comparison between analytical and numerical solution can be found in Figure 5.11.

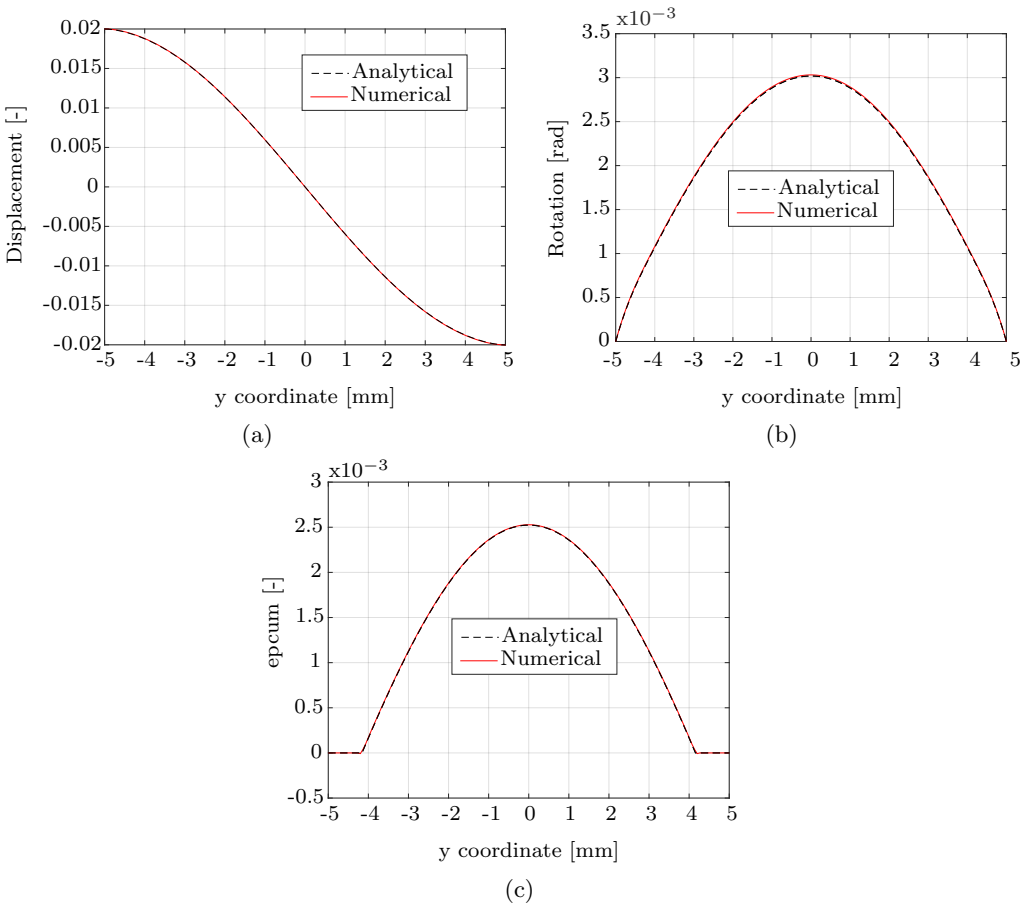

Figure 5.11: Stripe under glide with fixed rotational boundary conditions. Softening plastic behavior. Mechanical properties resumed in Table 5.2

5.3.5 Hardening, H>0

Assuming that the plastic modulus is positive, the following solutions are obtained:

$$\text{Hardening} \quad \begin{cases} \theta_P(y) = F\,\cosh(\omega_p\,y) + G\,\sinh(\omega_p\,y) + I, \\ u_P(y) = \dfrac{-2\,\mu_c + \beta\omega_p^2}{\omega_p \mu_c}\,[F\sinh(\omega_p\,y) + G\cosh(\omega_p\,y)] - 2\,I\,y + M, \\ p(y) = -\left[\dfrac{\mu\sqrt{3\,a_3}}{3\,\mu\,a_3 + H}\right]\left[\left(\dfrac{-2\,\mu_c + \beta\omega_p^2}{\mu_c}\right)(F\cosh(\omega_p\,y) + G\sinh(\omega_p\,y))\right] \\ \qquad\qquad - \dfrac{2\,I\,\mu\sqrt{3\,a_3}}{3\,\mu\,a_3 + H} - \dfrac{R_0}{3\,a\,\mu + H}. \end{cases} \tag{5.136}$$

The field Equations of the degrees of freedom for the three domains are the followings:

$$\text{Top Elastic} \quad \begin{cases} \theta_T(y) = A\,\cosh(\omega_e\,y) + B\,\sinh(\omega_e\,y) + C, \\ u_T(y) = -\dfrac{2\,\mu_c}{(\mu + \mu_c)\,\omega_e}\,[A\,\sinh(\omega_e\,y) + B\,\cosh(\omega_e\,y)] - 2\,C\,y + E, \end{cases} \tag{5.137}$$

$$\text{Center Plastic} \quad \begin{cases} \theta_P(y) = F\,\cosh(\omega_p\,y) + G\,\sinh(\omega_p\,y) + I, \\ u_P(y) = \dfrac{-2\,\mu_c + \beta\omega_p^2}{\omega_p \mu_c}\,[F\sinh(\omega_p\,y) + G\cosh(\omega_p\,y)] - 2\,I\,y + M, \\ p(y) = -\left[\dfrac{\mu\sqrt{3\,a_3}}{3\,\mu\,a_3 + H}\right]\left[\left(\dfrac{-2\,\mu_c + \beta\omega_p^2}{\mu_c}\right)(F\cosh(\omega_p\,y) + G\sinh(\omega_p\,y))\right] \\ \qquad\qquad - \dfrac{2\,I\,\mu\sqrt{3\,a_3}}{3\,\mu\,a_3 + H} - \dfrac{R_0}{3\,a\,\mu + H}, \end{cases} \tag{5.138}$$

$$\text{Bottom Elastic} \quad \begin{cases} \theta_B(y) = Q\,\cosh(\omega_e\,y) + R\,\sinh(\omega_e\,y) + S, \\ u_B(y) = -\dfrac{2\,\mu_c}{(\mu + \mu_c)\,\omega_e}\,[Q\,\sinh(\omega_e\,y) + R\,\cosh(\omega_e\,y)] - 2\,S\,y + U. \end{cases} \tag{5.139}$$

Dirichlet boundary conditions are applied on the displacement field:

$$u(L) = u_0, \tag{5.140}$$
$$u(-L) = -u_0, \tag{5.141}$$

and on the micro-rotational field:

$$\theta(L) = 0, \tag{5.142}$$
$$\theta(-L) = 0, \tag{5.143}$$

The symmetric boundary conditions allow us to assume that the solutions are even/odd functions:

$$\begin{cases} \theta_T(y) = \theta_B(-y) \quad \Longrightarrow \quad [A-Q]\cosh(\omega_e\, y) + [B+R]\sinh(\omega_e\, y) + [C-S] = 0, \\ \theta_T(y) = \theta_T(-y) \quad \Longrightarrow \quad [A-A]\cosh(\omega_e\, y) + [B+B]\sinh(\omega_e\, y) + [C-C] = 0, \\ u_T(y) = -u_B(-y) \quad \Longrightarrow \quad [D-T]\; y + [E+U] = 0, \\ \theta_P(y) = \theta_P(-y) \quad \Longrightarrow \quad [F-F]\cosh(\omega_p\, y) + [G+G]\sinh(\omega_p\, y) + [I-I] = 0, \\ u_P(y) = -u_P(-y) \quad \Longrightarrow \quad \dfrac{-2\,\mu_c + \beta\omega_p^2}{\omega_p \mu_c}\,[F-F]\sinh(\omega_p\, y) + [M-M]\; y + [N+N] = 0, \\ y_T^p = -y_B^p = y^0, \end{cases} \tag{5.144}$$

thus producing the following constraints:

- $A = Q$
- $B = R = 0$
- $C = S$
- $E = -U$
- $G = 0$
- $M = 0$
- $y_T^p = -y_B^p = y^0$

therefore the simplified field Equations will look like:

$$\begin{cases} \theta_T(y) = A\,\cosh(\omega_e\, y) + C, \\ u_T(y) = -\dfrac{2\,\mu_c}{(\mu+\mu_c)\,\omega_e}\,[A\,\sinh(\omega_e\, y)] + D\, y + E, \end{cases} \tag{5.145}$$

$$\begin{cases} \theta_P(y) = F\,\cosh(\omega_p\, y) + I, \\ u_P(y) = \dfrac{-2\,\mu_c + \beta\omega_p^2}{\omega_p \mu_c}\,[F\sinh(\omega_p\, y)] - 2\, I\, y, \\ p(y) = -\left[\dfrac{\mu\sqrt{3\,a_3}}{3\,\mu\,a_3 + H}\right]\left[\left(\dfrac{-2\,\mu_c + \beta\omega_p^2}{\mu_c}\right)(F\cosh(\omega_p\, y)) - 2\, I\right] - \dfrac{R_0}{3\,a\,\mu + H}, \end{cases} \tag{5.146}$$

$$\begin{cases} \theta_B(y) = A\,\cosh(\omega_e\, y) - B\,\sinh(\omega_e\, y) + C, \\ u_B(y) = -\dfrac{2\,\mu_c}{(\mu+\mu_c)\,\omega_e}\,[A\,\sinh(\omega_e\, y) - B\,\cosh(\omega_e\, y)] + D\, y - E, \end{cases} \tag{5.147}$$

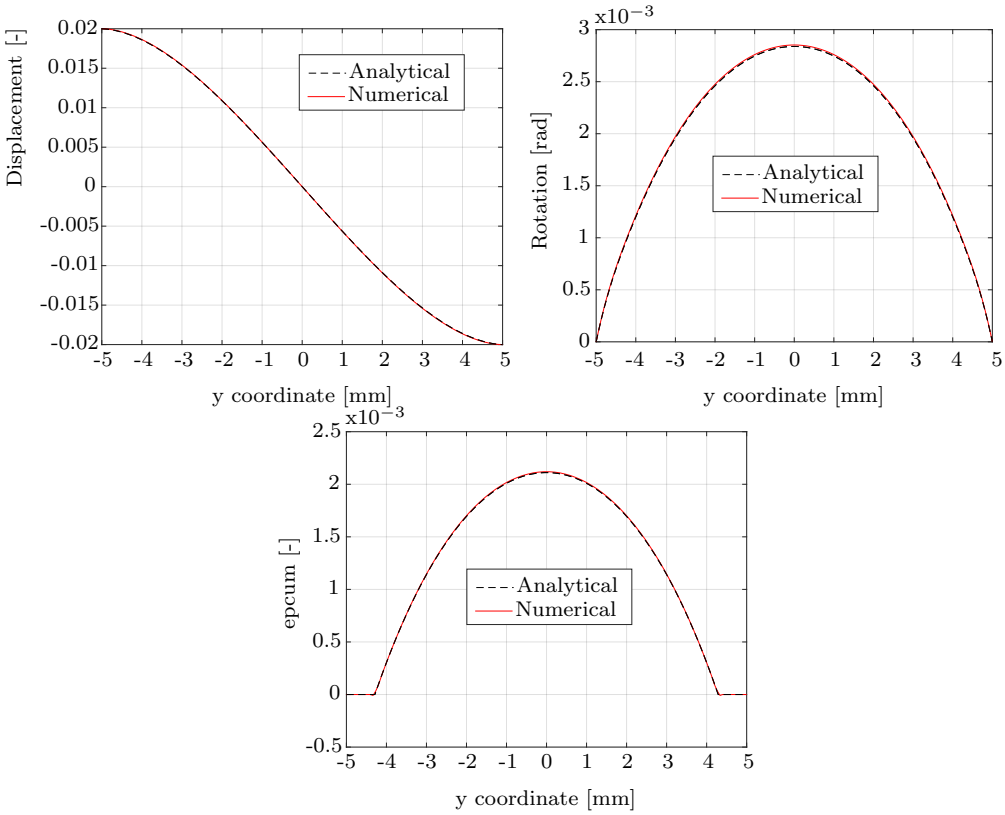

Figure 5.12: Stripe under glide with fixed rotational boundary conditions. Hardening plastic behavior.

and the tractions:

$$t_T(y) = -2\,\mu\,C, \tag{5.148}$$

$$t_{c_T}(y) = 2\,\beta\,\omega_e\,[A\,\sinh(\omega_e\,y) + B\cosh(\omega_e\,y)]\,, \tag{5.149}$$

$$t_P(y) = -2\,I\left[\frac{\mu\,H}{H + 3\,a_3\,\mu}\right] - \frac{\sqrt{3\,a_3}\mu\,R_0}{3\,a_3\mu + H}, \tag{5.150}$$

$$t_{c_P}(y) = 2\,\beta\,\omega_p\,[F\,\sinh(\omega_p\,y)]\,. \tag{5.151}$$

The application of the boundary conditions and of the continuity conditions at the coordinate y^0 will allow us to derive the exact values of the 6 unknowns. The system can be solved numerically with a Newton-Raphson algorithm. The solution can be found in Figure 5.12.

5.4 Choice of the mechanical properties.

Two sets of mechanical properties have been used to plot the fields in the previous cases, each for a different set of boundary condition. The mechanical properties used for the first case (free micro-rotation) are:

E	ν	β	σ_0	H
200000 MPa	0.3	77 MPa mm^2	250 MPa	0 MPa / $\pm$1000 MPa

whereas, for the second set of boundary conditions (fixed micro-rotation), the following material properties have been used:

E	ν	β	σ_0	H
200000 MPa	0.3	77000 MPa mm^2	250 MPa	0 MPa / $\pm$1000 MPa

We can appreciate that the Poisson ratio and the Young modulus are chosen to be reasonable values for the metal alloys. The yield stress has been chosen to be large enough to avoid negative yield stress in case of linear softening behavior. The hardening modulus has been assumed to be positive, null and negative in order to investigate the three different families of solutions for the fields in the plastic domain. The only difference among the two sets of mechanical properties is represented by the choice of the higher order modulus β. The elastic and plastic solutions are directly influenced by this modulus:

$$\omega_e^2 = \frac{2\,\mu\mu_c}{\beta(\mu+\mu_c)}, \tag{5.152}$$

$$\omega_p^2 = \pm\frac{2\,\mu\,\mu_c\,H}{\beta\,[(\mu+\mu_c)H+\mu\mu_c\,3\,a_3]}, \tag{5.153}$$

therefore choosing a value for β is equivalent to choosing a specific value for the characteristic lengths as well. In Section 5.2 our objectives were to induce a localization of the equivalent plastic strain and to control the thickness of the shear band through the choice of β; the thickness of the shear band (Equation (5.94)) is here reported:

$$l_{ch}^p = \frac{2\,\pi}{\omega_p^2} = -\frac{\pi\beta\,[(\mu+\mu_c)H+\mu\mu_c\,3\,a_3]}{\mu\,\mu_c\,H}. \tag{5.154}$$

Therefore, we chose β in order to obtain a shear band thickness that was large enough to be observable, but smaller that the domain length $2\,L$. In the second set of boundary conditions, if we simply consider an elastic medium, the restriction on the micro-rotation to be null at the boundaries induces a deviation from the solutions of the first set of boundary conditions (Equations (5.49) and (5.49)); in the latter, the expected micro-rotational field is constant. The distance from the boundary required for the micro-rotational field to recover a constant value is inversely dependent on ω_e (see Figure 5.8b):

$$l_{ch}^e \propto \frac{1}{\omega_e^2}. \tag{5.155}$$

However, for the specific material properties that we used in the free-micro rotations case, l_{ch}^{e} is much smaller than l_{ch}^{p}. Therefore, if the the same value of β (77 MPa mm^2) was used also for the second set of boundary conditions, the distance required for the solution to retrieve a constant value would be too small. In order to emphasize the effect of the restrictions on the micro-rotation, a larger value of the modulus β has been used for the second set of boundary conditions (77000 MPa mm^2).

5.5 Summary of the Analytical Solutions

Here the general solution (prior to the application o the boundary condition) to the boundary value problems are reported.

$$\text{Elastic} \begin{cases} \theta(y) = A\,\cosh(\omega_e\,y) + B\,\sinh(\omega_e\,y) + C; \\ u(y) = -\dfrac{2\,\mu_c}{(\mu+\mu_c)\,\omega_e}\left[A\,\sinh(\omega_e\,y) + B\,\cosh(\omega_e\,y)\right] - 2\,I\,y + E; \end{cases} \tag{5.156}$$

$$\text{Softening} \begin{cases} \theta_P(y) = F\,\cos\left(\omega_p\,y\right) + I \\ u_P(y) = -\left[\dfrac{2\,\mu_c + \beta\,\omega_p^2}{\omega_p\,\mu_c}\right]\left[F\,\sin\left(\omega_p\,y\right)\right] - 2\,I\,y \\ p(y) = \left[\dfrac{\mu\sqrt{3\,a_3}}{\mu 3\,a_3 + H}\right]\left[\dfrac{2\,\mu_c + \beta\,\omega_p^2}{\mu_c}\right]\left[F\,\cos\left(\omega_p\,y\right)\right] \\ \qquad\qquad + \dfrac{2\,\mu\sqrt{3\,a_3}}{\mu 3\,a_3 + H} I - \dfrac{R_0}{3\,\mu\,a_3 + H} \end{cases} \tag{5.157}$$

$$\text{Hardening} \begin{cases} \theta_P(y) = F\,\cosh\left(\omega_p\,y\right) + G\,\sinh\left(\omega_p\,y\right) + I, \\ u_P(y) = \dfrac{-2\,\mu_c + \beta\omega_p^2}{\omega_p\mu_c}\left[F\sinh\left(\omega_p\,y\right) + G\cosh\left(\omega_p\,y\right)\right] - 2\,I\,y + M, \\ p(y) = -\left[\dfrac{\mu\sqrt{3\,a_3}}{3\,\mu\,a_3 + H}\right]\left[\left(\dfrac{-2\,\mu_c + \beta\omega_p^2}{\mu_c}\right)\left(F\cosh\left(\omega_p\,y\right) + G\sinh\left(\omega_p\,y\right)\right)\right] \\ \qquad\qquad - \dfrac{2\,I\,\mu\sqrt{3\,a_3}}{3\,\mu\,a_3 + H} - \dfrac{R_0}{3\,a\,\mu + H}. \end{cases} \tag{5.158}$$

$$\text{Perfect Plasticity} \quad \begin{cases} \theta_P(y) = F\,y^2 + G\,y + I; \\ u_P(y) = -\dfrac{2\,F}{3}\,y^3 - G\,y^2 + y\left[\dfrac{2\,\beta\,F}{\mu_c} - 2\,I\right] + M; \\ p(y) = \dfrac{2}{\sqrt{3\,a_3}}\left[F\,y^2 + G\,y - \dfrac{\beta\,F}{\mu_c} + I\right] - \dfrac{R_0}{3\,\mu\,a_3}; \end{cases} \tag{5.159}$$

Chapter 6

Large deformation Cosserat thermomechanics

This chapter presents the theoretical aspects of the Cosserat theory under a Finite Deformation assumption. Whenever deformations are considered as finite, all the simplifications relative to the infinitesimal displacement fall and various descriptions of the continuum can be used, depending on the final application. The main feature in which the Cosserat theory differs from the standard finite deformation theories is the micro-rotation, which, as the deformations, also requires proper handling when the rotations are not infinitesimal anymore. For this reason, the first section of this chapter dwells on the description of finite rotations. The full thermodynamically compatible Cosserat theory under large deformations will be presented through increasing levels of complexity, until the full treatment is reached. Sections 6.2 and 6.3 present the kinematics and the balance laws of the Cosserat media under large deformations. The purely elastic behavior of the Cosserat continuum is introduced in Section 6.4 through the definition of an hyper-elastic potential, such as to propose a potentials-derived general theory, whereas the visco-plastic and elasto-plastic behaviors is detailed in Sections 6.5 and 6.6. In this report, the free energy potential associated with the curvature has been taken from the simplified version proposed by Neff [Neff 2004; Neff 2006]. Both Plastic and visco-plastic models are proposed in this report. For the visco-plastic model, the general visco-plastic potential as originally proposed by Chaboche has been used [J. L. Chaboche 2008]. The yield functions employ a linear hardening combined with a double exponential curves. A version of the theory has also been proposed in which the curvature is fully elastic. Finally, the thermal aspects of the theory are detailed in Section 6.7.

6.1 Recalls of algebraic rotations

Rigid rotations in a three-dimensional Euclidean space $\{\underline{\mathbf{e}}_1; \underline{\mathbf{e}}_2; \underline{\mathbf{e}}_3\}$ endowed with Cartesian norm are isomorphic $\mathcal{R}^3 \to \mathcal{R}^3$ transformations, and they can be uniquely identified through a set of three independent parameters [Bauchau 2011]. More parameters can be used to uniquely identify a rotation, but then they are not anymore independents from each other. Every description of the rotation is based on a different choice of parametriza-

Parametrization	$p(\theta)$	ν	ε
Cartesian Rotation Vector	θ	$\left[\sin\frac{\theta}{2}\right] / \left[\frac{\theta}{2}\right]$	$\left[\tan\frac{\theta}{2}\right] / \left[\frac{\theta}{2}\right]$
Linear	$\sin(\theta)$	$\cos^{-1}\left(\frac{\theta}{2}\right)$	$\cos^{-2}\left(\frac{\theta}{2}\right)$
Euler Rodrigues	$2\sin\left(\frac{\theta}{2}\right)$	1	$\cos^{-1}\left(\frac{\theta}{2}\right)$
Cayley-Gibbs-Rodrigues	$2\tan\left(\frac{\theta}{2}\right)$	$\cos\left(\frac{\theta}{2}\right)$	1
Wiener-Milenkovic	$4\tan(\theta/4)$	$\cos^2\left(\frac{\theta}{4}\right)$	$\left[1-\tan^2\left(\frac{\theta}{4}\right)\right]^{-1}$

Table 6.1: Some parametrization methods reported from [Bauchau 2011].

tion. Parameterizing the rotation is a useful procedure which can facilitate the numerical implementation of a code that deals with large rotations. It is important to highlight that the parameters do not include information on the orientation of an object in the space, but they rather describe the rotation transformation which is to be applied to said orientation. The most general rotation operation can be embodied in a rotation matrix $\underset{\sim}{\mathbf{R}}$, which can be applied to a general vector $\underline{\boldsymbol{a}}$ by left multiplying the vector by the matrix:

$$\underset{\sim}{\mathbf{R}} \cdot \underline{\boldsymbol{a}}, \tag{6.1}$$

and the resulting vector would be trivially equal to the original vector $\underline{\boldsymbol{a}}$ rotated. Although the rotation matrix is a second order tensor (9 entries), it can be constructed by using less parameters.
In general, rotation parametrization can be distinguished between vectorial and non-vectorial parametrization, depending on the number of parameters used. The minimum set of independent parameters is three, and every form of parametrization that uses only three parameters belongs to the group of vectorial parametrization. Other solutions that use more than three parameters, e.g. quaternions, are part of the non-vectorial rotation parametrizations. The parameter vector can be expressed as:

$$\underline{\boldsymbol{\theta}} = p(\theta)\,\underline{\hat{\mathbf{n}}}, \tag{6.2}$$

where $p(\theta)$ is the *generating function*, it can assume different values depending on the chosen parametrization (see Table 6.1) and $\underline{\hat{\mathbf{n}}}$ is the unit vector defining the direction around which the rotation takes place. Choosing different generating function is equivalent to choosing a different parametrization. The most common rotation parametrizations are summarized in Table 6.1. The rotation matrix can be expressed as function of the vectorial parameters in a general form as:

$$\underset{\sim}{\mathbf{R}} = \underset{\sim}{\mathbf{I}} + \zeta_1(\theta)\underset{\sim}{\boldsymbol{\theta}} + \zeta_2(\theta)\underset{\sim}{\boldsymbol{\theta}} \cdot \underset{\sim}{\boldsymbol{\theta}}, \tag{6.3}$$

where:

$$\zeta_1(\theta) = \frac{\nu^2}{\varepsilon}, \tag{6.4}$$

$$\zeta_2(\theta) = \frac{\nu^2}{2}, \tag{6.5}$$

and the values of ν and ε are indicated in the Table 6.1 for different types of parametrization; the second order tensor $\underset{\sim}{\boldsymbol{\theta}}$ is the skew-symmetric tensor whose axial vector is the parameter vector $\underline{\boldsymbol{\theta}}$. The advantage of parameterizing the rotation operation is mainly in the reduced number of independent parameters that identify the rotation, and this leads to a reduced effort in terms of memory in case the rotation has to be numerically modeled. For instance, in case of the large rotations experienced by the Cosserat continuum, we would enhance the continuum with only three additional degrees of freedom, being the components of the vector $\underline{\boldsymbol{\theta}}$. In this manuscript we chose to use a **Cartesian Rotation Vector** to parametrize the rotation. The rotation tensor can also be expressed by means of the famous *Rodrigues formula*:

$$\underset{\sim}{\mathbf{R}} = \underset{\sim}{\mathbf{I}} + \frac{\sin\theta}{\theta}\,\underset{\sim}{\boldsymbol{\theta}} + \frac{1-\cos\theta}{\theta^2}\,\underset{\sim}{\boldsymbol{\theta}} \cdot \underset{\sim}{\boldsymbol{\theta}}, \tag{6.6}$$

which, through similarities that arise by adopting a Taylor expansion, can also be expresses as:

$$\underset{\sim}{\mathbf{R}} = \exp\left(\underset{\sim}{\boldsymbol{\theta}}\right) = \exp\left(-\underset{\sim}{\boldsymbol{\epsilon}} \cdot \underline{\boldsymbol{\theta}}\right) = \sum_{n=0}^{\infty} \frac{\underset{\sim}{\boldsymbol{\theta}}^n}{n!}. \tag{6.7}$$

6.2 Cosserat kinematics

In a Euclidean three-dimensional space, on which a Cartesian metric is defined $\{\underline{\mathbf{e}}_1; \underline{\mathbf{e}}_2; \underline{\mathbf{e}}_3\}$, we identify a continuous bounded region Ω as our material domain of interest. Our purpose is to characterize the evolution of the motion of our domain of interest in time. Let us consider an initial time t_0 at which the position and state variables, to be defined later, of the body are known. In this context, the right subscripts indicate the time at which the quantity is evaluated, for instance Ω_0 is our domain of interest at time 0.
At every time, all the points of the domain are endowed with three *degrees of freedom* (d.o.f.) that are the displacements that the continuum undergoes at that specific location. At time 0, the position vector is written as $\underline{\mathbf{X}}$. In the Cosserat description of the continuum, every point of the domain of interest does not only possess a position in the space, but also an orientation with the respect to a frame of reference. This orientation does not coincide with the material orientation in general, and in the Cosserat theory such additional degrees of freedom are used to describe the micro-structure orientation. A triad of directors $\left\{\underline{\boldsymbol{\phi}}_1; \underline{\boldsymbol{\phi}}_2; \underline{\boldsymbol{\phi}}_3\right\}$ is attached to every point in the domain, which could be used to describe, for example, the lattice orientation or the fibers orientation within a matrix. Therefore, besides the displacement vector $\underline{\mathbf{u}}$, every point of the domain is characterized also by a pseudo-vector $\underline{\boldsymbol{\theta}}$ which encapsulates the information about the rotations $\underset{\sim}{\mathbf{R}}(\boldsymbol{\theta})$ which is applied to the reference triad of directors in order to modify the micro-structure orientation and to obtain the directors' orientation at time t. In this context, the theory follows a Lagrangian description, meaning that the the continuum

description is given with respect a reference configuration that coincides with the original material configuration.
Following the discussion regarding the rotations, from Equation (6.7) it is clear that although the rotation operator is a second order tensor, $\underset{\sim}{\mathbf{R}}$, the body is endowed with only three additional degrees of freedom, being the three components of the pseudo-vector meant to represent the rotation of the micro-structure orientation with respect to the initial frame of reference (these three d.o.f.s are the variables of the three-dimensional Lie group associated to the rotation $\underset{\sim}{\mathbf{R}}$). At time t these d.o.f. are embraced in the pseudo-vector $\underline{\boldsymbol{\theta}}$:

$$\underset{\sim}{\mathbf{R}} = \exp\left(\underset{\sim}{\boldsymbol{\theta}}\right) = \exp\left(-\underset{\sim}{\boldsymbol{\epsilon}} \cdot \underline{\boldsymbol{\theta}}\right). \tag{6.8}$$

Given an initial configuration, $\underline{\mathbf{X}}$, and a current configuration, $\underline{\mathbf{x}}$, the evaluation of the deformation is performed by computing the variation of the position vector at time t with respect to the variation of the position vector at time 0:

$$\underset{\sim}{\mathbf{F}} = \frac{d\underline{\mathbf{x}}}{d\underline{\mathbf{X}}} = \underline{\mathbf{x}} \otimes \underline{\nabla}_0, \tag{6.9}$$

where $\underset{\sim}{\mathbf{F}}$ is the deformation gradient and its determinant is the Jacobian J = det $\left(\underset{\sim}{\mathbf{F}}\right)$. The Cosserat description of the media does not require only the deformation gradient as measure of the media distortion, but it also requires the following quantity to fully describe the state of the continuum [Kafadar et al. 1971; Eringen 1999b]:

$$\underset{\sim}{\boldsymbol{\Gamma}} = -\frac{1}{2}\underset{\sim}{\boldsymbol{\epsilon}} : \left[\underset{\sim}{\mathbf{R}}^T \cdot \left(\underset{\sim}{\mathbf{R}} \otimes \underline{\nabla}_0\right)\right], \tag{6.10}$$

which is referred to as *wryness*. Equation (6.10) quantifies the variation of the rotation tensor, in the reference configuration, meaning that it is a Lagrangian deformation measure. By defining the displacement field as $\underline{\mathbf{u}} = \underline{\mathbf{X}} - \underline{\mathbf{x}}$, we can consequently define:

$$\underline{\mathbf{v}} = \dot{\underline{\mathbf{u}}}, \tag{6.11}$$

$$\underset{\sim}{\boldsymbol{\omega}} = \dot{\underset{\sim}{\mathbf{R}}} \cdot \underset{\sim}{\mathbf{R}}^T, \tag{6.12}$$

which are the velocity vector and gyration tensor respectively. By combining these quantities we can define the Eulerian Cosserat deformation rate and Eulerian Cosserat wryness rate as:

$$\underline{\mathbf{v}} \otimes \underline{\nabla} - \underset{\sim}{\boldsymbol{\omega}}, \tag{6.13}$$

$$\underline{\boldsymbol{\omega}} \otimes \underline{\nabla}, \tag{6.14}$$

where $\underline{\boldsymbol{\omega}}$ is the axial vector of the skew-symmetric tensor $\underset{\sim}{\boldsymbol{\omega}}$. Standard relationship is valid:

$$\underline{\mathbf{v}} \otimes \underline{\nabla} = \dot{\underset{\sim}{\mathbf{F}}} \cdot \underset{\sim}{\mathbf{F}}^{-1}, \tag{6.15}$$

and, in the same way, the gradient of the gyration vector can be evaluated with respect to the reference configuration as:

$$\underline{\boldsymbol{\omega}} \otimes \underline{\nabla} = (\underline{\boldsymbol{\omega}} \otimes \underline{\nabla}_0) \cdot \underset{\sim}{\mathbf{F}}^{-1}. \tag{6.16}$$

In order to account for the difference between material and micro-structural rotations, the Cosserat theory employs a modified deformation gradient in which the coupling between these two rotations is explicitly stated:

$$\underset{\sim}{\bar{\mathbf{U}}} = \underset{\sim}{\mathbf{R}}^T \cdot \underset{\sim}{\mathbf{F}} = \underset{\sim}{\mathbf{R}}^T \cdot \underset{\sim}{\mathbf{Q}} \cdot \underset{\sim}{\mathbf{U}}, \tag{6.17}$$

where $\underset{\sim}{\mathbf{Q}}$ is the material rotation tensor and $\underset{\sim}{\mathbf{U}}$ is the classical right stretch tensor. It can be proved that $\underset{\sim}{\bar{\mathbf{U}}}$ can be used as an objective strain measure since it is invariant to a rigid rotation applied both to the material and to the Cosserat rotation [Steinmann 1994]. This can be easily proved by hypothesizing that the continuum is currently found under the following strain $\underset{\sim}{\boldsymbol{\Xi}}_0$:

$$\underset{\sim}{\bar{\mathbf{U}}}_0 = \underset{\sim}{\mathbf{R}}_0^T \underset{\sim}{\mathbf{Q}}_0 \underset{\sim}{\mathbf{U}}_0, \tag{6.18}$$

and by fetching the rotations $\underset{\sim}{\mathbf{R}}$ and $\underset{\sim}{\mathbf{Q}}$ with an increment of rotation $\underset{\sim}{\mathbf{R}}_\Delta$, such that they would result as:

$$\underset{\sim}{\mathbf{R}}_1 = \underset{\sim}{\mathbf{R}}_\Delta \underset{\sim}{\mathbf{R}}, \tag{6.19}$$

$$\underset{\sim}{\mathbf{Q}}_1 = \underset{\sim}{\mathbf{R}}_\Delta \underset{\sim}{\mathbf{Q}}, \tag{6.20}$$

so that the strain measure after the application of such rotation would be:

$$\underset{\sim}{\bar{\mathbf{U}}}_1 = \underset{\sim}{\mathbf{R}}_1^T \underset{\sim}{\mathbf{Q}}_1 = \underset{\sim}{\mathbf{R}}_0^T \underset{\sim}{\mathbf{R}}_\Delta^T \underset{\sim}{\mathbf{R}}_\Delta \underset{\sim}{\mathbf{Q}}_0 \underset{\sim}{\mathbf{U}}_0 = \underset{\sim}{\bar{\mathbf{U}}}_0, \tag{6.21}$$

thus proving that it is a suitable choice as strain measure. In terms of rates, the following relations are defined for the strain:

$$\dot{\underset{\sim}{\bar{\mathbf{U}}}} = \dot{\underset{\sim}{\mathbf{R}}}^T \underset{\sim}{\mathbf{F}} + \underset{\sim}{\mathbf{R}}^T \dot{\underset{\sim}{\mathbf{F}}}, \tag{6.22}$$

$$\dot{\underset{\sim}{\bar{\mathbf{U}}}} \cdot \underset{\sim}{\bar{\mathbf{U}}}^{-1} = \underset{\sim}{\mathbf{R}}^T \cdot \left[\underline{\mathbf{v}} \otimes \underline{\nabla} - \underset{\sim}{\boldsymbol{\omega}} \right] \cdot \underset{\sim}{\mathbf{R}}. \tag{6.23}$$

The rate of the wryness can be evaluated by taking the time derivative of Equation (6.10) and by exploiting the skew-symmetric character of the tensor:

$$\dot{\underset{\sim}{\boldsymbol{\Gamma}}} = \underset{\sim}{\mathbf{R}}^T \cdot [\underline{\boldsymbol{\omega}} \otimes \underline{\nabla}_0], \tag{6.24}$$

$$\dot{\underset{\sim}{\boldsymbol{\Gamma}}} \cdot \underset{\sim}{\bar{\mathbf{U}}}^{-1} = \underset{\sim}{\mathbf{R}}^T \cdot [\underline{\boldsymbol{\omega}} \otimes \underline{\nabla}] \cdot \underset{\sim}{\mathbf{R}}. \tag{6.25}$$

6.2.1 Choice of the elasto-plastic decomposition

The decomposition of the wryness in plastic and elastic parts is not a trivial kinematic aspect of the theory in large deformation, as two different wryness decomposition can be found in literature: one proposed by Dluzewski [Dluzeswki 1991]and the other by Steinmann [Steinmann 1994]. Both authors justified their choices with arguments that are reported in the following sub-sections. The model proposed by Dluzewski has been chosen for this report. The main difference between the two kinematics lies in the elasto-plastic decomposition of the rotation tensor: Steinnmann considers the rotation tensor as

elasto-plastic, whereas Dluzewski argues that it is not decomposable, thus to be treated as fully elastic. The decomposition of Steinnmann is:

$$\text{Steinmann} \quad \begin{cases} \underset{\sim}{\mathbf{R}} = \underset{\sim}{\mathbf{R}}^e \cdot \underset{\sim}{\mathbf{R}}^p, \\ \underset{\sim}{\boldsymbol{\Gamma}} = -\frac{1}{2} \underset{\approx}{\boldsymbol{\epsilon}} : \left[\underset{\sim}{\mathbf{R}}^{p^T} \underset{\sim}{\mathbf{R}}^{e^T} \left(\underset{\sim}{\mathbf{R}}^e \otimes \underline{\boldsymbol{\nabla}}_0 \right) \underset{\sim}{\mathbf{R}}^p + \underset{\sim}{\mathbf{R}}^{p^T} \left(\underset{\sim}{\mathbf{R}}^p \otimes \underline{\boldsymbol{\nabla}}_0 \right) \right] = \underset{\sim}{\boldsymbol{\Gamma}}^e + \underset{\sim}{\boldsymbol{\Gamma}}^p, \end{cases} \tag{6.26}$$

and, as extracted from [Steinmann 1994]: *'In the context of micro-polar elasto-plasticity the viewpoint is adopted that the dislocation flow influences the orientation of the independent triad as well, thus giving rise to the notion of the plastic micro-polar rotation* $\underset{\sim}{\mathbf{R}}^p$ *which is complemented by the elastic micro-polar rotation* $\underset{\sim}{\mathbf{R}}^e$*. Phenomenologically, an unloaded stress and couple stress-free configuration is therefore locally defined by* $\underset{\sim}{\mathbf{F}}^{e^{-1}}$ *together with* $\underset{\sim}{\mathbf{R}}^{e^T}$*. [...] as a consequence of these considerations, the objective stress and couple stress response will depend solely on the elastic parts of the (spatial) left stretch and curvature measures.'* Another advantage of using such decomposition is represented by the possibility of identifying an intermediate plastic configuration obtained through the transformations embedded by $\underset{\sim}{\mathbf{F}}^p$ and $\underset{\sim}{\mathbf{R}}^p$. This type of decomposition has been used also by Bauer et al. [Bauer, Schäfer, et al. 2010; Bauer, Dettmer, et al. 2012], Grammenoudis and Tsakamis [Grammenoudis et al. 2005; Grammenoudis et al. 2001]. Recently, Johanssen and Tsamakis published their work related to the connections between Lagrangian and Eulerian formulations of curvature [Johannsen et al. 2019] and they also adopted the formulation proposed by Steinmmann. The other possible decomposition follows from the work of Dluzewski:

$$\text{Dluzekwski} \quad \begin{cases} \underset{\sim}{\bar{\mathbf{U}}} = \underset{\sim}{\bar{\mathbf{U}}}^e \cdot \underset{\sim}{\mathbf{F}}^p, \\ \underset{\sim}{\boldsymbol{\Gamma}} = \underset{\sim}{\boldsymbol{\Gamma}}^e \cdot \underset{\sim}{\mathbf{F}}^p + \underset{\sim}{\boldsymbol{\Gamma}}^p, \end{cases} \tag{6.27}$$

and the argument for the adoption of such model is extracted from [Forest, Cailletaud, et al. 1997]: *'An elastic-plastic decomposition of the rotation [Steinmann 1994], as of the displacement, is not recommendable, because these non-objective variables can not be connected with the quantities of energy and dissipation. Such a connection is possible only on the level of strains. [...] The decomposition* (6.27) *enable one to define at each point the released state of the crystal for which stresses and couple stresses are removed and plastic deformation and curvature only remain. This is the reason why* (6.27) *is more suitable for crystals than a purely additional decomposition [Sansour and Keck 1994].'* This decomposition has also been used by Forest et al. [Forest, Cailletaud, et al. 1997; Forest and Sievert 2003], Sansour [Sansour 1998] and Ask et al. [Ask et al. 2019]. Another argument in favor of such decomposition is reported from the work of Sansour [Sansour 1998]: *'As a next step we consider the decomposition of the second Cosserat deformation tensor* $\underset{\sim}{\boldsymbol{\Gamma}}$*. Two observations are helpful. First, the deformation gradient* $\underset{\sim}{\mathbf{F}}$ *or the stretch tensor* $\underset{\sim}{\bar{\mathbf{U}}}$ *can be understood as elements of a matrix group acting on the tangent space at the identity. This is reflected also in their physical meaning by stretching (for* $\underset{\sim}{\mathbf{F}}$ *also rotating) the tangent space. For such an action, a multiplicative decomposition is a natural choice. Such a mathematical or physical meaning is not assigned to the tensor* $\underset{\sim}{\boldsymbol{\Gamma}}$*. Second, from its very definition, the tensor* $\underset{\sim}{\boldsymbol{\Gamma}}$ *is equivalent to the vectors [...], for which an additive decomposition is, due to lack of any motivation for a multiplicative decomposition, an*

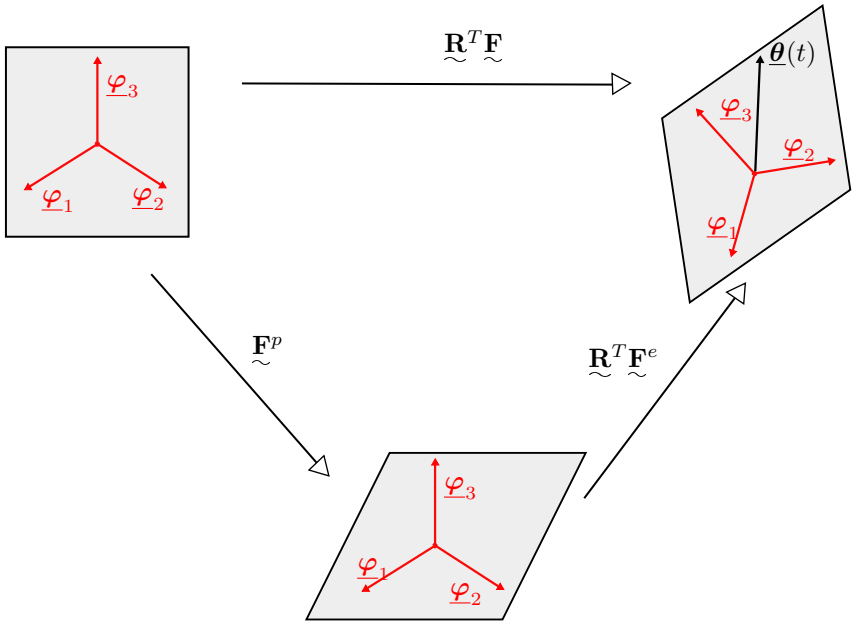

Figure 6.1: Schematic representation of the deformation decomposition in the Cosserat media.

appropriate operation.'
In this work, the Dluzekwski kinematic model has been used, and the following elasto-plastic decomposition is used:

$$\underset{\sim}{\bar{\mathbf{U}}} = \underset{\sim}{\bar{\mathbf{U}}}^e \cdot \underset{\sim}{\bar{\mathbf{U}}}^p, \tag{6.28}$$

$$\underset{\sim}{\boldsymbol{\Gamma}} = \underset{\sim}{\boldsymbol{\Gamma}}^e \cdot \underset{\sim}{\mathbf{F}}^p + \underset{\sim}{\boldsymbol{\Gamma}}^p, \tag{6.29}$$

where:

$$\underset{\sim}{\bar{\mathbf{U}}}^e = \underset{\sim}{\mathbf{R}}^T\underset{\sim}{\mathbf{F}}^e, \tag{6.30}$$

$$\underset{\sim}{\bar{\mathbf{U}}}^p \equiv \underset{\sim}{\mathbf{F}}^p. \tag{6.31}$$

In Figure 6.1 the deformation decomposition is reported. By deriving Equations (6.28) and (6.29) with respect to time, the rates of the elastic parts of the deformations can be identified as:

$$\dot{\underset{\sim}{\bar{\mathbf{U}}}}^e = \dot{\underset{\sim}{\bar{\mathbf{U}}}} \cdot \underset{\sim}{\bar{\mathbf{U}}}^{p^{-1}} - \underset{\sim}{\bar{\mathbf{U}}}^e \cdot \dot{\underset{\sim}{\bar{\mathbf{U}}}}^p \cdot \underset{\sim}{\bar{\mathbf{U}}}^{p^{-1}}, \tag{6.32}$$

$$\dot{\underset{\sim}{\boldsymbol{\Gamma}}}^e = \dot{\underset{\sim}{\boldsymbol{\Gamma}}} \cdot \underset{\sim}{\boldsymbol{\Xi}}^{p^{-1}} - \underset{\sim}{\boldsymbol{\Gamma}}^e \cdot \dot{\underset{\sim}{\boldsymbol{\Xi}}}^p \cdot \underset{\sim}{\boldsymbol{\Xi}}^{p^{-1}} - \dot{\underset{\sim}{\boldsymbol{\Gamma}}}^p \cdot \underset{\sim}{\boldsymbol{\Xi}}^{p^{-1}}. \tag{6.33}$$

6.3 Balance laws

To construct the theory of the Cosserat we can start from the definition of the internal power density as function of the quantities whose variations induce an energy variation of the media, that are, the strain rate and the wryness rate defined in Equations (6.13) and (6.14):

$$p^{(i)} = \underset{\sim}{\boldsymbol{\sigma}} : \left(\underline{\mathbf{v}} \otimes \underline{\nabla} - \underset{\sim}{\boldsymbol{\omega}}\right) + \underset{\sim}{\mathbf{m}} : (\underline{\boldsymbol{\omega}} \otimes \underline{\nabla}), \tag{6.34}$$

where $\underset{\sim}{\boldsymbol{\sigma}}$ is the stress tensor, power conjugate to the Cosserat strain rate, and $\underset{\sim}{\mathbf{m}}$ is the couple stress tensor, power conjugate to the Cosserat wryness rate. Note that the stress tensor is in general not symmetric, differently from the stress tensor typically used in classical continuum mechanics. Equivalently, the densities of power generated by external forces and contact forces can be expressed as:

$$p^{(e)} = \underline{\mathbf{f}}^e \cdot \underline{\mathbf{v}} + \underline{\mathbf{g}}^e \cdot \underline{\boldsymbol{\omega}}, \tag{6.35}$$

$$p^{(c)} = \underline{\mathbf{f}}^c \cdot \underline{\mathbf{v}} + \underline{\mathbf{g}}^c \cdot \underline{\boldsymbol{\omega}}, \tag{6.36}$$

from which the power balance law can be written as:

$$\begin{aligned}\int_\Omega \underline{\mathbf{v}} \cdot \left[\underset{\sim}{\boldsymbol{\sigma}} \cdot \underline{\nabla} + \underline{\mathbf{f}}^e\right] \mathrm{dv} + \int_{\partial\Omega} \underline{\mathbf{v}} \cdot \left[\underline{\mathbf{f}}^c - \underset{\sim}{\boldsymbol{\sigma}} \cdot \underline{\mathbf{n}}\right] \mathrm{ds} \\ + \int_\Omega \overset{\times}{\underline{\boldsymbol{\omega}}} \cdot \left[\underset{\sim}{\mathbf{m}} \cdot \underline{\nabla} + 2\overset{\times}{\underline{\boldsymbol{\sigma}}} + \underline{\mathbf{g}}^e\right] \mathrm{dv} + \int_{\partial\Omega} \overset{\times}{\underline{\boldsymbol{\omega}}} \cdot \left[\underline{\mathbf{g}}^c - \underset{\sim}{\mathbf{m}} \cdot \underline{\mathbf{n}}\right] \mathrm{ds} = 0,\end{aligned} \tag{6.37}$$

where $\underline{\mathbf{f}}^e$ is the external volume force, $\underline{\mathbf{g}}^e$ is the external volume couple, $\underline{\mathbf{f}}^c$ is the contact force, $\underline{\mathbf{g}}^c$ is the contact couple, $\underline{\mathbf{n}}$ is the outward normal unit vector of the boundary $\partial\Omega$ which closes the Ω domain and $\underline{\boldsymbol{\sigma}}$ is the axial vector obtained from the skew-symmetric part of the stress tensor. From the balance of power, given the arbitrariness of $\underline{\mathbf{v}}$ and $\overset{\times}{\underline{\boldsymbol{\omega}}}$, the local balance laws can be written for the Cosserat Media:

$$\underset{\sim}{\boldsymbol{\sigma}} \cdot \underline{\nabla} + \underline{\mathbf{f}}^e = \underline{0}, \tag{6.38}$$

$$\underset{\sim}{\mathbf{m}} \cdot \underline{\nabla} + 2\overset{\times}{\underline{\boldsymbol{\sigma}}} + \underline{\mathbf{g}}^e = \underline{0}, \tag{6.39}$$

which must be valid at every point in the domain Ω. On the boundary $\partial\Omega$ the followings must hold:

$$\underset{\sim}{\boldsymbol{\sigma}} \cdot \underline{\mathbf{n}} = \underline{\mathbf{f}}^c, \tag{6.40}$$

$$\underset{\sim}{\mathbf{m}} \cdot \underline{\mathbf{n}} = \underline{\mathbf{g}}^c. \tag{6.41}$$

Equation (6.34) expresses the internal power in an Eulerian frame of reference, but we can equivalently express the internal power in a Lagrangian frame of reference. Through Equations (6.23) and (6.16), and taking into account density modification, Equation (6.34) transforms into:

$$\mathrm{J}\, p^{(i)} = \mathrm{J}\, \underset{\sim}{\boldsymbol{\sigma}} \cdot \underset{\sim}{\mathbf{F}}^{-T} : \dot{\underset{\sim}{\mathbf{F}}} - \mathrm{J} \underset{\sim}{\boldsymbol{\sigma}} : \underset{\sim}{\boldsymbol{\omega}} + \mathrm{J}\, \underset{\sim}{\mathbf{m}} \cdot \underset{\sim}{\mathbf{F}}^{-T} : (\underline{\boldsymbol{\omega}} \otimes \underline{\boldsymbol{\nabla}}_0), \tag{6.42}$$

where we split the stress tensors in the two components that are related to the velocity gradient and the Cosserat rotation tensor. Equation (6.42) can be rewritten as:

$$\mathrm{J}\, p^{(i)} = \underset{\sim}{\mathbf{S}} : \dot{\underset{\sim}{\mathbf{F}}} - \underline{\mathbf{s}} \cdot \underline{\boldsymbol{\omega}} + \underset{\sim}{\underset{\sim}{\mathbf{M}}} : (\underline{\boldsymbol{\omega}} \otimes \underline{\nabla_0}) \,, \tag{6.43}$$

from which the power conjugates to $\dot{\underset{\sim}{\mathbf{F}}}$, $\underline{\boldsymbol{\omega}}$ and $(\underline{\boldsymbol{\omega}} \otimes \underline{\nabla_0})$ can be clearly identified. Writing the internal power as such allows to identify the two-point *first Piola-Kirchhoff* stress tensor and couple stress tensor:

$$\underset{\sim}{\mathbf{S}} = \mathrm{J}\, \underset{\sim}{\boldsymbol{\sigma}} \cdot \underset{\sim}{\mathbf{F}}^{-T}, \tag{6.44}$$

$$\underset{\sim}{\underset{\sim}{\mathbf{M}}} = \mathrm{J}\, \underset{\sim}{\underset{\sim}{\mathbf{m}}} \cdot \underset{\sim}{\mathbf{F}}^{-T}, \tag{6.45}$$

$$\underline{\mathbf{s}} = 2\,\mathrm{J}\,\mathrm{axl}\left(\underset{\sim}{\boldsymbol{\sigma}}\right) = -\underline{\underline{\boldsymbol{\epsilon}}} : \left(\underset{\sim}{\mathbf{S}} \cdot \underset{\sim}{\mathbf{F}}^{T}\right). \tag{6.46}$$

The internal power in Equation (6.34) can also be written such that the power conjugates to $\dot{\underset{\sim}{\mathbf{U}}} \cdot \bar{\underset{\sim}{\mathbf{U}}}^{-1}$ are highlighted (such as done by Ask et al. in [Ask et al. 2019]):

$$\mathrm{J}\, p^{(i)} = \mathrm{J}\underset{\sim}{\mathbf{R}}^{T}\underset{\sim}{\underset{\sim}{\boldsymbol{\sigma}}}\underset{\sim}{\mathbf{R}} : \left[\dot{\underset{\sim}{\mathbf{U}}} \cdot \bar{\underset{\sim}{\mathbf{U}}}^{-1}\right] + \mathrm{J}\underset{\sim}{\mathbf{R}}^{T}\underset{\sim}{\underset{\sim}{\mathbf{m}}}\underset{\sim}{\mathbf{R}} : \left[\dot{\underset{\sim}{\boldsymbol{\Gamma}}} \cdot \bar{\underset{\sim}{\mathbf{U}}}^{-1}\right], \tag{6.47}$$

which can be rewritten as:

$$\mathrm{J}\, p^{(i)} = \bar{\underset{\sim}{\boldsymbol{\sigma}}} : \left[\dot{\underset{\sim}{\mathbf{U}}} \cdot \bar{\underset{\sim}{\mathbf{U}}}^{-1}\right] + \bar{\underset{\sim}{\underset{\sim}{\mathbf{m}}}} : \left[\dot{\underset{\sim}{\boldsymbol{\Gamma}}} \cdot \bar{\underset{\sim}{\mathbf{U}}}^{-1}\right], \tag{6.48}$$

where the stress and couple stress can be gathered as:

$$\bar{\underset{\sim}{\boldsymbol{\sigma}}} = \mathrm{J}\underset{\sim}{\mathbf{R}}^{T}\underset{\sim}{\underset{\sim}{\boldsymbol{\sigma}}}\underset{\sim}{\mathbf{R}}, \tag{6.49}$$

$$\bar{\underset{\sim}{\underset{\sim}{\mathbf{m}}}} = \mathrm{J}\underset{\sim}{\mathbf{R}}^{T}\underset{\sim}{\underset{\sim}{\mathbf{m}}}\underset{\sim}{\mathbf{R}}. \tag{6.50}$$

The internal power can also be written in a framework that would correspond to the classical Lagrangian framework, that is, by identifying the power conjugates to the rates of the Cosserat strain and wryness as defined in Equations (6.22) and (6.24) respectively. In the classical Boltzmann continuum, these deformation rates would correspond to the rate of the Green-Lagrange deformation measure. It is possible to re-write the internal power definition from Equation (6.34) and we could re-arrange the terms such as to identify the power-conjugate stress of such deformation rate measures:

$$\mathrm{J}\, p^{(i)} = \mathrm{J}\underset{\sim}{\mathbf{R}}^{T}\underset{\sim}{\underset{\sim}{\boldsymbol{\sigma}}}\underset{\sim}{\mathbf{F}}^{-T} : \dot{\underset{\sim}{\mathbf{U}}} + \mathrm{J}\underset{\sim}{\mathbf{R}}^{T}\underset{\sim}{\underset{\sim}{\mathbf{m}}}\underset{\sim}{\mathbf{F}}^{-T} : \dot{\underset{\sim}{\boldsymbol{\Gamma}}}, \tag{6.51}$$

which can be simplified in:

$$\mathrm{J}\, p^{(i)} = \underset{\sim}{\mathbf{T}} : \dot{\underset{\sim}{\mathbf{U}}} + \underset{\sim}{\mathbf{T}}_c : \dot{\underset{\sim}{\boldsymbol{\Gamma}}}, \tag{6.52}$$

where we identified the equivalent *second Piola-Kirchhoff* stress and couple stress tensors:

$$\underset{\sim}{\mathbf{T}} = \mathrm{J}\underset{\sim}{\mathbf{R}}^{T}\underset{\sim}{\underset{\sim}{\boldsymbol{\sigma}}}\underset{\sim}{\mathbf{F}}^{-T}, \tag{6.53}$$

$$\underset{\sim}{\mathbf{T}}_c = \mathrm{J}\underset{\sim}{\mathbf{R}}^{T}\underset{\sim}{\underset{\sim}{\mathbf{m}}}\underset{\sim}{\mathbf{F}}^{-T}. \tag{6.54}$$

Configuration	Deformation Rate	Power Conjugate
Eulerian	$\dot{\underset{\sim}{\mathbf{F}}}\underset{\sim}{\mathbf{F}}^{-1} - \dot{\underset{\sim}{\mathbf{R}}}\underset{\sim}{\mathbf{R}}^T$	$\underset{\sim}{\boldsymbol{\sigma}}$
	$\underset{\sim}{\mathbf{R}}\dot{\bar{\underset{\sim}{\boldsymbol{\Gamma}}}}\bar{\underset{\sim}{\mathbf{U}}}^{-1}\underset{\sim}{\mathbf{R}}^T$	$\underline{\underset{\sim}{\mathbf{m}}}$
Mixed	$\dot{\underset{\sim}{\mathbf{F}}}$	$\underset{\sim}{\mathbf{S}}$
	$\text{axl}\left(-\dot{\underset{\sim}{\mathbf{R}}}\cdot\underset{\sim}{\mathbf{R}}^T\right)$	$\underline{\mathbf{s}}$
	$\underset{\sim}{\mathbf{R}}\cdot\dot{\underset{\sim}{\boldsymbol{\Gamma}}}$	$\underset{\sim}{\mathbf{M}}$
Lagrangian	$\dot{\underset{\sim}{\mathbf{U}}}$	$\underset{\sim}{\mathbf{T}}$
	$\dot{\underset{\sim}{\boldsymbol{\Gamma}}}$	$\underset{\sim}{\mathbf{T}}_c$
Cosserat	$\dot{\underset{\sim}{\mathbf{U}}}\bar{\underset{\sim}{\mathbf{U}}}^{-1}$	$\bar{\underset{\sim}{\boldsymbol{\sigma}}}$
	$\dot{\underset{\sim}{\boldsymbol{\Gamma}}}\bar{\underset{\sim}{\mathbf{U}}}^{-1}$	$\bar{\underline{\underset{\sim}{\mathbf{m}}}}$

Table 6.2: Deformations and power conjugates in different configurations.

By making use of these definitions, the equilibrium equations can also be written in the Lagrangian configuration. In particular, we could express the weak form of the balance equations (Equations (6.38) and (6.39)) in the reference configurations to achieve the following equilibrium equations:

$$\left(\underset{\sim}{\mathbf{R}}\underset{\sim}{\mathbf{T}}\right)\cdot\underline{\boldsymbol{\nabla}}_0 + \underline{\mathbf{f}}_0^e = \underline{0}, \tag{6.55}$$

$$\left(\underset{\sim}{\mathbf{R}}\underset{\sim}{\mathbf{T}}_c\right)\cdot\underline{\boldsymbol{\nabla}}_0 + \text{axl}\left(\underset{\sim}{\mathbf{R}}\underset{\sim}{\mathbf{T}}\underset{\sim}{\mathbf{F}}^T - \underset{\sim}{\mathbf{F}}\underset{\sim}{\mathbf{T}}^T\underset{\sim}{\mathbf{R}}^T\right) + \underline{\mathbf{g}}_0^e = \underline{0}, \tag{6.56}$$

bounded by (from Equations (6.40) and (6.41) using Nanson's formula):

$$\underset{\sim}{\mathbf{R}}\underset{\sim}{\mathbf{T}}\cdot\underline{\mathbf{n}}_0 = \underline{\mathbf{f}}_0^c, \tag{6.57}$$

$$\underset{\sim}{\mathbf{R}}\underset{\sim}{\mathbf{T}}_c\cdot\underline{\mathbf{n}}_0 = \underline{\mathbf{g}}_0^c, \tag{6.58}$$

where $\underline{\mathbf{f}}_0^e$ and $\underline{\mathbf{g}}_0^e$ are external forces and couple forces, and the subscript 0 indicates that they are acting on the reference configuration (they are different from $\underline{\mathbf{f}}^e$, $\underline{\mathbf{g}}^e$ and $\underline{\mathbf{n}}$ acting on the current configuration). In Table 6.2 the deformation rates and power stress and couple stress conjugates in the Eulerian, Lagrangian, mixed and Cosserat configurations are reported. The relationships among the different stress measures are computed in Table 6.3.

6.4 Hyper-elastic material

For this section the following assumption is made:

$$\underset{\sim}{\mathbf{F}}^p = \underset{\sim}{\mathbf{I}}, \tag{6.59}$$

$$\underset{\sim}{\mathbf{\Gamma}}^p = \underset{\sim}{\mathbf{0}}, \tag{6.60}$$

$$\dot{\underset{\sim}{\mathbf{F}}}^p = \underset{\sim}{\mathbf{0}}, \tag{6.61}$$

$$\dot{\underset{\sim}{\mathbf{\Gamma}}}^p = \underset{\sim}{\mathbf{0}}. \tag{6.62}$$

A complete description of the elastic constitutive material response begins with the definition of the Helmholtz free energy, or, in case of isothermal hyper-elastic description, elastic potential. Defining the relation between stress and strain through the elastic potential/Helmholtz free energy definition entails many advantages, for instance, if a potential exists, the fourth-order elastic tensor relating stress and strain benefits from major symmetry.
Although Kafadar and Eringen originally used $\underset{\sim}{\bar{\mathbf{U}}}$ and $\underset{\sim}{\mathbf{\Gamma}}$ as strain measures [Kafadar et al. 1971; Eringen 1999a], the modified deformation gradient $\underset{\sim}{\bar{\mathbf{U}}}$ is not null for the initial configuration so the following Cosserat strain is defined:

$$\underset{\sim}{\mathbf{\Xi}}^e = \underset{\sim}{\bar{\mathbf{U}}}^e - \underset{\sim}{\mathbf{I}}, \tag{6.63}$$

The deformations $\underset{\sim}{\mathbf{\Xi}}$ and $\underset{\sim}{\mathbf{\Gamma}}$ are called *micro-polar Lagrangian strain and curvature tensors* by Grammenoudis and Tsakmakis, and by Bauer et al. [Grammenoudis et al. 2001; Bauer, Schäfer, et al. 2010] and Biot-Like quantities by Erdelj et al. [Erdelj et al. 2020]. Here we stick to the first nomenclature. Note that:

$$\dot{\underset{\sim}{\mathbf{\Xi}}}^e = \dot{\underset{\sim}{\bar{\mathbf{U}}}}^e. \tag{6.64}$$

Clausius-Duhem inequality

The second principle of thermodynamics in isothermal case can be written as:

$$-\rho\dot{\psi} + p^{(i)} \geq 0, \tag{6.65}$$

	$\underset{\sim}{\mathbf{S}}$ (I P-K)	$\underset{\sim}{\mathbf{T}}$ (II P-K)	$\underset{\sim}{\bar{\boldsymbol{\sigma}}}$
$\underset{\sim}{\mathbf{S}}$ (I P-K)	-	$\underset{\sim}{\mathbf{S}} = \underset{\sim}{\mathbf{R}}\underset{\sim}{\mathbf{T}}$	$\underset{\sim}{\mathbf{S}} = \underset{\sim}{\mathbf{R}}\underset{\sim}{\bar{\boldsymbol{\sigma}}}\underset{\sim}{\mathbf{R}}^T \cdot \underset{\sim}{\mathbf{F}}^{-T}$
$\underset{\sim}{\mathbf{T}}$ (II P-K)	$\underset{\sim}{\mathbf{T}} = \underset{\sim}{\mathbf{R}}^T\underset{\sim}{\mathbf{S}}$	-	$\underset{\sim}{\mathbf{T}} = \underset{\sim}{\bar{\boldsymbol{\sigma}}}\underset{\sim}{\mathbf{R}}^T\underset{\sim}{\mathbf{F}}^{-T}$
$\underset{\sim}{\bar{\boldsymbol{\sigma}}}$	$\underset{\sim}{\bar{\boldsymbol{\sigma}}} = \underset{\sim}{\mathbf{R}}^T\underset{\sim}{\mathbf{S}}\underset{\sim}{\mathbf{F}}^T\underset{\sim}{\mathbf{R}}$	$\underset{\sim}{\bar{\boldsymbol{\sigma}}} = \underset{\sim}{\mathbf{T}}\underset{\sim}{\mathbf{F}}^T\underset{\sim}{\mathbf{R}}$	-

Table 6.3: Relationships between the different stresses.

where ρ is the Eulerian density of the continuum and $\dot{\psi}$ is the Helmholtz free energy rate per unit of mass. By substituting the internal power density and by assuming that the deformation is purely elastic, the inequality in a Lagrangian form can be obtained:

$$-\rho_0\dot{\psi} + \underset{\sim}{\mathbf{T}} : \dot{\underset{\sim}{\mathbf{\Xi}}}^e + \underset{\sim}{\mathbf{T}}_c : \dot{\underset{\sim}{\mathbf{\Gamma}}}^e \geq 0, \tag{6.66}$$

where ρ_0 is the density of the medium in the reference configuration. By considering the dependency of the Helmholtz free energy on the Cosserat deformations (which is purely elastic):

$$\rho_0\dot{\psi}\left(\underset{\sim}{\mathbf{\Xi}}^e, \underset{\sim}{\mathbf{\Gamma}}^e\right) = \rho_0\left[\frac{\partial\psi}{\partial\underset{\sim}{\mathbf{\Xi}}^e} : \dot{\underset{\sim}{\mathbf{\Xi}}}^e + \frac{\partial\psi}{\partial\underset{\sim}{\mathbf{\Gamma}}^e} : \dot{\underset{\sim}{\mathbf{\Gamma}}}^e\right], \tag{6.67}$$

then, the Clausius-Duhem inequality can be written as:

$$\left[-\rho_0\frac{\partial\psi}{\partial\underset{\sim}{\mathbf{\Xi}}^e} + \underset{\sim}{\mathbf{T}}\right] : \dot{\underset{\sim}{\mathbf{\Xi}}}^e + \left[-\rho_0\frac{\partial\psi}{\partial\underset{\sim}{\mathbf{\Gamma}}^e} + \underset{\sim}{\mathbf{T}}_c\right] : \dot{\underset{\sim}{\mathbf{\Gamma}}}^e \geq 0, \tag{6.68}$$

and since the material is purely hyper-elastic, no form of dissipation is allowed, therefore the followings can be written:

$$\underset{\sim}{\mathbf{T}} = \rho_0\frac{\partial\psi}{\partial\underset{\sim}{\mathbf{\Xi}}^e}, \tag{6.69}$$

$$\underset{\sim}{\mathbf{T}}_c = \rho_0\frac{\partial\psi}{\partial\underset{\sim}{\mathbf{\Gamma}}^e}, \tag{6.70}$$

from these, the constitutive behavior can be directly derived from the specific chosen form of the Helmholtz potential.

Helmholtz free energy definition

The Helmholtz free energy can be though to be dependent on the elastic Cosserat strain $\underset{\sim}{\bar{\mathbf{U}}}^e$ and elastic wryness $\underset{\sim}{\mathbf{\Gamma}}^e$[Erdelj et al. 2020; Neff 2006; Bauer, Dettmer, et al. 2012]:

$$\rho_0\psi^e\left(\underset{\sim}{\mathbf{\Xi}}^e, \underset{\sim}{\mathbf{\Gamma}}^e\right) = \frac{\lambda}{2}\left[\mathrm{tr}\left(\underset{\sim}{\mathbf{\Xi}}^e\right)\right]^2 + \mu||\mathrm{sym}\left(\underset{\sim}{\mathbf{\Xi}}^e\right)||^2 + \mu_c||\mathrm{skew}\left(\underset{\sim}{\mathbf{\Xi}}^e\right)||^2 + \frac{\alpha}{2}\left[\mathrm{tr}\left(\underset{\sim}{\mathbf{\Gamma}}^e\right)\right]^2 + \beta||\mathrm{sym}\underset{\sim}{\mathbf{\Gamma}}^e||^2 + \gamma||\mathrm{skew}\left(\underset{\sim}{\mathbf{\Gamma}}^e\right)||^2. \tag{6.71}$$

It was possible to define the Helmholtz free energy as function of $\underset{\sim}{\mathbf{\Xi}}^e$ and $\underset{\sim}{\mathbf{\Gamma}}^e$ thanks to the fact that these are objective quantities, i.e. the Cosserat configuration is obtained through an isomorphic transformation (the metric is unchanged). From Equations (6.71), (6.69) and (6.70), the stress and couple stress in the Cosserat configuration can be written for this specific choice of the Helmholtz free energy. The second Piola-Kirchhoff stress and couple stress tensors:

$$\underset{\sim}{\mathbf{T}} = \lambda\mathrm{tr}\left(\underset{\sim}{\mathbf{\Xi}}^e\right)\underset{\sim}{\mathbf{I}} + (\mu+\mu_c)\left[\underset{\sim}{\mathbf{\Xi}}^e\right] + (\mu-\mu_c)\left[\underset{\sim}{\mathbf{\Xi}}^{e^T}\right], \tag{6.72}$$

$$\underset{\sim}{\mathbf{T}}_c = \alpha\,\mathrm{tr}\left(\underset{\sim}{\mathbf{\Gamma}}^e\right)\underset{\sim}{\mathbf{I}} + (\beta+\gamma)\left[\underset{\sim}{\mathbf{\Gamma}}^e\right] + (\beta-\gamma)\left[\underset{\sim}{\mathbf{\Gamma}}^{e^T}\right]. \tag{6.73}$$

6.5 Rate-dependent elasto-viscoplastic material

In order to mathematically describe the plastic behavior of the medium, it might result useful to introduce plasticity through an internal state variable, which can coincide with the generalized cumulative equivalent plastic deformation measure, i.e. Λ^p_{eq}. The form here adopted to describe the Helmholtz free energy for a plastic material follows the same structure as the one in Equation (6.71), but, in addition, there is also the contribution of the plastic part of the deformation measure:

$$\rho\psi\left(\underset{\sim}{\boldsymbol{\Xi}}^e, \underset{\sim}{\boldsymbol{\Gamma}}^e, \Lambda^p_{eq}\right) = \rho\psi^e + \rho\psi^p, \tag{6.74}$$

where ψ^e is the part of the Helmholtz free energy associated with the elastic material behavior already stated in Equation (6.71), and ψ^p includes the free energy that depends on the plastic developments of the medium. The rate of the Helmholtz free energy thus reads:

$$\rho_0\dot{\psi}\left(\underset{\sim}{\boldsymbol{\Xi}}^e, \underset{\sim}{\boldsymbol{\Gamma}}^e, \Lambda^p_{eq}\right) = \rho_0\left[\frac{\partial\psi}{\partial\underset{\sim}{\boldsymbol{\Xi}}^e} : \dot{\underset{\sim}{\boldsymbol{\Xi}}}^e + \frac{\partial\psi}{\partial\underset{\sim}{\boldsymbol{\Gamma}}^e} : \dot{\underset{\sim}{\boldsymbol{\Gamma}}}^e + \frac{\partial\psi}{\partial\Lambda^p_{eq}}\dot{\Lambda}^p_{eq}\right], \tag{6.75}$$

The Clausius-Duhem inequality can be rewritten as:

$$-\rho\dot{\psi} + p^{(i)} \geq 0, \tag{6.76}$$

or in a Lagrangian framework:

$$-\rho_0\dot{\psi} + \underset{\sim}{\mathbf{T}} : \dot{\underset{\sim}{\boldsymbol{\Xi}}} + \underset{\sim}{\mathbf{T}}_c : \dot{\underset{\sim}{\boldsymbol{\Gamma}}} \geq 0. \tag{6.77}$$

At this point, considering that the time variation of the Helmholtz free energy can be developed based on the variables upon which it depends:

$$\rho_0\dot{\psi}\left(\underset{\sim}{\boldsymbol{\Xi}}^e, \underset{\sim}{\boldsymbol{\Gamma}}^e, \Lambda^p_{eq}\right) = \rho_0\left[\frac{\partial\psi}{\partial\underset{\sim}{\boldsymbol{\Xi}}^e} : \dot{\underset{\sim}{\boldsymbol{\Xi}}}^e + \frac{\partial\psi}{\partial\underset{\sim}{\boldsymbol{\Gamma}}^e} : \dot{\underset{\sim}{\boldsymbol{\Gamma}}}^e + \frac{\partial\psi}{\partial\Lambda^p_{eq}}\dot{\Lambda}^p_{eq}\right], \tag{6.78}$$

it is possible to use the elasto-plastic decompositions of deformation gradient and wryness as in Equations (6.28) and (6.29) to write Equation (6.77) as:

$$\left[-\rho_0\frac{\partial\psi}{\partial\underset{\sim}{\boldsymbol{\Xi}}^e} + \underset{\sim}{\mathbf{T}}\underset{\sim}{\mathbf{F}}^{p^T}\right] : \dot{\underset{\sim}{\boldsymbol{\Xi}}}^e + \left[-\rho_0\frac{\partial\psi}{\partial\underset{\sim}{\boldsymbol{\Gamma}}^e} + \underset{\sim}{\mathbf{T}}_c\underset{\sim}{\mathbf{F}}^{p^T}\right] : \dot{\underset{\sim}{\boldsymbol{\Gamma}}}^e + \left[\underset{\sim}{\bar{\mathbf{U}}}^{e^T}\underset{\sim}{\mathbf{T}} + \underset{\sim}{\boldsymbol{\Gamma}}^{e^T}\underset{\sim}{\mathbf{T}}_c\right] : \dot{\underset{\sim}{\boldsymbol{\Xi}}}^p + \left[\underset{\sim}{\mathbf{T}}_c\right] : \dot{\underset{\sim}{\boldsymbol{\Gamma}}}^p - \frac{\partial\psi}{\partial\Lambda^p_{eq}}\dot{\Lambda}^p_{eq} \geq 0, \tag{6.79}$$

where, by assuming that the first two entries are purely energetic, the followings can be inferred:

$$\underset{\sim}{\mathbf{T}} = \rho_0\frac{\partial\psi}{\partial\underset{\sim}{\boldsymbol{\Xi}}^e} \cdot \underset{\sim}{\mathbf{F}}^{p^{-T}}, \tag{6.80}$$

$$\underset{\sim}{\mathbf{T}}_c = \rho_0\frac{\partial\psi}{\partial\underset{\sim}{\boldsymbol{\Gamma}}^e} \cdot \underset{\sim}{\mathbf{F}}^{p^{-T}}, \tag{6.81}$$

which, for the chosen form of the Helmholtz free energy, become:

$$\underset{\sim}{\mathbf{T}} = \left\{ \lambda \mathrm{tr}\left(\underset{\sim}{\boldsymbol{\Xi}}^{e}\right) \underset{\sim}{\mathbf{I}} + (\mu + \mu_c)\left[\underset{\sim}{\boldsymbol{\Xi}}^{e}\right] + (\mu - \mu_c)\left[\underset{\sim}{\boldsymbol{\Xi}}^{e^T}\right] \right\} \cdot \underset{\sim}{\mathbf{F}}^{p^{-T}}, \tag{6.82}$$

$$\underset{\sim}{\mathbf{T}}_c = \left\{ \alpha \,\mathrm{tr}\left(\underset{\sim}{\mathbf{R}}^{T}\underset{\sim}{\boldsymbol{\Gamma}}^{e}\right) \underset{\sim}{\mathbf{I}} + (\beta + \gamma)\left[\underset{\sim}{\mathbf{R}}^{T}\underset{\sim}{\boldsymbol{\Gamma}}^{e}\right] + (\beta - \gamma)\left[\underset{\sim}{\boldsymbol{\Gamma}}^{e^T}\underset{\sim}{\mathbf{R}}\right] \right\} \cdot \underset{\sim}{\mathbf{F}}^{p^{-T}}. \tag{6.83}$$

It is worth mentioning here that in classical continuum mechanics the second Piola-Kirchhoff stress usually does not depend on the plastic part of the deformation, whereas the stresses and couple stresses presented in Equations (6.82) and (6.83) do. The reason for this behavior lies in the different configuration in which the theories have been written: usually the second Piola-Kirchhoff stress is defined in the intermediate released configuration, whereas the stresses and couple stresses defined in the Cosserat theories have been defined in the reference (initial) configuration.
In classical continuum mechanics, the power conjugates to $\dot{\underset{\sim}{\mathbf{F}}}^{p}\underset{\sim}{\mathbf{F}}^{p^{-1}}$ is called Mandel stress. In case of the Cosserat media we have both a Mandel stress and Mandel couple stress, and they can be clearly identified from the Clausius Duhem inequality once the elastic part of the strain rate has been considered as recoverable, thus removed from the inequality. After rearranging Equation (6.79):

$$\dot{\underset{\sim}{\mathbf{F}}}^{p}\underset{\sim}{\mathbf{F}}^{p^{-1}} : \left[\underset{\sim}{\mathbf{F}}^{e^T}\underset{\sim}{\mathbf{T}}\underset{\sim}{\mathbf{F}}^{p^T} + \underset{\sim}{\boldsymbol{\Gamma}}^{e^T}\underset{\sim}{\mathbf{T}}_c\underset{\sim}{\mathbf{F}}^{p^T}\right] + \dot{\underset{\sim}{\boldsymbol{\Gamma}}}^{p}\underset{\sim}{\mathbf{F}}^{p^{-1}} : \left[\underset{\sim}{\mathbf{T}}_c\underset{\sim}{\mathbf{F}}^{p^T}\right] - \frac{\partial \psi}{\partial \Lambda^{p}_{eq}}\dot{\Lambda}^{p}_{eq} \geq 0, \tag{6.84}$$

from which, the Mandel stress and couple stress can be identified as:

$$\underset{\sim}{\boldsymbol{\Pi}} = \underset{\sim}{\bar{\mathbf{U}}}^{e^T} \cdot \underset{\sim}{\mathbf{T}} \cdot \underset{\sim}{\mathbf{F}}^{p^T} + \underset{\sim}{\boldsymbol{\Gamma}}^{e^T} \cdot \underset{\sim}{\mathbf{T}}_c \cdot \underset{\sim}{\mathbf{F}}^{p^T}, \tag{6.85}$$

$$\underset{\sim}{\boldsymbol{\Pi}}_c = \underset{\sim}{\mathbf{T}}_c \cdot \underset{\sim}{\boldsymbol{\Xi}}^{p^T}, \tag{6.86}$$

and, by using the just derived formulations of $\underset{\sim}{\mathbf{T}}$ and $\underset{\sim}{\mathbf{T}}_c$, the Mandel stress and couple stress can be finally be written as:

$$\underset{\sim}{\boldsymbol{\Pi}} = \rho_0 \underset{\sim}{\bar{\mathbf{U}}}^{e^T} \cdot \frac{\partial \psi}{\partial \underset{\sim}{\boldsymbol{\Xi}}^{e}} + \rho_0 \underset{\sim}{\boldsymbol{\Gamma}}^{e^T} \cdot \frac{\partial \psi}{\partial \underset{\sim}{\boldsymbol{\Gamma}}^{e}}, \tag{6.87}$$

$$\underset{\sim}{\boldsymbol{\Pi}}_c = \rho_0 \frac{\partial \psi}{\partial \underset{\sim}{\boldsymbol{\Gamma}}^{e}}. \tag{6.88}$$

By using the chosen formulations of the Helmholtz free energy, the Mandel stress and couple stress can be written as:

$$\begin{aligned} \underset{\sim}{\boldsymbol{\Pi}} = \lambda \mathrm{tr}\left(\underset{\sim}{\bar{\mathbf{U}}}^{e}\right) \underset{\sim}{\boldsymbol{\Xi}}^{e} + (\mu + \mu_c)\left[\underset{\sim}{\bar{\mathbf{U}}}^{e^T} \cdot \underset{\sim}{\boldsymbol{\Xi}}^{e}\right] + (\mu - \mu_c)\left[\underset{\sim}{\bar{\mathbf{U}}}^{e^T} \cdot \underset{\sim}{\boldsymbol{\Xi}}^{e^T}\right] + \\ \alpha \,\mathrm{tr}\left(\underset{\sim}{\boldsymbol{\Gamma}}^{e}\right) \underset{\sim}{\boldsymbol{\Gamma}}^{e} + (\beta + \gamma)\left[\underset{\sim}{\boldsymbol{\Gamma}}^{e^T} \cdot \underset{\sim}{\boldsymbol{\Gamma}}^{e}\right] + (\beta - \gamma)\left[\underset{\sim}{\boldsymbol{\Gamma}}^{e^T} \cdot \underset{\sim}{\boldsymbol{\Gamma}}^{e^T}\right], \end{aligned} \tag{6.89}$$

$$\underset{\sim}{\boldsymbol{\Pi}}_c = \alpha \,\mathrm{tr}\left(\underset{\sim}{\boldsymbol{\Gamma}}^{e}\right) \underset{\sim}{\mathbf{I}} + (\beta + \gamma)\left[\underset{\sim}{\boldsymbol{\Gamma}}^{e}\right] + (\beta - \gamma)\left[\underset{\sim}{\boldsymbol{\Gamma}}^{e^T}\right]. \tag{6.90}$$

At this stage, it can be assumed that a dissipation potential exists and that it is a function of the Mandel stress and couple stress:

$$\Omega = \Omega\left(\underset{\sim}{\mathbf{\Pi}}, \underset{\sim}{\mathbf{\Pi}}_c\right), \tag{6.91}$$

and the power conjugates to Mandel stress and couple stress can be thought to be governed by the following flow rules:

$$\dot{\underset{\sim}{\mathbf{F}}}^p \cdot \underset{\sim}{\mathbf{F}}^{p^{-1}} = \frac{\partial \Omega}{\partial \underset{\sim}{\mathbf{\Pi}}}, \tag{6.92}$$

$$\dot{\underset{\sim}{\mathbf{\Gamma}}}^p \cdot \underset{\sim}{\mathbf{F}}^{p^{-1}} = \frac{\partial \Omega}{\partial \underset{\sim}{\mathbf{\Pi}}_c}, \tag{6.93}$$

from which, the remaining terms of the Clausius Duhem inequality can be re-written as:

$$\underset{\sim}{\mathbf{\Pi}} : \frac{\partial \Omega}{\partial \underset{\sim}{\mathbf{\Pi}}} + \underset{\sim}{\mathbf{\Pi}}_c : \frac{\partial \Omega}{\partial \underset{\sim}{\mathbf{\Pi}}_c} - \frac{\partial \psi}{\partial \Lambda^p_{eq}} \dot{\Lambda}^p_{eq} \geq 0. \tag{6.94}$$

The dissipation potential can be re-written in a form that allows us to define a generalized plastic deformation measure for the Cosserat medium $\underset{\sim}{\mathbf{\Lambda}}^p$, as well as its own generalized stress-like-conjugate $\underset{\sim}{\mathbf{\Pi}}_{eq}$ as:

$$\Omega = \underset{\sim}{\mathbf{\Pi}} : \left[\dot{\underset{\sim}{\mathbf{F}}}^p \cdot \underset{\sim}{\mathbf{F}}^{p^{-1}}\right] + \underset{\sim}{\mathbf{\Pi}}_c : \left[\dot{\underset{\sim}{\mathbf{\Gamma}}}^p \cdot \underset{\sim}{\mathbf{F}}^{p^{-1}}\right] = \underset{\sim}{\mathbf{\Pi}}_{eq} : \dot{\underset{\sim}{\mathbf{\Lambda}}}^p. \tag{6.95}$$

Dissipation potential definition

In this report, we are going to use the general form of dissipation potential as originally proposed by Chaboche [J. L. Chaboche 2008], and we are going to adopt a single-criterion plasticity theory as proposed by Forest and Sievert [Forest and Sievert 2003]:

$$\Omega = \frac{K}{n+1} \left\langle \frac{f}{K} \right\rangle^{n+1}, \tag{6.96}$$

where f is the over-stress which can be written as:

$$f = \Pi_{eq} - \phi, \tag{6.97}$$

which is complemented by a newly proposed von Mises-derived Cosserat equivalent stress as presented in Section 5.1:

$$\Pi_{eq} = \sqrt{\frac{3}{2}\left[a_1 I_1(\underset{\sim}{\mathbf{\Pi}}) + a_2 I_2(\underset{\sim}{\mathbf{\Pi}}) + b_1 I_1(\underset{\sim}{\mathbf{\Pi}}_c) + b_2 I_2(\underset{\sim}{\mathbf{\Pi}}_c) + b_3 I_3(\underset{\sim}{\mathbf{\Pi}}_c)\right]}, \tag{6.98}$$

in which the I_i indicates the i-th invariant of the tensor. In this case, the chosen invariants are:

- $I_1(\underset{\sim}{\mathbf{\Pi}}) = \text{sym}\left(\underset{\sim}{\mathbf{\Pi}}_d\right) : \text{sym}\left(\underset{\sim}{\mathbf{\Pi}}_d\right)$,
- $I_2(\underset{\sim}{\mathbf{\Pi}}) = \text{skew}\left(\underset{\sim}{\mathbf{\Pi}}_d\right) : \text{skew}\left(\underset{\sim}{\mathbf{\Pi}}_d\right)$,
- $I_1(\underset{\sim}{\mathbf{\Pi}}_c) = \text{tr}\left(\underset{\sim}{\mathbf{\Pi}}_c^2\right)$,
- $I_2(\underset{\sim}{\mathbf{\Pi}}_c) = \text{sym}\left(\underset{\sim}{\mathbf{\Pi}}_{c_d}\right) : \text{sym}\left(\underset{\sim}{\mathbf{\Pi}}_{c_d}\right)$,
- $I_3(\underset{\sim}{\mathbf{\Pi}}_c) = \text{skew}\left(\underset{\sim}{\mathbf{\Pi}}_{c_d}\right) : \text{skew}\left(\underset{\sim}{\mathbf{\Pi}}_{c_d}\right)$,

where $_d$ indicates the deviatoric part of the tensor. Several forms can be assigned to the yield radius (assuming isotropic hardening), for example, a linear-bi-exponential isotropic hardening evolution law could be used:

$$\phi = \phi_0 + H\Lambda_{eq}^p + Q_1\left[1 - \exp\left(-g_1\Lambda_{eq}^p\right)\right] + Q_2\left[1 - \exp\left(-g_2\Lambda_{eq}^p\right)\right], \tag{6.99}$$

where ϕ is the radius of the yield surface in the principal stresses space. Chosen the form of the potential, it is possible to give the explicit form of the power conjugates to the Mandel stress and Mandel couple stress:

$$\dot{\underset{\sim}{\mathbf{F}}}^p \cdot \underset{\sim}{\mathbf{F}}^{p^{-1}} = \frac{\partial\Omega}{\partial\underset{\sim}{\mathbf{\Pi}}} = \frac{\partial\Omega}{\partial f}\frac{\partial f}{\partial\underset{\sim}{\mathbf{\Pi}}} = \dot{\lambda}\,\underset{\sim}{\mathbf{n}}, \tag{6.100}$$

$$\dot{\underset{\sim}{\mathbf{\Gamma}}}^p \cdot \underset{\sim}{\mathbf{F}}^{p^{-1}} = \frac{\partial\Omega}{\partial\underset{\sim}{\mathbf{\Pi}}_c} = \frac{\partial\Omega}{\partial f}\frac{\partial f}{\partial\underset{\sim}{\mathbf{\Pi}}_c} = \dot{\lambda}\,\underset{\sim}{\mathbf{n}}_c, \tag{6.101}$$

where $\dot{\lambda}$ is the plastic multiplier and $\underset{\sim}{\mathbf{n}}$ and $\underset{\sim}{\mathbf{n}}_c$ are the plastic flow directions (normal to the yield surface in the principal stresses space if the normality rule is assumed to hold). In the elasto-viscoplastic framework, the visco-plastic multiplier can be written as:

$$\dot{\lambda} = \left\langle \frac{f}{K} \right\rangle^n, \tag{6.102}$$

and the directions normal to the yield surfaces can be written as:

$$\underset{\sim}{\mathbf{n}} = \frac{3}{2}\frac{a_1\,\text{sym}\left(\underset{\sim}{\mathbf{\Pi}}_d\right) + a_2\,\text{skew}\left(\underset{\sim}{\mathbf{\Pi}}_d\right)}{\Pi_{eq}}, \tag{6.103}$$

$$\underset{\sim}{\mathbf{n}}_c = \frac{3}{2}\frac{b_1\,\underset{\sim}{\mathbf{\Pi}}_c^T + b_2\,\text{sym}\left(\underset{\sim}{\mathbf{\Pi}}_{c_d}\right) + b_3\,\text{skew}\left(\underset{\sim}{\mathbf{\Pi}}_{c_d}^T\right)}{\Pi_{eq}}. \tag{6.104}$$

6.5.1 Rate-dependent elasto-viscoplastic material with no dissipated wryness

In case the wryness is considered fully recoverable, it cannot be split into elastic and plastic parts:

$$\underset{\sim}{\mathbf{\Gamma}} \equiv \underset{\sim}{\mathbf{\Gamma}}^e, \tag{6.105}$$

so, from the second thermodynamic principle:

$$\left[-\rho_0\frac{\partial\psi}{\partial\underset{\sim}{\mathbf{\Xi}}^e} + \underset{\sim}{\mathbf{T}}\underset{\sim}{\mathbf{F}}^{p^T}\right] : \dot{\underset{\sim}{\mathbf{\Xi}}}^e + \left[-\rho_0\frac{\partial\psi}{\partial\underset{\sim}{\mathbf{\Gamma}}} + \underset{\sim}{\mathbf{T}}_c\right] : \dot{\underset{\sim}{\mathbf{\Gamma}}} + \left[\bar{\underset{\sim}{\mathbf{U}}}^{e^T}\underset{\sim}{\mathbf{T}}\right] : \dot{\underset{\sim}{\mathbf{\Xi}}}^p \geq 0, \tag{6.106}$$

and again:

$$\underset{\sim}{\mathbf{T}} = \rho_0 \frac{\partial \psi}{\partial \underset{\sim}{\mathbf{\Xi}}^e} \cdot \underset{\sim}{\mathbf{\Xi}}^{p^{-T}}, \tag{6.107}$$

$$\underset{\sim}{\mathbf{T}}_c = \rho_0 \frac{\partial \psi}{\partial \underset{\sim}{\mathbf{\Gamma}}}, \tag{6.108}$$

$$\underset{\sim}{\mathbf{\Pi}} = \rho_0 \underset{\sim}{\bar{\mathbf{U}}}^{e^T} \cdot \frac{\partial \psi}{\partial \underset{\sim}{\mathbf{\Xi}}^e}, \tag{6.109}$$

but no couple Mandel stress exists, therefore the J2 von Mises equivalent stress measure reads:

$$\Pi_{eq} = \sqrt{\frac{3}{2}\left[a_1 I_1(\underset{\sim}{\mathbf{\Pi}}_d) + a_2 I_2(\underset{\sim}{\mathbf{\Pi}}_d)\right]}. \tag{6.110}$$

Assuming the existence of a viscoplastic potential, we can write the Clausius-Duhem inequality as:

$$\underset{\sim}{\mathbf{\Pi}} : \frac{\partial \Omega}{\partial \underset{\sim}{\mathbf{\Pi}}} - \frac{\partial \psi}{\partial \Lambda^p_{eq}} \dot{\Lambda}^p_{eq} \geq 0, \tag{6.111}$$

and we can also assume that:

$$\dot{\underset{\sim}{\mathbf{F}}}^p \cdot \underset{\sim}{\mathbf{F}}^{p^{-1}} = \frac{\partial \Omega}{\partial \underset{\sim}{\mathbf{\Pi}}} = \frac{\partial \Omega}{\partial f} \frac{\partial f}{\partial \underset{\sim}{\mathbf{\Pi}}} = \dot{\lambda} \underset{\sim}{\mathbf{n}}, \tag{6.112}$$

and the viscoplastic multiplier is:

$$\dot{\lambda} = \left\langle \frac{f}{K} \right\rangle^n. \tag{6.113}$$

6.6 Rate-independent elasto-plastic materials

The rate-independent elasto-plastic material is a special case of the rate-dependent elasto-viscoplastic case. The description of the Helmholtz energy is the same, and the Clausius-Duhem inequality also still holds. The main difference is that the plastic multiplier is found by applying a specific condition on the plastic development, namely, the stress remains on the yield surface. Thus the plastic multiplier is implicitly evaluated by applying the so called consistency condition.

Consistency condition

In case of plastic material, the plastic increment is not arbitrarily chosen through the definition of a plastic potential as it is possible to do in the definition of the visco-plastic material, but rather it is the solution of a system of equations (constraints) applied on the plastic evolution of the medium, i.e. the consistency condition. Such condition ensures that through the plastic loading, the radius of yield surface coincides with the equivalent

stress applied, and it mathematically reads:

$$\begin{cases} f = 0, \\ \\ \dot{f} = 0, \end{cases} \tag{6.114}$$

for every positive increment of the plastic multiplier. By using the same definition of the yield function as in Equation (6.97), the previous system of Equations becomes:

$$\begin{cases} \mathrm{G}_{eq} = \phi, \\ \\ \dfrac{\partial f}{\partial \underset{\sim}{\mathbf{\Pi}}} : \dot{\underset{\sim}{\mathbf{\Pi}}} + \dfrac{\partial f}{\partial \underset{\sim}{\mathbf{\Pi}}_c} : \dot{\underset{\sim}{\mathbf{\Pi}}}_c + \dfrac{\partial f}{\partial \phi}\dot{\phi} = 0, \end{cases} \tag{6.115}$$

that is, the variation of the yield function is null although the continuum is under plastic loading, and this implies that the stress remains on the yield surface. In order to solve the consistency condition we will consider the followings:

$$\begin{aligned} \underset{\sim}{\mathbf{\Pi}} = \lambda \mathrm{tr}\left(\underset{\sim}{\mathbf{\Xi}}^e\right)\underset{\sim}{\bar{\mathbf{U}}}^e + (\mu+\mu_c)\left[\underset{\sim}{\bar{\mathbf{U}}}^{e^T}\cdot\underset{\sim}{\mathbf{\Xi}}^e\right] + (\mu-\mu_c)\left[\underset{\sim}{\bar{\mathbf{U}}}^{e^T}\cdot\underset{\sim}{\mathbf{\Xi}}^{e^T}\right] + \\ \alpha\,\mathrm{tr}\left(\underset{\sim}{\mathbf{\Gamma}}^e\right)\underset{\sim}{\mathbf{\Gamma}}^e + (\beta+\gamma)\left[\underset{\sim}{\mathbf{\Gamma}}^{e^T}\cdot\underset{\sim}{\mathbf{\Gamma}}^e\right] + (\beta-\gamma)\left[\underset{\sim}{\mathbf{\Gamma}}^{e^T}\cdot\underset{\sim}{\mathbf{\Gamma}}^{e^T}\right], \end{aligned} \tag{6.116}$$

$$\underset{\sim}{\mathbf{\Pi}}_c = \alpha\,\mathrm{tr}\left(\underset{\sim}{\mathbf{\Gamma}}^e\right)\underset{\sim}{\mathbf{I}} + (\beta+\gamma)\left[\underset{\sim}{\mathbf{\Gamma}}^e\right] + (\beta-\gamma)\left[\underset{\sim}{\mathbf{\Gamma}}^{e^T}\right], \tag{6.117}$$

then, considering the dependency of the Mandel stress and Mandel couple stress on the elastic parts of the deformation measures, of the micro-rotation and of wryness, and considering the dependency of ϕ on the equivalent cumulative plastic strain, the followings can be written:

$$\dot{\underset{\sim}{\mathbf{\Pi}}} = \frac{\partial \underset{\sim}{\mathbf{\Pi}}}{\partial \underset{\sim}{\mathbf{\Xi}}^e} : \dot{\underset{\sim}{\mathbf{\Xi}}}^e + \frac{\partial \underset{\sim}{\mathbf{\Pi}}}{\partial \underset{\sim}{\mathbf{\Gamma}}^e} : \dot{\underset{\sim}{\mathbf{\Gamma}}}^e, \tag{6.118}$$

$$\dot{\underset{\sim}{\mathbf{\Pi}}}_c = \frac{\partial \underset{\sim}{\mathbf{\Pi}}_c}{\partial \underset{\sim}{\mathbf{\Xi}}^e} : \dot{\underset{\sim}{\mathbf{\Xi}}}^e + \frac{\partial \underset{\sim}{\mathbf{\Pi}}_c}{\partial \underset{\sim}{\mathbf{\Gamma}}^e} : \dot{\underset{\sim}{\mathbf{\Gamma}}}^e, \tag{6.119}$$

$$\dot{\phi} = \frac{\partial \phi}{\partial \Lambda^p_{eq}}\dot{\Lambda}^p_{eq}. \tag{6.120}$$

Furthermore, it could be demonstrated that if we use an associated plastic flow, the variation of the yield stress with respect to the equivalent cumulative plastic strain is equal to the variation of the latter with respect to the plastic multiplier [Dunne et al. 2005]:

$$\frac{\partial \phi}{\partial \Lambda^p_{eq}}\dot{\Lambda}^p_{eq} = \frac{\partial \phi}{\partial \lambda}\dot{\lambda}. \tag{6.121}$$

With all the ingredients presented so far, the consistency condition reads:

$$\underset{\sim}{\mathbf{n}} : \left(\frac{\partial \underset{\sim}{\mathbf{\Pi}}}{\partial \underset{\sim}{\mathbf{\Xi}}^e} : \dot{\underset{\sim}{\mathbf{\Xi}}}^e + \frac{\partial \underset{\sim}{\mathbf{\Pi}}}{\partial \underset{\sim}{\mathbf{\Gamma}}^e} : \dot{\underset{\sim}{\mathbf{\Gamma}}}^e\right) + \underset{\sim}{\mathbf{n}}_c : \left(\frac{\partial \underset{\sim}{\mathbf{\Pi}}_c}{\partial \underset{\sim}{\mathbf{\Xi}}^e} : \dot{\underset{\sim}{\mathbf{\Xi}}}^e + \frac{\partial \underset{\sim}{\mathbf{\Pi}}_c}{\partial \underset{\sim}{\mathbf{\Gamma}}^e} : \dot{\underset{\sim}{\mathbf{\Gamma}}}^e\right) - \dot{\phi} = 0, \tag{6.122}$$

and this condition must be fed with the derivatives of the Mandel stress and Mandel couple stress with respect to the elastic deformation gradient and the elastic curvatures, which can be derived from equations (6.89) and (6.90), and the increments of the latter deformation measures can be derived from from Equations (6.32) and (6.33). Solving the consistency condition for the increment of the plastic multiplier will give:

$$\dot{\lambda} = \frac{\underset{\sim}{\mathbf{n}} : \left[\frac{\partial \underset{\sim}{\underset{\sim}{\mathbf{\Pi}}}}{\partial \underset{\sim}{\underset{\sim}{\mathbf{\Xi}}}^e} : \left(\dot{\underset{\sim}{\underset{\sim}{\mathbf{\Xi}}}} \underset{\sim}{\underset{\sim}{\mathbf{F}}}^{p^{-1}} \right) + \frac{\partial \underset{\sim}{\underset{\sim}{\mathbf{\Pi}}}}{\partial \underset{\sim}{\mathbf{\Gamma}}^e} : \left(\dot{\underset{\sim}{\mathbf{\Gamma}}} \underset{\sim}{\underset{\sim}{\mathbf{F}}}^{p^{-1}} \right) \right] + \underset{\sim}{\mathbf{n}}_c : \left[\frac{\partial \underset{\sim}{\underset{\sim}{\mathbf{\Pi}}}_c}{\partial \underset{\sim}{\underset{\sim}{\mathbf{\Xi}}}^e} : \left(\dot{\underset{\sim}{\underset{\sim}{\mathbf{\Xi}}}} \underset{\sim}{\underset{\sim}{\mathbf{F}}}^{p^{-1}} \right) + \frac{\partial \underset{\sim}{\underset{\sim}{\mathbf{\Pi}}}_c}{\partial \underset{\sim}{\mathbf{\Gamma}}^e} : \left(\dot{\underset{\sim}{\mathbf{\Gamma}}} \underset{\sim}{\underset{\sim}{\mathbf{F}}}^{p^{-1}} \right) \right]}{\frac{\partial \phi}{\partial \lambda} + \underset{\sim}{\mathbf{n}} : \left[\frac{\partial \underset{\sim}{\underset{\sim}{\mathbf{\Pi}}}}{\partial \underset{\sim}{\underset{\sim}{\mathbf{\Xi}}}^e} : \left(\underset{\sim}{\bar{\mathbf{U}}}^e \underset{\sim}{\mathbf{n}} \right) + \frac{\partial \underset{\sim}{\underset{\sim}{\mathbf{\Pi}}}}{\partial \underset{\sim}{\mathbf{\Gamma}}^e} : \left(\underset{\sim}{\mathbf{\Gamma}}^e \underset{\sim}{\mathbf{n}} + \underset{\sim}{\mathbf{n}}_c \right) \right] + \underset{\sim}{\mathbf{n}}_c : \left[\frac{\partial \underset{\sim}{\underset{\sim}{\mathbf{\Pi}}}_c}{\partial \underset{\sim}{\underset{\sim}{\mathbf{\Xi}}}^e} : \left(\underset{\sim}{\bar{\mathbf{U}}}^e \underset{\sim}{\mathbf{n}} \right) + \frac{\partial \underset{\sim}{\underset{\sim}{\mathbf{\Pi}}}_c}{\partial \underset{\sim}{\mathbf{\Gamma}}^e} : \left(\underset{\sim}{\mathbf{\Gamma}}^e \underset{\sim}{\mathbf{n}} + \underset{\sim}{\mathbf{n}}_c \right) \right]}. \tag{6.123}$$

Although the formulation seems complex, it is very much similar to its counterpart in a small deformation framework:

$$\dot{\lambda} = \frac{\underset{\sim}{\mathbf{n}} : \underset{\approx}{\mathbf{E}} : \dot{\underset{\sim}{\mathbf{e}}} + \underset{\sim}{\mathbf{n}}_c : \underset{\approx}{\mathbf{C}} : \dot{\underset{\sim}{\mathbf{k}}}}{\frac{\partial \phi}{\partial \lambda} + \underset{\sim}{\mathbf{n}} : \underset{\approx}{\mathbf{E}} : \underset{\sim}{\mathbf{n}} + \underset{\sim}{\mathbf{n}}_c : \underset{\approx}{\mathbf{C}} : \underset{\sim}{\mathbf{n}}_c}, \tag{6.124}$$

where $\underset{\approx}{\mathbf{E}}$ and $\underset{\approx}{\mathbf{C}}$ are the fourth-order elastic operators for the Cosserat strain, $\underset{\sim}{\mathbf{e}}$, and curvature ,$\underset{\sim}{\mathbf{k}}$, respectively. The first difference is that in small deformation the strain is defined as combination of displacement gradient and micro-rotation vector, whereas in the formulation we provided the explicit dependency on the deformation gradient and micro-rotation operator; the second difference is that in the linearized version the coupling between the stress/couple stress and the wryness/deformation gradient/rotation disappears.

6.6.1 Rate-independent elasto-plastic materials with no dissipative wryness

In this case it is necessary to re-write the consistency condition:

$$\begin{cases} \Pi_{eq} = \phi, \\ \dfrac{\partial f}{\partial \underset{\sim}{\underset{\sim}{\mathbf{\Pi}}}} : \dot{\underset{\sim}{\underset{\sim}{\mathbf{\Pi}}}} + \dfrac{\partial f}{\partial \phi} \dot{\phi} = 0, \end{cases} \tag{6.125}$$

thus:

$$\underset{\sim}{\mathbf{n}} : \left(\frac{\partial \underset{\sim}{\underset{\sim}{\mathbf{\Pi}}}}{\partial \underset{\sim}{\underset{\sim}{\mathbf{\Xi}}}^e} : \dot{\underset{\sim}{\underset{\sim}{\mathbf{\Xi}}}}^e + \frac{\partial \underset{\sim}{\underset{\sim}{\mathbf{\Pi}}}}{\partial \underset{\sim}{\mathbf{\Gamma}}^e} : \dot{\underset{\sim}{\mathbf{\Gamma}}}^e \right) - \dot{\phi} = 0, \tag{6.126}$$

and by isolating the $\dot{\lambda}$:

$$\dot{\lambda} = \frac{\underset{\sim}{\mathbf{n}} : \left[\frac{\partial \underset{\sim}{\underset{\sim}{\mathbf{\Pi}}}}{\partial \underset{\sim}{\underset{\sim}{\mathbf{\Xi}}}^e} : \left(\dot{\underset{\sim}{\underset{\sim}{\mathbf{U}}}} \underset{\sim}{\underset{\sim}{\mathbf{F}}}^{p^{-1}} \right) + \frac{\partial \underset{\sim}{\underset{\sim}{\mathbf{\Pi}}}}{\partial \underset{\sim}{\mathbf{\Gamma}}^e} : \left(\dot{\underset{\sim}{\mathbf{\Gamma}}}^e \right) \right]}{\frac{\partial \phi}{\partial \lambda} + \underset{\sim}{\mathbf{n}} : \left[\frac{\partial \underset{\sim}{\underset{\sim}{\mathbf{\Pi}}}}{\partial \underset{\sim}{\underset{\sim}{\mathbf{\Xi}}}^e} : \left(\underset{\sim}{\mathbf{\Xi}}^e \underset{\sim}{\mathbf{n}} \right) \right]}. \tag{6.127}$$

6.7 Thermal analysis

In case the temperature plays a relevant role in the analysis, its contribution must be included, and the whole framework should still obey the second thermodynamic principle. We restrict the analysis to an adiabatic scenario, in which the heat flux does not have time to flow within the bulk. Another assumption is that no additional deformations are induced by changes of temperature, and that the temperature only affects the radius of the yield surface. In this case, the temperature is not a degree of freedom, rather a state variable. In this case, the Helmholtz free energy is function of the temperature as well, and an additive decomposition of the contributions coming from elastic and thermo-plastic can be hypothesized [Grammenoudis et al. 2001]:

$$\rho_0\psi\left(\underset{\sim}{\Xi}^e, \underset{\sim}{\Gamma}^e, \Lambda^p_{eq}, T\right) = \rho_0\psi^e + \rho_0\psi^{p,T}, \tag{6.128}$$

and for the present investigation, we assumed it to have the following specific form:

$$\rho_0\psi^{p,T}\left(\Lambda^p_{eq}, T\right) = \left\{\frac{1}{2}H\Lambda^{p^2}_{eq} + Q_1\left[\Lambda^p_{eq} + \frac{e_1^{-b_1\Lambda^p_{eq}}}{b_1}\right] + Q_2\left[\Lambda^p_{eq} + \frac{e_1^{-b_2\Lambda^p_{eq}}}{b_2}\right]\right\}\cdot\left(\frac{T-T_0}{T_{\text{melt}}-T_0}\right) - \frac{1}{2}\rho_0\frac{C_\varepsilon}{T_0}\left(T-T_0\right)^2. \tag{6.129}$$

Considering that the Helmholtz free energy depends also on the temperature, its rate of variation can be expressed as:

$$\rho_0\dot{\psi}\left(\underset{\sim}{\Xi}^e, \underset{\sim}{\Gamma}^e, \Lambda^p_{eq}, T\right) = \rho_0\left[\frac{\partial\psi}{\partial\underset{\sim}{\Xi}^e} : \dot{\underset{\sim}{\Xi}}^e + \frac{\partial\psi}{\partial\underset{\sim}{\Gamma}^e} : \dot{\underset{\sim}{\Gamma}}^e + \frac{\partial\psi}{\partial\Lambda^p_{eq}}\dot{\Lambda}^p_{eq} + \frac{\partial\psi}{\partial T}\dot{T}\right], \tag{6.130}$$

and, in a non-isothermal case, it can also be expressed as:

$$\rho_0\dot{\psi} = J\,p^{(i)} - T\,\dot{\eta} - \dot{T}\,\eta. \tag{6.131}$$

By combining them we can write the heat equation as:

$$J\,p^{(i)} - \rho_0\left[\frac{\partial\psi}{\partial\underset{\sim}{\Xi}^e} : \dot{\underset{\sim}{\Xi}}^e + \frac{\partial\psi}{\partial\underset{\sim}{\Gamma}^e} : \dot{\underset{\sim}{\Gamma}}^e + \frac{\partial\psi}{\partial\Lambda^p_{eq}}\dot{\Lambda}^p_{eq} + \frac{\partial\psi}{\partial T}\dot{T}\right] - \dot{T}\,\eta - T\dot{\eta} = 0, \tag{6.132}$$

from the Equation above, considering that the temperature expressed in Kelvin can only be positive and considering that the internal power can be expressed as in Equation (6.52), the following Clausius-Duhem, inequality can be assumed to be valid:

$$\left[-\rho_0\frac{\partial\psi}{\partial\underset{\sim}{\Xi}^e} + \underset{\sim}{\mathbf{T}}\underset{\sim}{\mathbf{F}}^{p^T}\right] : \dot{\underset{\sim}{\Xi}}^e + \left[-\rho_0\frac{\partial\psi}{\partial\underset{\sim}{\Gamma}^e} + \underset{\sim}{\mathbf{T}}_c\underset{\sim}{\mathbf{F}}^{p^T}\right] : \dot{\underset{\sim}{\Gamma}}^e - \left[\rho_0\frac{\partial\psi}{\partial T} + \eta\right]\dot{T} - \left[\underset{\sim}{\bar{\mathbf{U}}}^{e^T}\underset{\sim}{\mathbf{T}} + \underset{\sim}{\mathbf{\Gamma}}^{e^T}\underset{\sim}{\mathbf{T}}_c\right] : \dot{\underset{\sim}{\mathbf{F}}}^p + \left[\underset{\sim}{\mathbf{T}}_c\right] : \dot{\underset{\sim}{\Gamma}}^p - R\,\dot{\Lambda}^p_{eq} \geq 0, \tag{6.133}$$

where we identified the thermodynamical force associated to the variation of the equivalent plastic strain:

$$R = \rho_0\frac{\partial\psi}{\partial\Lambda^p_{eq}} = \left\{H\Lambda^p_{eq} + Q_1\left[1 - e^{(-b_1\Lambda^p_{eq})}\right] + Q_2\left[1 - e^{(-b_2\Lambda^p_{eq})}\right]\right\}\left(\frac{T-T_0}{T_{\text{melt}}-T_0}\right), \tag{6.134}$$

which can be used to write the radius of the yield surface for the temperature-dependent case:

$$\phi = \phi_0 \left(\frac{T - T_0}{T_{\text{melt}} - T_0} \right) + R. \tag{6.135}$$

where ϕ_0 is the initial yield stress. Once again, the elastic parts of the deformation are recoverable. Furthermore, the following relationship can be derived:

$$\eta = -\rho_0 \frac{\partial \psi}{\partial T}. \tag{6.136}$$

Thus, the second thermodynamic principle would be exactly the same as in the plastic case, except for R, which, in this case, depends on the temperature. The most important element of this section, however, is the definition of the thermal increment, based on thermodynamical considerations. The adiabatic thermal rate (thus fully due to plastic power) can be computed from the heat Equation (6.132). The entropy can be evaluated from Equation (6.136):

$$\eta = -\left\{ \frac{1}{2} H \Lambda_{eq}^{p^2} + Q_1 \left[\Lambda_{eq}^p + \frac{e_1^{-b_1 \Lambda_{eq}^p}}{b_1} \right] + Q_2 \left[\Lambda_{eq}^p + \frac{e_2^{-b_2 \Lambda_{eq}^p}}{b_2} \right] \right\} \frac{1}{T_{\text{melt}} - T_0} + \rho_0 \frac{C_\varepsilon}{T_0} \left(T - T_0 \right), \tag{6.137}$$

from which, its variation is:

$$\dot{\eta} = \frac{\partial \eta}{\partial T} \dot{T} + \frac{\partial \eta}{\partial \Lambda_{eq}^p} \dot{\Lambda}_{eq}^p. \tag{6.138}$$

At this point, the heat Equation (6.132) can be rewritten by using Equations (6.52) and (6.130):

$$\left[\underset{\sim}{\bar{\mathbf{U}}}^{e^T} \underset{\sim}{\mathbf{T}} + \underset{\sim}{\mathbf{\Gamma}}^{e^T} \underset{\sim}{\mathbf{T}}_c \right] : \dot{\underset{\sim}{\mathbf{F}}}^p + \left[\underset{\sim}{\mathbf{T}}_c \right] : \dot{\underset{\sim}{\mathbf{\Gamma}}}^p + T \, \dot{\eta} - R \, \dot{\Lambda}_{eq}^p = 0, \tag{6.139}$$

which, by making use of Equation (6.138), becomes:

$$\left[\underset{\sim}{\bar{\mathbf{U}}}^{e^T} \underset{\sim}{\mathbf{T}} + \underset{\sim}{\mathbf{\Gamma}}^{e^T} \underset{\sim}{\mathbf{T}}_c \right] : \dot{\underset{\sim}{\mathbf{F}}}^p + \left[\underset{\sim}{\mathbf{T}}_c \right] : \dot{\underset{\sim}{\mathbf{\Gamma}}}^p - \rho_0 C_\varepsilon \dot{T} - T \frac{\partial \eta}{\partial \Lambda_{eq}^p} \dot{\Lambda}_{eq}^p - R \, \dot{\Lambda}_{eq}^p = 0. \tag{6.140}$$

After simplification, the final form of the heat equation is:

$$\left[\underset{\sim}{\bar{\mathbf{U}}}^{e^T} \underset{\sim}{\mathbf{T}} + \underset{\sim}{\mathbf{\Gamma}}^{e^T} \underset{\sim}{\mathbf{T}}_c \right] : \dot{\underset{\sim}{\mathbf{F}}}^p + \left[\underset{\sim}{\mathbf{T}}_c \right] : \dot{\underset{\sim}{\mathbf{\Gamma}}}^p - \rho_0 \, C_\varepsilon \, \dot{T} + \left[\frac{H \Lambda_{eq}^p + Q_1 \left[1 - e^{(-g_1 \Lambda_{eq}^p)} \right] + Q_2 \left[1 - e^{(-g_2 \Lambda_{eq}^p)} \right]}{T_{\text{melt}} - T_0} \right] T_0 \, \dot{\Lambda}_{eq}^p = 0, \tag{6.141}$$

from which, the $\dot{T}$ term can be evaluated as:

$$\dot{T} = \frac{\left[\underset{\sim}{\bar{\mathbf{U}}}^{e^T} \underset{\sim}{\mathbf{T}} + \underset{\sim}{\mathbf{\Gamma}}^{e^T} \underset{\sim}{\mathbf{T}}_c \right] : \dot{\underset{\sim}{\mathbf{F}}}^p + \left[\underset{\sim}{\mathbf{T}}_c \right] : \dot{\underset{\sim}{\mathbf{\Gamma}}}^p}{\rho_0 \, C_\varepsilon} + \left[\frac{H \Lambda_{eq}^p + Q_1 \left[1 - e^{(-g_1 \Lambda_{eq}^p)} \right] + Q_2 \left[1 - e^{(-g_2 \Lambda_{eq}^p)} \right]}{\left(T_{\text{melt}} - T_0 \right) \left(\rho_0 \, C_\varepsilon \right)} \right] T_0 \, \dot{\Lambda}_{eq}^p. \tag{6.142}$$

in which the first term of the right hand side is the term which is classically used to evaluate an adiabatic temperature variation due to plastic work, and the second term is often neglected.

Chapter 7

Numerical implementation of the large deformation Cosserat model

This chapter presents the fundamental steps which are required for the numerical implementation of the Cosserat theory that has been presented in the previous chapter. The focus will be on the numerical treatment of the rotation when its magnitude is finite. In case of a small deformation framework, in fact, the rotations are linearized and their non-linearity is thus neglected. However,since the rotations are characterized by a non-linear mapping between the parameters and the Eulerian $\mathcal{R}^3$ space, proper handling is required for the description of many aspects, such as: incremental fields, differentials and update of the parameter fields. These aspects are extremely important for the numerical treatment, since the FEM analysis involves incremental increase of the loadings, evaluation of the element and material tangent matrices, and subsequent update of the fields at the end of the load increment.

Two versions of the numerical implementation will be presented, the first one for an unconstrained three-dimensional conditions, and the second one for plane-strain condition. The differentiation is required here because many steps are significantly simplified when plane conditions are applied. For instance, the parameters that are required to describe the rotation are reduced to one, and many non-linearities in the analysis disappear. For this reason, both 3D and 2D versions of the numerical treatment are presented.

The main objective of the FEM implementation is to provide the software with the element stiffness matrix and the external force vector. The formulation has been implemented in the software Z-SET, in which it was possible to include the Finite Element as an object in a C++ environment by mean of dynamic libraries.

The chapter begins with the description of the streps required to write the Cosserat theory in its strong form, which is a necessary passage in order to adapt the formulation for a finite element implementation. The weak form of the equilibrium equations proposed in the previous chapter are written for a general domain, and such domain is then transformed in finite elements, into which shape functions are used to discretize the fields of the degrees of freedom. Once the element stiffness matrix is obtained, the focus is the

treatment of the material behavior, to be specific, the evaluation of the material tangent matrix, which is used to integrate the material behavior. The variations of the Mandel stress and couple stress are also included in the treatment, which are used to evaluate the increments of the state variable used to monitor the plastic developments in the continuum. Finally, the topic of updating the micro-rotational degrees of freedom is addressed, and linearized versions of the differentials of rotations and wryness are provided.

The numerical implementation of the theory has been done while considering the following Helholtz free energy:

$$\rho_0\psi^e\left(\underset{\sim}{\underset{\sim}{\mathbf{RF}}}^e, \underset{\sim}{\boldsymbol{\Gamma}}^e\right) = \frac{\lambda}{2}\left(\mathrm{J}^e-1\right)^2 + \mu||\mathrm{sym}\left(\underset{\sim}{\underset{\sim}{\mathbf{RF}}}^e - \underset{\sim}{\mathbf{I}}\right)||^2 + \mu_c||\mathrm{skew}\left(\underset{\sim}{\underset{\sim}{\mathbf{RF}}}^e - \underset{\sim}{\mathbf{I}}\right)||^2 + \frac{\alpha}{2}\mathrm{tr}^2\left(\underset{\sim}{\boldsymbol{\Gamma}}^e\right) + \beta||\mathrm{sym}\underset{\sim}{\boldsymbol{\Gamma}}^e||^2 + \gamma||\mathrm{skew}\left(\underset{\sim}{\boldsymbol{\Gamma}}^e\right)||^2; \quad (7.1)$$

Most of the treatment of the rotations has been taken from the book of Bauchau, *"Flexible multibody dynamics"* [Bauchau 2011].

7.1 Strong form of the equilibrium equation and virtual work principle

The discretization procedure starts with the discretization of the entire domain of interest Ω in n sub-domains, which are commonly referred to as *mesh elements*. The equilibrium equations relative to the reference configuration (Lagrangian) have been derived in the previous chapter (Equations (6.55) and (6.56)), and they are here reported in absence of external body forces and moments:

$$\left(\underset{\sim}{\underset{\sim}{\mathbf{RT}}}\right)\cdot\underline{\boldsymbol{\nabla}}_0 = \underline{0}, \quad (7.2)$$

$$\left(\underset{\sim}{\underset{\sim}{\mathbf{RT}}}_c\right)\cdot\underline{\boldsymbol{\nabla}}_0 + \mathrm{axl}\left(\underset{\sim}{\underset{\sim}{\mathbf{RTF}}}^T - \underset{\sim}{\underset{\sim}{\mathbf{F}}}\,\underset{\sim}{\underset{\sim}{\mathbf{T}}}^T\underset{\sim}{\underset{\sim}{\mathbf{R}}}^T\right) = \underline{0}, \quad (7.3)$$

where $\underset{\sim}{\underset{\sim}{\mathbf{T}}}$ and $\underset{\sim}{\underset{\sim}{\mathbf{T}}}_c$ are the II Piola-Kirchhoff stress and couples stress tensors. The equilibrium equations are bounded by:

$$\underset{\sim}{\underset{\sim}{\mathbf{RT}}}\cdot\underline{\mathbf{n}}_0 = \underline{\mathbf{f}}_0^c, \quad (7.4)$$

$$\underset{\sim}{\underset{\sim}{\mathbf{RT}}}_c\cdot\underline{\mathbf{n}}_0 = \underline{\mathbf{g}}_0^c, \quad (7.5)$$

and this set of equations must hold for every configuration $\mathcal{C}$ (to which a couple $\{\underline{\mathbf{u}}, \underline{\boldsymbol{\theta}}\}$ corresponds) in which equilibrium holds. We could use this condition to our advantage and find the set of degrees of freedom that, for a given set of external boundary conditions (either in displacement or traction form), are in equilibrium. Let us assume that at time t the domain configuration is identified by $\underline{\mathbf{u}}^t, \underline{\boldsymbol{\theta}}^t$ and characterized by the stresses $\underset{\sim}{\underset{\sim}{\mathbf{T}}}^t, \underset{\sim}{\underset{\sim}{\mathbf{T}}}_c^t$, and that is in equilibrium. It is then possible to apply a perturbation to the equilibrium configuration by applying a virtual infinitesimal variation to the degrees of freedom; the virtual internal work associated to such perturbation would then be equal to:

$$\underline{\mathbf{u}}^*\cdot\left(\underset{\sim}{\underset{\sim}{\mathbf{RT}}}\right)^t\cdot\underline{\boldsymbol{\nabla}}_0 = \underline{0}, \quad (7.6)$$

$$\underline{\boldsymbol{\theta}}^*\cdot\left(\underset{\sim}{\underset{\sim}{\mathbf{RT}}}_c\right)^t\cdot\underline{\boldsymbol{\nabla}}_0 + \mathrm{axl}\left(\underset{\sim}{\underset{\sim}{\mathbf{RTF}}}^T - \underset{\sim}{\underset{\sim}{\mathbf{F}}}\,\underset{\sim}{\underset{\sim}{\mathbf{T}}}^T\underset{\sim}{\underset{\sim}{\mathbf{R}}}^T\right)^t\cdot\underline{\boldsymbol{\theta}}^* = \underline{0}, \quad (7.7)$$

where $\underline{\mathbf{u}}^*$ and $\underline{\boldsymbol{\theta}}^*$ are the virtual variations. By integrating these conditions over the domain, we end up with the following formulation of the internal virtual work $\mathcal{L}^i$:

$$\mathcal{L}^i = \int_{\Omega_0} \left\{ \underset{\sim}{\mathbf{T}}^t : \underset{\sim}{\mathbf{R}}^{T^t} \underset{\sim}{\mathbf{F}}^* + \underset{\sim}{\mathbf{T}}_c^t : \left[\underset{\sim}{\mathbf{R}}^{T^t} \left(\underline{\boldsymbol{\theta}}^* \otimes \underline{\boldsymbol{\nabla}}_0 \right) \right] + \operatorname{axl} \left(\underset{\sim\sim}{\mathbf{R}\mathbf{T}\mathbf{F}}^T - \underset{\sim\sim}{\mathbf{F}\mathbf{T}}^T \underset{\sim}{\mathbf{R}}^T \right)^t \cdot \underline{\boldsymbol{\theta}}^* \right\} d\Omega_0, \tag{7.8}$$

and we can similarly apply the same reasoning to the boundary equations to obtain the virtual variation of the external work as:

$$\mathcal{L}^e = \int_{\partial\Omega_0} \left[\underline{\mathbf{f}}_0^{c^t} \cdot \underline{\mathbf{u}}^* + \underline{\mathbf{g}}_0^{c^t} \cdot \underline{\boldsymbol{\theta}}^* \right] dS_0. \tag{7.9}$$

The *Virtual Work Principle* ensures that the configuration at time t is under equilibrium as long as the external virtual work is equal to the internal one for every virtual variation of the degrees of freedom (which are compatible with the applied constraints):

$$\mathcal{L}^{i^t} = \mathcal{L}^{e^t}, \quad \forall \left(\underline{\mathbf{u}}^*, \underline{\boldsymbol{\theta}}^* \right) \in \mathcal{R}^3. \tag{7.10}$$

We could make use of the virtual work principle to find the configuration at time $t + \Delta t$ that would be in equilibrium under the set of external forces balance:

$$\underline{\mathbf{u}}^* \cdot \left(\underset{\sim\sim}{\mathbf{R}\mathbf{T}} \right)^{t+\Delta t} \cdot \underline{\boldsymbol{\nabla}}_0 = \underline{0}, \tag{7.11}$$

$$\underline{\boldsymbol{\theta}}^* \cdot \left(\underset{\sim\sim}{\mathbf{R}\mathbf{T}}_c \right)^{t+\Delta t} \cdot \underline{\boldsymbol{\nabla}}_0 + \underline{\boldsymbol{\theta}}^* \cdot \operatorname{axl} \left(\underset{\sim\sim}{\mathbf{R}\mathbf{T}\mathbf{F}}^T - \underset{\sim\sim}{\mathbf{F}\mathbf{T}}^T \underset{\sim}{\mathbf{R}}^T \right)^{t+\Delta t} = \underline{0}, \tag{7.12}$$

leading to the following internal virtual work:

$$\mathcal{L}^i = \int_{\Omega_0} \left\{ \underset{\sim}{\mathbf{T}}^{t+\Delta t} : \underset{\sim}{\mathbf{R}}^{T^{t+\Delta t}} \underset{\sim}{\mathbf{F}}^* + \underset{\sim}{\mathbf{T}}_c^{t+\Delta t} : \left[\underset{\sim}{\mathbf{R}}^{T^{t+\Delta t}} \left(\underline{\boldsymbol{\theta}}^* \otimes \underline{\boldsymbol{\nabla}}_0 \right) \right] + \operatorname{axl} \left(\underset{\sim\sim}{\mathbf{R}\mathbf{T}\mathbf{F}}^T - \underset{\sim\sim}{\mathbf{F}\mathbf{T}}^T \underset{\sim}{\mathbf{R}}^T \right)^{t+\Delta t} \cdot \underline{\boldsymbol{\theta}}^* \right\} d\Omega_0, \tag{7.13}$$

and external virtual work

$$\mathcal{L}^e = \int_{\partial\Omega_0} \left[\underline{\mathbf{f}}^{c^{t+\Delta t}} \cdot \underline{\mathbf{u}}^* + \underline{\mathbf{g}}^{c^{t+\Delta t}} \cdot \underline{\boldsymbol{\theta}}^* \right] dS_0. \tag{7.14}$$

Considering the standard FEA treatment in terms of nodes and shape functions, the displacement and micro-rotational virtual fields can be discretized as:

$$u_i^* \left(x, y, z \right) = N_{ij}^u \left(x, y, z \right) \chi_j^{*\,u}, \tag{7.15}$$

$$\theta_i^* \left(x, y, z \right) = N_{ij}^\theta \left(x, y, z \right) \chi_j^{*\,\theta}, \tag{7.16}$$

where $\chi_j^{*\,u}$ and $\chi_j^{*\,\theta}$ are j-th nodal virtual variations of the degrees of freedom, and N_{ij}^u and N_{ij}^θ are the shape functions of the respective degrees of freedom (which could be in general different among each others). In many FE codes, the nodal degrees of freedom

are assembled in vectors:

$$\begin{bmatrix} \begin{bmatrix} \chi_1^{*u_1} & \chi_2^{*u_1} & \cdots & \chi_n^{*u_1} \end{bmatrix} & \begin{bmatrix} \chi_1^{*u_2} & \chi_2^{*u_2} & \cdots & \chi_n^{*u_2} \end{bmatrix} & \begin{bmatrix} \chi_1^{*u_3} & \chi_2^{*u_3} & \cdots & \chi_n^{*u_3} \end{bmatrix} \end{bmatrix}^T, \tag{7.17}$$

where n is the number of nodes. The same is done for the micro-rotational degrees of freedom:

$$\begin{bmatrix} \begin{bmatrix} \chi_1^{*\theta_1} & \chi_2^{*\theta_1} & \cdots & \chi_n^{*\theta_1} \end{bmatrix} & \begin{bmatrix} \chi_1^{*\theta_2} & \chi_2^{*\theta_2} & \cdots & \chi_n^{*\theta_2} \end{bmatrix} & \begin{bmatrix} \chi_1^{*\theta_3} & \chi_2^{*\theta_3} & \cdots & \chi_n^{*\theta_3} \end{bmatrix} \end{bmatrix}^T. \tag{7.18}$$

The shape functions are therefore assemble into matrices as:

$$\begin{bmatrix} \begin{bmatrix} N_1^u & N_2^u & \ldots & N_n^u \end{bmatrix} & \begin{bmatrix} 0 & 0 & \ldots & 0 \end{bmatrix} & \begin{bmatrix} 0 & 0 & \ldots & 0 \end{bmatrix} \\ \begin{bmatrix} 0 & 0 & \ldots & 0 \end{bmatrix} & \begin{bmatrix} N_1^u & N_2^u & \ldots & N_n^u \end{bmatrix} & \begin{bmatrix} 0 & 0 & \ldots & 0 \end{bmatrix} \\ \begin{bmatrix} 0 & 0 & \ldots & 0 \end{bmatrix} & \begin{bmatrix} 0 & 0 & \ldots & 0 \end{bmatrix} & \begin{bmatrix} N_1^u & N_2^u & \ldots & N_n^u \end{bmatrix} \end{bmatrix}. \tag{7.19}$$

The shape functions interpolate the nodal values inside the elements, and they can be functions of any order. Generally, first or second order polynomials are used, whereas third order functions are usually employed for isogeometric structural analysis [Russo and B. Chen 2020]. In order to evaluate the deformations within the element domain, the derivatives of the displacement and micro-rotational fields must be evaluated, and in classical FEA this is achieved through the employment of the so-known B matrix, which

contains the derivatives of the shape functions, and it is constructed as:

$$
\begin{bmatrix}
\begin{bmatrix} \frac{\partial N_1^u}{\partial x} & \frac{\partial N_2^u}{\partial x} & \dots & \frac{\partial N_n^u}{\partial x} \end{bmatrix} & \begin{bmatrix} 0 & 0 & \dots & 0 \end{bmatrix} & \begin{bmatrix} 0 & 0 & \dots & 0 \end{bmatrix} \\
\begin{bmatrix} 0 & 0 & \dots & 0 \end{bmatrix} & \begin{bmatrix} \frac{\partial N_1^u}{\partial y} & \frac{\partial N_2^u}{\partial y} & \dots & \frac{\partial N_n^u}{\partial y} \end{bmatrix} & \begin{bmatrix} 0 & 0 & \dots & 0 \end{bmatrix} \\
\begin{bmatrix} 0 & 0 & \dots & 0 \end{bmatrix} & \begin{bmatrix} 0 & 0 & \dots & 0 \end{bmatrix} & \begin{bmatrix} \frac{\partial N_1^z}{\partial z} & \frac{\partial N_2^u}{\partial z} & \dots & \frac{\partial N_n^u}{\partial z} \end{bmatrix} \\
\begin{bmatrix} \frac{\partial N_1^u}{\partial y} & \frac{\partial N_2^u}{\partial y} & \dots & \frac{\partial N_n^u}{\partial y} \end{bmatrix} & \begin{bmatrix} 0 & 0 & \dots & 0 \end{bmatrix} & \begin{bmatrix} 0 & 0 & \dots & 0 \end{bmatrix} \\
\begin{bmatrix} 0 & 0 & \dots & 0 \end{bmatrix} & \begin{bmatrix} \frac{\partial N_1^u}{\partial z} & \frac{\partial N_2^u}{\partial z} & \dots & \frac{\partial N_n^u}{\partial z} \end{bmatrix} & \begin{bmatrix} 0 & 0 & \dots & 0 \end{bmatrix} \\
\begin{bmatrix} 0 & 0 & \dots & 0 \end{bmatrix} & \begin{bmatrix} 0 & 0 & \dots & 0 \end{bmatrix} & \begin{bmatrix} \frac{\partial N_1^z}{\partial x} & \frac{\partial N_2^u}{\partial x} & \dots & \frac{\partial N_n^u}{\partial x} \end{bmatrix} \\
\begin{bmatrix} 0 & 0 & \dots & 0 \end{bmatrix} & \begin{bmatrix} \frac{\partial N_1^u}{\partial x} & \frac{\partial N_2^u}{\partial x} & \dots & \frac{\partial N_n^u}{\partial x} \end{bmatrix} & \begin{bmatrix} 0 & 0 & \dots & 0 \end{bmatrix} \\
\begin{bmatrix} 0 & 0 & \dots & 0 \end{bmatrix} & \begin{bmatrix} 0 & 0 & \dots & 0 \end{bmatrix} & \begin{bmatrix} \frac{\partial N_1^u}{\partial y} & \frac{\partial N_2^u}{\partial y} & \dots & \frac{\partial N_n^u}{\partial y} \end{bmatrix} \\
\begin{bmatrix} \frac{\partial N_1^z}{\partial z} & \frac{\partial N_2^u}{\partial z} & \dots & \frac{\partial N_n^u}{\partial z} \end{bmatrix} & \begin{bmatrix} 0 & 0 & \dots & 0 \end{bmatrix} & \begin{bmatrix} 0 & 0 & \dots & 0 \end{bmatrix}
\end{bmatrix}, \tag{7.20}
$$

and the same can be done with the micro-rotational degree of freedom (here not included for brevity). The application of this B matrix to the vector of the nodal degrees of freedom as defined in Equation (7.17) returns a column vector that contains the 9 entries of the deformation gradient tensor in the following order:

$$\begin{bmatrix} 1 & 4 & 9 \\ 7 & 2 & 5 \\ 6 & 8 & 3 \end{bmatrix}, \tag{7.21}$$

and such particular choice is strictly related to the structure of the FE code, Z-set in this case. By discretizing the virtual fields by mean of the N and B matrices, the internal work of a single element is:

$$\mathcal{L}^i_{(e)} = \left\{ \int_{\Omega_0} \left[(\mathbf{RT})^{t+\Delta t} \cdot \mathbf{B}^u \right] d\Omega \right\} \cdot \boldsymbol{\chi}^{*\,u} + \left\{ \int_{\Omega_0} \left[(\mathbf{RT}_c)^{t+\Delta t} \cdot \mathbf{B}^\theta \right] d\Omega \right\} \cdot \boldsymbol{\chi}^{*\,\theta} + \left\{ \int_{\Omega_0} \left[\mathrm{axl}\left(\mathbf{RTF}^T - \mathbf{FT}^T\mathbf{R}^T \right)^{t+\Delta t} \cdot \mathbf{N}^\theta \right] d\Omega \right\} \cdot \boldsymbol{\chi}^{*\,\theta}. \tag{7.22}$$

Accordingly, assuming that the only existing external forces are due to contact, from Equation (7.14) the external virtual work can of one element be discretized as:

$$\mathcal{L}^e_{(e)} = \left[\int_{\partial\Omega_{0_i}} \left(\mathbf{f}_0^{c^{t+\Delta t}} \cdot \mathbf{N}^u \right) dS \right] \cdot \boldsymbol{\chi}^{*\,u} + \left[\int_{\partial\Omega_i} \left(\mathbf{g}_0^{c^{t+\Delta t}} \cdot \mathbf{N}^\theta \right) dS \right] \cdot \boldsymbol{\chi}^{*\,\theta}, \tag{7.23}$$

from which, the discretized work balance equation in one element looks like:

$$\left\{ \int_{\Omega_0} \left[(\mathbf{RT})^{t+\Delta t} \cdot \mathbf{B}^u \right] d\Omega \right\} \boldsymbol{\chi}^{*\,u} + \left\{ \int_{\Omega_0} \left[(\mathbf{RT})^{t+\Delta t}\, \mathbf{B}^\theta + \mathrm{axl}\left(\mathbf{RTF}^T - \mathbf{FT}^T\mathbf{R}^T \right)^{t+\Delta t} \mathbf{N}^\theta \right] d\Omega \right\} \underline{\boldsymbol{\chi}}^{*\,\theta} = \left[\int_{\partial\Omega_0} \left(\mathbf{f}_0^{c^{t+\Delta t}} \mathbf{N}^u \right) dS \right] \boldsymbol{\chi}^{*\,u} + \left[\int_{\partial\Omega_0} \left(\mathbf{g}_0^{c^{t+\Delta t}} \mathbf{N}^\theta \right) dS \right] \boldsymbol{\chi}^{*\,\theta}, \tag{7.24}$$

and given the arbitrariness of the virtual variation of the nodal degrees of freedom, it is possible to remove them from the Equations, which would then transform into a balance equation among the internal an external forces:

$$\mathbf{f}_{\mathrm{int}}^{t+\Delta t} = \mathbf{f}_{\mathrm{ext}}^{t+\Delta t}, \tag{7.25}$$

which can be expressed in a column vector form as:

$$\begin{bmatrix} \\ \mathrm{f}_{\mathrm{int}_1}^{u\ t+\Delta t} \\ \\ \mathrm{f}_{\mathrm{int}_2}^{u\ t+\Delta t} \\ \\ \vdots \\ \\ \mathrm{f}_{\mathrm{int}_n}^{u\ t+\Delta t} \\ \mathrm{f}_{\mathrm{int}_1}^{\theta\ t+\Delta t} \\ \mathrm{f}_{\mathrm{int}_2}^{\theta\ t+\Delta t} \\ \vdots \\ \mathrm{f}_{\mathrm{int}_n}^{\theta\ t+\Delta t} \end{bmatrix} = \begin{bmatrix} \\ \mathrm{f}_{\mathrm{ext}_1}^{u\ t+\Delta t} \\ \\ \mathrm{f}_{\mathrm{ext}_2}^{u\ t+\Delta t} \\ \\ \vdots \\ \\ \mathrm{f}_{\mathrm{ext}_n}^{u\ t+\Delta t} \\ \mathrm{f}_{\mathrm{ext}_1}^{\theta\ t+\Delta t} \\ \mathrm{f}_{\mathrm{ext}_2}^{\theta\ t+\Delta t} \\ \vdots \\ \mathrm{f}_{\mathrm{ext}_n}^{\theta\ t+\Delta t} \end{bmatrix} \tag{7.26}$$

where the subscripts and superscripts of the forces indicate the number of the node and the type of degree of freedom respectively. The previous equation ensures the equivalence among the external and internal forces acting at every node i. Assuming that n nodes exist in the element, the internal and external force vectors will be n-dimensional. By

explicitly expressing the internal and external force vectors, they can be written as:

$$\begin{bmatrix} \int_{\Omega_0} \left\{ \underset{\sim}{\mathbf{B}}^{u^T} \underline{\mathbf{RT}}^{t+\Delta t} \right\} d\Omega \\ \int_{\Omega_0} \left\{ \underset{\sim}{\mathbf{B}}^{\theta^T} \underline{\mathbf{RT}}_c{}^{t+\Delta t} \right. \\ \left. + \underset{\sim}{\mathbf{N}}^{\theta^T} \left[\mathrm{axl} \left(\underset{\sim}{\underset{\sim}{\mathbf{RTF}}}^T - \underset{\sim}{\underset{\sim}{\mathbf{FT}}}^T \underset{\sim}{\mathbf{R}}^T \right)^{t+\Delta t} \right] \right\} d\Omega \end{bmatrix} = \begin{bmatrix} \int_{\partial\Omega_0} \left(\underset{\sim}{\mathbf{N}}^{u^T} \cdot \underline{\mathbf{f}}_0^{c^{t+\Delta t}} \right) dS \\ \int_{\partial\Omega_0} \left(\underset{\sim}{\mathbf{N}}^{\theta^T} \cdot \underline{\mathbf{g}}_0^{c^{t+\Delta t}} \right) dS \end{bmatrix}. \quad (7.27)$$

Some transposes appeared in the formulation to retain matrix multiplication compatibility. The equilibrium condition imposed by Equation (7.27) must be verified at every point of the load-path. We can define the residual vector $\underline{\mathbf{R}}$ as given by the difference between internal and external forces at time $t + \Delta t$, which should ideally equal to a null vector:

$$\underline{\mathbf{R}}^{t+\Delta t} = \underline{\mathbf{f}}_{int}^{t+\Delta t} - \underline{\mathbf{f}}_{ext}^{t+\Delta t}. \quad (7.28)$$

By assuming continuity in the deformation process of the continuum, the residual at time $t + \Delta t$ can be thought as derived from the one defined at time t:

$$\underline{\mathbf{R}}^{t+\Delta t} = \underline{\mathbf{R}}^{t} + \frac{\partial \underline{\mathbf{R}}^t}{\partial \underline{\boldsymbol{\chi}}} \cdot \underline{\boldsymbol{\delta\chi}}, \quad (7.29)$$

by hypothesizing that the external force does not depend on the d.o.f. variation,

$$\frac{\partial \underline{\mathbf{R}}^t}{\partial \underline{\boldsymbol{\chi}}} = \frac{\partial \underline{\mathbf{f}}_{\mathrm{int}}^t}{\partial \underline{\boldsymbol{\chi}}} = \underset{\sim}{\boldsymbol{K}}^t, \quad (7.30)$$

where $\underset{\sim}{\boldsymbol{K}}^t$ is the element stiffness matrix evaluated at time t, representing a perturbation of the internal forces with respect to the variations of the nodal degrees of freedom. In

order to write Equation (7.30) in a consistent way, the $\underset{\sim}{\boldsymbol{K}}$ matrix has the following entries:

$$\underset{\sim}{\boldsymbol{K}} = \begin{bmatrix} \frac{\partial \mathrm{f}^u_{\mathrm{int}_1}}{\partial u^1_1} & \frac{\partial \mathrm{f}^u_{\mathrm{int}_1}}{\partial u^2_1} & \frac{\partial \mathrm{f}^u_{\mathrm{int}_1}}{\partial u^3_1} & \cdots & \frac{\partial \mathrm{f}^u_{\mathrm{int}_1}}{\partial u^3_n} & \frac{\partial \mathrm{f}^u_{\mathrm{int}_1}}{\partial \theta^1_1} & \frac{\partial \mathrm{f}^u_{\mathrm{int}_1}}{\partial \theta^2_1} & \cdots & \frac{\partial \mathrm{f}^u_{\mathrm{int}_1}}{\partial \theta^3_n} \\ \vdots & \vdots & \vdots & \vdots & \vdots & \vdots & \vdots & \vdots & \vdots \\ \frac{\partial \mathrm{f}^u_{\mathrm{int}_n}}{\partial u^1_1} & \frac{\partial \mathrm{f}^u_{\mathrm{int}_n}}{\partial u^2_1} & \frac{\partial \mathrm{f}^u_{\mathrm{int}_n}}{\partial u^3_1} & \cdots & \frac{\partial \mathrm{f}^u_{\mathrm{int}_n}}{\partial u^3_n} & \frac{\partial \mathrm{f}^u_{\mathrm{int}_n}}{\partial \theta^1_1} & \frac{\partial \mathrm{f}^u_{\mathrm{int}_n}}{\partial \theta^2_1} & \cdots & \frac{\partial \mathrm{f}^u_{\mathrm{int}_n}}{\partial \theta^3_n} \\ \frac{\partial \mathrm{f}^\theta_{\mathrm{int}_1}}{\partial u^1_n} & \frac{\partial \mathrm{f}^\theta_{\mathrm{int}_1}}{\partial u^2_1} & \frac{\partial \mathrm{f}^\theta_{\mathrm{int}_1}}{\partial u^3_1} & \cdots & \frac{\partial \mathrm{f}^\theta_{\mathrm{int}_1}}{\partial u^3_n} & \frac{\partial \mathrm{f}^\theta_{\mathrm{int}_1}}{\partial \theta^1_1} & \frac{\partial \mathrm{f}^\theta_{\mathrm{int}_1}}{\partial \theta^2_1} & \cdots & \frac{\partial \mathrm{f}^\theta_{\mathrm{int}_1}}{\partial \theta^3_n} \\ \vdots & \vdots & \vdots & \vdots & \vdots & \vdots & \vdots & \vdots & \vdots \\ \frac{\partial \mathrm{f}^\theta_{\mathrm{int}_n}}{\partial u^1_n} & \frac{\partial \mathrm{f}^\theta_{\mathrm{int}_n}}{\partial u^2_1} & \frac{\partial \mathrm{f}^\theta_{\mathrm{int}_n}}{\partial u^3_1} & \cdots & \frac{\partial \mathrm{f}^\theta_{\mathrm{int}_n}}{\partial u^3_n} & \frac{\partial \mathrm{f}^\theta_{\mathrm{int}_n}}{\partial \theta^1_1} & \frac{\partial \mathrm{f}^\theta_{\mathrm{int}_n}}{\partial \theta^2_1} & \cdots & \frac{\partial \mathrm{f}^\theta_{\mathrm{int}_n}}{\partial \theta^3_n} \end{bmatrix} \tag{7.31}$$

which can also be re-written as:

$$\underset{\sim}{\boldsymbol{K}} = \left[\begin{array}{c|c} \int_{\Omega_0} \left(\underset{\sim}{\mathbf{B}}^{u^T} \cdot \frac{\partial \underline{\mathbf{RT}}}{\partial \underline{\boldsymbol{\chi}}^u} \right) d\Omega & \int_{\Omega_0} \left(\underset{\sim}{\mathbf{B}}^{u^T} \cdot \frac{\partial \underline{\mathbf{RT}}}{\partial \underline{\boldsymbol{\chi}}^\theta} \right) d\Omega \\ \hline \int_{\Omega_0} \left(\underset{\sim}{\mathbf{B}}^{\theta^T} \cdot \frac{\partial \underline{\mathbf{RT}}_c}{\partial \underline{\boldsymbol{\chi}}^u} + \underset{\sim}{\mathbf{N}}^{\theta^T} \cdot \frac{\partial \mathrm{axl}\left(\underset{\sim}{\mathbf{RTF}}^T - \underset{\sim}{\mathbf{FT}}^T \underset{\sim}{\mathbf{R}}^T \right)}{\partial \underline{\boldsymbol{\chi}}^u} \right) d\Omega & \int_{\Omega_0} \left(\underset{\sim}{\mathbf{B}}^{\theta^T} \cdot \frac{\partial \underline{\mathbf{RT}}_c}{\partial \underline{\boldsymbol{\chi}}^\theta} + \underset{\sim}{\mathbf{N}}^{\theta^T} \cdot \frac{\partial \mathrm{axl}\left(\underset{\sim}{\mathbf{RTF}}^T - \underset{\sim}{\mathbf{FT}}^T \underset{\sim}{\mathbf{R}}^T \right)}{\partial \underline{\boldsymbol{\chi}}^\theta} \right) d\Omega \end{array}\right], \tag{7.32}$$

where four groups composing the stiffness matrix can be clearly identified. The stresses appearing in the stiffness matrix are modified I Piola-Kirchhoff stresses and they are equal to:

$$\underline{\mathbf{S}} = \underline{\mathbf{RT}}, \tag{7.33}$$

$$\underline{\mathbf{s}} = \mathrm{axl}\left(\underset{\sim}{\mathbf{SF}}^T - \underset{\sim}{\mathbf{FS}}^T \right) = 2\,\mathrm{axl}\left(\underset{\sim}{\mathbf{SF}}^T \right), \tag{7.34}$$

$$\underline{\mathbf{M}} = \underline{\mathbf{RT}}_c, \tag{7.35}$$

which can also be evaluated as:

$$\underset{\sim}{\mathbf{S}} = \rho_0 \underset{\sim}{\mathbf{R}} \cdot \frac{\partial \psi}{\partial^\sharp \underset{\sim}{\mathbf{F}}^e} \underset{\sim}{\mathbf{F}}^{p^{-T}}, \tag{7.36}$$

$$\underset{\sim}{\mathbf{M}} = \rho_0 \underset{\sim}{\mathbf{R}} \cdot \frac{\partial \psi}{\partial^\sharp \underset{\sim}{\boldsymbol{\Gamma}}^e} \underset{\sim}{\mathbf{F}}^{p^{-T}}, \tag{7.37}$$

$$\underline{\mathbf{s}} = 2\,\mathrm{axl}\left(\underset{\sim}{\mathbf{R}} \cdot \frac{\partial \psi}{\partial^\sharp \underset{\sim}{\mathbf{F}}^e} \underset{\sim}{\mathbf{F}}^{e^T} + \underset{\sim}{\mathbf{R}} \cdot \frac{\partial \psi}{\partial^\sharp \underset{\sim}{\boldsymbol{\Gamma}}^e} \underset{\sim}{\boldsymbol{\Gamma}}^{e^T} \right) = 2\,\mathrm{axl}\left(\underset{\sim}{\mathbf{S}} \cdot \underset{\sim}{\mathbf{F}}^T + \underset{\sim}{\mathbf{M}} \cdot \underset{\sim}{\boldsymbol{\Gamma}}^T \right), \tag{7.38}$$

and, by using the chosen Helmholtz free energy in Equation (7.1):

$$\underset{\sim}{\mathbf{S}} = \left\{ \mathrm{J}^e \lambda \left(\mathrm{J} - 1\right) \underset{\sim}{\mathbf{F}}^{e^{-T}} + \left(\mu + \mu_c\right) \left[\underset{\sim}{\mathbf{F}}^e\right] + \left(\mu - \mu_c\right) \left[\underset{\sim}{\mathbf{R}} \cdot \underset{\sim}{\mathbf{F}}^{e^T} \cdot \underset{\sim}{\mathbf{R}}\right] - 2\mu \underset{\sim}{\mathbf{R}} \right\} \cdot \underset{\sim}{\mathbf{F}}^{p^{-T}}, \quad (7.39)$$

$$\underline{\mathbf{s}} = -\underline{\underline{\boldsymbol{\epsilon}}} : \left\{ \mathrm{J}^e \lambda \left(\mathrm{J}^e - 1\right) \underset{\sim}{\mathbf{I}} + \left(\mu + \mu_c\right) \left[\underset{\sim}{\mathbf{F}}^e \cdot \underset{\sim}{\mathbf{F}}^{e^T}\right] + \left(\mu - \mu_c\right) \left[\underset{\sim}{\mathbf{R}} \cdot \underset{\sim}{\mathbf{F}}^{e^T} \cdot \underset{\sim}{\mathbf{R}} \cdot \underset{\sim}{\mathbf{F}}^{e^T}\right] - 2\mu \left[\underset{\sim}{\mathbf{R}} \cdot \underset{\sim}{\mathbf{F}}^{e^T}\right] \right\}, \quad (7.40)$$

$$\underset{\sim}{\mathbf{M}} = \left\{ \alpha \, \mathrm{tr} \left(\underset{\sim}{\mathbf{R}}^T \cdot \underset{\sim}{\boldsymbol{\Gamma}}^e\right) \underset{\sim}{\mathbf{R}} + \left(\beta + \gamma\right) \left[\underset{\sim}{\boldsymbol{\Gamma}}^e\right] + \left(\beta - \gamma\right) \left[\underset{\sim}{\mathbf{R}} \cdot \underset{\sim}{\boldsymbol{\Gamma}}^{e^T} \cdot \underset{\sim}{\mathbf{R}}\right] \right\} \cdot \underset{\sim}{\mathbf{F}}^{p^{-T}}. \quad (7.41)$$

The stiffness matrix can therefore be written as:

$$\underset{\sim}{\boldsymbol{K}} = \left[\begin{array}{c|c} \int_{\Omega_0} \left(\underset{\sim}{\mathbf{B}}^{u^T} \cdot \dfrac{\partial \underline{\mathbf{S}}}{\partial \underline{\boldsymbol{\chi}}^u} \right) d\Omega & \int_{\Omega_0} \left(\underset{\sim}{\mathbf{B}}^{u^T} \cdot \dfrac{\partial \underline{\mathbf{S}}}{\partial \underline{\boldsymbol{\chi}}^\theta} \right) d\Omega \\ \hline \int_{\Omega_0} \left(\underset{\sim}{\mathbf{B}}^{\theta^T} \cdot \dfrac{\partial \underline{\mathbf{M}}}{\partial \underline{\boldsymbol{\chi}}^u} - \underset{\sim}{\mathbf{N}}^{\theta^T} \cdot \dfrac{\partial \underline{\mathbf{s}}}{\partial \underline{\boldsymbol{\chi}}^u} \right) d\Omega & \int_{\Omega_0} \left(\underset{\sim}{\mathbf{B}}^{\theta^T} \cdot \dfrac{\partial \underline{\mathbf{M}}}{\partial \underline{\boldsymbol{\chi}}^\theta} - \underset{\sim}{\mathbf{N}}^{\theta^T} \cdot \dfrac{\partial \underline{\mathbf{s}}}{\partial \underline{\boldsymbol{\chi}}^\theta} \right) d\Omega \end{array} \right]. \quad (7.42)$$

Note that geometrical non-linearities embedded in the evaluation of the variation of the B matrices are not included because we are integrating over the domain Ω_0 which is a fixed domain in time. In the classical continuum mechanics only the top-left part of the matrix is used. Regarding the external forces vector in Equation (7.27), $\underline{\mathbf{f}}_0^c$ and $\underline{\mathbf{g}}_0^c$ can be substituted by using the boundary conditions in Equations (7.4) and (7.5), then the application of the divergence theorem and the substitution of the chosen stress forms

leads to:

$$\begin{bmatrix} \int_{\partial\Omega_0} \left(\underset{\sim}{\mathbf{N}}^{u^T} \cdot \underline{\mathbf{f}}_0^c \right) dS \\ \int_{\partial\Omega_0} \left(\underset{\sim}{\mathbf{N}}^{\theta^T} \cdot \underline{\mathbf{g}}_0^c \right) dS \end{bmatrix} = \begin{bmatrix} \int_{\Omega_0} \left(\underset{\sim}{\mathbf{B}}^{u^T} \cdot \underline{\mathbf{S}} \right) d\Omega \\ \int_{\Omega_0} \left(\underset{\sim}{\mathbf{B}}^{\theta^T} \cdot \underline{\mathbf{M}} - \underset{\sim}{\mathbf{N}}^{\theta^T} \cdot \underline{\mathbf{s}} \right) d\Omega \end{bmatrix}. \tag{7.43}$$

The variation of the stresses and couple stresses in the element stiffness matrix (7.42) with respect to variations of the nodal degrees of freedom must be evaluated. In the derivation of such elements, the chain rule will be used: the stresses (or fluxes) are function of the deformations, which, in turn, are functions of the degrees of freedom. Furthermore, the integration of the entries in the stiffness matrix will be performed at the quadrature points (or integration points, *IP*) inside the domain, and we are considering the variation of such entries with respect to the degrees of freedom at the nodes (not at the IPs), thus proper handling of the link of the fields between IPs and nodal values must be included. By virtue of the chain rule, the following terms can be used:

$$\frac{\partial \underline{\mathbf{S}}}{\partial \underline{\boldsymbol{\chi}}^u} = \frac{\partial \underline{\mathbf{S}}}{\partial \underline{\mathbf{F}}} \cdot \frac{\partial \underline{\mathbf{F}}}{\partial \underline{\boldsymbol{\chi}}^u}, \tag{7.44}$$

$$\frac{\partial \underline{\mathbf{S}}}{\partial \underline{\boldsymbol{\chi}}^\theta} = \frac{\partial \underline{\mathbf{S}}}{\partial \underline{\mathbf{R}}} \cdot \frac{\partial \underline{\mathbf{R}}}{\partial \underline{\boldsymbol{\chi}}^{\boldsymbol{\theta}}} + \frac{\partial \underline{\mathbf{S}}}{\partial \underline{\boldsymbol{\Gamma}}} \cdot \frac{\partial \underline{\boldsymbol{\Gamma}}}{\partial \underline{\boldsymbol{\chi}}^{\boldsymbol{\theta}}}, \tag{7.45}$$

$$\frac{\partial \underline{\mathbf{M}}}{\partial \underline{\boldsymbol{\chi}}^u} = \frac{\partial \underline{\mathbf{M}}}{\partial \underline{\mathbf{F}}} \cdot \frac{\partial \underline{\mathbf{F}}}{\partial \underline{\boldsymbol{\chi}}^u}, \tag{7.46}$$

$$\frac{\partial \underline{\mathbf{M}}}{\partial \underline{\boldsymbol{\chi}}^\theta} = \frac{\partial \underline{\mathbf{M}}}{\partial \underline{\mathbf{R}}} \cdot \frac{\partial \underline{\mathbf{R}}}{\partial \underline{\boldsymbol{\chi}}^{\boldsymbol{\theta}}} + \frac{\partial \underline{\mathbf{M}}}{\partial \underline{\boldsymbol{\Gamma}}} \cdot \frac{\partial \underset{\sim}{\boldsymbol{\Gamma}}}{\partial \underline{\boldsymbol{\chi}}^{\boldsymbol{\theta}}}, \tag{7.47}$$

$$\frac{\partial \underline{\mathbf{s}}}{\partial \underline{\boldsymbol{\chi}}^u} = \frac{\partial \underline{\mathbf{s}}}{\partial \underline{\mathbf{F}}} \cdot \frac{\partial \underline{\mathbf{F}}}{\partial \underline{\boldsymbol{\chi}}^u}, \tag{7.48}$$

$$\frac{\partial \underline{\mathbf{s}}}{\partial \underline{\boldsymbol{\chi}}^\theta} = \frac{\partial \underline{\mathbf{s}}}{\partial \underline{\mathbf{R}}} \cdot \frac{\partial \underline{\mathbf{R}}}{\partial \underline{\boldsymbol{\chi}}^{\boldsymbol{\theta}}} + \frac{\partial \underline{\mathbf{s}}}{\partial \underline{\boldsymbol{\Gamma}}} \cdot \frac{\partial \underline{\boldsymbol{\Gamma}}}{\partial \underline{\boldsymbol{\chi}}^{\boldsymbol{\theta}}}, \tag{7.49}$$

and, by considering these relationships in the element stiffness matrix, it becomes:

$$\underset{\sim}{\boldsymbol{K}} = \left[\begin{array}{c|c} \int_{\Omega_{0_i}} \left[\underset{\sim}{\mathbf{B}}^{u^T} \cdot \left(\frac{\partial \underline{\mathbf{S}}}{\partial \underline{\mathbf{F}}}\right) \cdot \underset{\sim}{\mathbf{B}}^{u}\right] d\Omega & \int_{\Omega_{0_i}} \left[\underset{\sim}{\mathbf{B}}^{u^T} \cdot \left(\frac{\partial \underline{\mathbf{S}}}{\partial \underline{\mathbf{R}}} \cdot \frac{\partial \underline{\mathbf{R}}}{\partial \underline{\boldsymbol{\chi}}^{\boldsymbol{\theta}}} + \frac{\partial \underline{\mathbf{S}}}{\partial \underline{\boldsymbol{\Gamma}}} \cdot \frac{\partial \underline{\boldsymbol{\Gamma}}}{\partial \underline{\boldsymbol{\chi}}^{\boldsymbol{\theta}}}\right)\right] d\Omega \\ \hline \int_{\Omega_{0_i}} \left[\underset{\sim}{\mathbf{B}}^{\theta^T} \cdot \left(\frac{\partial \underline{\mathbf{M}}}{\partial \underline{\mathbf{F}}}\right) \cdot \underset{\sim}{\mathbf{B}}^{u} - \underset{\sim}{\mathbf{N}}^{\theta^T} \cdot \left(\frac{\partial \underline{\mathbf{s}}}{\partial \underline{\mathbf{F}}}\right) \cdot \underset{\sim}{\mathbf{B}}^{u}\right] d\Omega & \int_{\Omega_{0_i}} \left[\underset{\sim}{\mathbf{B}}^{\theta^T} \cdot \left(\frac{\partial \underline{\mathbf{M}}}{\partial \underline{\mathbf{R}}} \cdot \frac{\partial \underline{\mathbf{R}}}{\partial \underline{\boldsymbol{\chi}}^{\boldsymbol{\theta}}} + \frac{\partial \underline{\mathbf{M}}}{\partial \underline{\boldsymbol{\Gamma}}} \cdot \frac{\partial \underline{\boldsymbol{\Gamma}}}{\partial \underline{\boldsymbol{\chi}}^{\boldsymbol{\theta}}}\right) - \underset{\sim}{\mathbf{N}}^{\theta^T} \cdot \left(\frac{\partial \underline{\mathbf{s}}}{\partial \underline{\mathbf{R}}} \cdot \frac{\partial \underline{\mathbf{R}}}{\partial \underline{\boldsymbol{\chi}}^{\boldsymbol{\theta}}} + \frac{\partial \underline{\mathbf{s}}}{\partial \underline{\boldsymbol{\Gamma}}} \cdot \frac{\partial \underline{\boldsymbol{\Gamma}}}{\partial \underline{\boldsymbol{\chi}}^{\boldsymbol{\theta}}}\right)\right] d\Omega \end{array}\right]. \tag{7.50}$$

This specific expression of the element stiffness matrix still presents some terms that require further developing. To be specific: the variations of the fluxes with respect to the deformation measures at the IP, and the variations of wryness and rotation tensor at the IP with respect to the variation of the micro-rotational degree of freedom at the node. The formers are the entries of the material tangent matrix, whereas the latter terms given the non-linearity of the parameter fields, must be addressed separately (the fields are not additive as is case of the displacements). Both the elements that need further investigation will be addressed in the next sections in case of a 3D and 2D analysis.

7.2 Three dimensional model

7.2.1 Material tangent matrix

The variations of these stresses with respect to the deformation measures are entries of the material tangent matrix:

$$\mathrm{K}_{M_{ijkl}} = \frac{\partial (\mathrm{flux})_{ij}}{\partial (\mathrm{def})_{kl}}, \tag{7.51}$$

where the fluxes are:

$$\{\mathbf{S}, \mathbf{s}, \mathbf{M}\}, \tag{7.52}$$

and the deformations are:

$$\{\mathbf{F}, \mathbf{R}, \boldsymbol{\Gamma}\}. \tag{7.53}$$

If the fluxes and the deformations are rearranged in column vectors following the order defined in Equation (8.19d), the material tangent can be written as:

$$\mathrm{K}_{M_{ij}} = \frac{\partial (\mathrm{flux})_{i}}{\partial (\mathrm{def})_{j}}, \tag{7.54}$$

and the matrix would be composed as:

$$\left[\begin{array}{c|c|c} \dfrac{\partial \mathbf{S}_i}{\partial \mathbf{F}_j} & \dfrac{\partial \mathbf{S}_i}{\partial \mathbf{R}_j} & \dfrac{\partial \mathbf{S}_i}{\partial \mathbf{\Gamma}_j} \\ \hline \dfrac{\partial \mathbf{s}_i}{\partial \mathbf{F}_j} & \dfrac{\partial \mathbf{s}_i}{\partial \mathbf{R}_j} & \dfrac{\partial \mathbf{s}_i}{\partial \mathbf{\Gamma}_j} \\ \hline \dfrac{\partial \mathbf{M}_i}{\partial \mathbf{F}_j} & \dfrac{\partial \mathbf{M}_i}{\partial \mathbf{R}_j} & \dfrac{\partial \mathbf{M}_i}{\partial \mathbf{\Gamma}_j} \end{array}\right]. \tag{7.55}$$

Regarding the micro-rotation, we might want to make use of the chain rule, expressing the variations of the **flux** with respect to the micro-rotation matrix $\underset{\sim}{\mathbf{R}}$ at first (at the Gauss points), and then analyzing the variation of the latter with respect to the the nodal variation of the rotation parameters. The material tangent matrix that we require for the code implementation would provide the variation of the fluxed with respect to the deformations. In case plasticity occurs, the variation of the stresses $\underset{\sim}{\mathbf{S}}$, $\underline{\mathbf{s}}$ and $\underset{\sim}{\underset{\sim}{\mathbf{M}}}$ cannot be found explicitly anymore, but it must be rather implicitly evaluated through the identification of the consistent tangent matrix. Due to the lack of time, the evaluation of the consistent material tangent matrix has not been performed as it should have been. Such procedure can be found in the recent investigations carried out by Scherer et al. and Ling et al. in case of micromorphic and strain gradient theory respectively [Scherer, Phalke, et al. 2020b; Ling 2018]. In order to improve convergence, the material tangent matrix for the Cosserat media under finite deformation has been evaluated through the followings:

$$\frac{\partial (\bullet)}{\partial \underset{\sim}{\mathbf{F}}} = \frac{\partial (\bullet)}{\partial \underset{\sim}{\mathbf{F}}^e} \cdot \frac{\partial \underset{\sim}{\mathbf{F}}^e}{\partial \underset{\sim}{\mathbf{F}}} + \frac{\partial (\bullet)}{\partial \underset{\sim}{\mathbf{F}}^p} \cdot \frac{\partial \underset{\sim}{\mathbf{F}}^p}{\partial \underset{\sim}{\mathbf{F}}}, \tag{7.56}$$

$$\frac{\partial (\bullet)}{\partial \underset{\sim}{\mathbf{\Gamma}}} = \frac{\partial (\bullet)}{\partial \underset{\sim}{\mathbf{\Gamma}}^e} \cdot \frac{\partial \underset{\sim}{\mathbf{\Gamma}}^e}{\partial \underset{\sim}{\mathbf{\Gamma}}} + \frac{\partial (\bullet)}{\partial \underset{\sim}{\mathbf{F}}^p} \cdot \frac{\partial \underset{\sim}{\mathbf{F}}^p}{\partial \underset{\sim}{\mathbf{\Gamma}}} + \frac{\partial (\bullet)}{\partial \underset{\sim}{\mathbf{\Gamma}}^p} \cdot \frac{\partial \underset{\sim}{\mathbf{\Gamma}}^p}{\partial \underset{\sim}{\mathbf{\Gamma}}}. \tag{7.57}$$

By reporting the fluxes in their index forms:

$$S_{ij} = \left[\mathrm{J}^e \lambda (\mathrm{J}-1) \left(\underset{\sim}{\mathbf{F}}^{e\,-T} \right)_{ip} + (\mu + \mu_c) \left[F^e_{ip} \right] + (\mu - \mu_c) \left[R_{im} F^e_{nm} R_{np} \right] - 2\mu R_{ip} \right] F^{p^{-1}}_{jp}, \tag{7.58}$$

$$s_i = -\epsilon_{ilm}\Big\{ J^e\,\lambda\,(J^e-1)\,\delta_{lm} + (\mu+\mu_c)\,[F^e_{ln}F^e_{mn}] + (\mu-\mu_c)\,[R_{ln}F^e_{on}R_{op}F_{mp}] - 2\mu R_{ln}F^e_{mn}\Big\}, \tag{7.59}$$

$$M_{ij} = \Big\{\alpha R_{ip}R_{mn}\Gamma^e_{mn} + (\beta+\gamma)\,\Gamma^e_{ip} + (\beta-\gamma)\,[R_{im}\Gamma^e_{nm}R_{np}]\Big\}F^{p^{-1}}_{jp}, \tag{7.60}$$

we can evaluate their variation with respect to the elastic and plastic parts of the deformations:

$$\frac{\partial \mathrm{S}_{ij}}{\partial \mathrm{F}^e_{kl}} = \lambda \mathrm{J}^e\Bigg\{ (\mathrm{J}^e-1)\left[\left(\underset{\sim}{\mathbf{F}}^{e\,-1}\right)_{lk}\left(\underset{\sim}{\mathbf{F}}^{e\,-1}\right)_{pi}\left(\underset{\sim}{\mathbf{F}}^{p\,-1}\right)_{jp} - \left(\underset{\sim}{\mathbf{F}}^{e\,-1}\right)_{pk}\left(\underset{\sim}{\mathbf{F}}^{e\,-1}\right)_{li}\left(\underset{\sim}{\mathbf{F}}^{p\,-1}\right)_{jp}\right] +$$

$$+\mathrm{J}\left(\underset{\sim}{\mathbf{F}}^{e\,-1}\right)_{lk}\left(\underset{\sim}{\mathbf{F}}^{e\,-1}\right)_{pi}\left(\underset{\sim}{\mathbf{F}}^{p\,-1}\right)_{jp}\Bigg\} + (\mu+\mu_c)\left[\delta_{ik}\left(\underset{\sim}{\mathbf{F}}^{p\,-1}\right)_{jl}\right] + (\mu-\mu_c)\left[\mathrm{R}_{il}\mathrm{R}_{kp}\left(\underset{\sim}{\mathbf{F}}^{p\,-1}\right)_{jp}\right], \tag{7.61}$$

$$\frac{\partial \mathrm{S}_{ij}}{\partial \mathrm{F}^p_{kl}} = -\Bigg\{ \mathrm{J}^e\lambda\,(\mathrm{J}-1)\left(\underset{\sim}{\mathbf{F}}^{e\,-T}\underset{\sim}{\mathbf{F}}^{p\,-T}\right)_{il} + (\mu+\mu_c)\left[\underset{\sim}{\mathbf{F}}^{e}\underset{\sim}{\mathbf{F}}^{p^{-T}}\right]_{il} + (\mu-\mu_c)\left[\underset{\sim\sim}{\mathbf{R}\mathbf{F}}^{e^T}\underset{\sim\sim}{\mathbf{R}\mathbf{F}}^{p^{-T}}\right] - 2\mu\underset{\sim\sim}{\mathbf{R}\mathbf{F}}^{p^{-T}}_{il}\Bigg\}\underset{\sim}{\mathbf{F}}^{p^{-T}}_{kj}, \tag{7.62}$$

$$\frac{\partial \mathrm{S}_{ij}}{\partial \mathrm{R}_{kl}} = (\mu-\mu_c)\left[\delta_{ik}F^e_{ml}R_{mp}\left(\underset{\sim}{\mathbf{F}}^{p\,-1}\right)_{jp} + R_{im}F_{km}\left(\underset{\sim}{\mathbf{F}}^{p\,-1}\right)_{jl}\right] - 2\,\mu\delta_{ik}\left(\underset{\sim}{\mathbf{F}}^{p\,-1}\right)_{jl}, \tag{7.63}$$

$$\frac{\partial \mathrm{S}_{ij}}{\partial \Gamma^e_{kl}} = 0, \tag{7.64}$$

$$\frac{\partial \mathrm{S}_{ij}}{\partial \Gamma^p_{kl}} = 0, \tag{7.65}$$

$$\frac{\partial \mathrm{s}_{i}}{\partial \mathrm{F}^e_{jk}} = -\epsilon_{ilm}\Bigg\{ (\mu+\mu_c)\,[\delta_{lj}\delta_{nk}F^e_{mn} + F^e_{ln}\delta_{mj}\delta_{nk}] +$$

$$(\mu-\mu_c)\left[R_{ln}\delta_{oj}\delta_{nk}R_{op}F^e_{mp} + R_{ln}F^e_{on}R_{op}\delta_{mj}\delta_{pk}\right] - 2\,\mu R_{ln}\delta_{mj}\delta_{nk}\Bigg\}, \tag{7.66}$$

$$\frac{\partial \mathrm{s}_{i}}{\partial \mathrm{F}^p_{jk}} = 0, \tag{7.67}$$

$$\frac{\partial \mathrm{s}_{i}}{\partial \mathrm{R}_{jk}} = -\epsilon_{ilm}\Bigg\{ (\mu-\mu_c)\left[\delta_{lj}\delta_{nk}F^e_{on}R_{op}F^e_{mp} + R_{ln}F^e_{on}\delta_{oj}\delta_{pk}F^e_{mp}\right] - 2\,\mu\delta_{lj}\delta_{nk}F^e_{mn}\Bigg\}, \tag{7.68}$$

$$\frac{\partial \mathrm{s}_{i}}{\partial \Gamma^e_{jk}} = 0, \tag{7.69}$$

$$\frac{\partial \mathrm{s}_{i}}{\partial \Gamma^p_{jk}} = 0, \tag{7.70}$$

$$\frac{\partial \mathrm{M}_{ij}}{\partial \mathrm{F}^e_{kl}} = 0, \tag{7.71}$$

$$\frac{\partial \mathrm{M}_{ij}}{\partial \mathrm{F}^p_{kl}} = -\left\{ \alpha \mathrm{tr}\left(\underset{\sim}{\mathbf{R}}^T \underset{\sim}{\mathbf{\Gamma}}^e\right) R_{ip} + (\beta+\gamma)\,\Gamma^e_{ip} + (\beta-\gamma)\left[\underset{\sim}{\mathbf{R}}\underset{\sim}{\mathbf{\Gamma}}^{e^T}\underset{\sim}{\mathbf{R}}\right]_{ip} \right\} F^{p^{-1}}_{jk} F^{p^{-1}}_{lp}, \tag{7.72}$$

$$\frac{\partial \mathrm{M}_{ij}}{\partial \mathrm{R}_{kl}} = \alpha\left[\delta_{ik} F^{p^{-T}}_{lj} R_{mn}\Gamma^e_{mn} + \left(RF^{p^{-T}}\right)_{ij}\Gamma^e_{kl}\right] + (\beta-\gamma)\left[\delta_{ik}\left(\Gamma^{e^T} RF^{p^{-T}}\right)_{lj} + \left(R\Gamma^{e^T}\right)_{ik} F^{p^{-T}}_{lj}\right], \tag{7.73}$$

$$\frac{\partial \mathrm{M}_{ij}}{\partial \Gamma^e_{kl}} = \alpha\left[\left(RF^{p^{-T}}\right)_{ij} R_{kl}\right] + (\beta+\gamma)\left[\delta_{ik} F^{p^{-T}}_{lj}\right] + (\beta-\gamma)\left[R_{il}\left(RF^{p^{-T}}\right)_{kj}\right], \tag{7.74}$$

$$\frac{\partial \mathrm{M}_{ij}}{\partial \Gamma^p_{kl}} = 0. \tag{7.75}$$

By reporting Equations (7.56) and (7.57) in an index form:

$$\frac{\partial(\bullet)}{\partial \mathrm{F}_{ij}} = \frac{\partial(\bullet)}{\partial \mathrm{F}^e_{kl}}\frac{\partial \mathrm{F}^e_{kl}}{\partial \mathrm{F}_{ij}} + \frac{\partial(\bullet)}{\partial \mathrm{F}^p_{kl}}\frac{\partial \mathrm{F}^p_{kl}}{\partial \mathrm{F}_{ij}}, \tag{7.76}$$

$$\frac{\partial(\bullet)}{\partial \Gamma_{ij}} = \frac{\partial(\bullet)}{\partial \Gamma^e_{kl}}\frac{\partial \Gamma^e_{kl}}{\partial \Gamma_{ij}} + \frac{\partial(\bullet)}{\partial \Gamma^p_{kl}}\frac{\partial \Gamma^p_{kl}}{\partial \Gamma_{ij}} + \frac{\partial(\bullet)}{\partial \mathrm{F}^p_{kl}}\frac{\partial \mathrm{F}^p_{kl}}{\partial \Gamma_{ij}}, \tag{7.77}$$

which become:

$$\frac{\partial(\bullet)}{\partial \mathrm{F}_{ij}} = \frac{\partial(\bullet)}{\partial \mathrm{F}^e_{kl}}\delta_{ki}\mathrm{F}^{p^{-1}}_{jl} + \frac{\partial(\bullet)}{\partial \mathrm{F}^p_{kl}}\mathrm{F}^{e^{-1}}_{ki}\delta_{lj}, \tag{7.78}$$

$$\frac{\partial(\bullet)}{\partial \Gamma_{ij}} = \frac{\partial(\bullet)}{\partial \Gamma^e_{kl}}\delta_{ki}\mathrm{F}^{p^{-1}}_{jl} + \frac{\partial(\bullet)}{\partial \Gamma^p_{kl}}\delta_{ki}\delta_{lj} + \frac{\partial \bullet}{\partial \mathrm{F}^p_{kl}}\Gamma^{e^{-1}}_{ki}\delta_{lj}, \tag{7.79}$$

the entries that we just derived can be grouped as:

$$\frac{\partial \mathrm{S}_{ij}}{\partial \mathrm{F}_{kl}} = \lambda \mathrm{J}^e\left\{(\mathrm{J}^e-1)\left[\left(\underset{\sim}{\mathbf{F}}^{-1}\right)_{lk}\left(\underset{\sim}{\mathbf{F}}^{-1}\right)_{ji} - \left(\underset{\sim}{\mathbf{F}}^{-1}\right)_{jk}\left(\underset{\sim}{\mathbf{F}}^{-1}\right)_{li}\right] + \mathrm{J}\left(\underset{\sim}{\mathbf{F}}^{-1}\right)_{lk}\left(\underset{\sim}{\mathbf{F}}^{-1}\right)_{ji}\right\} + (\mu+\mu_c)\left[\delta_{ik}\delta_{lj}\right] + (\mu-\mu_c)\left[\underset{\sim}{\mathbf{R}}_{il}\mathrm{R}_{kj}\right], \tag{7.80}$$

$$\frac{\partial \mathrm{S}_{ij}}{\partial \mathrm{R}_{kl}} = (\mu-\mu_c)\left[\delta_{ik}F^e_{ml}R_{mp}\left(\underset{\sim}{\mathbf{F}}^{p\,-1}\right)_{jp} + R_{im}F_{km}\left(\underset{\sim}{\mathbf{F}}^{p\,-1}\right)_{jl}\right] - 2\,\mu\delta_{ik}\left(\underset{\sim}{\mathbf{F}}^{p\,-1}\right)_{jl}, \tag{7.81}$$

$$\frac{\partial \mathrm{s}_i}{\partial \mathrm{F}_{jk}} = -\epsilon_{ilm}\left\{(\mu+\mu_c)\left[\delta_{lj}\left(\underset{\sim}{\mathbf{F}}^{p^{-1}}\cdot\underset{\sim}{\mathbf{F}}^{e\,T}\right)_{km} + \left(\underset{\sim}{\mathbf{F}}^{p^{-1}}\cdot\underset{\sim}{\mathbf{F}}^{e\,T}\right)_{kl}\delta_{mj}\right] + (\mu-\mu_c)\left[\left(\underset{\sim}{\mathbf{F}}^{e}\cdot\underset{\sim}{\mathbf{R}}^{T}\right)_{mj}\left(\underset{\sim}{\mathbf{F}}^{p\,-1}\cdot\underset{\sim}{\mathbf{R}}^{T}\right)_{kl} + \left(\underset{\sim}{\mathbf{R}}\cdot\underset{\sim}{\mathbf{F}}^{e\,T}\cdot\underset{\sim}{\mathbf{R}}\underset{\sim}{\mathbf{F}}^{p\,-T}\right)_{lk}\delta_{mj}\right] - 2\,\mu\left[\left(\underset{\sim}{\mathbf{R}}\cdot\underset{\sim}{\mathbf{F}}^{p\,-T}\right)_{lk}\delta_{mj}\right]\right\}, \tag{7.82}$$

$$\frac{\partial \mathrm{s}_i}{\partial \mathrm{R}_{jk}} = -\epsilon_{ilm}\Big\{ (\mu-\mu_c)\left[\delta_{lj}\delta_{nk}F^e_{on}R_{op}F^e_{mp} + R_{ln}F^e_{on}\delta_{oj}\delta_{pk}F^e_{mp}\right] - 2\,\mu\delta_{lj}\delta_{nk}F^e_{mn}\Big\}, \tag{7.83}$$

$$\frac{\partial \mathrm{s}_i}{\partial \Gamma_{jk}} = 0, \tag{7.84}$$

$$\frac{\partial \mathrm{M}_{ij}}{\partial \Gamma_{kl}} = \alpha\left[R_{ij}\left(\underset{\sim}{\mathbf{F}}^{p-1}\cdot\underset{\sim}{\mathbf{R}}\right)_{lk}\right] + (\beta+\gamma)\left[\delta_{ik}\underset{\sim}{\mathbf{F}}^{p-1}_{lj}\right] + (\beta-\gamma)\left[\left(\underset{\sim}{\mathbf{F}}^{p-1}\cdot\underset{\sim}{\mathbf{R}}\right)_{li}R_{kj}\right], \tag{7.85}$$

which cen be used to fill the material tangent matrix for a the three dimesional unconstrained case:

$$\underset{\sim}{\boldsymbol{K}}_M = \left[\begin{array}{c|c|c} \dfrac{\partial \underline{\mathbf{S}}}{\partial \underline{\mathbf{F}}} & \dfrac{\partial \underline{\mathbf{S}}}{\partial \underline{\mathbf{R}}} & \dfrac{\partial \underline{\mathbf{S}}}{\partial \underline{\mathbf{\Gamma}}} \\ \hline \dfrac{\partial \underline{\mathbf{s}}}{\partial \underline{\mathbf{F}}} & \dfrac{\partial \underline{\mathbf{s}}}{\partial \underline{\mathbf{R}}} & \dfrac{\partial \underline{\mathbf{s}}}{\partial \underline{\mathbf{\Gamma}}} \\ \hline \dfrac{\partial \underline{\mathbf{M}}}{\partial \underline{\mathbf{F}}} & \dfrac{\partial \underline{\mathbf{M}}}{\partial \underline{\mathbf{R}}} & \dfrac{\partial \underline{\mathbf{M}}}{\partial \underline{\mathbf{\Gamma}}} \end{array}\right] = \left[\begin{array}{c|c|c} (7.80) & (7.81) & \underset{\sim}{0} \\ \hline (7.82) & (7.83) & \underset{\sim}{0} \\ \hline \underset{\sim}{0} & \underset{\sim}{0} & (7.85) \end{array}\right] \tag{7.86}$$

7.2.2 Variation of Mandel stress and couple stress tensors

The Mandel stress and couple stress can be written as:

$$\underset{\sim}{\mathbf{\Pi}} = \underset{\sim}{\mathbf{F}}^{e^T}\cdot\underset{\sim}{\mathbf{S}}\cdot\underset{\sim}{\mathbf{F}}^{p^T} + \underset{\sim}{\mathbf{\Gamma}}^{e^T}\cdot\underset{\sim}{\mathbf{M}}\cdot\underset{\sim}{\mathbf{F}}^{p^T}; \tag{7.87}$$

$$\underset{\sim}{\mathbf{\Pi}}_c = \underset{\sim}{\mathbf{M}}\cdot\underset{\sim}{\mathbf{F}}^{p^T}; \tag{7.88}$$

and, if they are expanded:

$$\begin{aligned}\underset{\sim}{\mathbf{\Pi}} = \mathrm{J}^e\lambda\left(\mathrm{J}^e-1\right)\underset{\sim}{\mathbf{I}} + (\mu+\mu_c)\left[\underset{\sim}{\mathbf{F}}^{e^T}\underset{\sim}{\mathbf{F}}^e\right] + (\mu-\mu_c)\left[\underset{\sim}{\mathbf{F}}^{e^T}\underset{\sim}{\mathbf{R}}\underset{\sim}{\mathbf{F}}^{e^T}\underset{\sim}{\mathbf{R}}\right] - 2\mu\underset{\sim}{\mathbf{F}}^{e^T}\underset{\sim}{\mathbf{R}} + \\ \alpha\mathrm{tr}\left(\underset{\sim}{\mathbf{R}}^T\underset{\sim}{\mathbf{\Gamma}}^e\right)\underset{\sim}{\mathbf{\Gamma}}^{e^T}\underset{\sim}{\mathbf{R}} + (\beta+\gamma)\left[\underset{\sim}{\mathbf{\Gamma}}^{e^T}\underset{\sim}{\mathbf{\Gamma}}^e\right] + (\beta-\gamma)\left[\underset{\sim}{\mathbf{\Gamma}}^{e^T}\underset{\sim}{\mathbf{R}}\underset{\sim}{\mathbf{\Gamma}}^{e^T}\underset{\sim}{\mathbf{R}}\right];\end{aligned} \tag{7.89}$$

$$\underset{\sim}{\mathbf{\Pi}}_c = \alpha\,\mathrm{tr}\left(\underset{\sim}{\mathbf{R}}^T\underset{\sim}{\mathbf{\Gamma}}^e\right)\underset{\sim}{\mathbf{R}} + (\beta+\gamma)\left[\underset{\sim}{\mathbf{\Gamma}}^e\right] + (\beta-\gamma)\left[\underset{\sim}{\mathbf{R}}\underset{\sim}{\mathbf{\Gamma}}^{e^T}\underset{\sim}{\mathbf{R}}\right]; \tag{7.90}$$

from which their variation with respect to the elastic deformations and micro-rotation are:

$$\frac{\partial \Pi_{ij}}{\partial F^e_{kl}} = \lambda\, J^e \delta_{ij} \underset{\sim}{\mathbf{F}}^{-T}_{kl} \left(2\, J^e - 1\right) + (\mu + \mu_c) \left[\delta_{il} F^e_{kj} + \delta_{jl} F^e_{ki}\right] + (\mu - \mu_c) \left[\delta_{il} \underset{\sim}{\mathbf{R}}\underset{\sim}{\mathbf{F}}^{e^T} \underset{\sim}{\mathbf{R}}_{kj} + \underset{\sim}{\mathbf{F}}^{e^T} \underset{\sim}{\mathbf{R}}_{il} R_{kj}\right] - 2\,\mu \delta_{il} R_{kj}; \tag{7.91}$$

$$\frac{\partial \Pi_{ij}}{\partial R_{kl}} = (\mu - \mu_c) \left[F^e_{ki} \underset{\sim}{\mathbf{F}}^{e^T} \underset{\sim}{\mathbf{R}}_{lj} + \underset{\sim}{\mathbf{F}}^{e^T} \underset{\sim}{\mathbf{R}}\underset{\sim}{\mathbf{F}}^{e^T}_{ik} \delta_{jl}\right] - 2\,\mu F^e_{ki} \delta_{jl} + \alpha \Gamma^e_{kl} \underset{\sim}{\mathbf{\Gamma}}^{e^T} \underset{\sim}{\mathbf{R}}_{ij} + \alpha \text{trace}\left(\underset{\sim}{\mathbf{R}}^T \underset{\sim}{\mathbf{\Gamma}}^e\right) \Gamma^e_{ki} \delta_{jl} + (\beta - \gamma) \left[\Gamma^e_{ki} \underset{\sim}{\mathbf{\Gamma}}^e \underset{\sim}{\mathbf{R}}_{lj} + \underset{\sim}{\mathbf{\Gamma}}^{e^T} \underset{\sim}{\mathbf{R}}\underset{\sim}{\mathbf{\Gamma}}^{e^T}_{ik} \delta_{jl}\right]; \tag{7.92}$$

$$\frac{\partial \Pi_{ij}}{\partial \Gamma^e_{kl}} = \alpha R_{kl} \underset{\sim}{\mathbf{\Gamma}}^{e^T} \underset{\sim}{\mathbf{R}}_{ij} + \alpha\, \text{trace}\left(\underset{\sim}{\mathbf{T}}^T \underset{\sim}{\mathbf{\Gamma}}^{e^T}\right) \delta_{il} R_{kj} + (\beta + \gamma) \left[\delta_{il} \Gamma^e_{kj} + \Gamma^e_{ki} \delta_{jl}\right] + (\beta - \gamma) \left[\delta_{il} \underset{\sim}{\mathbf{R}}\underset{\sim}{\mathbf{\Gamma}}^{e^T} \underset{\sim}{\mathbf{R}}_{kj} + \underset{\sim}{\mathbf{\Gamma}}^{e^T} \underset{\sim}{\mathbf{R}}_{il} R_{kj}\right]; \tag{7.93}$$

$$\frac{\partial \Pi_{c_i j}}{\partial R_{kl}} = \alpha \Gamma^e_{kl} R_{ij} + \alpha\, \text{trace}\left(\underset{\sim}{\mathbf{R}}^T \underset{\sim}{\mathbf{\Gamma}}^e\right) \delta_{ik} \delta_{jl} + (\beta - \gamma) \left[\delta_{ik} \underset{\sim}{\mathbf{\Gamma}}^{e^T} \underset{\sim}{\mathbf{R}}_{lj} + \underset{\sim}{\mathbf{R}}\underset{\sim}{\mathbf{\Gamma}}^{e^T}_{ik} \delta_{jl}\right]; \tag{7.94}$$

$$\frac{\partial \Pi_{c_i j}}{\partial \Gamma^e_{kl}} = \alpha R_{kl} R_{ij} + (\beta + \gamma) \left[\delta_{ik} \delta_{jl}\right] + (\beta - \gamma) \left[R_{il} R_{kl}\right]; \tag{7.95}$$

7.2.3 Derivatives of $\underset{\sim}{\mathbf{R}}$ and $\underset{\sim}{\mathbf{\Gamma}}$

The second group of terms that need further development are the ones expressing variations of the micro-rotation tensor and wryness at the integration points with respect to nodal variations of the degrees of freedom:

$$\frac{\partial \underset{\sim}{\mathbf{R}}}{\partial \underline{\boldsymbol{\chi}}^\theta}, \quad \frac{\partial \underset{\sim}{\mathbf{\Gamma}}}{\partial \underline{\boldsymbol{\chi}}^\theta}.$$

These quantities can be expressed as:

$$\frac{\partial \underset{\sim}{\mathbf{R}}}{\partial \underline{\boldsymbol{\chi}}^\theta} = \frac{\partial \underset{\sim}{\mathbf{R}}}{\partial \underline{\boldsymbol{\theta}}} \frac{\partial \underline{\boldsymbol{\theta}}}{\partial \underline{\boldsymbol{\chi}}^\theta}, \quad \frac{\partial \underset{\sim}{\mathbf{\Gamma}}}{\partial \underline{\boldsymbol{\theta}}} \frac{\partial \underline{\boldsymbol{\theta}}}{\partial \underline{\boldsymbol{\chi}}^\theta}.$$

where the relationship between the parameters at the IP $\underline{\boldsymbol{\theta}}$ and the parameters at the nodes $\underline{\boldsymbol{\chi}}^\theta$ are given by the shape functions contained in the $\mathbf{N}^\theta$ matrix, and the other terms that need further development are the ones expressing variations of the deformation measures, $\underset{\sim}{\mathbf{R}}$ and $\underset{\sim}{\mathbf{\Gamma}}$, at the integration points with respect to a variation of the parameters:

$$\frac{\partial \underset{\sim}{\mathbf{R}}}{\partial \underline{\boldsymbol{\theta}}}, \quad \frac{\partial \underset{\sim}{\mathbf{\Gamma}}}{\partial \underline{\boldsymbol{\theta}}}.$$

where the parameter vector $\underline{\boldsymbol{\theta}}$ is presented in Table 8.19d. It is remembered that for this research a Cartesian parameterization was chosen. The variations of the micro-rotation and of the wryness with respect to the parameters can be evaluated starting from the expression of the rotation matrix as [Bauchau 2011]:

$$\underset{\sim}{\mathbf{R}}(\underline{\boldsymbol{\theta}}) = \underset{\sim}{\mathbf{I}} + \frac{\sin(\theta)}{\theta} \underset{\sim}{\boldsymbol{\theta}} + \frac{1 - \cos(\theta)}{\theta} \underset{\sim}{\boldsymbol{\theta}} \cdot \underset{\sim}{\boldsymbol{\theta}}; \tag{7.96}$$

where, once again, $\underset{\sim}{\boldsymbol{\theta}}$ is the skew-symmetric tensor whose axial vector is $\underline{\boldsymbol{\theta}}$ and θ is the norm of the parameters vector. We want now to express the variation of the rotation tensor with respect to a variation of the parameters that embody it. This can be evaluated after considering that:

$$\theta = \sqrt{\theta_1^2 + \theta_2^2 + \theta_3^2}; \qquad \frac{\partial \theta}{\partial \theta_i} = \frac{\theta_i}{\theta}; \qquad \frac{\partial \underset{\sim}{\boldsymbol{\theta}}}{\partial \theta_i} = \frac{\partial - \underset{\simeq}{\boldsymbol{\epsilon}} \cdot \underline{\boldsymbol{\theta}}}{\partial \theta_i} = -\underset{\simeq}{\boldsymbol{\epsilon}} \cdot \underline{\mathbf{e}}_i; \tag{7.97}$$

where θ_i is the *i-th* component of the parameter vector, and $\underline{\mathbf{e}}_i$ is the *i-th* unit vector forming the orthonormal basis of the Euclidean space. The final expression of the variation of the rotation with respect to the *i-th* parameter is:

$$\begin{aligned}\frac{\partial \underset{\sim}{\mathbf{R}}}{\partial \theta_i} = \left[\cos(\theta)\,\theta_i - \sin(\theta)\frac{\theta_i}{\theta}\right]\frac{\underset{\sim}{\boldsymbol{\theta}}}{\theta^2} - \frac{\sin(\theta)}{\theta}\underset{\simeq}{\boldsymbol{\epsilon}} \cdot \underline{\mathbf{e}}_i + \\ \left[\sin(\theta)\,\theta\,\theta_i - (1 - cos(\theta))2\,\theta_i\right]\frac{\underset{\sim}{\boldsymbol{\theta}} \cdot \underset{\sim}{\boldsymbol{\theta}}}{\theta^4} - \frac{1-\cos(\theta)}{\theta^2}\left[\underset{\simeq}{\boldsymbol{\epsilon}} \cdot \underline{\mathbf{e}}_i\right] \cdot \underset{\sim}{\boldsymbol{\theta}} \\ - \frac{1-\cos(\theta)}{\theta^2}\underset{\sim}{\boldsymbol{\theta}} \cdot \left[\underset{\simeq}{\boldsymbol{\epsilon}} \cdot \underline{\mathbf{e}}_i\right];\end{aligned} \tag{7.98}$$

This expression has been simplified by Gallego and Yezzi [Gallego et al. 2015], obtaining the following:

$$\frac{\partial \underset{\sim}{\mathbf{R}}}{\partial \theta_i} = \frac{\theta_i \underset{\sim}{\boldsymbol{\theta}} + \left[\underline{\boldsymbol{\theta}} \times \left(\underset{\sim}{\mathbf{I}} - \underset{\sim}{\mathbf{R}}\right) \cdot \underline{\mathbf{e}}_i\right]_\times}{\theta^2} \cdot \underset{\sim}{\mathbf{R}}; \tag{7.99}$$

where $(\cdot)_\times$ is the operator that returns the skew-symmetric tensor of a given vector. The final third order tensor is composed by the three bi-dimensional tensors expressed in Equation 7.99, and is here denoted as $\underset{\simeq}{\mathbf{R}}^*$:

$$R^*_{ijk} = \frac{\partial R_{ij}}{\partial \theta_k}; \tag{7.100}$$

Therefore, the variation of the micro-rotation tensor $\underset{\sim}{\mathbf{R}}$ with respect to a nodal variation of the parameter vector $\underline{\boldsymbol{\chi}}^\theta$ can be written as:

$$\frac{\partial R_{ij}}{\partial \chi^\theta_k} = \frac{\partial R_{ij}}{\partial \theta_l}\frac{\partial \theta_l}{\partial \chi^\theta_k} = R^*_{ijl} N^\theta_{lk}, \quad \Longleftrightarrow \quad \frac{\partial \underset{\sim}{\mathbf{R}}}{\partial \underline{\boldsymbol{\chi}}^\theta} = \underset{\simeq}{\mathbf{R}}^* \cdot \underset{\sim}{\mathbf{N}}^\theta, \tag{7.101}$$

The derivation of the second term can be performed as:

$$\frac{\partial \Gamma_{ij}}{\partial \chi^\theta_k} = \frac{\partial \Gamma_{ij}}{\partial \theta_l}\frac{\partial \theta_l}{\partial \chi^\theta_k} = \frac{\partial \Gamma_{ij}}{\partial R_{mn}}\frac{\partial R_{mn}}{\partial \theta_l}\frac{\partial \theta_l}{\partial \chi^\theta_k}, \quad \Longleftrightarrow \quad \frac{\partial \underset{\sim}{\boldsymbol{\Gamma}}}{\partial \underline{\boldsymbol{\chi}}^\theta} = \left(\frac{\partial \underset{\sim}{\boldsymbol{\Gamma}}}{\partial \underset{\sim}{\mathbf{R}}} : \underset{\simeq}{\mathbf{R}}^*\right) \cdot \underset{\sim}{\mathbf{N}}^\theta, \tag{7.102}$$

where the derivative of the wryness with respect to the micro-rotation must be evaluated. It can be done by reporting the wryness in an index form (Equation (6.10)):

$$\Gamma_{ij} = -\frac{1}{2}\epsilon_{ikl} R_{mk}\frac{\partial R_{mn}}{\partial X_l}, \tag{7.103}$$

whose variation with respect to the micro-rotation tensor would look like:

$$\frac{\partial \Gamma_{ij}}{\partial R_{kl}} = -\frac{1}{2}\epsilon_{ilm}\frac{\partial R_{km}}{\partial X_j} = -\frac{1}{2}\epsilon_{ilm}\frac{\partial R_{km}}{\partial \theta_n}\frac{\partial \theta_n}{\partial X_j} = -\frac{1}{2}\epsilon_{ilm}R^*_{kmn}\frac{\partial \theta_n}{\partial X_j}, \quad \Longleftrightarrow \quad \frac{\partial \underset{\sim}{\boldsymbol{\Gamma}}}{\partial \underset{\sim}{\mathbf{R}}} = -\frac{1}{2}\underset{\simeq}{\boldsymbol{\epsilon}} \cdot \underset{\simeq}{\mathbf{R}}^{*^T} \cdot \underset{\simeq}{\mathbf{B}}^{\theta} \cdot \underline{\boldsymbol{\chi}}^{\theta}, \tag{7.104}$$

where the transpose of the third order tensor acts on the first two indices. Therefore, the variation of the wryness tensor with respect to the rotational degrees of freedom can be written as:

$$\frac{\partial \Gamma_{ij}}{\partial \chi^{\theta}_k} = -\frac{1}{2}\epsilon_{ilm}R^*_{pmn}\frac{\partial \theta_n}{\partial X_j}R^*_{plq}N^{\theta}_{qk}. \tag{7.105}$$

In classical continuum mechanics the gradient of the displacements $\underset{\sim}{\mathbf{F}}$ can be simply evaluated by applying the B matrix onto the nodal displacements. The wryness, however, cannot be simply evaluated as done with the deformation gradient because of its non-linearity. From the definition of the wryness in Equation (6.10), using the property of the permutation symbol and Equation (7.100), the wryness tensor can be evaluated as:

$$\Gamma_{ij} = -\frac{1}{2}\epsilon_{ikl}R_{mk}\frac{\partial R_{ml}}{\partial X_j} = -\frac{1}{2}\epsilon_{ikl}R_{mk}\frac{\partial R_{ml}}{\partial \theta_n}\frac{\partial \theta_n}{\partial X_j}, \quad \Longleftrightarrow \quad \underset{\sim}{\boldsymbol{\Gamma}} = -\frac{1}{2}\underset{\simeq}{\boldsymbol{\epsilon}} : \left[\underset{\sim}{\mathbf{R}}^T \cdot \underset{\simeq}{\mathbf{R}}^*\right] \cdot \underset{\simeq}{\mathbf{B}}^{\theta} \cdot \underline{\boldsymbol{\chi}}^{\theta}. \tag{7.106}$$

Similar works found in the literature, for example the one by Erdelj et al. [Erdelj et al. 2020], evaluate the wryness as:

$$\underset{\sim}{\boldsymbol{\Gamma}} = \underset{\sim}{\mathbf{R}}^T \cdot \underset{\sim}{\mathbf{H}}(\underline{\boldsymbol{\theta}}) \cdot \underset{\simeq}{\mathbf{B}}^{\theta} \cdot \underline{\boldsymbol{\chi}}^{\theta}, \tag{7.107}$$

where $\underset{\sim}{\mathbf{H}}(\underline{\boldsymbol{\theta}})$ is the tangent operator of the rotational operator in the parametric space $\{\theta_1, \theta_2, \theta_3\}$ [Erdelj et al. 2020; Bauchau 2011]. By comparing it with the formulation that we derived, the following can be asserted:

$$\underset{\sim}{\mathbf{H}}(\underline{\boldsymbol{\theta}}) = -\frac{1}{2}\underset{\simeq}{\boldsymbol{\epsilon}} : \left[\underset{\sim}{\mathbf{R}}\underset{\simeq}{\mathbf{R}}^*\right]. \tag{7.108}$$

7.3 Plane strain model

In case of plane strain condition, the rotation has only one degree of freedom, so that there will be only one active rotation on the continuum:

$$\underline{\boldsymbol{\theta}} = \begin{bmatrix} 0 \\ 0 \\ \theta_3 \end{bmatrix}, \tag{7.109}$$

therefore, also the vector $\underline{\mathbf{s}}$ (which is the skew-symmetric part of the Cauchy stress tensor) has only one non vanishing component:

$$\underline{\mathbf{s}} = \begin{bmatrix} 0 \\ 0 \\ s_3 \end{bmatrix}. \tag{7.110}$$

Subsequently, another consequence is that the only active components of the wryness tensor are $\Gamma_{31} = {}^{\partial\theta_3}/_{\partial x}$ and $\Gamma_{32} = {}^{\partial\theta_3}/_{\partial y}$:

$$\underset{\sim}{\boldsymbol{\Gamma}} = \begin{bmatrix} 0 & 0 & 0 \\ 0 & 0 & 0 \\ \Gamma_{31} & \Gamma_{32} & 0 \end{bmatrix}. \tag{7.111}$$

which can be evaluated as:

$$\underline{\boldsymbol{\Gamma}} = \begin{bmatrix} \Gamma_1 \\ \Gamma_2 \end{bmatrix} = \begin{bmatrix} \dfrac{\partial\theta^3}{\partial X_1} \\ \dfrac{\partial\theta^3}{\partial X_2} \end{bmatrix} = \underset{\sim}{\mathbf{B}}^{\theta} \cdot \underline{\boldsymbol{\chi}}^{\theta}. \tag{7.112}$$

The Helmholtz free energy becomes:

$$\rho\psi\left(\underset{\sim}{\mathbf{R}}^T\underset{\sim}{\mathbf{F}}^e, \underset{\sim}{\boldsymbol{\Gamma}}^e\right) = \frac{\lambda}{2}\left(\mathrm{J}-1\right)^2 + \mu||\mathrm{sym}\left(\underset{\sim}{\mathbf{R}}^T\underset{\sim}{\mathbf{F}}^e\right) - \underset{\sim}{\mathbf{I}}||^2 + \mu_c||\mathrm{skew}\left(\underset{\sim}{\mathbf{R}}^T\underset{\sim}{\mathbf{F}}^e - \underset{\sim}{\mathbf{I}}\right)||^2 + \frac{\beta}{2}||\underset{\sim}{\boldsymbol{\Gamma}}^e||^2, \tag{7.113}$$

and the stresses are:

$$\underset{\sim}{\mathbf{S}} = \left\{ \mathrm{J}^e\lambda\left(\mathrm{J}-1\right)\underset{\sim}{\mathbf{F}}^{e^{-T}} + \left(\mu+\mu_c\right)\left[\underset{\sim}{\mathbf{F}}^e\right] + \left(\mu-\mu_c\right)\left[\underset{\sim}{\mathbf{R}}\cdot\underset{\sim}{\mathbf{F}}^{e^T}\cdot\underset{\sim}{\mathbf{R}}\right] - 2\mu\underset{\sim}{\mathbf{R}}\right\}\cdot\underset{\sim}{\mathbf{F}}^{p^{-T}}, \tag{7.114}$$

$$\underline{\mathbf{s}} = -\underset{\approx}{\boldsymbol{\epsilon}} : \left\{ \mathrm{J}^e\lambda\left(\mathrm{J}^e-1\right)\underset{\sim}{\mathbf{I}} + \left(\mu+\mu_c\right)\left[\underset{\sim}{\mathbf{F}}^e\cdot\underset{\sim}{\mathbf{F}}^{e^T}\right] + \left(\mu-\mu_c\right)\left[\underset{\sim}{\mathbf{R}}\cdot\underset{\sim}{\mathbf{F}}^{e^T}\cdot\underset{\sim}{\mathbf{R}}\cdot\underset{\sim}{\mathbf{F}}^{e^T}\right] - 2\mu\left[\underset{\sim}{\mathbf{R}}\cdot\underset{\sim}{\mathbf{F}}^{e^T}\right]\right\} + \\ - \underset{\approx}{\boldsymbol{\epsilon}} : \left[2\,\beta\underset{\sim}{\boldsymbol{\Gamma}}^e\underset{\sim}{\boldsymbol{\Gamma}}^{e^T}\right]; \tag{7.115}$$

$$\underset{\sim}{\mathbf{M}} = 2\,\beta \underset{\sim}{\boldsymbol{\Gamma}}^{e} \underset{\sim}{\mathbf{F}}^{p^{-T}}. \tag{7.116}$$

With the simplifications done so far, the element stiffness matrix looks like:

$$\underset{\sim}{\boldsymbol{K}} = \left[\begin{array}{c|c} \int_{\Omega_i} \left(\underset{\sim}{\mathbf{B}}^{v^T} \cdot \dfrac{\partial \underline{\mathbf{S}}}{\partial \underline{\mathbf{F}}} \cdot \underset{\sim}{\mathbf{B}}^{u} \right) d\Omega & \int_{\Omega_i} \left(\underset{\sim}{\mathbf{B}}^{v^T} \cdot \dfrac{\partial \underline{\mathbf{S}}}{\partial \theta^3} \otimes \underline{\mathbf{N}}^{\theta} \right) d\Omega \\ \hline - \int_{\Omega_i} \left(\underline{\mathbf{N}}^{\theta^T} \otimes \dfrac{\partial \mathrm{s}^3}{\partial \underline{\mathbf{F}}} \cdot \underset{\sim}{\mathbf{B}}^{u} \right) d\Omega & \int_{\Omega_i} \left(\underset{\sim}{\mathbf{B}}^{\theta^T} \cdot \dfrac{\partial \underline{\mathbf{M}}}{\partial \underline{\boldsymbol{\Gamma}}} \cdot \underset{\sim}{\mathbf{B}}^{\theta} - \dfrac{\partial \mathrm{s}^3}{\partial \theta^3} \underset{\sim}{\mathbf{N}}^{\theta^T} \otimes \underline{\mathbf{N}}^{\theta} \right) d\Omega \end{array}\right]. \tag{7.117}$$

7.3.1 Material tangent matrix in 2D

From these simplifications, it is possible to compose the material tangent matrix, which can be written as:

$$\mathrm{K}_{M_{ijkl}} = \frac{\partial (\mathrm{flux})_{ij}}{\partial (\mathrm{def})_{kl}}, \tag{7.118}$$

where, under the assumption we made, the fluxes are:

$$\{\mathbf{S}, s_3, \mathbf{M}\}, \tag{7.119}$$

and the deformations are:

$$\{\mathbf{F}, \theta_3, \boldsymbol{\Gamma}\}, \tag{7.120}$$

where the couple stress and the wryness only contain two not vanishing components, that are $\{\mathrm{M}_{31}, \mathrm{M}_{32}\}$ and $\{\Gamma_{31}, \Gamma_{32}\}$ respectively. It is important to note here that we used the degree of freedom θ_3 itself as a measure of deformation rather than the rotation matrix, and the reason is that this simplifies the derivation. Following the considerations mentioned in the three-dimensional treatment of the material tangent matrix, the following can be written:

$$\boldsymbol{K}_{M_{ij}} = \left[\begin{array}{c|c|c} \dfrac{\partial \mathbf{S}_i}{\partial \mathbf{F}_j} & \dfrac{\partial \mathbf{S}_i}{\partial \theta^3} & \underset{\sim}{\mathbf{0}} \\ \hline \dfrac{\partial \mathrm{s}_3}{\partial \mathbf{F}_j} & \dfrac{\partial \mathrm{s}_3}{\partial \theta^3} & \underset{\sim}{\mathbf{0}} \\ \hline \underset{\sim}{\mathbf{0}} & \mathbf{0} & \dfrac{\partial \mathbf{M}_i}{\partial \boldsymbol{\Gamma}_j} \end{array}\right] \tag{7.121}$$

In two dimensions, the variation of the micro-rotation tensor with respect to θ_3 can be simply obtained as (see next subsection 7.3.3):

$$\frac{\partial \underset{\sim}{\mathbf{R}}}{\partial \theta_3} = \underset{\sim}{\mathbf{A}} \cdot \underset{\sim}{\mathbf{R}}, \tag{7.122}$$

where :

$$\begin{bmatrix} 0 & -1 & 0 \\ 1 & 0 & 0 \\ 0 & 0 & 0 \end{bmatrix}. \tag{7.123}$$

By reporting the fluxes in their index forms:

$$S_{ij} = \left[\mathrm{J}^e \lambda \left(\mathrm{J} - 1 \right) \left(\underset{\sim}{\mathbf{F}}^{e\,-T} \right)_{ip} + (\mu + \mu_c) \left[F^e_{ip} \right] + (\mu - \mu_c) \left[R_{im} F^e_{nm} R_{np} \right] - 2\mu R_{ip} \right] F^{p^{-1}}_{jp}, \tag{7.124}$$

$$s_3 = -\epsilon_{3lm} \left\{ J^e \, \lambda \left(J^e - 1 \right) \delta_{lm} + (\mu + \mu_c) \left[F^e_{ln} F^e_{mn} \right] + (\mu - \mu_c) \left[R_{ln} F^e_{on} R_{op} F^e_{mp} \right] \right\}, \tag{7.125}$$

$$M_{3s} = 2\,\beta \Gamma^e_{3q} F^{p^{-1}}_{sq}, \tag{7.126}$$

where the subscript s and q range from 1 to 2. The entries of the material tangent matrix can be evaluated as:

$$\frac{\partial \mathrm{S}_{ij}}{\partial \mathrm{F}^e_{kl}} = \lambda \mathrm{J}^e \Bigg\{ \left(\mathrm{J}^e - 1 \right) \left[\left(\underset{\sim}{\mathbf{F}}^{e\,-1} \right)_{lk} \left(\underset{\sim}{\mathbf{F}}^{e\,-1} \right)_{pi} \left(\underset{\sim}{\mathbf{F}}^{p\,-1} \right)_{jp} - \left(\underset{\sim}{\mathbf{F}}^{e\,-1} \right)_{pk} \left(\underset{\sim}{\mathbf{F}}^{e\,-1} \right)_{li} \left(\underset{\sim}{\mathbf{F}}^{p\,-1} \right)_{jp} \right] +$$
$$+ \mathrm{J} \left(\underset{\sim}{\mathbf{F}}^{e\,-1} \right)_{lk} \left(\underset{\sim}{\mathbf{F}}^{e\,-1} \right)_{pi} \left(\underset{\sim}{\mathbf{F}}^{p\,-1} \right)_{jp} \Bigg\} + (\mu + \mu_c) \left[\delta_{ik} \left(\underset{\sim}{\mathbf{F}}^{p\,-1} \right)_{jl} \right] + (\mu - \mu_c) \left[\mathrm{R}_{il} \mathrm{R}_{kp} \left(\underset{\sim}{\mathbf{F}}^{p\,-1} \right)_{jp} \right], \tag{7.127}$$

$$\frac{\partial \mathrm{S}_{ij}}{\partial \mathrm{F}^p_{kl}} = -\left\{ \mathrm{J}^e \lambda \left(\mathrm{J} - 1 \right) \left(\underset{\sim}{\mathbf{F}}^{e\,-T} \underset{\sim}{\mathbf{F}}^{p\,-T} \right)_{il} + (\mu + \mu_c) \left[\underset{\sim}{\mathbf{F}}^{e} \underset{\sim}{\mathbf{F}}^{p^{-T}} \right]_{il} + (\mu - \mu_c) \left[\underset{\sim\sim}{\mathbf{RF}}^{e^T} \underset{\sim\sim}{\mathbf{RF}}^{p^{-T}} \right] - 2\mu \underset{\sim\sim}{\mathbf{RF}}^{p^{-T}}_{il} \right\} \mathbf{F}^{p^{-T}}_{kj}, \tag{7.128}$$

$$\frac{\partial \mathrm{S}_{ij}}{\partial \mathrm{R}_{kl}} \frac{\partial \mathrm{R}_{kl}}{\partial \theta_3} = (\mu - \mu_c) \left[ARF^{e^T} RF^{p^{-T}}_{ij} + RF^{e^T} ARF^{p^{-T}}_{ij} \right] - 2\,\mu ARF^{p^{-T}}_{ij}, \tag{7.129}$$

$$\frac{\partial \mathrm{S}_{ij}}{\partial \Gamma^e_{kl}} = 0, \tag{7.130}$$

$$\frac{\partial \mathrm{S}_{ij}}{\partial \Gamma^p_{kl}} = 0, \tag{7.131}$$

$$\frac{\partial \mathrm{s}_3}{\partial \mathrm{F}^e_{jk}} = -\epsilon_{3lm}\Bigg\{ (\mu+\mu_c)\left[\delta_{lj}\delta_{nk}F^e_{mn} + F^e_{ln}\delta_{mj}\delta_{nk}\right] + (\mu-\mu_c)\left[R_{ln}\delta_{oj}\delta_{nk}R_{op}F^e_{mp} + R_{ln}F^e_{on}R_{op}\delta_{mj}\delta_{pk}\right] - 2\,\mu R_{ln}\delta_{mj}\delta_{nk}\Bigg\}, \tag{7.132}$$

$$\frac{\partial \mathrm{s}_i}{\partial \mathrm{F}^p_{jk}} = 0, \tag{7.133}$$

$$\frac{\partial \mathrm{s}_3}{\partial \mathrm{R}_{jk}}\frac{\partial R_{jk}}{\partial \theta_3} = -\epsilon_{3lm}\Bigg\{ (\mu-\mu_c)\left[ARF^{e^T}RF^{e^T}_{lm} + RF^{e^T}ARF^{e^T}_{lm}\right] - 2\,\mu ARF^{e^T}_{lm}\Bigg\}, \tag{7.134}$$

$$\frac{\partial \mathrm{s}_i}{\partial \Gamma^e_{jk}} = 0, \tag{7.135}$$

$$\frac{\partial \mathrm{s}_i}{\partial \Gamma^p_{jk}} = 0, \tag{7.136}$$

$$\frac{\partial \mathrm{M}_{ij}}{\partial \mathrm{F}^e_{kl}} = 0, \tag{7.137}$$

$$\frac{\partial \mathrm{M}_{3j}}{\partial \mathrm{F}^p_{kl}} = -2\,\beta\,\left(\underset{\sim}{\mathbf{\Gamma}}^e\underset{\sim}{\mathbf{F}}^{p^{-T}}\right)_{3l}F^{p^{-1}}_{jk}, \tag{7.138}$$

$$\frac{\partial \mathrm{M}_{ij}}{\partial R_{kl}} = 0, \tag{7.139}$$

$$\frac{\partial \mathrm{M}_{3j}}{\partial \Gamma^e_{3l}} = 2\,\beta\,F^{p^{-T}}_{lj}, \tag{7.140}$$

$$\frac{\partial \mathrm{M}_{ij}}{\partial \Gamma^p_{kl}} = 0. \tag{7.141}$$

The considerations previously done in case of a three-dimensional material treatment (not consistent tangent matrix) are still valid for the plane-strain condition as well. . By reporting Equations (7.56) and (7.57) in an index form:

$$\frac{\partial(\bullet)}{\partial \mathrm{F}_{ij}} = \frac{\partial(\bullet)}{\partial \mathrm{F}^e_{kl}}\frac{\partial \mathrm{F}^e_{kl}}{\partial \mathrm{F}_{ij}} + \frac{\partial(\bullet)}{\partial \mathrm{F}^p_{kl}}\frac{\partial \mathrm{F}^p_{kl}}{\partial \mathrm{F}_{ij}}, \tag{7.142}$$

$$\frac{\partial(\bullet)}{\partial \Gamma_{ij}} = \frac{\partial(\bullet)}{\partial \Gamma^e_{kl}}\frac{\partial \Gamma^e_{kl}}{\partial \Gamma_{ij}} + \frac{\partial(\bullet)}{\partial \Gamma^p_{kl}}\frac{\partial \Gamma^p_{kl}}{\partial \Gamma_{ij}} + \frac{\partial(\bullet)}{\partial \mathrm{F}^p_{kl}}\frac{\partial \mathrm{F}^p_{kl}}{\partial \Gamma_{ij}}, \tag{7.143}$$

which become:

$$\frac{\partial(\bullet)}{\partial \mathrm{F}_{ij}} = \frac{\partial(\bullet)}{\partial \mathrm{F}^e_{kl}}\delta_{ki}\mathrm{F}^{p^{-1}}_{jl} + \frac{\partial(\bullet)}{\partial \mathrm{F}^p_{kl}}\mathrm{F}^{e^{-1}}_{ki}\delta_{lj}, \tag{7.144}$$

$$\frac{\partial(\bullet)}{\partial \Gamma_{ij}} = \frac{\partial(\bullet)}{\partial \Gamma^e_{kl}}\delta_{ki}\mathrm{F}^{p^{-1}}_{jl} + \frac{\partial(\bullet)}{\partial \Gamma^p_{kl}}\delta_{ki}\delta_{lj} + \frac{\partial \bullet}{\partial \mathrm{F}^p_{kl}}\Gamma^{e^{-1}}_{ki}\delta_{lj}. \tag{7.145}$$

Therefore, the entries of the material tangent matrix are:

$$\frac{\partial \mathrm{S}_{ij}}{\partial \mathrm{F}_{kl}} = \lambda \mathrm{J}^e \Bigg\{ (\mathrm{J}^e - 1) \left[\left(\underset{\sim}{\mathbf{F}}^{-1} \right)_{lk} \left(\underset{\sim}{\mathbf{F}}^{-1} \right)_{ji} - \left(\underset{\sim}{\mathbf{F}}^{-1} \right)_{jk} \left(\underset{\sim}{\mathbf{F}}^{-1} \right)_{li} \right] + \mathrm{J} \left(\underset{\sim}{\mathbf{F}}^{-1} \right)_{lk} \left(\underset{\sim}{\mathbf{F}}^{-1} \right)_{ji} \Bigg\}$$
$$+ (\mu + \mu_c) \left[\delta_{ik} \delta_{lj} \right] + (\mu - \mu_c) \left[\underset{\sim}{\mathbf{R}}_{il} \mathrm{R}_{kj} \right], \quad (7.146)$$

$$\frac{\partial \mathrm{S}_{ij}}{\partial \mathrm{R}_{kl}} \frac{\partial \mathrm{R}_{kl}}{\partial \theta_3} = (\mu - \mu_c) \left[ARF^{e^T} RF_{ij}^{p^{-T}} + RF^{e^T} ARF_{ij}^{p^{-T}} \right] - 2\,\mu ARF_{ij}^{p^{-T}}, \quad (7.147)$$

$$\frac{\partial \mathrm{s}_3}{\partial \mathrm{F}_{ij}} = -\epsilon_{3kl} \Bigg\{ (\mu + \mu_c) \left[\delta_{ki} \left(\underset{\sim}{\mathbf{F}}^{p^{-1}} \cdot \underset{\sim}{\mathbf{F}}^{e\,T} \right)_{jl} + \left(\underset{\sim}{\mathbf{F}}^{p^{-1}} \cdot \underset{\sim}{\mathbf{F}}^{e\,T} \right)_{jk} \delta_{li} \right] +$$
$$(\mu - \mu_c) \left[\left(\underset{\sim}{\mathbf{F}}^{e} \cdot \underset{\sim}{\mathbf{R}}^{T} \right)_{li} \left(\underset{\sim}{\mathbf{F}}^{p\,-1} \cdot \underset{\sim}{\mathbf{R}}^{T} \right)_{jk} + \left(\underset{\sim}{\mathbf{R}} \cdot \underset{\sim}{\mathbf{F}}^{e\,T} \cdot \underset{\sim\sim}{\mathbf{R}\mathbf{F}}^{p\,-T} \right)_{kj} \delta_{li} \right] - 2\,\mu \left[\left(\underset{\sim}{\mathbf{R}} \cdot \underset{\sim}{\mathbf{F}}^{p\,-T} \right)_{kj} \delta_{li} \right] \Bigg\}, \quad (7.148)$$

$$\frac{\partial \mathrm{s}_3}{\partial \Gamma_{ij}} = 0, \quad (7.149)$$

$$\frac{\partial \mathrm{M}_{3j}}{\partial \Gamma_{3l}} = 2\,\beta \delta_{lj}. \quad (7.150)$$

The final elements of the material tangent matrix can be found by reference in the following Equations:

$$\underset{\sim\sim}{\boldsymbol{K}}_M = \begin{bmatrix} \dfrac{\partial \underline{\mathbf{S}}}{\partial \underline{\mathbf{F}}} & \dfrac{\partial \underline{\mathbf{S}}}{\partial \underline{\mathbf{R}}} & \dfrac{\partial \underline{\mathbf{S}}}{\partial \underline{\boldsymbol{\Gamma}}} \\ \dfrac{\partial \underline{\mathbf{s}}}{\partial \underline{\mathbf{F}}} & \dfrac{\partial \underline{\mathbf{s}}}{\partial \underline{\mathbf{R}}} & \dfrac{\partial \underline{\mathbf{s}}}{\partial \underline{\boldsymbol{\Gamma}}} \\ \dfrac{\partial \underline{\mathbf{M}}}{\partial \underline{\mathbf{F}}} & \dfrac{\partial \underline{\mathbf{M}}}{\partial \underline{\mathbf{R}}} & \dfrac{\partial \underline{\mathbf{M}}}{\partial \underline{\boldsymbol{\Gamma}}} \end{bmatrix} = \begin{bmatrix} (7.146) & (7.129) & \underset{\sim}{0} \\ (7.148) & (7.134) & \underset{\sim}{0} \\ \underset{\sim}{0} & \underset{\sim}{0} & (7.150) \end{bmatrix} \quad (7.151)$$

7.3.2 Variation of Mandel stress and couple stress in 2D

In 2D the Mandel stress and couple stress are:

$$\underset{\sim}{\mathbf{\Pi}} = \underset{\sim}{\mathbf{F}}^{e^T} \cdot \underset{\sim}{\mathbf{S}} \cdot \underset{\sim}{\mathbf{F}}^{p^T} + \underset{\sim}{\mathbf{\Gamma}}^{e^T} \cdot \underset{\sim}{\mathbf{M}} \cdot \underset{\sim}{\mathbf{F}}^{p^T}; \tag{7.152}$$

$$\underset{\sim}{\mathbf{\Pi}}_c = \underset{\sim}{\mathbf{M}} \cdot \underset{\sim}{\mathbf{F}}^{p^T}; \tag{7.153}$$

and if these terms are expanded:

$$\underset{\sim}{\mathbf{\Pi}} = \mathrm{J}^e \lambda \left(\mathrm{J}^e - 1\right) \underset{\sim}{\mathbf{I}} + (\mu + \mu_c) \left[\underset{\sim}{\mathbf{F}}^{e^T} \underset{\sim}{\mathbf{F}}^e\right] + (\mu - \mu_c) \left[\underset{\sim}{\mathbf{F}}^{e^T} \underset{\sim}{\mathbf{R}} \underset{\sim}{\mathbf{F}}^{e^T} \underset{\sim}{\mathbf{R}}\right] - 2\mu \underset{\sim}{\mathbf{F}}^{e^T} \underset{\sim}{\mathbf{R}} + 2\,\beta \underset{\sim}{\mathbf{\Gamma}}^{e^T} \underset{\sim}{\mathbf{\Gamma}}^e, \tag{7.154}$$

$$\underset{\sim}{\mathbf{\Pi}}_c = 2\,\beta \underset{\sim}{\mathbf{\Gamma}}^e, \tag{7.155}$$

and the variation with respect to the deformations can be evaluated as:

$$\begin{aligned} \frac{\partial \Pi^M_{ij}}{\partial F^e_{kl}} = {} & \lambda\, J^e \delta_{ij} \underset{\sim}{\mathbf{F}}^{-T}_{kl} \left(2\, J^e - 1\right) + (\mu + \mu_c) \left[\delta_{il} F^e_{kj} + \delta_{jl} F^e_{ki}\right] + \\ & (\mu - \mu_c) \left[\delta_{il} \underset{\sim}{\mathbf{R}} \underset{\sim}{\mathbf{F}}^{e^T} \underset{\sim}{\mathbf{R}}_{kj} + \underset{\sim}{\mathbf{F}}^{e^T} \underset{\sim}{\mathbf{R}}_{il} R_{kj}\right] - 2\,\mu \delta_{il} R_{kj}, \end{aligned} \tag{7.156}$$

$$\frac{\partial \Pi^M_{ij}}{\partial \theta_3} = (\mu - \mu_c) \left[\underset{\sim}{\mathbf{F}}^{e^T} \underset{\sim}{\mathbf{A}} \underset{\sim}{\mathbf{R}} \underset{\sim}{\mathbf{F}}^{e^T} \underset{\sim}{\mathbf{R}}_{ij} + \underset{\sim}{\mathbf{F}}^{e^T} \underset{\sim}{\mathbf{R}} \underset{\sim}{\mathbf{F}}^{e^T} \underset{\sim}{\mathbf{A}} \underset{\sim}{\mathbf{R}}_{ij}\right] - 2\,\mu \underset{\sim}{\mathbf{F}}^{e^T} \underset{\sim}{\mathbf{A}} \underset{\sim}{\mathbf{R}}_{ij}, \tag{7.157}$$

$$\frac{\partial \Pi^M_{ij}}{\partial \Gamma^e_{kl}} = 2\,\beta \left[\delta_{il} \Gamma^e_{kj} + \Gamma^e_{ki} \delta_{jl}\right], \tag{7.158}$$

$$\frac{\partial \Pi^M_{c_{ij}}}{\partial \theta_k} = 0, \tag{7.159}$$

$$\frac{\partial \Pi^M_{c_{ij}}}{\partial \Gamma^e_{kl}} = 2\,\beta \delta_{ik} \delta_{jl}. \tag{7.160}$$

7.3.3 Derivatives of $\underset{\sim}{\mathbf{R}}$ and $\underset{\sim}{\mathbf{\Gamma}}$ in 2D

Given a generic rotation matrix, if the parameter vector has only one non-zero component (simple rotation around one of the axis), for example θ_3 around the z-axis, it can be written as:

$$\underset{\sim}{\mathbf{R}} = \exp\left(-\underset{\simeq}{\boldsymbol{\epsilon}} \cdot \begin{bmatrix} 0 \\ 0 \\ \theta_3 \end{bmatrix}\right) = \exp\left(0 \begin{bmatrix} 0 & 0 & 0 \\ 0 & 0 & -1 \\ 0 & 1 & 0 \end{bmatrix} + 0 \begin{bmatrix} 0 & 0 & 1 \\ 0 & 0 & 0 \\ -1 & 0 & 0 \end{bmatrix} + \theta_3 \begin{bmatrix} 0 & -1 & 0 \\ 1 & 0 & 0 \\ 0 & 0 & 0 \end{bmatrix}\right) = \exp\left(\theta_3 \underset{\sim}{\mathbf{A}}\right), \tag{7.161}$$

which can be simply differentiated with respect to θ_3 obtaining:

$$\frac{\partial \underset{\sim}{\mathbf{R}}}{\partial \theta_3} = \underset{\sim}{\mathbf{A}} \cdot \underset{\sim}{\mathbf{R}} = \underset{\sim}{\mathbf{R}}', \tag{7.162}$$

$$\frac{\partial \underset{\sim}{\mathbf{R}}^T}{\partial \theta_3} = \underset{\sim}{\mathbf{A}}^T \cdot \underset{\sim}{\mathbf{R}}^T = \underset{\sim}{\mathbf{R}}'^T, \tag{7.163}$$

$$\frac{\partial \underset{\sim}{\mathbf{R}}'}{\partial \theta_3} = \underset{\sim}{\mathbf{A}} \cdot \underset{\sim}{\mathbf{R}}' = \underset{\sim}{\mathbf{A}}^2 \cdot \underset{\sim}{\mathbf{R}}., \tag{7.164}$$

In FEA, the gradient of $\underset{\sim}{\mathbf{R}}$ and $\underset{\sim}{\mathbf{R}}'$ at the integration points can be evaluated using the B matrix as:

$$\frac{\partial \mathrm{R}_{ij}}{\partial X_k} = \frac{\partial \mathrm{R}_{ij}}{\partial \theta_3}\frac{\partial \theta_3}{\partial X_k} = \mathrm{R}'_{ij}\mathrm{B}^{\theta}_{kl}\chi^{\theta}_l, \tag{7.165}$$

$$\frac{\partial \mathrm{R}'_{ij}}{\partial X_k} = \frac{\partial \mathrm{R}'_{ij}}{\partial \theta_3}\frac{\partial \theta_3}{\partial X_k} = \mathrm{A}_{im}\mathrm{R}'_{mj}\mathrm{B}^{\theta}_{kl}\chi^{\theta}_l. \tag{7.166}$$

Also the wryness can be simplified in case of a 2D assumption:

$$\underset{\sim}{\mathbf{\Gamma}} = -\frac{1}{2}\underset{\sim}{\underset{\sim}{\boldsymbol{\epsilon}}} : \left[\underset{\sim}{\mathbf{R}}^T \cdot \left(\underset{\sim}{\mathbf{R}} \otimes \underline{\boldsymbol{\nabla}}_0\right)\right], \tag{7.167}$$

and, recalling that the rotation matrix in 2D is:

$$\underset{\sim}{\mathbf{R}} = \begin{bmatrix} \cos(\theta_3) & -\sin(\theta_3) & 0 \\ \sin(\theta_3) & \cos(\theta_3) & 0 \\ 0 & 0 & 1 \end{bmatrix}, \tag{7.168}$$

from which:

$$\underset{\sim}{\mathbf{R}} \otimes \underline{\boldsymbol{\nabla}}_0 = \left\{ \theta_{3,X} \begin{bmatrix} -\sin(\theta_3) & -\cos(\theta_3) & 0 \\ \cos(\theta_3) & -\sin(\theta_3) & 0 \\ 0 & 0 & 0 \end{bmatrix} \quad \theta_{3,Y} \begin{bmatrix} -\sin(\theta_3) & -\cos(\theta_3) & 0 \\ \cos(\theta_3) & -\sin(\theta_3) & 0 \\ 0 & 0 & 0 \end{bmatrix} \quad \begin{bmatrix} \underset{\sim}{0} \end{bmatrix} \right\}, \tag{7.169}$$

then:

$$\underset{\sim}{\mathbf{R}}^T\left(\underset{\sim}{\mathbf{R}}\otimes\underline{\boldsymbol{\nabla}}_0\right)=\left\{\begin{bmatrix}0&-\theta_{3,X}&0\\ \theta_{3,X}&0&0\\ 0&0&0\end{bmatrix}\quad\begin{bmatrix}0&-\theta_{3,Y}&0\\ \theta_{3,Y}&0&0\\ 0&0&0\end{bmatrix}\quad\begin{bmatrix}\underset{\sim}{0}\end{bmatrix}\right\},\tag{7.170}$$

and finally:

$$\underset{\sim}{\boldsymbol{\Gamma}}=-\frac{1}{2}\underset{\simeq}{\boldsymbol{\epsilon}}:\left[\underset{\sim}{\mathbf{R}}^T\left(\underset{\sim}{\mathbf{R}}\otimes\underline{\boldsymbol{\nabla}}\right)\right]=\begin{bmatrix}0&0&0\\ 0&0&0\\ \theta_{3,X}&\theta_{3,Y}&0\end{bmatrix}.\tag{7.171}$$

Under the same simplifying assumption, it is also possible to evaluate the derivative of the wryness with respect to the rotation θ_3:

$$\frac{\partial\underset{\sim}{\boldsymbol{\Gamma}}}{\partial\theta_3}=\underset{\sim}{\boldsymbol{\Gamma}}'=\frac{1}{2}\underset{\simeq}{\boldsymbol{\epsilon}}:\left[\frac{\partial\underset{\sim}{\mathbf{R}}}{\partial\theta_3}\cdot\left(\underset{\sim}{\mathbf{R}}^T\otimes\underline{\nabla}_0\right)+\underset{\sim}{\mathbf{R}}\cdot\left(\frac{\partial\underset{\sim}{\mathbf{R}}^T}{\partial\theta_3}\otimes\underline{\nabla}_0\right)\right].\tag{7.172}$$

7.4 Updating the deformation measures

One disadvantage of using the rotation parameters as degrees of freedom is that the rotation and the wryness operators cannot be, in general, handled as classically done with the displacement degrees of freedom, for instance:

$$\underset{\sim}{\mathbf{R}}(\underline{\boldsymbol{\theta}}_3)=\underset{\sim}{\mathbf{R}}(\underline{\boldsymbol{\theta}}_1)\cdot\underset{\sim}{\mathbf{R}}(\underline{\boldsymbol{\theta}}_2)\neq\underset{\sim}{\mathbf{R}}(\underline{\boldsymbol{\theta}}_1+\underline{\boldsymbol{\theta}}_2),\tag{7.173}$$

meaning that the operation of updating the rotational degrees of freedom requires proper procedure rather than simple addition of the parameters (as done for example with displacement degrees of freedom). Given a rotation tensor $\underset{\sim}{\mathbf{R}}$ derived from a composition of two rotations $\underset{\sim}{\mathbf{R}}_1$ and $\underset{\sim}{\mathbf{R}}_2$:

$$\underset{\sim}{\mathbf{R}}_3(\underline{\boldsymbol{\theta}}_3)=\underset{\sim}{\mathbf{R}}_1(\underline{\boldsymbol{\theta}}_1)\cdot\underset{\sim}{\mathbf{R}}_2(\underline{\boldsymbol{\theta}}_2),\tag{7.174}$$

its rotation parameter vector $\underline{\boldsymbol{\theta}}_3$ can be computed through a two step procedure that involves the two rotation parameters vectors $\underline{\boldsymbol{\theta}}_1$ and $\underline{\boldsymbol{\theta}}_2$ [Bauchau 2011]:

$$\begin{cases} \theta_3 = 2\,\mathrm{acos}\left[\nu_1\nu_2\left(\dfrac{1}{\varepsilon_1\varepsilon_2} - \dfrac{1}{4}\underline{\boldsymbol{\theta}}_1\cdot\underline{\boldsymbol{\theta}}_2\right)\right] \\ \underline{\boldsymbol{\theta}}_3 = \dfrac{\nu_1\nu_2}{\nu_3}\left[\dfrac{1}{\varepsilon_2}\underline{\boldsymbol{\theta}}_1 + \dfrac{1}{\varepsilon_1}\underline{\boldsymbol{\theta}}_2 + \dfrac{1}{2}\underset{\sim}{\boldsymbol{\theta}}_1\cdot\underline{\boldsymbol{\theta}}_2\right] \end{cases}, \tag{7.175}$$

where the terms ν and ϵ depend on the chosen parameterization and can be found in Table 6.1. The first Equation returns the angle of the rotation, θ_3, thus enabling the computation of ν_3, and the second Equation returns its respective vectorial parametrization ($\underline{\boldsymbol{\theta}}_3$). The update of the rotation parameter vector must therefore be performed through the presented two-step procedure.
The updating procedure of the wryness tensor also requires proper handling. Given the definition of the wryness tensor:

$$\underset{\sim}{\boldsymbol{\Gamma}}^3 = -\frac{1}{2}\underset{\simeq}{\boldsymbol{\epsilon}} : \left[\underset{\sim}{\mathbf{R}}_3^T\cdot\left(\underset{\sim}{\mathbf{R}}_3\otimes\underline{\nabla}_0\right)\right], \tag{7.176}$$

the updated wryness can be simply evaluated by applying the wryness operator on the updated rotation matrix, $\underset{\sim}{\mathbf{R}}^3$, as in Equation (7.174), resulting in:

$$\Gamma^3_{ij} = -\frac{1}{2}\epsilon_{ikl}R^3_{mk}\frac{\partial R^3_{ml}}{\partial X_j} = -\frac{1}{2}\epsilon_{ikl}R^1_{mp}R^2_{pk}\frac{\partial\left(R^1_{mq}R^2_{ql}\right)}{\partial X_j} = \Gamma^2_{ij} - \frac{1}{2}\epsilon_{ikl}R^3_{mk}R^2_{ql}\frac{\partial R^1_{mq}}{\partial X_j}. \tag{7.177}$$

Chapter 8

Simulations of Cosserat thermo-mechanics at finite deformation

This chapter includes the tests performed to verify the correctness of the implemented formulation and applications to the simulation of strain localization phenomena in thermo-elastoviscoplastic materials. The Cosserat element under large deformation has been implemented under 2D plane strain conditions, therefore, all the simulations here presented are under plane strain conditions. All the elements used in the following tests are quadrilateral and they have 8 nodes, interpolating the fields with quadratic shape functions. Each element possesses 24 DOFs, 16 of which are in-plane nodal displacements u_1 and u_2, and the other 8 are the nodal micro-rotations (only the third component of $\underline{\boldsymbol{\theta}}$ in a 2D space).
In the following section, two homogeneous-field bench tests are presented. The first series of tests have been performed on a single element with proper boundary condition in order to test the pure mechanical response of the implemented theory under tensile loading, and the second one under gliding. Hyper-elastic, Elasto-plastic and elasto-visco-plastic material behavior were tested. Subsequently, more complex multi-elements tests were used to a assess the element capability to simulate the proper behavior. Forest et al. proposed a micro-rotation boundary test [Forest and Sievert 2003], and the same test has been here performed using a large deformation element. Then, the localization problem analyzed in Section 5.2.3 has been simulated using the finite deformation theory proposed in the previous chapter, and the same test has been used to present the problem of saturating yield stress during localization. The same test has been used also to investigate the separate and opposite effects that thermal softening and strain rate hardening have on localization process. The hat-shaped specimen was previously used to investigate the size effect using the small deformation Cosserat theory [Russo, Forest, et al. 2020], and the same test has been here used to investigate over the saturating yield stress in case of geometrically-induced localizations. Finally, the theory has been used to simulate a simplified case of manufacturing operation, and the numerical predictions have been quantitatively compared with the experimental results obtained at the University of

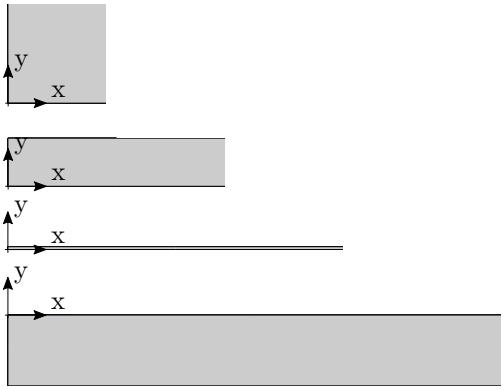

(a) Deformation history of the single element tensile test in a SD framework.

(b) Deformation history of the single element tensile test in a LD framework.

λ [MPa]	μ	μ_c [MPa]	β [MPa·mm^2]
40384.0	26923.0	100000.0	60000.0

Table 8.1: Elastic material properties used to run the tensile and glide tests.

Bordeaux.

8.1 Homogeneous fields: single element tests

8.1.1 Hyper-elastic, visco-plastic and elasto-plastic tension test

The tensile tests is meant to verify the correctness of the part of the stiffness matrix that acts on the displacement degrees of freedom. A single square element of 1 mm long edge has been used. The left bottom corner of the element has coordinates (0,0) and the top right corner lies in (1,1). Homogeneous deformation fields have been achieved through application of the following BCs:

$$\begin{cases} u_1 = 0\ mm & @x = 0\ mm, \\ u_1 = 4\ mm & @x = 1\ mm, \\ u_1 = 0\ mm & @y = 0\ mm, \end{cases} \tag{8.1}$$

representing a stretching of the element by 400%. Referring to the mechanical elastic response reported in Equations (7.114), (7.115) and (7.116), the elastic mechanical properties used to run this bench test are summarized in Table 8.1. As expected, when large

ϕ_0 [MPa]	H [MPa]	Q_1 [MPa]	g_1 [-]	Q_2 [MPa]	g_2 [-]
900	1000	1500	0.2	1200	0.2

a_1 [-]	a_2 [-]	b_1 [-]	b_2 [-]	b_3 [-]	K [MPa]	n [-]
1.0	0.0	0.0	0.0	0.0	1000	1.2

Table 8.2: Visco-plastic material properties used to run the tensile and glide tests.

deformations are simulated while using a SD framework, the theory is not anymore reliable, in fact, as reported in Figure 8.1a, the element linearly and continuously shrinks along the y direction and reaches a point in which the thickness becomes null. The simulation continues and the top nodes are brought below the bottom ones. This condition occurs due to the fact that in a SD simulation the deformations are expected to be small so that a check of the Jacobian is not required, and the non-linear behaviors are linearized. On the contrary, the geometrical non-linear behavior of the element along the y-axis has been perfectly captured by the LD formulation as it has been reported in Figure 8.1b. The results in terms of load-displacement are reported in Figure 8.2, where it is appreciable that, as expected, the two curves diverge from each due to the nonlinearity. The tensile tests has been also used to verify the correctness of the implementation of the elasto-plastic and elasto-visco-plastic material model in the Cosserat element in large deformation under plane-strain condition. For clarity, the plastic hardening law is here reported:

$$\phi = \phi_0 + H\Lambda^p + Q_1 \left[1 - \exp\left(-g_1\Lambda^p\right)\right] + Q_2 \left[1 - \exp\left(-g_2\Lambda^p\right)\right], \tag{8.2}$$

and the equivalent stress is evaluated as in Equation (6.98) here reported:

$$\Pi_{eq} = \sqrt{\frac{3}{2}\left[a_1 I_1(\underset{\sim}{\mathbf{\Pi}}) + a_2 I_2(\underset{\sim}{\mathbf{\Pi}}) + b_1 I_1(\underset{\sim}{\mathbf{\Pi}}_c) + b_2 I_2(\underset{\sim}{\mathbf{\Pi}}_c) + b_3 I_3(\underset{\sim}{\mathbf{\Pi}}_c)\right]}. \tag{8.3}$$

The material properties concerning the hyper-elastic part of the model have been taken from the already performed test (Table 8.1), whereas the coefficients used to characterize the elasto-plastic and elasto-visco-plastic parts have been summarized in Table 8.2. The visco-plastic and elasto-plastic tests were performed by applying a reduced displacement of 0.1 mm, still maintaining the same boundary conditions as in Equation (8.1). Regarding the visco-plastic tests, they were performed by using two different durations of application of the loads, such as to emphasize the viscous effect. In Figure 8.2 the responses in terms of load-displacement have been reported, and they highlight a correct implementation of the model. The visco-plastic behavior correctly predicts a stiffer response for loads applied during shorter periods of time, and then the theory reduces to the elasto-plastic one when the loads are applied for long periods of time.

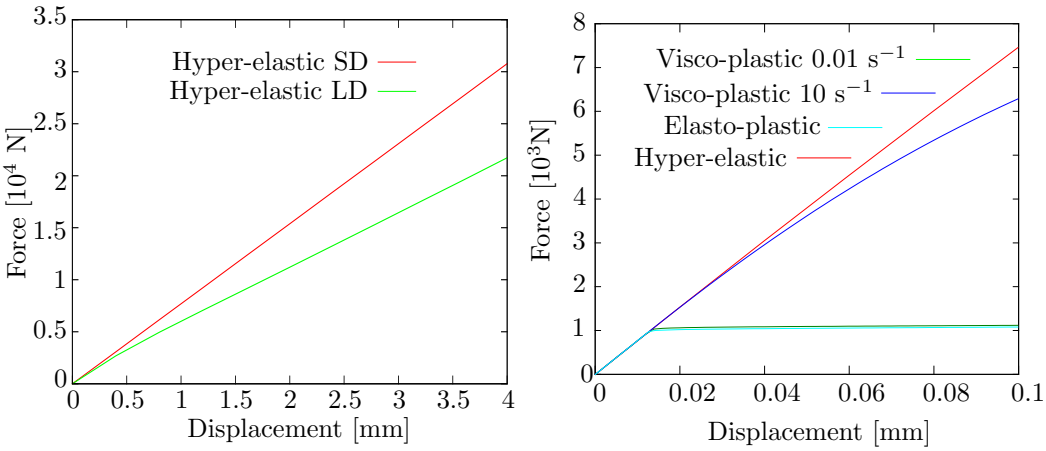

Figure 8.2: Load-displacement graph of the tensile test on a single element. Comparison of SD and LD formulations (a) and comparison of hyper-elastic, elasto-visco-plastic and elasto-plastic models (b). The legend in (b) indicates the strain rates.

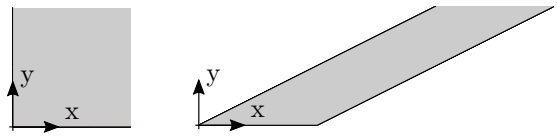

Figure 8.3: Undeformed and deformed shape assumed by the element during the glide test

8.1.2 Hyper-elastic, visco-plastic and elasto-plastic glide test

This test is meant to verify the correctness of the implementation of the terms related to the skew-symmetric part of the tensors. The geometry and the mechanical properties used for this test are the same as the ones used for the tensile test: the element was a 1 mm square whose vertexes have coordinates of (0,0) and (1,1), and the properties are reported in Table 8.2. An homogeneous shear field is induced in the element by applying the following boundary conditions:

$$\begin{cases} u_1 = 0\ mm & @y = 0\ mm, \\ u_1 = 2\ mm & @y = 1\ mm, \\ u_2 = 0\ mm & @y = 0\ mm, \\ u_2 = 0\ mm & @y = 1\ mm. \end{cases} \tag{8.4}$$

Ideally, this set of BCs shall induce the element to return an equivalent shear strain of 1 in a SD framework. This value was indeed reproduced during the SD test. The micro-rotation was left free to follow the macro-rotation, therefore the micro-rotation was expected to have the same value of the macro-rotation in the whole element. This condition was verified in the SD test, where the micro-rotation had an homogeneous value of -1 (micro-rotation notation follows the right-hand rule). As expected, the LD test produced a smaller but uniform micro rotation value equal to 0.7878 rad. The difference in produced micro-rotation is due to the fact that the large value of μ_c acts as a penalty term constraining the micro-rotation and the material rotation in both SD and LD framework, however, the material rotation in SD is linearized and it is fully non-linear in the LD framework. Figure 8.3 shows the deformed configuration of the element during the glide test. The tests performed under SD and LD conditions produced the same deformed configuration, but the difference between the two formulations can be found in the different predicted value of micro-rotation. In Figure 8.4a the force-displacement are reported for the glide test performed under LD and SD. Once again, it is evident that the LD framework is able to capture the additional tensile stiffness induced by the geometrical non-linearity of the test. In Figure 8.4b the response in terms of load-displacement can be observed in case of hyper-elastic, visco-plastic and elasto-plastic behaviors, where the viscous element was tested for two different total time of application of the load. As expected, also under shear loading, the viscous response in fact reduces to a plastic one in case of large application time. As per the tensile test, the inelastic tests used the same boundary conditions of the hyper-elastic one, but the applied load was reduced to 0.1 mm, so that the distinctions between the different behaviors would be more appreciable.

8.2 Simple micro-rotation boundary layer

This test aims at verifying the correctness of the method for a multi-element case, that is, verifying that the element stiffness matrix is properly written and that the assembly of the stiffness matrices of adjacent elements is correctly performed. This test has been

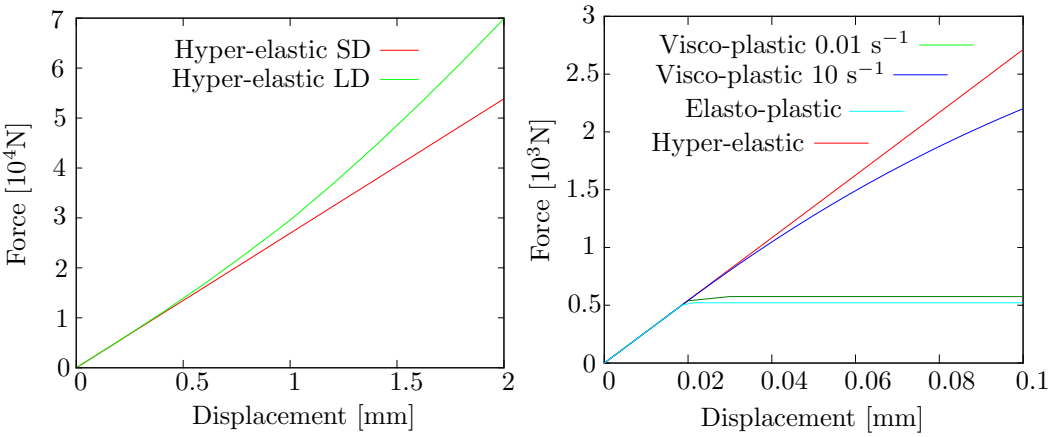

Figure 8.4: Load-displacement graph of the glide test on a single element. Comparison of hyper-elastic SD and LD formulations (a) and comparison of hyper-elastic, elasto-visco-plastic and elasto-plastic models (b). The legend in (b) indicates the strain rates.

previously used by [Forest and Sievert 2003]. They developed the analytical solution of the boundary value problem in case of monotonic load application, which can be used as a solid and reliable candidate for the verification of the numerical method. In this test, the gradient of the micro-rotation is of central importance, such as the entangling between the displacement and micro-rotational degrees of freedom. The geometry of the performed test is pictured in Figure 8.5. The following BCs are applied to the specimen:

$$\begin{cases} u_1 = 0\ mm & @y = 0mm, \\ u_2 = 0\ mm & @y = 0mm, \\ \theta_3 = 0\ rad & @y = 0mm, \\ \theta_3 = 0.001\ rad & @y = 5mm, \end{cases} \tag{8.5}$$

and the application of a micro-rotation at the top boundary induces plasticity at the same location, in a thin layer, that then expands as the load increases. Elasto-plasticity is the chosen mechanical behavior for this test. The applied micro-rotation, due to the entanglement characterizing the Cosserat media, produces material rotation and shear strain. The generated deformation fields are not homogeneous, and this means that in this test we can observe the effect of the gradient of the micro-rotation and also verify its implementation. The fields numerically predicted are compared against the analytical solutions, which has been obtained under the assumption of infinitesimal variations of the degrees of freedom [Forest and Sievert 2003]. The distribution of the shear stress and of the couple-stress have been used to verify the correctness of the formulation. In Figure 8.6 these comparisons are reported against their analytical solution. It must be mentioned

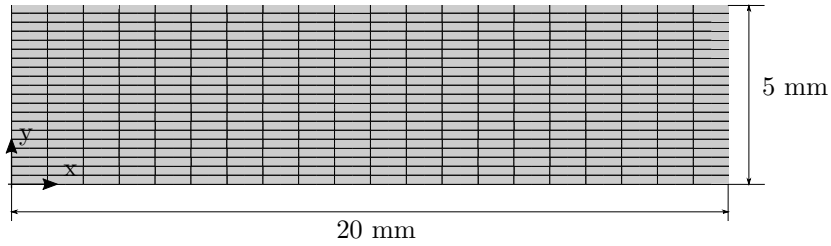

Figure 8.5: Geometry used for the micro-rotation boundary layer test.

λ [MPa]	μ [MPa]	μ_c [MPa]	β [MPa·mm^2]	ϕ_0 [MPa]
115348	76923	100000	76923	100.0
H [MPa]	Q_1 [MPa]	g_1 [-]	Q_2 [MPa]	g_2 [-]
0.0	0.0	0.0	0.0	0.
a_1 [-]	a_2 [-]	b_1 [-]	b_2 [-]	b_3 [-]
1.0	1.0	0.0	1.0	1.0

Table 8.3: Elasto-plastic material properties used for the micro-rotational boundary layer test.

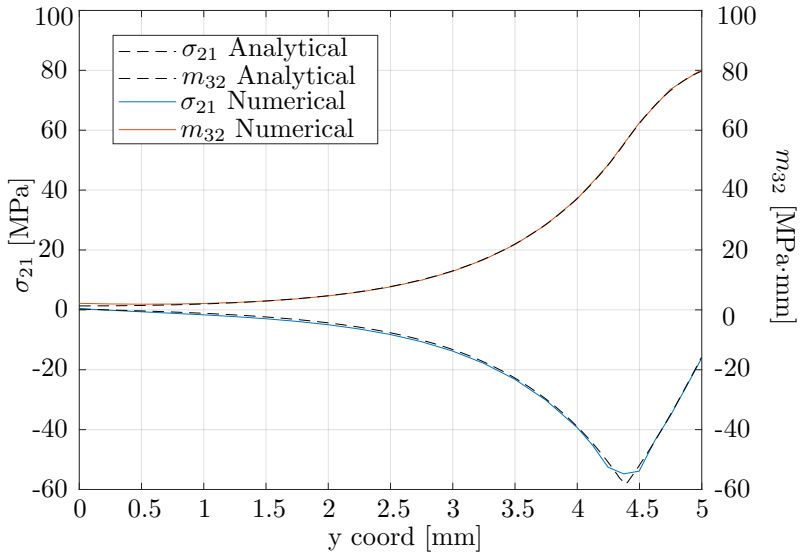

Figure 8.6: Comparison between the numerically predicted and analytical derived distributions of the shear stress σ_{12} and of the couple stress m_{32} fields along the y-direction of the specimen.

that the predicted fields coincide with the analytical solution because the applied micro-rotation on the top boundary is small enough to induce small deformations, thus the produced results still remain infinitesimal. Application of larger micro-rotations would induce appreciable differences in the predicted fields andd a departure from the analytical solution.

8.3 Semi-infinite plane under glide: shear band analysis

Besides the standard tests, the main benchmark for the validation of the numerical method has been to retrieve the analytical solution for the localization of a semi-infinite plane under glide. The focus on this test follows the requirement of the proposed method to be used for manufacturing operations in which the prediction of the correct thickness of the adiabatic shear band must be correctly addressed. The numerical fields are compared against the analytical solutions derived in Chapter 5. The cumulative plastic strain has been selected as main field to be used for the comparison. The geometry and boundary conditions used to reproduce a glide test were previously summarized in Figure 5.1 in Chapter 5. The simplified meshed geometry used for the test is reported in Figure 8.7a,

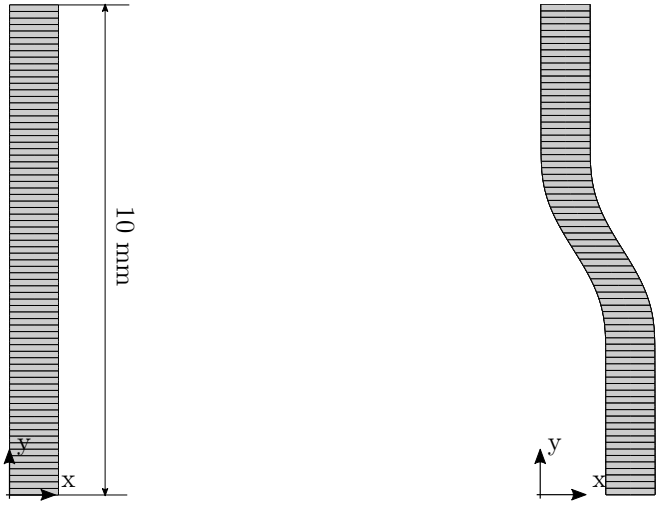

(a) (b)

Figure 8.7: Meshed geometry of the strip test used to verify the numerical implementation for a localization phenomenon (a) and deformed shape assumed by the specimen during the application of the load (b).

and the boundary conditions are the followings:

$$\begin{cases} u_1 = 0.02\ mm & @y = -5mm \\ u_1 = -0.02\ mm & @y = 5\ mm \\ u_2 = 0\ mm & @\text{everywhere} \end{cases} . \tag{8.6}$$

The mechanical properties used to perform the simulation can be found in Table 8.4: a linear softening behavior has been assigned to the material such as to induce strain localization in the strip. It is well known that if this material behavior was to be assigned to the classical continuum mechanics, the simulations would not be not able to deliver a finite and mesh-independent localization zone, and this was also previously reported in Figure 5.4. Given the fact that the problem can be simplified to a mono-dimensional analysis, the fields must only be discretized along the y direction, therefore a vertical strip has been modeled, and periodic boundary conditions were applied to the right and left nodes of the elements. In Figure 8.7 the mesh and the deformed shape assumed by the specimen are reported. The assigned system of boundary conditions would lead to an homogeneous solution in which it is not possible to study localization: the localization process was in fact triggered to initialize in the center of the geometry through the reduction by a small negligible percentage ($\approx 1.5\%$) of the yield stress of the central element. Different features of the Cosserat media were analyzed while studying the localization test. For example, in Figure 8.8 the effect of using different characteristic lengths is reported. Here the analytical solution of the thickness of the shear band is reported from

λ [MPa]	μ [MPa]	μ_c [MPa]	β [MPa·mm^2]	ϕ_0 [MPa]
115348.0	76923.0	100000.0	77.0	250.0
H [MPa]	Q_1 [MPa]	g_1 [-]	Q_2 [MPa]	g_2 [-]
-250.0	0.0	0.0	0.0	0.
a_1 [-]	a_2 [-]	b_1 [-]	b_2 [-]	b_3 [-]
1.0	1.0	0.0	0.0	0.0

Table 8.4: Elasto-plastic material properties used for the shear band test.

Equation (5.94):

$$l^p_{ch} = \frac{2\,\pi}{\omega_p} = \sqrt{-\frac{\pi\beta\,[(\mu+\mu_c)H + \mu\mu_c\,3\,a_3]}{\mu\,\mu_c\,H}}. \tag{8.7}$$

In order to obtain two different thicknesses of the shear band, two different values for the couple stress modulus β have been used. Such behavior has been correctly captured by both numerical and analytical models. The fact that the thickness of the shear band can be easily tuned by changing the value of the higher order modulus β indicates the clear connection between this additional parameter included in the model and the observed experimental value of the thickness of the shear band if such model ought to be calibrated.
In order to verify that the thickness of the shear band does not expand with the increasing loads, the applied displacements have been amplified and the cumulative plastic strain has been reported for the two different values of the applied displacement in Figure 8.9. As expected, the localization zone does not get broader with an increase of the applied displacement. This was expected from the analytical model, in which we can observe that the period of the sin/cos functions does not depend on the boundary conditions or on the state of the continuum, but it rather depends only on the mechanical properties of the material.

8.3.1 Shear band broadening for saturating yield stress

Although it is useful to mimic localization in the shear band through purely softening plastic behavior, this type of material characterization does not correspond to any realistic material model. Many types of metals, in fact, exhibit an hardening behavior at first, followed by a plateau, in their stress-strain curve [Babu and Lindgren 2013]. The softening behavior that the material experiences during localization is often, in fact, of a thermal nature: the plastic work is converted into heat, and, depending on the thermal diffusion coefficient of the material and on the developed strain rates, the heat might be locally retained and not be diffused, thus inducing local thermal softening. Without the thermal effect (and in absence of any geometry that might induce localization), in fact, it is not certain that the deformations are able to localize. These doubts have, in fact, arose when

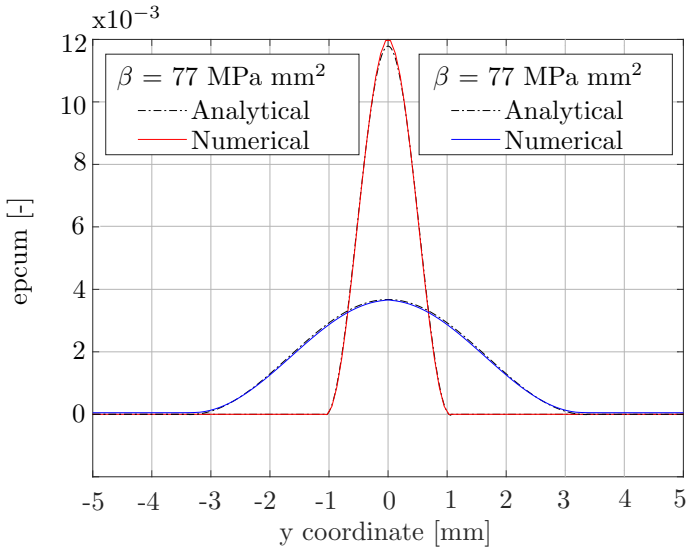

Figure 8.8: Comparison between the analytical solution and the numerical prediction for the distribution of the cumulative plastic strain along the strip using different characteristic lengths.

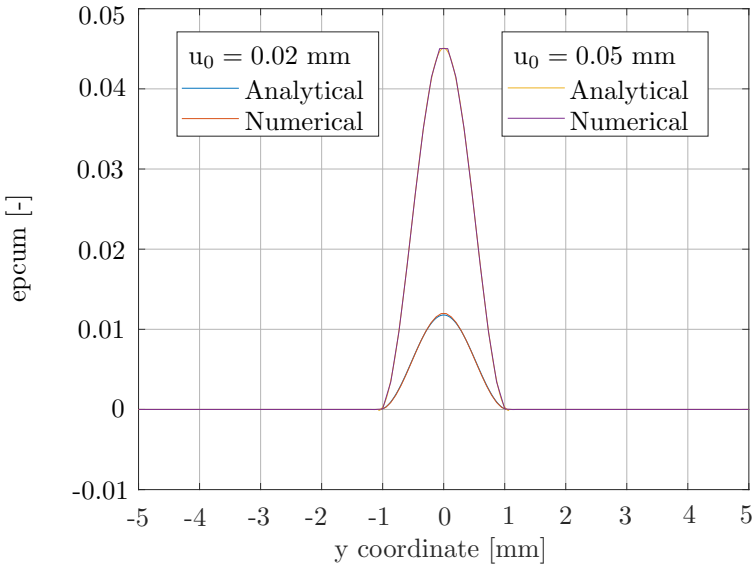

Figure 8.9: Comparison between the analytical solution and the numerical prediction for the distribution of the cumulative plastic strain along the strip using different applied displacements.

the distribution of the plastic field was analyzed analytically in the previous Section 5.3.3, and it was found that the localization zone might not be bounded. The differential equations governing the fields in the plastic zone in case of perfectly plastic behavior, regardless of the boundary conditions, are here reported, suggesting a parabolic-type of solution for the distribution of the cumulative plastic strain in case of perfectly plastic behavior:

$$p(y)_{H=0} = \frac{2}{\sqrt{3}\,a_3}\left[A\,y^2 + B\,y - \frac{\beta\,A}{\mu_c} + C\right] - \frac{\phi_0}{3\,\mu\,a_3}. \tag{8.8}$$

The equation describing the cumulative plastic fields suggests that, differently from the softening case, the solutions are not periodic, thus not bounded by the periodicity of the function. Due to the form of the general solution, one might be induced to infer that, differently from the softening case, the localization zone might broaden. In order to verify weather the localization zone broadens or not after localization and subsequent saturation of the stress-strain curve, a numerical escamotage has been used. In this case, in fact, the Cosserat material has been characterized with the following plastic behavior:

$$\phi = \phi_\infty + (R_0 - \phi_\infty)\,e^{-b\,p}, \tag{8.9}$$

where ϕ_∞ is the asymptotic stress of saturation, R_0 is the initial yield stress, b is a constant and p is the cumulative plastic strain. In Figure 8.11 the representation of such curve is reported for the parameters given in Table 8.5. The adoption of a yield stress as the one indicated in Equation (8.9) has a double advantage: the initial negative slope of the curve ensures that localization would be initiated, and the saturation of the curve is used to simulate the saturation of the real stress-strain curve. The initial distribution of the cumulative plastic strain should follow a sinusoidal function, and once the yield stress start saturating, however, the cumulative plastic strain field should shift its distribution from a sinusoidal (belonging to the softening analytical solution) to a parabolic one (belonging to the perfectly plastic analytical solution), thus losing its property of periodicity.
The exponential material model was not planned to be used in the beginning, therefore it has been subsequently implemented in the numerical solver and the localization test has been performed using such model. The mechanical properties used for this test are reported in Table 8.5. For this test, the distribution of the cumulative plastic strain has been reported at different loading stages in order to follow its development, and the results can be appreciated in Figure 8.10. From this Figure, it is evident that the shear band broadens when the asymptotic values of yield stress are reached. In order to have a reference, the exponential stress-strain curve has been linearized at its origin, so as to obtain a linear softening behavior which would lead to a similar shear band thickness (at least in the first step of the loading). Since the correct linearization of the curve would lead to the adoption of an extreme slope of the curve, the choice of the steepness of the curve has been performed via observation of the produced two curves as reported already in Figure 8.11. It can be appreciated that the linearized softening behavior is acceptably approximating the exponential curve until the cumulative plastic strain reaches the values of ≈ 0.02. The slope of the linearized curve in Figure 8.11 can be estimated to be ≈ -1250 [MPa]. By plugging this value, along with the other mechanical properties, in Equation (8.8), the expected characteristic length is ≈ 1.9 mm. The localization problem was then also simulated by using a linear softening slope of -1250 MPa, such as to obtain the same shear band thickness that would develop in the first stages of the simulation using the exponential plastic behavior. In Figure 8.10 the comparison between the development

λ [MPa]	μ	μ_c [MPa]	β [MPa·mm^2]
115348.0	76923.0	100000.0	77.0
ϕ_0[Mpa]	ϕ_∞[Mpa]	b[-]	a_1 [-]
250.0	200.0	40.0	1.0
a_2 [-]	b_1 [-]	b_2 [-]	b_3 [-]
s1.0	0.0	0.0	0.0

Table 8.5: Elasto-plastic material properties used for the localization problem using exponential softening behavior.

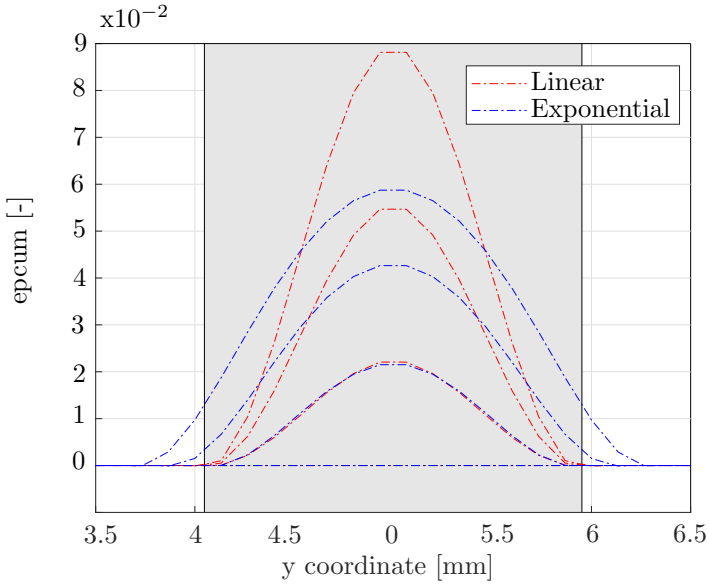

Figure 8.10: Development of the cumulative plastic strain fields at 33%, 66% and 100% of the applied load. Comparison between linearized softening and exponential/saturation plastic behaviors.

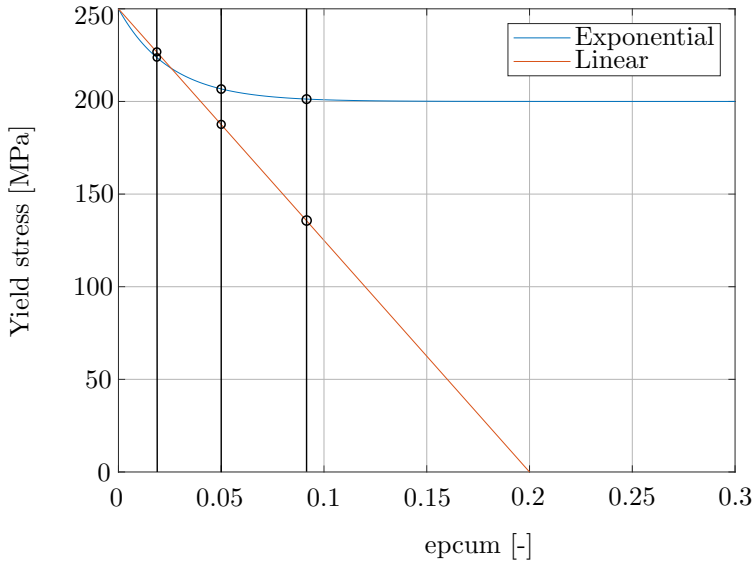

Figure 8.11: Yield function used to verify the broadening of the shear band. The specific curve has been obtained by using the following parameters: $\phi_\infty = 200$MPa, $R_0 = 250$MPa, $b = 40$.

of the plastic fields between the exponential and linear plastic behavior are reported. Three different stages are reported, each corresponding to different percentages of the load application (33%, 66% and 100% of the displacement u_0), and the same stages (in terms of maximum reached cumulative plastic strain) are reported in Figure 8.11 by mean of intersections with the yield curves. In the first stage, the plastic strain distributions are almost identical, because the maximum plastic strain experienced (≈ 0.02) still lies within the zone in which the linearization of the exponential curve is a good approximation (by looking at Figure 8.11). The second reported stage of development of the plastic field already presents major differences between each other, due to the saturation effect introduced in the exponential curve: the developed plastic strain is, in fact, beyond the point at which the two curves diverge from each other, that is, ≈ 0.05 (see Figure 8.11). The third reported stage is characterized by an even more pronounced difference. The gray area in Figure 8.10 represents the thickness of the shear band as predicted by the analytical solution trough Equation 8.8. From the Figure, it can be appreciated that the shear band thickness remains bounded in case of purely linear softening behavior, but this is not the case for the softening-saturating plastic behavior. In the latter case, in fact, the shear band thickness increases as soon as the yield stress saturates.
This small example highlights the necessity for an additional element which should enforce material softening during simulation, such as to retrieve the harmonicity of the plastic field solutions producing a constant shear band thickness. The proposed solution is the adoption of another source of softening which would ensure such behavior even during the stages in which the stress-strain curve saturates, that is, a thermal softening.

λ [MPa]	μ [MPa]	μ_c [MPa]	β [MPa·mm^2]	ρ [kg/mm^3]	m[-]
115348.0	76923.0	100000.0	77.0	4.57 e^{-6}	1.5

ϕ_0[Mpa]	ϕ_∞[Mpa]	b[-]	C_ϵ [J/Kg/°C]	T_m [°C]
250.0	200.0	200.0	5.25e^5	1100

a_1 [-]	a_2 [-]	b_1 [-]	b_2 [-]	b_3 [-]
1.0	1.0	0.0	0.0	0.0

Table 8.6: Thermo-elasto-plastic material properties used for the localization test.

8.3.2 Viscous and thermal effects on shear band broadening

The previous section analyzed the localization process in a simple yet essential test, using a rate-independent elasto-plastic material model. The objective of this section is to push further the localization test with the final goal of approaching, step-by-step, the conditions which characterize the machining process. The first element which must be added is the viscous component of the material model. It is fundamental to understand what are the consequences of adopting a viscous material model for the thickness of the shear band. Subsequently, the thermal contribution is introduced in the analysis, following the theory presented in Section 6.7, and then the effect of the thermal softening, on top of the viscous one, is investigated by looking at the thickness of the shear band.
As a first step, the elasto-visco-plastic model is used while fetching the behavior with viscous parameter that allow to retrieve rate-independent elasto-plasticity, that are $K = 3$ MPa and $n = 18$ (these parameters are used to define the plastic multiplier in Equation (6.102)). The reason to do so is to make sure that visco-plasticity can be reduced to rate-independent plasticity in case the proper material parameters are chosen regardless of the chosen strain-rate. The exponential plastic law is used in this test, such that localization occurs but then the shear band thickness should be prone to thickening. The mechanical properties used to run the thermal-elasto-plastic simulations are summarized in Table 8.6. In Figure 8.12a the plastic strain distribution is depicted for different applied strain-rates, and, as it can be appreciated, the viscous effect is removed thanks to the choice of the K and n parameters. The thermal contribution of the theory was tested for this special choice of viscous parameters. With the given viscous material properties there exists no viscous stress, however, the thermal contribution is time-dependent, due to the adiabatic assumption made during the development of the theory. The same test was performed maintaining the viscous parameters $K = 3$ MPa and $n = 18$, an initial temperature of 25° C was assigned to the specimen, and the other material properties used to evaluate the increment of temperature can be found in Table 8.6. In Figure 8.12b the distribution of the plastic strain can be observed for different applied strain rates. Although the meaning of such results is not physically reliable (because the adiabatic assumption does not hold for long periods of time), these curves suggest an interesting

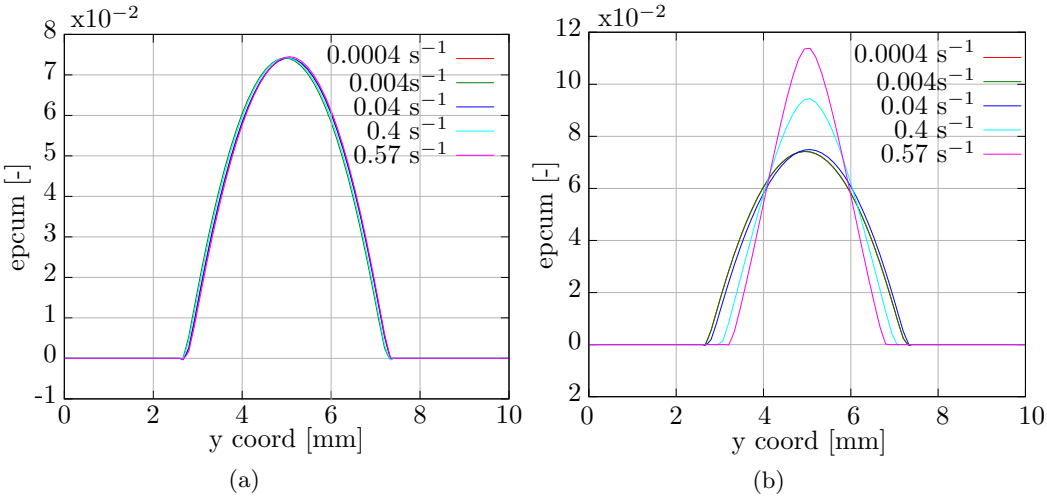

Figure 8.12: Distribution of the plastic strain for different applied strain-rates. The choice of the viscous parameters allows to retrieve rate-independent plastic behavior.

effect of the thermal contribution of the theory: by observing the variation of the plastic strain distribution, in fact, it is possible to infer that including a thermal softening in the theory allows to counterbalance the spreading of the shear band due to saturation of the stress-strain curve. This result must be confirmed also while using more realistic values for the viscous behavior, but it is here shown nonetheless that the thermal softening is a fundamental ingredient for the simulation of high strain-rate plastically-driven processes. As third step, the same localization tests were performed by fetching the material model with more realistic viscosity parameters so as to investigate the effect of viscosity on the localization phenomenon. The viscous material parameters used are $K = 300$ MPa and $n = 7$, and no thermal effect at this stage. Once again the load was applied in different time step in order to emphasize the viscous effect. In Figure 8.13a the cumulative plastic strain fields are reported. As it can be observed there exist a strong viscous effect since the average plastic strain outside the expected shear band is not negligible, so it can be observed that the viscous effect limits localization, as expected. However, the thickness of the shear band seems to be influenced by the viscous effect: the observable amplitudes of the plastic strain distribution in fact decreases by applying the load in shorter interval of time. Figure 8.13a shows the fields for an adjusted range of the y-axis, the localized plastic strain in the middle of the specimen would otherwise be not noticeable if the y-axis spanned from 0 to the maximum reached valued. This to say that, despite the tiny localization in the middle, the viscous effect overcompensates the localization phenomenon. Adding the thermal effect to the analysis does not noticeable improve the situation. In fact, as it can be appreciated in Figure 8.13b, the localization process is boosted by the introduction of thermal softening, but only in case of the highest applied strain-rate. The curves with or without thermal effect are similar up to the case in which the load was applied during 0.001 seconds. The fact that the thermal effect starts only with relatively large values of strain rates is the expected behavior. The point at which the thermal softening starts to play in favor of the localization can be adjusted by selecting a proper

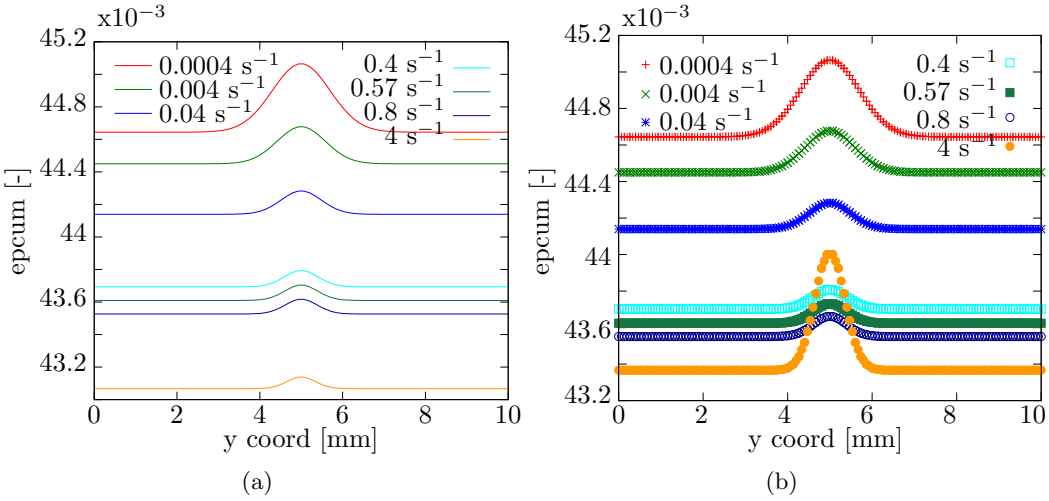

Figure 8.13: Distribution of the plastic strain for different applied strain-rates. The choice of the viscous parameters allows to retrieve rate-independent plastic behavior.

value of the exponent m. The choice of m influences the dependence of the yield stress on temperature, thus increasing or decreasing the softening effect.
Finally, these tests indicated that the viscous and thermal features of the Cosserat theory play respectively against and in favor of the localization process. Therefore, during the calibration phase of the viscous and thermo mechanical parameters, the trade-off between these two phenomena must be pursued.

8.4 Hat-shaped specimen

The hat-shaped specimen has been used many times to test newly developed material models because it is a relatively easy experiment to conduct [J. C. Li et al. 2010; Russo, Forest, et al. 2020; Peirs, Verleysen, and Degrieck 2008; Peirs, Verleysen, Degrieck, and Coghe 2010; El-Magd et al. 2006; Hor et al. 2013; Kuhn et al. 2000]. In the context of this PhD thesis, such model has been used to attempt to simulate the localization phenomenon (which is one of the main feature of this test) in a controlled manner, which takes place under conditions which resemble the ones characterizing machining operations. In Figure 8.14 the geometry and the boundary conditions of the test are reported, whereas in Figure 8.15a it is possible to appreciate the distribution of the plastic strain and the shear band formation. The field pictured in Figure 8.15a has been obtained by fetching the material model with the properties listed in Table 8.7, that is, by characterizing the material with a linear softening behavior. This test has also been conducted using an exponential softening-plateauing yield stress function, in order to study the effect of the saturation of the yield stress on the geometry induced localization. The properties used for this material model can be found in Table 8.8. In Figure 8.15b the comparison in terms of cumulative plastic strain is reported between the linear softening behavior and the exponential softening-plateauing behavior. The plastic strain fields have been probed along a central horizontal line at the center of the shear band. As it can be observed, the

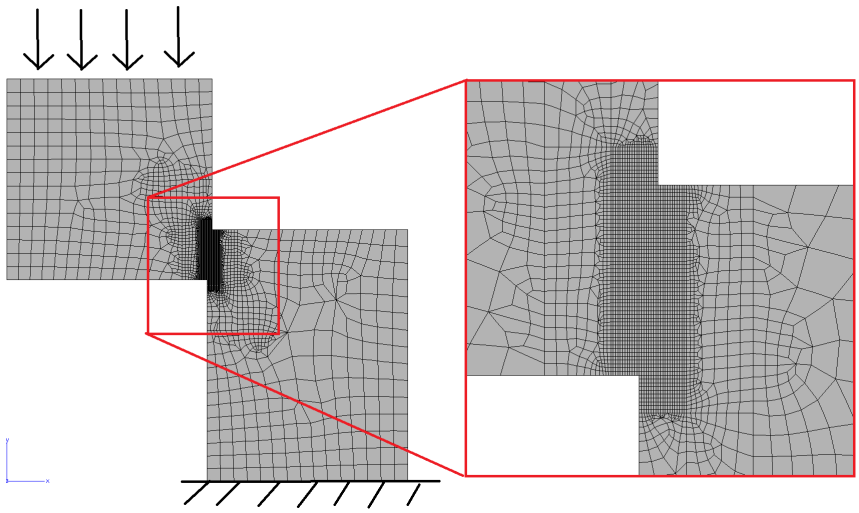

Figure 8.14: Meshed geometry and boundary conditions of the hat-shaped specimen test.

λ [MPa]	μ	μ_c [MPa]	β [MPa·mm^2]	ϕ_0 [MPa]
115348.0	76923.0	100000.0	0.77	250.0
H [MPa]	Q_1 [MPa]	g_1 [-]	Q_2 [MPa]	g_2 [-]
-1250.0	0.0	0.0	0.0	0.
a_1 [-]	a_2 [-]	b_1 [-]	b_2 [-]	b_3 [-]
1.0	0.0	0.0	0.0	0.0

Table 8.7: Elasto-plastic material properties used for the hat-shaped specimen test using linear softening behavior.

λ [MPa]	μ	μ_c [MPa]	β [MPa·mm^2]
115348.0	76923.0	100000.0	0.77
ϕ_0[Mpa]	ϕ_∞[Mpa]	b[-]	a_1 [-]
250.0	200.0	40.0	1.0
a_2 [-]	b_1 [-]	b_2 [-]	b_3 [-]
0.0	0.0	0.0	0.0

Table 8.8: Elasto-plastic material properties used for the hat-shaped specimen test using exponential softening behavior.

saturation of the yield stress still induces a broadening of the shear band, even in case the localization was enforced also by geometry. As previously established in [Russo, Forest, et al. 2020], the only characteristic length that plays a major role in the localization phenomenon is the one that compares shear stress and couple stress moduli:

$$l^e_{ch} = \sqrt{\frac{\mu}{\beta}}. \tag{8.10}$$

Assuming to fetch the material model with properties that belong to a specific known metal, the only additional material parameter which requires further calibration is the couple stress modulus β.
If the shear band thickness was

8.5 Manufacturing simulations

The final test of the developed theory would be to simulate machining operations by using a thermodynamically-compatible elasto-visco-plastic Cosserat theory under a large deformation assumption. The objective would be to calibrate the higher order modulus against experimental data, which could be, for example, displacement or strain fields. Ideally, since the thermal part of the theory should also be properly calibrated, it would be ideal to compare the numerically-predicted thermal fields against the ones experimentally produce. The thermal fields, however, are not as easily obtainable as the strain fields, due to the technical requirements of the cameras which must be used to capture the process. It was possible, within the ENABLE project, to capture the displacement distribution for a specific orthogonal cutting process performed at the University of Bordeaux, and it was also possible to post-process the data through digital image correlation to obtain the strain fields. All the details of the experimental set-up and of the field measurements can be found in Zouabi et al. [Zouabi et al. 2021]. This last part of the present PhD thesis, in fact, focuses on using the strain fields measured during the orthogonal cutting process as input for at least an estimation of the higher order modulus to be

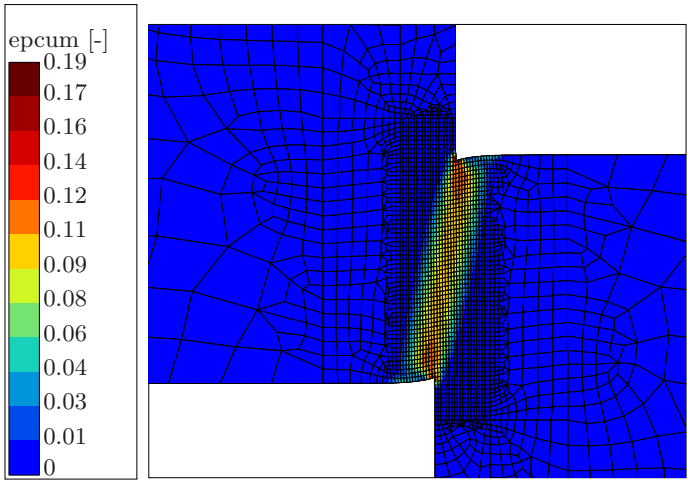

(a)

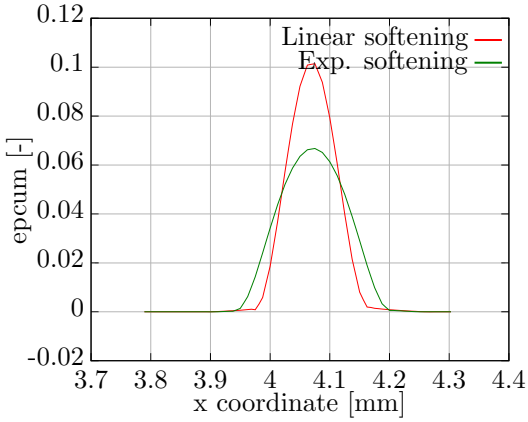

(b)

Figure 8.15: Distribution of plastic strain in the hat-shaped specimen during shear band formation (a) and comparison between the cumulative plastic strain fields in case of linear softening behavior and exponential softening-plateauing behavior (b).

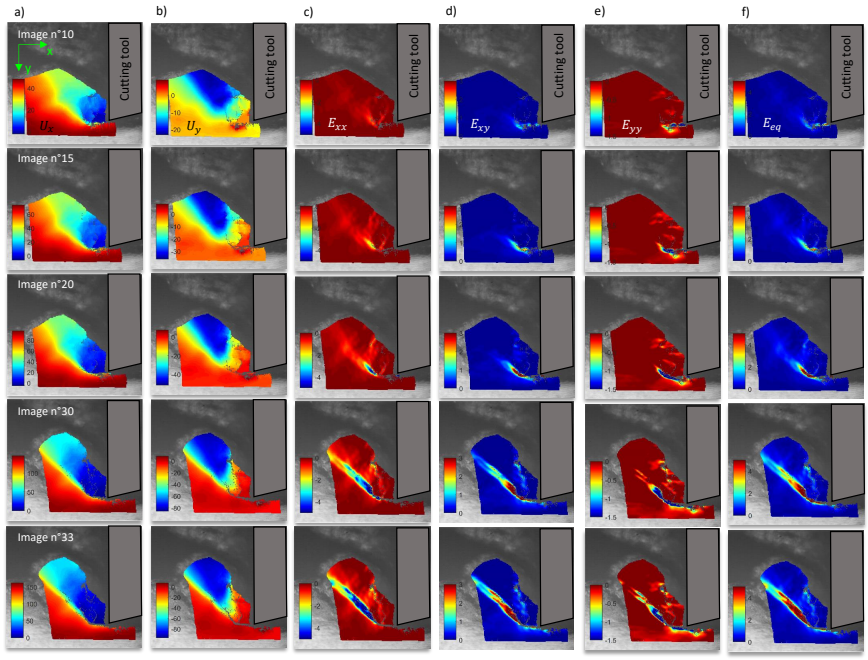

Figure : displacement along a) x-axis ; and b) y-axis (in µm) ; Euler-Almansi strain field :c) E_{xx} ; d) E_{xy} and e) E_{yy} ; and f) equivalent strain field.

Figure 8.16: Displacement fields obtained during orthogonal cutting by mean of digital image correlation. Every raw indicates a different time at which the image was taken and processed [Zouabi et al. 2021].

used. A proper calibration of the modulus would require a more extensive experimental and numerical investigation, but it is here shown that at least such procedure is a viable option for enhancing the models used for complex machining simulations. Figure 8.16 shows, in a progressive series of frames, the development of the measured fields during the machining operations. The last column contains the Euler-Almansi estimated strain measure. In order to avoid the complexity deriving from the adoption of a remeshing algorithm for the Cosserat LD model, the morphology of the metal as depicted in the first frame of Figure 8.16 has been chosen as initial geometry for the numerical model, and the meshed part can be observed in Figure 8.17. The simulation of the machining process was also performed by using an initial simple rectangular metal initial geometry, in which the tool was cutting the chip from the metal to create the typical geometries produced in machining simulations [Calamaz et al. 2008]. However, whereas the small deformation framework does not include any check on the Jacobian of the deformation (which is used as indicator for excessive distortion of the media and subsequent stop of the simulation), the large deformation implementation uses this value to perform the numerical integration in the deformed element, therefore excessively distorted elements cannot be processed by the numerical routine. Because of this reason, the simulations using a rectangular initial geometry led to numerical error when elements reached excessive distortion. In order to avoid such problem, investigations on a remeshing algorithm in the

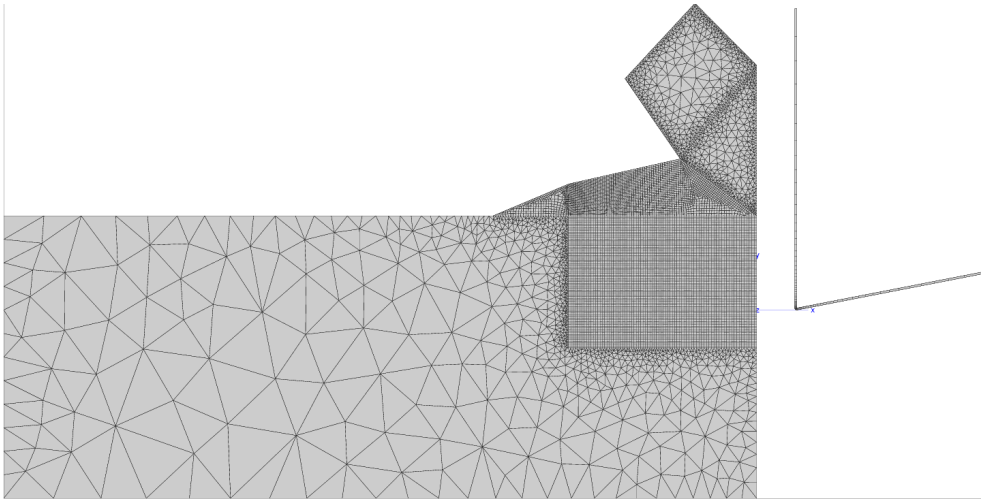

Figure 8.17: Meshed geometry used for the orthogonal cutting test.

Z-Set code were pursued, but due to lack of time and due to the complexity of the subject, no good results were achieved in this regard. This is the reason why it was chosen to use the geometry depicted in Figure 8.17 as the initial one. In terms of boundary conditions, displacements and micro-rotations were fixed at the bottom edge of the machined part, whereas a constant horizontal displacement was applied to the advancing tool, and its vertical movement was constrained. The advancing velocity (also known as feed rate in machining community) was 1 mm/s. The entire tool was modeled as a rigid body. The original test was performed on the Ti-6Al-4V titanium alloy, so the mechanical properties belonging to this specific metal were implemented in the numerical model. The mechanical properties to simulate the elasto-plastic behavior were taken by the investigation carried out by Babu for his PhD at the University of Lulea [Babu 2018] (also obtainable through the journal papers [Babu and Lindgren 2013; Babu, Lundbäck, et al. 2019]); the viscous properties of the Ti-6Al-4V were estimated from the investigations of de Sotto et al [de Sotto et al. 2020]; finally, the required thermal properties of the Ti-6Al-4V were already known [*ASM Handbook Volume 02: Properties and Selection: Nonferrous Alloys and Special-Purpose Materials.* 1990]. All the thermo-mechanical properties are listed in Table 8.9, and they must be considered to be valid at the initial temperature of 25 ° C. Besides the explicit dependence of the yield stress on temperature, also the Young's modulus, the Poisson ratio and the specific heat coefficient are temperature-dependent; the reader is referred to the work of Babu to know more about the exact values of these coefficients as the temperature varies [Babu 2018]. The contact between the tool (on the most right in Figure 8.17) and the machined part has been modeled through a simple Coulomb law, in which no special treatment was given to the additional degrees of freedom. A friction coefficient of 0.1 was assigned to the contact. The entire part was assumed to have an initial temperature of 25° Celsius. In Figure 8.18 the distributions of cumulative plastic strain and temperature are reported for different stages of the simulation. As it can be seen from Figure 8.18, the temperature in the shear band rapidly reaches the melting value, therefore lowering down the yield stress to 0 in the localization

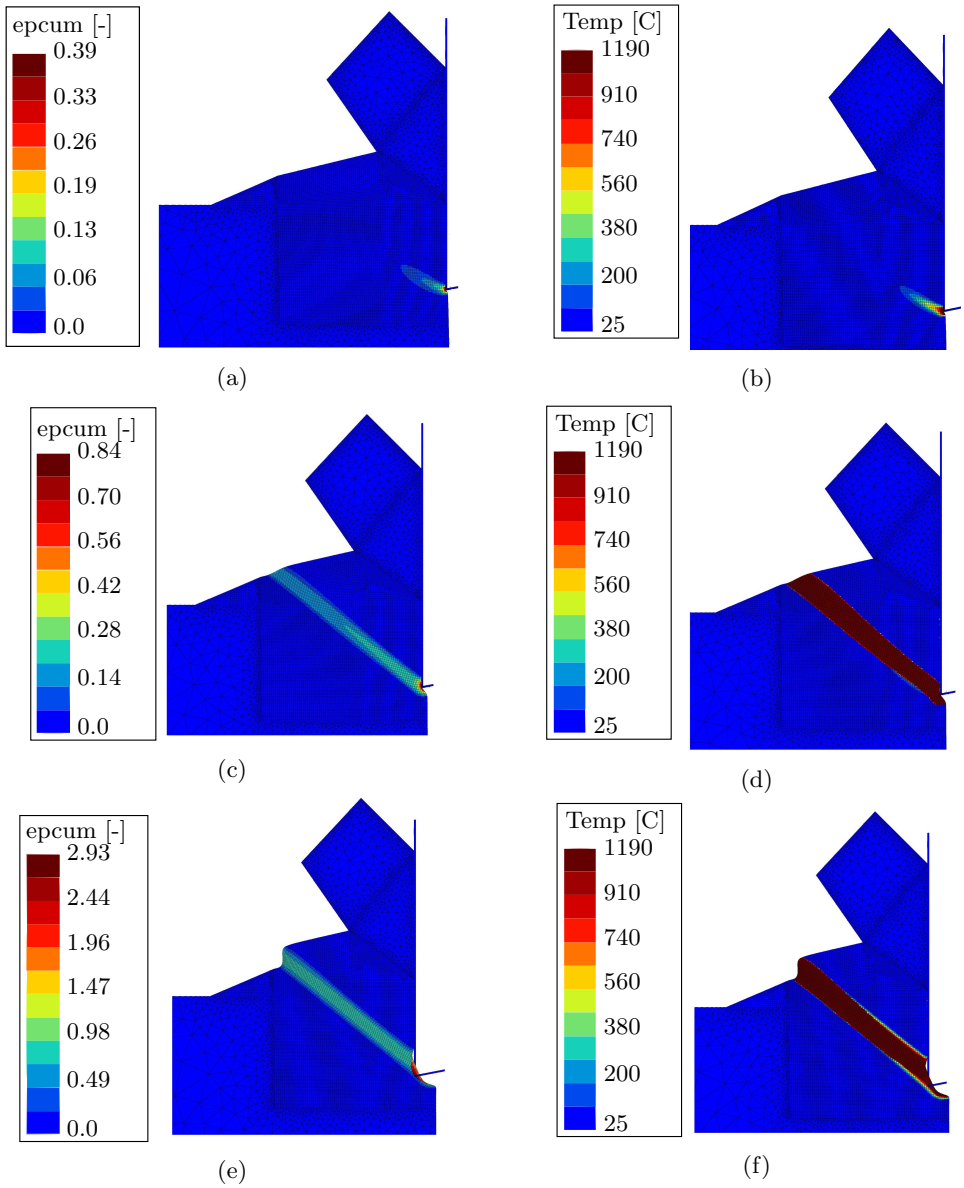

Figure 8.18: Cumulative plastic strain (on the left) and temperature fields (on the right) simulated during the orthogonal cutting simulation. The fields have been captured at three different time step.

λ [MPa]	μ	μ_c [MPa]	β [MPa·mm^2]	ρ [kg/mm^3]	m[-]
86291.0	39865.0	100000.0	1.0e^{-4}	4.5 e^{-6}	1.0
ϕ_0[Mpa]	ϕ_∞[Mpa]	b[-]	C_ϵ [J/Kg/°C]	T_m [°C]	K [MPa]
970.0	1400.0	200.0	5.25e^5	1100	155.0
a_1 [-]	a_2 [-]	b_1 [-]	b_2 [-]	b_3 [-]	n [-]
1.0	1.0	0.0	0.0	0.0	7.0

Table 8.9: Thermo-elasto-visco-plastic material properties used for the orthogonal cutting simulation.

zone. Once the temperature reaches its maximum value, the Lamé parameters (Young's modulus and Poisson ratio) vanish, meaning that the the deformations in the shear band become stress-free. Contrary to what was observed in the previous Section (8.13), the viscous-thermal properties used in this test induce the softening to overcompensate the viscous effect, and for this reason the temperature in the shear band rapidly rise up to the melting point. This suggests that the material model should be properly adjusted such as to find a more suitable trade-off between the thermal and viscous effects.
In order to capture the size effect (strain gradient effect) during cutting simulations, different values of characteristic length were used, and the results are reported in Figure 8.19. The mechanical properties still are the ones reported in Table 8.9, but different values of the couple stress modulus were used. From the plastic fields distributions depicted in the Figure it is possible to conclude that the strain gradient effect was properly simulated numerically. Once again, the actual value of the higher order modulus must be adequately calibrated by comparing the thickness of the simulated shear band with the one experimentally measured. In Figure 8.19 the cumulative plastic strain fields are reported for different higher order moduli, at the smaller one reported is equal to 10^{-3} MPa·mm^2. Simulations have been run for smaller values of β, but no difference was noticed, and it is here recalled that for smaller values of β a smaller characteristic length is used, meaning that, ultimately, the classical continuum mechanics is retrieved. This suggests that, for the specific case here simulated, the strain-rate hardening (viscous part of the process) is overcompensating the thermal softening even in the classical continuum mechanics case. The thickness of the adiabatic shear band predicted by the Cosserat theory can only be increased (with respect to the classical mechanics result) by using larger values of the higher order modulus, but it cannot reduce it further.
The shear band thickness evaluated in Equation (8.7) was derived under specific conditions, and a negative hardening module was the main one. For this reason it would be difficult to relate the conditions in the cutting test with the ones used in the simple glide test. However, it is still possible to evaluate the thickness of the shear band produced in the experiments and to compare it to the one numerically predicted. From the analysis of the equivalent strain in Figure 8.16, it is possible to estimate the thickness of the shear

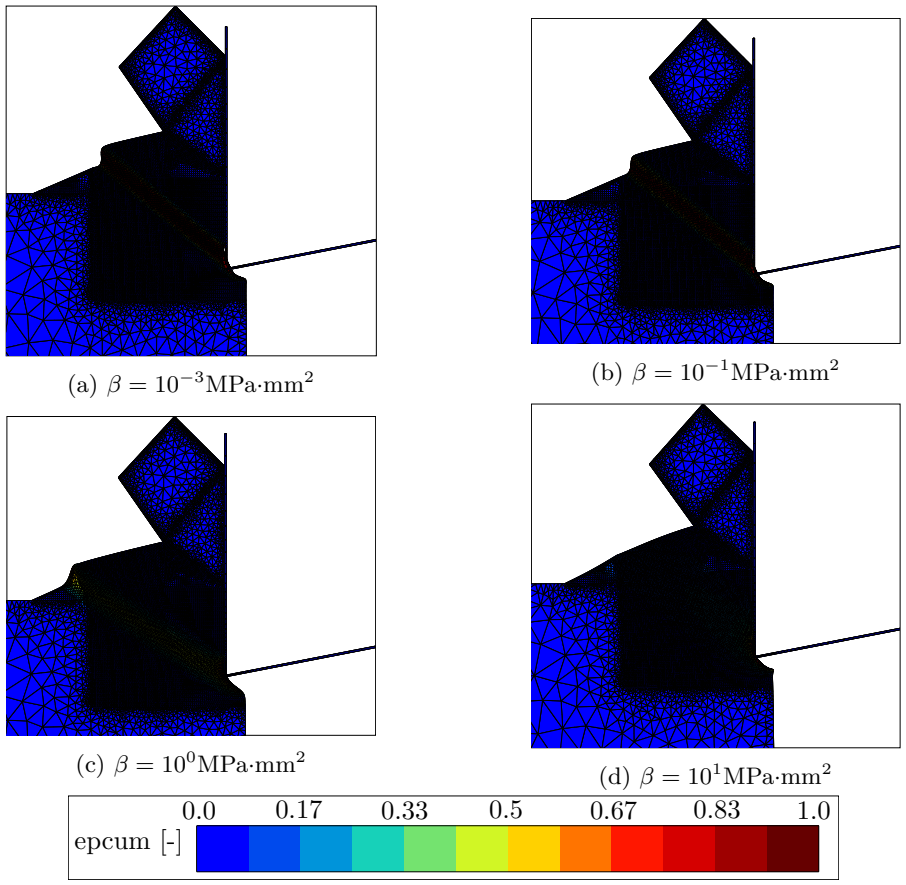

Figure 8.19: Shear band thickness prediction while using different values of the couple stress modulus β.

band to be 0.032 mm. The numerical simulation of the same process using an higher order modulus of 10^{-3}MPa·mm^2 (and lower) induces the formation of a shear band of 0.043mm. Despite the fact that the experimental and numerical thickness values are close, this result does not indicate that a numerical twin of the experimental test was created, but rather this only suggests that it is possible to use the thermodynamically-compatible Cosserat model to simulate machining processes. There is still room for improvements, which will be discussed in the next Chapter.

Chapter 9

Conclusion and future developments

This PhD thesis investigated over the application of the Cosserat media as a substitute to the strain gradient theory to capture size effects and gradient effects during simulations of thermomechanical processes. The features required to simulate these processes have been defined in Chapter 1, and the concept of generalized continuum mechanics was introduces. The context of the present PhD thesis is also given, identifying it as part of a bigger project called ENABLE. A deeper analysis of the topics of generalized continuum mechanics is proposed in Chapter 2, in which a broad literature review on these theories and on their application to manufacturing simulations is presented. Every theory is individually addressed in terms of additional elements that are used to enhance the classical continuum mechanics. One of the many frameworks presented in this Chapter is further analyzed in the next Chapter, that is Chapter 3. The scalar micromorphic plastic strain gradient theory is in fact not only dissected, but also implemented in the software PamCrash in collaboration with researchers from within the ESI company and ESR 4 Vikram Phalke. The team of 4 collaborated in exploiting a thermal-micromorphic analogy to easily implement the numerical framework in the software and in simulating size-effects and mesh-independence with the scalar micromorphic framework. The collaboration led to a recently published journal paper. The present PhD manuscript continued with investigating the extents of the additional features brought by the Cosserat theory in terms of size-effects, mesh independence and characteristic lengths. In Chapter 4 a general thermodynamically-consistent Cosserat theory under small deformations was provided, and applications of a specific model (TANH [Calamaz et al. 2008]) were presented in case of a localization problems induced by the geometry of the specimen. The hat-shaped specimen was used to investigate the effect of the elastic and plastic characteristic lengths on the shear band formed in the specimen, and the main conclusion of the Chapter was that the elastic characteristic length was enough to regularize the shear band. Chapter 5 is used to present many analytical solutions to problems that are extremely relevant to the localization that occurs during machining operations. The analytical solutions were derived under the assumption of small deformations in the Cosserat media. The profiles of the cumulative plastic strain during localization tests were the main outcome of this Chapter, because, besides proving the analytical solution of the

thickness of the shear band, they will be used to verify the numerical implementation of the Cosserat theory under large deformations. The thermodynamically-compatible elasto-visco-plastic Cosserat theory under large deformation in presented in Chapter 6, and its numerical implementation in the software Z-SET is provided in Chapter 7, alongside the discretization process of the weak form of the equilibrium equations. The handling of the rotations requires proper care because of their strong nonlinear nature, so its parameterization, parameters-treatment and parameters updating is explicitly addressed. Finally, the Chapter 8 includes the validation tests of the implemented theory on a single element and on more complex tests, such as the localization one whose analytical solution was derived in Chapter 5. The last part of the last Chapter focuses on predicting the correct thickness of the shear band in an orthogonal cutting test. The experimental test was conducted in the University of Bordeaux [Zouabi et al. 2021], and the aim was to calibrate the additional material parameter based on the comparison of the thickness of the shear band between numerical and experimental solution.
Overall this PhD thesis highlighted the necessity of the adoption of a theory that incorporates the following aspects for manufacturing operation simulations:

- gradient-based additional deformation measure to capture size effects;
- strong thermodynamic description to cope with the extreme temperatures that rise during machining;
- information from the micro-structure to create a mechanism-based material behavior,

and the answer to these requirements was found in the thermodynamically-compatible elasto-visco-plastic Cosserat theory under large deformations. It was proved that this framework can capture size effect, and that it can regularize localization occurring in machining. Finally, it was demonstrated that this theory can be used to simulate adiabatic shear band formation in machining.
However, the present investigation cannot be considered as complete. In fact, the adoption of remeshing algorithm is not only strongly advised, but it is required to complete the simulations up to the point in which it is possible to observe the chip formation. This is definitely the next step of investigation, and it is also the direction in which there is more room for improvement. As mentioned earlier, the amount of time and effort required to carry on the investigations aiming at achieving a working remeshing algorithm was not compatible with the remaining time left for this PhD and the objective became to work further on the complex handling on the nonlinearities of the rotations. Still the remeshing algorithm is a fundamental feature for simulating machining and it must be included in the future. A large deformation framework is necessary but it does not solve the problem.
Another major point for the completeness of the theory would be the flawless implementation of the three-dimensional framework, which has not been completed because the focus was the bi-dimensional one. The complete framework was presented already in Chapter 6, its numerical implementation was discussed in Chapter 7, but the actual numerical implementation requires refinement, especially the routines performing the updates of the rotation/wryness and the ones evaluating the tangent plane in the parametric space of the same quantities.
Another point which can be further improved is the material behavior in the plastic regime. The present model makes use of the cumulative plastic strain as internal state

variable to track the inelastic state of the continuum. However, a more appropriate choice of state variable would be the dislocation density. This quantity expresses a scalar equivalent value of the tensorial measures of the distortion of the metal lattice through evaluation of the geometrically necessary dislocations. The application of a similar model in the Cosserat media was proposed by Bîrsan and Neff et al. [Bîrsan et al. 2016]. Furthermore, the plastic model behavior can also be improved by attempting the implementation of a mechanism-based framework in the Cosserat media [Babu and Lindgren 2013]. Lastly, also the contact algorithm can be further improved. Right now a simple Coulomb friction law is considered, in which only the displacement degrees of freedom play a role. However, more complex contact models can be considered, in which also the grain rotation is involved[Lewandowski-Szewczyk et al. 2020; H. W. Zhang et al. 2005; S. Zhang et al. 2013]. For instance, it is possible to enforce a contact boundary condition at the contact surface such that micro-rotations are allowed or not to be modified, similarly to what is done using a Coulomb model.

Bibliography

A., Seupel, Hütter G., and Kuna M. (2018). "An efficient FE-implementation of implicit gradient-enhanced damage models to simulate ductile failure". In: *Engineering Fracture Mechanics* 199, pp. 41–60.

Acharya, A. and J. L. Bassani (1996). "On Non-Local Flow Theories that Preserve the Classical Structure of Incremental Boundary Value Problems". In: *IUTAM Symposium on Micromechanics of Plasticity and Damage of Multiphase Materials*. Springer, pp. 3–9.

Ackroyd, B., S. Chandrasekar, and W. D. Compton (2003). "A Model for the Contact Conditions at the Chip-Tool Interface in Machining". In: *Journal of Tribology* 125.3, p. 649.

Aifantis, E. C. (1984). "On the Microstructural Origin of Certain Inelastic Models". In: *Journal of Engineering Materials and Technology* 106.4, p. 326.

Aifantis, E. C. (1987). "The physics of plastic deformation". In: *International Journal of Plasticity* 3.3, pp. 211–247.

Aifantis, E. C. (1999). "Strain gradient interpretation of size effects". In: *International Journal of Fracture* 95.1996, pp. 299–314.

Aldakheel, F. and C. Miehe (2017). "Coupled thermomechanical response of gradient plasticity". In: *International Journal of Plasticity* 91, pp. 1–24.

Anand, L., O. Aslan, and S. A. Chester (2012). "A large-deformation gradient theory for elastic-plastic materials: Strain softening and regularization of shear bands". In: *International Journal of Plasticity* 30-31, pp. 116–143.

Asad, M. (2010). "Elaboration of concepts and methodologies to study peripheral down-cut milling process from macro-to-micro scales". PhD thesis. Institut national des sciences appliquees de Lyon.

Asad, M., T. Mabrouki, and J. F. Rigal (2010). "Finite-element-based hybrid dynamic cutting model for aluminium alloy milling". In: *Proceedings of the Institution of Mechanical Engineers, Part B: Journal of Engineering Manufacture* 224.1, pp. 1–13.

Ashby, M. F. (1970). "The deformation of plastically non-homogeneous materials". In: *Philosophical Magazine* 21.170, pp. 399–424.

Ask, A. et al. (2019). “A Cosserat–phase-field theory of crystal plasticity and grain boundary migration at finite deformation”. In: *Continuum Mechanics and Thermodynamics* 31, pp. 1109–1141.

Askes, H. and E. C. Aifantis (June 2011). “Gradient elasticity in statics and dynamics: An overview of formulations, length scale identification procedures, finite element implementations and new results”. In: *International Journal of Solids and Structures* 48.13, pp. 1962–1990.

ASM Handbook Volume 02: Properties and Selection: Nonferrous Alloys and Special-Purpose Materials. (1990). Vol. 2. ASM International.

Astakov, Viktor (2006). “Tribology of the Tool-Chip and Tool-Workpiece Interfaces”. In: *Tribology and Interface Engineering Series*. Ed. by Viktor Astakov. Elsevier B.V. Chap. 3, pp. 124–219.

Babu, B. (2018). “Mechanism-Based Flow Stress Model for Ti-6Al-4V applicable for simulation of additive manufacturing and machining”. PhD thesis. Luleå University of Technology.

Babu, B. and L. E. Lindgren (2013). “Dislocation density based model for plastic deformation and globularization of Ti-6Al-4V”. In: *International Journal of Plasticity* 50, pp. 94–108.

Babu, B., A. Lundbäck, and L. E. Lindgren (2019). “Simulation of Ti-6Al-4V Additive Manufacturing Using Coupled Physically Based Flow Stress and Metallurgical Model”. In: *Materials* 12.23, p. 3844.

Bahi, S. et al. (2011). “A new friction law for sticking and sliding contacts in machining”. In: *Tribology International* 44.7-8, pp. 764–771.

Bahi, S. et al. (2012). “Hybrid modelling of sliding-sticking zones at the tool-chip interface under dry machining and tool wear analysis”. In: *Wear* 286-287, pp. 45–54.

Bassani, J. L. (2001). “Incompatibility and a simple gradient theory of plasticity”. In: *Journal of the Mechanics and Physics of Solids* 49.9, pp. 1983–1996.

Bauchau, O. A. (2011). *Flexible Multibody Dynamics*. Vol. 176. Dordrecht: Springer.

Bauer, S., W. G. Dettmer, et al. (2012). “Micropolar hyper-elastoplasticity: constitutive model, consistent linearization, and simulation of 3D scale effects”. In: *International Journal for Numerical Methods in Engineering* 91.1, pp. 39–66.

Bauer, S., M. Schäfer, et al. (2010). “Three-dimensional finite elements for large deformation micropolar elasticity”. In: *Computer Methods in Applied Mechanics and Engineering* 199.41-44, pp. 2643–2654.

Begley, M. R. and J. W. Hutchinson (1998). “The mechanics of size-dependent indentation”. In: *Journal of the Mechanics and Physics of Solids* 46.10, pp. 2049–2068.

Benallal, A. et al. (2010). “Uniqueness, loss of ellipticity and localization for the time-discretized, rate-dependent boundary value problem with softening”. In: *International Journal for Numerical Methods in Engineering* 84.7, pp. 864–882.

Bîrsan, M. and P. Neff (2016). "On the dislocation density tensor in the Cosserat theory of elastic shells". In: *Advanced Methods of Continuum Mechanics for Materials and Structures*, pp. 391–413.

Brepols, T., S. Wulfinghoff, and S. Reese (2017). "Gradient-extended two-surface damage-plasticity: Micromorphic formulation and numerical aspects". In: *International Journal of Plasticity* 97, pp. 64–106.

Burns, T. J. and M. A. Davies (2002). "On repeated adiabatic shear band formation during high-speed machining". In: *International Journal of Plasticity* 18.4, pp. 487–506.

Cahuc, O., P. Darnis, and R. Laheurte (2007). "Mechanical and Thermal Experiments in Cutting Process for New Behaviour Law". In: *International Journal of Forming Processes* 10.2, pp. 235–269.

Calamaz, M., D. Coupard, and F. Girot (2008). "A new material model for 2D numerical simulation of serrated chip formation when machining titanium alloy Ti-6Al-4V". In: *International Journal of Machine Tools and Manufacture* 48.3-4, pp. 275–288.

Chaboche, J. L. (2008). "A review of some plasticity and viscoplasticity constitutive theories". In: *International Journal of Plasticity* 24.24, pp. 1642–1693.

Chaboche, J.L. (1989). "Constitutive equations for cyclic plasticity and cyclic viscoplasticity". In: *International Journal of Plasticity* 5.3, pp. 247–302.

Chambon, R., D. Caillerie, and N. El Hassan (1998). "One-dimensional localisation studied with a second grade model". In: *European Journal of Mechanics, A/Solids* 17.4, pp. 637–656.

Chen, G. et al. (Oct. 2011). "Finite element simulation of high-speed machining of titanium alloy (Ti–6Al–4V) based on ductile failure model". In: *The International Journal of Advanced Manufacturing Technology* 56.9, pp. 1027–1038.

Cheng, C. and R. Mahnken (2015). "A multi-mechanism model for cutting simulations based on the concept of generalized stresses". In: *Computational Materials Science*. Vol. 100, pp. 144–158.

Childs, T. H. C. (2006). "Friction modelling in metal cutting". In: *Wear* 260.3, pp. 310–318.

Chinesta, F., P. Ladeveze, and E. Cueto (2011). "A Short Review on Model Order Reduction Based on Proper Generalized Decomposition". In: *Archives of Computational Methods in Engineering* 18.4, pp. 395–404.

Cordero, N. M. et al. (2010). "Size effects in generalised continuum crystal plasticity for two-phase laminates". In: *Journal of the Mechanics and Physics of Solids* 58.11, pp. 1963–1994.

Cosserat, E. and F. Cosserat (1909). *Theorie des corps deformables*. A. Hermann et fils.

Dahlberg, C. F. O. and M. Boåsen (Jan. 2019). "Evolution of the length scale in strain gradient plasticity". In: *International Journal of Plasticity* 112.February, pp. 220–241.

Dahlberg, C. F. O. and J. Faleskog (2013). "An improved strain gradient plasticity formulation with energetic interfaces: Theory and a fully implicit finite element formulation". In: *Computational Mechanics* 51.5, pp. 641–659.

Davaze, V. et al. (2021). "A non-local damage approach compatible with dynamic explicit simulations and parallel computing". In: *International Journal of Solids and Structures* 228, p. 110999.

de Borst, R. (1991a). "Simulation of strain localization: a reappraisal of the cosserat continuum". In: *Engineering Computations* 8.4, pp. 317–332.

de Borst, R. (1991b). "Simulation of strain localization: a reappraisal of the cosserat continuum". In: *Engineering Computations* 8.4, pp. 317–332.

de Borst, R. (1993). "A generalisation of J2-flow theory for polar continua". In: *Computer Methods in Applied Mechanics and Engineering* 103.3, pp. 347–362.

de Borst, R. and H. Mühlhaus (1992). "Gradient-dependent plasticity: Formulation and algorithmic aspects". In: *International Journal for Numerical Methods in Engineering* 35.3, pp. 521–539.

de Borst, R. and L. J. Sluys (1991). "Localisation in a Cosserat continuum under static and dynamic loading conditions". In: *Computer Methods in Applied Mechanics and Engineering* 90.1-3, pp. 805–827.

de Sotto, R. M. et al. (2020). "A constitutive model for a rate and temperature-dependent, plastically anisotropic titanium alloy". In: *International Journal of Plasticity* 134, p. 102777.

Demir, E. (2009). "A Taylor-based plasticity model for orthogonal machining of single-crystal FCC materials including frictional effects". In: *The International Journal of Advanced Manufacturing Technology*. Vol. 40. 9, pp. 847–856.

Demiral, M., A. Roy, and V. V. Silberschmidt (2016). "Strain-gradient crystal-plasticity modelling of micro-cutting of b.c.c. single crystal". In: *Meccanica* 51.2, pp. 371–381.

Diamantopoulou, E. et al. (2017). "Micromorphic constitutive equations with damage applied to metal forming". In: *International Journal of Damage Mechanics* 26.2, pp. 314–339.

Diaz, A, J. M. Alegre, and I.I. Cuesta (2016). "Coupled hydrogen diffusion simulation using a heat transfer analogy". In: *International Journal of Mechanical Sciences* 115-116, pp. 360–369.

Dillard, T., S. Forest, and P. Ienny (2006). "Micromorphic continuum modelling of the deformation and fracture behaviour of nickel foams". In: *European Journal of Mechanics, A/Solids* 25.3, pp. 526–549.

Dixit, U. S., S. N. Joshi, and J. P. Davim (2011). "Incorporation of material behavior in modeling of metal forming and machining processes: A review". In: *Materials and Design* 32.7, pp. 3655–3670.

Dluzeswki, P. (1991). "Finite deformations of polar media in angular coordinates". In: *Archives of Mechanics* 43.6, pp. 783–793.

Dong, F. et al. (2018). “In-situ measurement of Ti-6Al-4V grain size distribution using laser-ultrasonic technique”. In: *Scripta Materialia* 154, pp. 40–44.

Duan, D. M. et al. (2001). “Length scale effect on mechanical behavior due to strain gradient plasticity”. In: *Materials Science and Engineering A* 303.1-2, pp. 241–249.

Dunne, F. and N. Petrinic (2005). *Introduction to computational plasticity*. Oxford University Press.

Dunstan, D. J. et al. (2009). “Elastic Limit and Strain Hardening of Thin Wires in Torsion”. In: *Physical Review Letters* 103.15, p. 155501.

Ehrler, B. et al. (2008). “Grain size and sample size interact to determine strength in a soft metal”. In: *Philosophical Magazine* 88.25, pp. 3043–3050.

Erdelj, S. G., G. Jelenić, and A. Ibrahimbegović (2020). “Geometrically non-linear 3D finite-element analysis of micropolar continuum”. In: *International Journal of Solids and Structures* 202, pp. 745–764.

Eringen, A. C. (1962). *Nonlinear theory of continuous media*. McGraw-Hill.

Eringen, A. C. (1999a). *Microcontinuum Field Theories: I. Foundations and Solids*. 1st ed. Springer-Verlag New York.

Eringen, A. C. (1999b). “Theory of Micropolar Elasticity”. In: *Microcontinuum Field Theories*. New York, NY: Springer New York, pp. 101–248.

Eringen, A. C. and E. S. Suhubi (1964). “Nonlinear theory of simple micro-elastic solids-I”. In: *International Journal of Engineering Science* 2.2, pp. 189–203.

ESI Group (2000). “PAM-CRASH Theory Notes Manual”. In: *Pam System International*.

Fleck, N. A. and J. W. Hutchinson (1993). “A phenomenological theory for strain gradient effects in plasticity”. In: *Journal of the Mechanics and Physics of Solids* 41.12, pp. 1825–1857.

Fleck, N. A. and J. W. Hutchinson (1997). “Strain Gradient Plasticity”. In: *Advances in Applied Mechanics* 33, pp. 295–361.

Fleck, N. A. and J. W. Hutchinson (2001). “A reformulation of strain gradient plasticity”. In: *Journal of the Mechanics and Physics of Solids* 49.10, pp. 2245–2271.

Fleck, N. A., G. M. Muller, et al. (1994). “Strain gradient plasticity: Theory and experiment”. In: *Acta Metallurgica Et Materialia* 42.2, pp. 475–487.

Fleck, N. A. and J. R. Willis (2009a). “A mathematical basis for strain-gradient plasticity theory—Part I: Scalar plastic multiplier”. In: *Journal of the Mechanics and Physics of Solids* 57.1, pp. 161–177.

Fleck, N. A. and J. R. Willis (2009b). “A mathematical basis for strain-gradient plasticity theory. Part II: Tensorial plastic multiplier”. In: *Journal of the Mechanics and Physics of Solids* 57.7, pp. 1045–1057.

Forest, S. (2009). “Micromorphic Approach for Gradient Elasticity, Viscoplasticity, and Damage”. In: *Journal of Engineering Mechanics* 135.3, pp. 117–131.

Forest, S. (2016). "Nonlinear regularization operators as derived from the micromorphic approach to gradient elasticity, viscoplasticity and damage". In: *Proceedings of the Royal Society A: Mathematical, Physical and Engineering Sciences* 472.2188.

Forest, S., G. Cailletaud, and R. Sievert (1997). "A Cosserat theory for elastoviscoplastic single crystals at finite deformation". In: *Archives of Mechanics* 49.4, pp. 705–736.

Forest, S., J. M. Cardona, and R. Sievert (2000). "Thermoelasticity of second-grade media". In: *Continuum Thermomechanics, The Art and Science of Modellig Material Behaviour, Paul Germain's Anniversary Volume*. Ed. by G. A. Maugin, R. Drouot, and F. Sidoroff, pp. 163–176.

Forest, S. and R. Sievert (2003). "Elastoviscoplastic constitutive frameworks for generalized continua". In: *Acta Mechanica* 160.1, pp. 71–111.

Forest, S. and R. Sievert (2006). "Nonlinear microstrain theories". In: *International Journal of Solids and Structures* 43.24, pp. 7224–7245.

Forest, S., R. Sievert, and E.C. Aifantis (2002). "Strain gradient crystal plasticity: Thermomechanical formulations and applications". In: *Journal of the Mechanical Behavior of Materials* 13, pp. 219–232.

Gallego, G. and A. Yezzi (2015). "A Compact Formula for the Derivative of a 3-D Rotation in Exponential Coordinates". In: *Journal of Mathematical Imaging and Vision* 51.3, pp. 378–384.

Gao, H. and Y. Huang (2001). "Taylor-based nonlocal theory of plasticity". In: *International Journal of Solids and Structures* 38.15, pp. 2615–2637.

Gao, H., Y. Huang, et al. (1999). "Mechanism-based strain gradient plasticity–I. Theory". In: *Journal of the Mechanics and Physics of Solids* 47.6, pp. 1239–1263.

González, D. et al. (2014). "Numerical analysis of the indentation size effect using a strain gradient crystal plasticity model". In: *Computational Materials Science* 82, pp. 314–319.

Grammenoudis, P. and C. Tsakmakis (2001). "Hardening rules for finite deformation micropolar plasticity: Restrictions imposed by the second law of thermodynamics and the postulate of Il'iushin". In: *Continuum Mechanics and Thermodynamics* 13.5, pp. 325–363.

Grammenoudis, P. and C. Tsakmakis (2005). "Finite element implementation of large deformation micropolar plasticity exhibiting isotropic and kinematic hardening effects". In: *International Journal for Numerical Methods in Engineering* 62.12, pp. 1691–1720.

Gudmundson, P. (2004). "A unified treatment of strain gradient plasticity". In: *Journal of the Mechanics and Physics of Solids* 52.6, pp. 1379–1406.

Guha, S., S. Sangal, and S. Basu (2014). "Numerical investigations of flat punch molding using a higher order strain gradient plasticity theory". In: *International Journal of Material Forming* 7.4, pp. 459–467.

Guo, Y. B., Q. Wen, and K. A. Woodbury (2006). "Dynamic material behavior modeling using internal state variable plasticity and its application in hard machining simulations". In: *Journal of Manufacturing Science and Engineering* 128.3, pp. 749–759.

Gurtin, M. E. (1982). *An Introduction to Continuum Mechanics*. Ed. by Richard Bellman. Academic Press.

Gurtin, M. E. (1996). "Generalized Ginzburg-Landau and Cahn-Hilliard equations based on a microforce balance". In: *Physica D: Nonlinear Phenomena* 92.3-4, pp. 178–192.

Gurtin, M. E. (2002). "A gradient theory of single-crystal viscoplasticity that accounts for geometrically necessary dislocations". In: *Journal of the Mechanics and Physics of Solids* 50.1, pp. 5–32.

Gurtin, M. E. and L. Anand (2005a). "A theory of strain-gradient plasticity for isotropic, plastically irrotational materials. Part I: Small deformations". In: *Journal of the Mechanics and Physics of Solids* 53.7, pp. 1624–1649.

Gurtin, M. E. and L. Anand (2005b). "A theory of strain-gradient plasticity for isotropic, plastically irrotational materials. Part II: Finite deformations". In: *International Journal of Plasticity* 21.12, pp. 2297–2318.

Gurtin, M. E. and L. Anand (2009). "Thermodynamics applied to gradient theories involving the accumulated plastic strain: The theories of Aifantis and Fleck and Hutchinson and their generalization". In: *Journal of the Mechanics and Physics of Solids* 57.3, pp. 405–421.

Han, C. S. et al. (2007). "A Finite Element approach with patch projection for strain gradient plasticity formulations". In: *International Journal of Plasticity* 23.4, pp. 690–710.

He, L. et al. (2018). "Simulation analysis of the influence of dynamic flow stress behavior on chip formation". In: *International Journal of Advanced Manufacturing Technology* 95.5-8, pp. 2301–2313.

Hor, A. et al. (2013). "Modelling, identification and application of phenomenological constitutive laws over a large strain rate and temperature range". In: *Mechanics of Materials* 64, pp. 91–110.

Huang, J et al. (2001). "Gradient Plasticity : Implications to Chip Formation in Machining". In: *4th International ESAFORM Conference on Material Forming*, pp. 527–530.

Huang, Y. et al. (2000). "Mechanism-based strain gradient plasticity - II. Analysis". In: *Journal of the Mechanics and Physics of Solids* 48.1, pp. 99–128.

Hutchinson, J. W. (2012). "Generalizing J2 flow theory: Fundamental issues in strain gradient plasticity". In: *Acta Mechanica Sinica* 28.4, pp. 1078–1086.

Jebahi, M., L. Cai, and F. Abed-Meraim (2020). "Strain gradient crystal plasticity model based on generalized non-quadratic defect energy and uncoupled dissipation". In: *International Journal of Plasticity* 126, p. 102617.

Jing, X. B., B. Lin, and D. W. Zhang (2013). "Modeling and analysis of factors of size effect in micro-cutting: The tool geometry and the depth of cutting". In: *2013 International Conference on Manipulation, Manufacturing and Measurement on the Nanoscale*. August, pp. 314–318.

Jirásek, M. and S. Rolshoven (2009). "Localization properties of strain-softening gradient plasticity models. Part I: Strain-gradient theories". In: *International Journal of Solids and Structures* 46.11-12, pp. 2225–2238.

Johannsen, D. and C. Tsakmakis (2019). "Micropolar plasticity—Part I: modeling based on curvature tensors related by mixed transformations". In: *Acta Mechanica* 230.5, pp. 1565–1606.

Johnson, Gordon R. and William H. Cook (1985). "Fracture characteristics of three metals subjected to various strains, strain rates, temperatures and pressures". In: *Engineering Fracture Mechanics* 21.1, pp. 31–48.

Joshi, S. S. and S. N. Melkote (2004). "An explanation for the size-effect in machining using strain gradient plasticity". In: *Journal of Manufacturing Science and Engineering* 126.4, pp. 679–684.

Kafadar, C. B. and A. C. Eringen (1971). "Micropolar Media - The Classical Theory". In: *International Journal of Engineering Science* 9.3, pp. 271–305.

Khoei, A. R., S. Yadegari, and S. O.R. Biabanaki (2010). "3D finite element modeling of shear band localization via the micro-polar Cosserat continuum theory". In: *Computational Materials Science* 49.4, pp. 720–733.

Koiter, W. T. (1964). "Couple Stresses in the Theory of Elasticity, I & II". In: *Philosophical Transactions of the Royal Society of London B* 67, pp. 17–44.

Kratochvíl, J. et al. (1999). "On physically motivated mesoscale Cosserat model of shear band formation". In: *Scripta Materialia* 41.7, pp. 761–766.

Kuhn, H. and D. Medlin (2000). "High Strain Rate Shear Testing". In: *ASM Handbook*. Vol. 8. ASM International, pp. 447–461.

Laheurte, R. et al. (2006). "Behaviour law for cutting process". In: *International Journal of Advanced Manufacturing Technology* 29.1, pp. 17–23.

Lee, S. et al. (2006). "Large strain deformation field in machining". In: *Metallurgical and Materials Transactions A: Physical Metallurgy and Materials Science* 37.5, pp. 1633–1643.

Lele, S. P. and L. Anand (2009). "A large-deformation strain-gradient theory for isotropic viscoplastic materials". In: *International Journal of Plasticity* 25.3, pp. 420–453.

Lewandowski-Szewczyk, M. J. and S. Stupkiewicz (2020). "Non-standard contact conditions in generalized continua: microblock contact model for a Cosserat body". In: *International Journal of Solids and Structures* 202, pp. 881–894.

Li, J. C., X. W. Chen, and G. Chen (2010). "Numerical simulations on adiabatic shear behaviour of 921A steel pure shear hat-shaped specimens". In: *WIT Transactions on the Built Environment* 113, pp. 323–334.

Li, L. et al. (2009). “Numerical study on the size effect in the ultra-thin sheet’s micro-bending forming process”. In: *Materials Science and Engineering: A* 499, pp. 32–35.

Ling, C. (2018). “Modeling the intragranular ductile fracture of irradiated steels . Effects of crystal anisotropy and strain gradient”. PhD thesis. MINES ParisTech.

Ling, C. et al. (2018). “A reduced micromorphic single crystal plasticity model at finite deformations. Application to strain localization and void growth in ductile metals”. In: *International Journal of Solids and Structures* 134, pp. 43–69.

Lippmann, H. (1969). “Eine Cosserat-Theorie des plastischen Fließens”. In: *Acta Mechanica* 8.3-4, pp. 255–284.

List, G. et al. (2013). “Strain, strain rate and velocity fields determination at very high cutting speed”. In: *Journal of Materials Processing Technology* 213.5, pp. 693–699.

Liu, D. and D. J. Dunstan (2017). “Material length scale of strain gradient plasticity: A physical interpretation”. In: *International Journal of Plasticity* 98, pp. 156–174.

Liu, D., Y. He, et al. (2013a). “Anomalous plasticity in the cyclic torsion of micron scale metallic wires”. In: *Physical Review Letters* 110.24, p. 244301.

Liu, D., Y. He, et al. (2013b). “Toward a further understanding of size effects in the torsion of thin metal wires: An experimental and theoretical assessment”. In: *International Journal of Plasticity* 41, pp. 30–52.

Liu, K. and S. N. Melkote (2006). “Material strengthening mechanisms and their contribution to size effect in micro-cutting”. In: *Journal of Manufacturing Science and Engineering* 128.3, pp. 730–738.

Liu, K. and S. N. Melkote (2007). “Finite element analysis of the influence of tool edge radius on size effect in orthogonal micro-cutting process”. In: *International Journal of Mechanical Sciences* 49.5, pp. 650–660.

Liu, Kai (2005). “Process modeling of micro-cutting including strain gradient effects”. PhD thesis. Georgia Institute of Technology.

Ma, Q. and D. R. Clarke (1995). “Size dependent hardness of silver single crystals”. In: *Journal of Materials Research* 10.04, pp. 853–863.

Mabrouki, T. et al. (2016). “Some insights on the modelling of chip formation and its morphology during metal cutting operations”. In: *Comptes Rendus - Mecanique* 344.4-5, pp. 335–354.

El-Magd, E. and M. Abouridouane (2006). “Characterization, modelling and simulation of deformation and fracture behaviour of the light-weight wrought alloys under high strain rate loading”. In: *International Journal of Impact Engineering* 32.5, pp. 741–758.

Marchand, A. and J. Duffy (1988). “An experimental study of the formation process of adiabatic shear bands in a structural steel”. In: *Journal of the Mechanics and Physics of Solids* 36.3, pp. 251–283.

Mazière, M. and S. Forest (2013). "Strain gradient plasticity modeling and finite element simulation of Lüders band formation and propagation". In: *Continuum Mechanics and Thermodynamics* 27.1-2, pp. 83–104.

Mazière, M. and S. Forest (2015). "Strain gradient plasticity modeling and finite element, simulation of Lüders band formation and propagation". In: *Continuum Mechanics and Thermodynamics* 27, pp. 83–104.

Mediavilla, J., R. H.J. Peerlings, and M. G.D. Geers (2006). "An integrated continuous-discontinuous approach towards damage engineering in sheet metal forming processes". In: *Engineering Fracture Mechanics* 73.7, pp. 895–916.

Menzel, A. and P. Steinmann (2000). "On the continuum formulation of higher gradient plasticity for single and polycrystals". In: *Journal of the Mechanics and Physics of Solids* 48.8, pp. 1777–1796.

Mindlin, R. D. (1963). *Micro-structure in linear elasticity.* Tech. rep. Columbia Univ New York Dept of Civil Engineering and Engineering Mechanics.

Molinari, A., C. Musquar, and G. Sutter (2002). "Adiabatic shear banding in high speed machining of Ti-6Al-4V: Experiments and modeling". In: *International Journal of Plasticity* 18.4, pp. 443–459.

Molinari, A., X. Soldani, and M. H. Miguélez (2013). "Adiabatic shear banding and scaling laws in chip formation with application to cutting of Ti-6Al-4V". In: *Journal of the Mechanics and Physics of Solids* 61.11, pp. 2331–2359.

Mühlhaus, H. and I. Vardoulakis (1987). "The thickness of shear bands in granular". In: *Géotechnique* 37.3, pp. 271–283.

Nedjar, B. (2001). "Elastoplastic-damage modelling including the gradient of damage: Formulation and computational aspects". In: *International Journal of Solids and Structures* 38.30-31, pp. 5421–5451.

Needleman, A. (1979). "Non-normality and bifurcation in plane strain tension and compression". In: *Journal of the Mechanics and Physics of Solids* 27.3, pp. 231–254.

Neff, P. (2004). "A geometrically exact Cosserat shell-model including size effects, avoiding degeneracy in the thin shell limit. Part I: Formal dimensional reduction for elastic plates and existence of minimizers for positive Cosserat couple modulus". In: *Continuum Mechanics and Thermodynamics* 16.6, pp. 577–628.

Neff, P. (2006). "A finite-strain elastic-plastic Cosserat theory for polycrystals with grain rotations". In: *International Journal of Engineering Science* 44.8-9, pp. 574–594.

Nguyen, G. D., A. M. Korsunsky, and J. P. H. Belnoue (2015). "A nonlocal coupled damage-plasticity model for the analysis of ductile failure". In: *International Journal of Plasticity* 64, pp. 56–75.

Nielsen, K. L., C. F. Niordson, and J. W. Hutchinson (2016). "Rolling at small scales". In: *Journal of Manufacturing Science and Engineering* 138.4, pp. 1–10.

Niordson, C. F. and J. W. Hutchinson (2003). "On lower order strain gradient plasticity theories". In: *European Journal of Mechanics, A/Solids* 22.6, pp. 771–778.

Nix, W.D and H. Gao (1998). "Indentation size effects in crystalline materials: A law for strain gradient plasticity". In: *Journal of the Mechanics and Physics of Solids* 46.3, pp. 411–425.

Nye, J. F. (1953). "Some geometrical relations in dislocated crystals". In: *Acta Metallurgica* 1.2, pp. 153–162.

Pamin, J., B. Wcisło, and K. Kowalczyk-Gajewska (2017). "Gradient-enhanced large strain thermoplasticity with automatic linearization and localization simulations". In: *Journal of Mechanics of Materials and Structures* 12.1, pp. 123–146.

Panteghini, A. and L. Bardella (2016). "On the Finite Element implementation of higher-order gradient plasticity, with focus on theories based on plastic distortion incompatibility". In: *Computer Methods in Applied Mechanics and Engineering* 310, pp. 840–865.

Panteghini, A. and R. Lagioia (2021). "A micropolar isotropic plasticity formulation for non-associated flow rule and softening featuring multiple classical yield criteria Part I – Theory". In: *International Journal for Numerical and Analytical Methods in Geomechanics*.

Peerlings, R. H. J. (2007). "On the role of moving elastic-plastic boundaries in strain gradient plasticity". In: *Modelling and Simulation in Materials Science and Engineering* 15.1.

Peerlings, R. H. J. et al. (1996). "Gradient Enhanced Damage for Quasi-brittle Materials". In: *International Journal for Numerical Methods in Engineering* 39.19, pp. 3391–3403.

Peirs, J., P. Verleysen, and J. Degrieck (2008). "The Use of Hat-Shaped Specimens for Dynamic Shear Testing". In: *Foundations of Civil and Environmental Engineering* 11, pp. 97–111.

Peirs, J., P. Verleysen, J. Degrieck, and F. Coghe (2010). "The use of hat-shaped specimens to study the high strain rate shear behaviour of Ti-6Al-4V". In: *International Journal of Impact Engineering* 37.6, pp. 703–714.

Poh, L. H. et al. (2011). "An implicit tensorial gradient plasticity model - Formulation and comparison with a scalar gradient model". In: *International Journal of Solids and Structures* 48.18, pp. 2595–2604.

Poole, W. J., M. F. Ashby, and N. A. Fleck (1996). "Micro-hardness of annealed and work-hardened copper polycrystals". In: *Scripta Materialia* 34.4, pp. 559–564.

Qiu, X. et al. (2003). "The flow theory of mechanism-based strain gradient plasticity". In: *Mechanics of Materials* 35.3-6, pp. 245–258.

Rahmaan, T. et al. (2018). "Strain rate and thermal softening effects in shear testing of AA7075-T6 sheet". In: *EPJ Web of Conferences*. Vol. 183. EDP Sciences, p. 02037.

Rattez, H. et al. (2018). "Numerical Analysis of Strain Localization in Rocks with Thermo-hydro-mechanical Couplings Using Cosserat Continuum". In: *Rock Mechanics and Rock Engineering* 51.10, pp. 3295–3311.

Royer, R. et al. (2011). "Finite strain gradient plasticity theory for high speed machining". In: *Procedia Engineering* 10, pp. 2312–2317.

Al-Rub, R. K. A. and G. Z. Voyiadjis (2004). "Analytical and experimental determination of the material intrinsic length scale of strain gradient plasticity theory from micro- and nano-indentation experiments". In: *International Journal of Plasticity* 20.6, pp. 1139–1182.

Al-Rub, R. K. A. and G. Z. Voyiadjis (2005). "Determination of the Material Intrinsic Length Scale of Gradient Plasticity Theory". In: *International Journal for Multiscale Computational Engineering* 2.3, pp. 377–400.

Russo, R. and B. Chen (2020). "Overcoming the cohesive zone limit in composites delamination: modeling with slender structural elements and higher-order adaptive integration". In: *International Journal for Numerical Methods in Engineering* 121.24, pp. 5511–5545.

Russo, R., S. Forest, and F. A. Girot Mata (2020). "Thermomechanics of Cosserat medium: modeling adiabatic shear bands in metals". In: *Continuum Mechanics and Thermodynamics*, pp. 1–20.

Saanouni, K. (2013). *Damage mechanics in metal forming*. Wiley–ISTE.

Saanouni, K. and M. Hamed (2013). "Micromorphic approach for finite gradient-elastoplasticity fully coupled with ductile damage: Formulation and computational aspects". In: *International Journal of Solids and Structures* 50.14-15, pp. 2289–2309.

Sabet, S. A. and R. de Borst (2019). "Structural softening, mesh dependence, and regularisation in non-associated plastic flow". In: *International Journal for Numerical and Analytical Methods in Geomechanics* 43.13, pp. 2170–2183.

Sansour, C. (1998). "A theory of the elastic-viscoplastic Cosserat continuum". In: *Archives of Mechanics* 50.3, pp. 577–597.

Sansour, C. and J. Keck (1994). "Zum elasto-viskoplastischen Cosserat-Kontinuum". In: *Große plastische Formänderungen, Mitteilungen aus dem Institut für Mechanik, Ruhr-Universit at Bochum*, pp. 38–41.

Scherer, J. M., J. Besson, et al. (2019). "Strain gradient crystal plasticity with evolving length scale: Application to voided irradiated materials". In: *European Journal of Mechanics, A/Solids* 77, p. 103768.

Scherer, J. M., V. Phalke, et al. (2020a). "Lagrange multiplier based vs micromorphic gradient-enhanced rate-(in)dependent crystal plasticity modelling and simulation". In: *Computer Methods in Applied Mechanics and Engineering* 372, p. 113426.

Scherer, J. M., V. Phalke, et al. (2020b). "Lagrange multiplier based vs micromorphic gradient-enhanced rate-(in)dependent crystal plasticity modelling and simulation". In: *Computer Methods in Applied Mechanics and Engineering* 372, p. 113426.

Shirakashi, T. and E. Usui (1973). "Friction Characteristics on Tool Face in Metal Machining". In: *Journal of the Japan Society of Precision Engineering* 39.9, pp. 966–972.

Shu, J. Y. and N. A. Fleck (1998). "The prediction of a size effect in micro-indentation". In: *International Journal of Solids and Structures* 35.13, pp. 1363–1383.

Śloderbach, Z. and J. Pajak (2018). "Thermodynamic potential of free energy for thermo-elastic-plastic body". In: *Continuum Mechanics and Thermodynamics* 30.1, pp. 221–232.

Smyshlyaev, V. P. and N. A. Fleck (1996). "The role of strain gradients in the grain size effect for polycrystals". In: *Journal of the Mechanics and Physics of Solids* 44.4, pp. 465–495.

Stathas, A. and I. Stefanou (2022). "The role of viscous regularization in dynamical problems, strain localization and mesh dependency". In: *Computer Methods in Applied Mechanics and Engineering* 388, p. 114185.

Steinmann, P. (1994). "A micropolar theory of finite deformation and finite rotation multiplicative elastoplasticity". In: *International Journal of Solids and Structures* 31.8, pp. 1063–1084.

Steinmann, P. (1996). "Views on multiplicative elastoplasticity and the continuum theory of dislocations". In: *International Journal of Engineering Science* 34.15, pp. 1717–1735.

Steinmann, P. and K. William (1991). "Localization within the framework of micropolar elasto-plasticity". In: *Advances in Continuum Mechanics*, pp. 296–313.

Stelmashenko, N. A. et al. (1993). "Microindentations on W and Mo oriented single crystals: An STM study". In: *Acta Metallurgica Et Materialia* 41.10, pp. 2855–2865.

Stölken, J. S. and A. G. Evans (1998). "A microbend test method for measuring the plasticity length scale". In: *Acta Materialia* 46.14, pp. 5109–5115.

Tang, B. et al. (2018). "The formation and evolution of shear bands in plane strain compressed nickel-base superalloy". In: *Metals* 8.2, p. 141.

Taylor, G. I. (1938). "Plastic Strain in Metals". In: *The Journal of the Institute of Metals* 62, pp. 307–325.

Taylor, G. I. and H. Quinney (1934). "The latent energy remaining in a metal after cold working". In: *Proceedings of the Royal Society of London. Series A, Containing Papers of a Mathematical and Physical Character* 143.849, pp. 307–326.

Tordesillas, A., J. F. Peters, and B. S. Gardiner (2004). "Shear band evolution and accumulated microstructural development in Cosserat media". In: *International Journal for Numerical and Analytical Methods in Geomechanics* 28.10, pp. 981–1010.

Toupin, R. A. (1962). "Elastic materials with couple-stresses". In: *Archive for rational mechanics and analysis* 11.1, pp. 385–414.

Toupin, R. A. (1964). "Theories of elasticity with couple-stress". In: *Archive for Rational Mechanics and Analysis* 17.2, pp. 85–112.

Vardoulakis, I. (1980). "Shear band inclination and shear modulus of sand in biaxial tests". In: *International Journal for Numerical and Analytical Methods in Geomechanics* 4.2, pp. 103–119.

Voyiadjis, G. Z. and B. Deliktas (2009). "Formulation of strain gradient plasticity with interface energy in a consistent thermodynamic framework". In: *International Journal of Plasticity* 25.10, pp. 1997–2024.

Wang, W. M., L. J. Sluys, and R. de Borst (1997). "Viscoplasticity for instabilities due to strain softening and strain-rate softening". In: *International Journal for Numerical Methods in Engineering* 40.20, pp. 3839–3864.

Wang, X. (2007). "Adiabatic Shear Localization for Steels Based on Johnson-Cook Model and Second- and Fourth-Order Gradient Plasticity Models". In: *Journal of Iron and Steel Research International* 14.5, pp. 56–61.

Wcisło, B. and J. Pamin (2017). "Local and non-local thermomechanical modeling of elastic-plastic materials undergoing large strains". In: *International Journal for Numerical Methods in Engineering* 109.1, pp. 102–124.

Wcisło, B., J. Pamin, et al. (2018). "Numerical analysis of ellipticity condition for large strain plasticity". In: *AIP Conference Proceedings*. Vol. 1922. 1, p. 140008.

Wu, J. and Z. Liu (2010). "Modeling of flow stress in orthogonal micro-cutting process based on strain gradient plasticity theory". In: *International Journal of Advanced Manufacturing Technology* 46.1, pp. 143–149.

Wulfinghoff, S., E. Bayerschen, and T. Böhlke (2013). "A gradient plasticity grain boundary yield theory". In: *International Journal of Plasticity* 51, pp. 33–46.

Wulfinghoff, S. and T. Böhlke (2012). "Equivalent plastic strain gradient enhancement of single crystal plasticity: theory and numerics". In: *Proceedings of the Royal Society A: Mathematical, Physical and Engineering Sciences* 468.2145, pp. 2682–2703.

Ye, G. G. et al. (2014). "Critical cutting speed for onset of serrated chip flow in high speed machining". In: *International Journal of Machine Tools and Manufacture* 86, pp. 18–33.

Yuan, H. and J. Chen (2001). "Identification of the intrinsic material length in gradient plasticity theory from micro-indentation tests". In: *International Journal of Solids and Structures* 38, pp. 8171–8187.

Z-set (2013). "Non-linear material & structure analysis suite, www.zset-software. com". In: Accessed: 2020-03-02.

Zhang, H. W. et al. (2005). "A finite element model for contact analysis of multiple Cosserat bodies". In: *Computational Mechanics* 36.6, pp. 444–458.

Zhang, S. et al. (2013). "Finite element analysis of 3D elastic-plastic frictional contact problem for Cosserat materials". In: *Computational Mechanics* 51.6, pp. 911–925.

Zhang, X. and K. Aifantis (2015). "Interpreting the internal length scale in strain gradient plasticity". In: *Reviews on Advanced Materials Science* 41.1, pp. 72–83.

Zheng, Q. S. (1994). "Theory of Representations for Tensor Functions—A Unified Invariant Approach to Constitutive Equations". In: *Applied Mechanics Reviews* 47.11, p. 545.

Zhu, J. et al. (2020). “Plasticity and size effects of micro-forming sheet processed by electropulsing”. In: *Materials and Manufacturing Processes* 35.10, pp. 1146–1155.

Zorev, N. N. (1963). “Inter-relationship between shear processes occurring along tool face and shear plane in metal cutting”. In: *International research in production engineering* 49, pp. 143–152.

Zouabi, H. et al. (2021). “Local scale analysis of Ti-6Al-4V chip formation during orthogonal cutting using high-speed optical system - HSM”. In: *16th International Conference on High Speed Machining*. Darmstadt, pp. 1–9.